

University of Southampton Research Repository ePrints Soton

Copyright © and Moral Rights for this thesis are retained by the author and/or other copyright owners. A copy can be downloaded for personal non-commercial research or study, without prior permission or charge. This thesis cannot be reproduced or quoted extensively from without first obtaining permission in writing from the copyright holder/s. The content must not be changed in any way or sold commercially in any format or medium without the formal permission of the copyright holders.

When referring to this work, full bibliographic details including the author, title, awarding institution and date of the thesis must be given e.g.

AUTHOR (year of submission) "Full thesis title", University of Southampton, name of the University School or Department, PhD Thesis, pagination

UNIVERSITY OF SOUTHAMPTON

FACULTY OF NATURAL AND ENVIRONMENTAL SCIENCES
Ocean and Earth Science
PhD
Exploring Frontogenesis Processes in New Satellite Sea Surface Temperature Data Sets
by
Mounir Lekouara
Thesis for the degree of Doctor of Philosophy
June 2013

UNIVERSITY OF SOUTHAMPTON

ABSTRACT

FACULTY OF NATURAL AND ENVIRONMENTAL SCIENCES

Ocean and Earth Science

Doctor of Philosophy

EXPLORING FRONTOGENESIS PROCESSES IN NEW SATELLITE SEA SURFACE TEMPERATURE DATA SETS

Mounir Lekouara

This PhD thesis is about understanding some aspects of the dynamics of the ocean surface mixed layer by means of satellite Sea Surface Temperature (SST) measurements. The focus is on surface density fronts which are used as a measure of the dynamical activity at the meso- and submesoscale. A review of the current knowledge on the non-linear physical mechanisms that occur in the vicinity of fronts is presented in Chapter 2. Chapter 3 characterizes the ability of two algorithms for detecting fronts of various sizes and strengths that are embedded in a complex turbulent flow and sampled on noisy two-dimensional images. Chapter 4 explores and compares the performances of several new multi-sensor Level-4 SST products in resolving the small scale gradients. These Group for High Resolution Sea Surface Temperature (GHRSST) data sets offer an unprecedented spatial and temporal SST coverage. Their production however involves a variable and partially unknown level of smoothing which "hides" some of the small scale variability. In Chapter 5, a robust, flexible, automatic and optimized Matlab-based methodology for detecting fronts on SST images and calculating a frontal index is presented. A basic frontal index capturing the frontal length and strength is exploited to quantify the spatial scales present in the various Level-4 SST products. More advanced frontal indexes based on physical oceanography results by others are constructed in order to estimate vertical exchanges occurring at fronts from their signature on the SST. These new frontal indexes, which characterize fronts according to their dynamical significance, allow the quantification of the upwelling, subduction and restratification associated with frontal submesoscale

processes. Finally, the spatial and temporal variability of ocean fronts is explored in order to determine their sensitivity to climatic signals.

Contents

ABSTRAC [*]	Γ	i
Contents		i
List of tak	oles	v
List of fig	ures	vii
J		
DECLARA [®]	TION OF AUTHORSHIP	xxi
Acknowle	dgements	xxiii
Abbreviat	ions	xxvii
•		
1. Chap	ter 1: Introduction	1
1.1	General introduction	1
1.1.1	Climate science context	1
1.1.2	Rationale for the small scales exploration	2
1.1.3	Focus on surface density fronts	3
1.1.4	From SST images to surface density fronts	5
1.1.5	Scope of the research	6
1.1.6	Summary of the objectives	8
1.2	The scientific context	8
1.2.1	Generalities about ocean fronts	8
1.2.2	Satellite observations of fronts	10
1.2.3	Previous efforts to combine observations with theory	13
1.3	Outline of the thesis content	15
1.3.1	The approach: bridging between scientific communities	15
1.3.2	Road map for the thesis	16
2. Chap	oter 2: Dynamics of ocean fronts	18
2.1	Fronts within the wider context of upper ocean processes	18
2.2	Frontogenesis	21
2.2.1	Time evolution of the horizontal density gradient	23
2.2.2 Geostro	The theory of strain driven frontogenesis in the Quasi-ophic (QG) regime	23
2.2.3 (SG) reg	The theory of strain driven frontogenesis in the Semi-Geost gime	•
2.2.4	The theory of frontogenesis in the SQG regime	33
2.2.5	Scaling of the Omega equation	35

2.3	Restratification effect of frontal submesoscale instabilities	36
2.4	Basin-wide models combining several mechanisms	42
2.5	Questions that are left to be answered	47
3. Chapt	er 3: SATELLITE-BASED FRONT DETECTION TECHNIQU	ES.53
3.1	Front detection methods based on local statistics of the SST	
3.2	The Canny method	56
3.2.1	A new implementation of the Canny method	57
3.3	The Cayula method	61
3.3.1	Description of the Cayula method	62
3.3.2	Implementation of the Cayula method	65
3.4	Definition of simple Frontal Indexes	70
3.5	A critical analysis of frontal detection techniques	73
3.5.1	Characterization of the Canny algorithm	74
3.5.2	Characterization of the Cayula algorithm	80
3.5.2.1 scene	The Cayula algorithm at the window level on a noise-free 81	ž
3.5.2.2	The Cayula algorithm at the window level on a noisy sce	ne . 85
3.5.3	Cross-comparisons of the front detection techniques	86
3.5.3.1 noisy i	Detection of fronts of all scales and strength on potentia mages	-
3.5.	3.1.1 Resolution of front length on noise-free images	88
3.5.	3.1.2 Resolution of front length on noisy images	91
3.5.	3.1.3 Resolution of front strength on noise-free images	101
3.5.	3.1.4 Resolution of front strength on noisy images	103
3.5.3.2	Detection of intricate fronts and fronts of high sinuosity.	104
3.5.3.3	B Detection of fronts of all orientations	105
3.5.3.4	Detection of fronts on images that suffer from missing p 108	ixels
3.5.3.5 project	Detection of fronts on images projected on a cylindrical tion 111	
3.5.3.6	Robustness to arbitrary parameters	111
3.5.3.7	7 Computational efficiency	114
3.6	Algorithm selection in relation to ocean dynamics objectives	s 115
4. Chapt	er 4: SST datasets for front detection	117
4.1	Introduction to the SST products	118
	Level-2 SST	118

	4.1.2	Level-4 SST	12 <i>6</i>
	4.1.2. (OSTIA	•	nalysis
	4.1.2.2 analys	,	
	4.1.2.3 analys	5 , , , , , , , , , , , , , , , , , , ,	
	4.1.2.4 and Al	The NOAA's National Climatic Data Center (NCDC) AVHR	•
	4.1.3	Level-3 SST	13 <i>6</i>
	4.2	Limitations of the Level-4 SST for front detection	139
	4.2.1	General considerations	139
	4.2.2	Level-4 analyses are spatially smoothed	140
	4.2.3	Level-4 analysis smoothing scales vary spatially	144
	4.2.4	Level-4 analysis smoothing scales vary in time	153
	4.3	Qualitative comparisons of the gradients	155
	4.4	Qualitative comparison of detected fronts	161
	4.5	From temperature gradient to density gradient	167
	4.6	Conclusion on the dataset/method to use	169
5	. Chapt	er 5: Frontal Indices	171
	5.1	Introduction	171
	5.1.1	General aspects of the frontal indexes	172
	5.1.2	Computational aspects	174
	5.1.2.	Approach to handle a large number of files	175
	5.1.2.2	2 Approach to handle a large number of parameters	175
	5.1.2.3	Approach to handle a very large processing load	177
	5.1.3	Density gradient calculation	181
	5.2	Frontal Gradient Index	182
	5.2.1	FLI and FGI from OSTIA	189
	5.2.2	FLI and FGI from ODYSSEA	204
	5.2.3	FLI and FGI from REMSS_MW	213
	5.2.4	FLI and FGI from IFREMER_L3_IR	216
	5.3	Spall (1995) Index Of Subduction	223
	5.4	Lapeyre and Klein (2006) index of vertical velocity	227
	5.5	Capet et al. (2008) index of frontogenesis	234
	5.6	Fox-Kemper and Ferrari (2008) index of restratification at fi	
	5.7	Conclusion	
<u>ج</u>		er 6: Climatic variability of frontal activity	
•		EL OL GIIIIALIC VALIADIIILY OL HVIILAL ACLIVILY	1

	6.1	Wavenumber spectrum of OSTIA_RAN	258
	6.2	Global spatial distribution of the FGI	259
	6.3	Temporal distribution of the FGI	262
	6.4	Comparison of the OSTIA_RAN FGI with the OSTIA FGI	265
	6.5	Climatological variability of the FGI	270
	6.6	High spatial resolution signal exploration	275
	6.7	Quantitative trends of the FGI	277
	6.8	Correlations with climatic indexes	285
	6.9	Conclusion	294
7.	Chapte	er 7: Conclusion	297
	7.1	Overview of the achievements in a multi-faceted research landscape	297
	7.2	Summary of scientific achievements	
	7.2.1 SST imag	Objective 1: define a methodology for the detection of fronts des	on
	7.2.2 dynamica	Objective 2: the derivation of information about oceanographial parameters	
	7.2.3 variability	Objective 3: the characterization of the spatial and temporal y of the frontal activity	303
	7.3	Technical achievements	304
	7.3.1	Implementation of the front detection algorithms	304
	7.3.2	Implementation of the geo-physical routines	305
	7.3.3	Implementation of a software engineering layer	305
	7.4	Where the study can be taken further	306
	7.4.1	Improving the Level-4 products feature resolution knowledge	306
	7.4.2	Improving the knowledge of the frontal width	308
	7.4.3	Improving the understanding of the density compensation $\ldots\ldots$	308
	7.4.4 assumpti	Developing the dynamical parameterizations and refining the ons	309
	7.4.5	Using the tools for regional studies	309
i	st of Refe	rences	211

List of tables

Table 4-1: summ	ary of the GHRSST Level-4 and Level-3 products mentioned ir
this	s thesis13
Table 4-2: type o	f SST input data available for the 3 NCDC Level-4 SST
pro	oducts as a function of the cloud conditions15
Table 4-3: summ	ary of the two stages of frontal exploration17
Table 5-1: Set of	parameters for the detection of fronts and the calculation of
fro	ntal indexes with the routines developed in the context of
thi	s thesis17

List of figures

Figure	2-1:	Schematic configuration for an intensifying straight horizontal density front	24
Figure	2-2:	Confluence, vorticity and vertical velocity at a front	26
Figure	2-3:	Ageostrophic streamfunctions ψ for two legs across a surveyed front	28
Figure	2-4:	Ageostrophic circulation driven by a negative point-source Q-vector	31
Figure	2-5:	Development of mixed layer baroclinic instabilities along a temperature front undergoing geostrophic adjustment	39
Figure	2-6:	Increase in domain-averaged buoyancy frequency N2 as a result of slumping of the mixed layer front shown in Figure 2-5	
Figure	2-7:	Simulated instantaneous surface temperature field	44
Figure	2-8:	Instantaneous horizontal patterns for simulated frontal quantities	46
Figure	3-1:	Daily SST gradient derived from a 25 km resolution Optimal Interpolation of Microwave SST dataset	55
Figure	3-2:	Canny front detection algorithm applied to an OSTIA SST image .	50
Figure	3-3:	AVHRR/2 SST fields with clouds zeroed and detected edges	55
Figure	3-4:	Illustration of the different levels in the Cayula algorithm 1/2	57
Figure	3-5:	Illustration of the different levels in the Cayula algorithm 2/2	58
Figure	3-6:	OSTIA SST and the frontal strength FTDI of the fronts detected by the Cayula algorithm	
Figure	3-7:	Probability of detecting a front over the California Current	73
Figure	3-8.	Smoothing affect of Caussian filters on a simple front	76

front
Figure 3-10: Scaling factor of the front maximum gradient as a function of **Rgauss**
Figure 3-11: Scaling factor of the front maximum gradient as a function of **Rmean**
Figure 3-12: Two simplified configurations under which a window of the Cayula algorithm can see a front
Figure 3-13: Temperature difference measured by the Cayula algorithm at the window level during the segmentation test
Figure 3-14: Maximum noise (in K) allowed on top of synthetic SST frontal scenes for both the segmentation and cohesion tests to be positive in the histogram algorithm
Figure 3-15: Relative Front Length (FLI _{detected} /FLI _{actual}) of the Canny algorithm. 89
Figure 3-16: Relative Front Length (FLI _{detected} /FLI _{actual}) of the Cayula algorithm.90
Figure 3-17: Relative Front Length ($FLI_{detected}/FLI_{actual}$) of the Canny algorithm. The synthetic SST suffer from a Gaussian noise of $\sigma n = 0.1K93$
Figure 3-18: Relative Front Length (FLI _{detected} /FLI _{actual}) of the Canny algorithm. The synthetic SST suffer from a Gaussian noise of $\sigma n=0.2K94$
Figure 3-19: Relative Front Length (FLI _{detected} /FLI _{actual}) of the Canny algorithm. The synthetic SST suffer from a Gaussian noise of $\sigma n = 0.3K95$
Figure 3-20: Example of the Canny algorithm detecting too many fronts because of the presence of noise
Figure 3-21: Relative Front Length (FLI _{detected} /FLI _{actual}) of the Cayula algorithm. Synthetic SST scenes suffer from a Gaussian noise $\sigma n=0.1~K.$ 97
Figure 3-22: Relative Front Length (FLI _{detected} /FLI _{actual}) of the Cayula algorithm. Synthetic SST scenes suffer from a Gaussian noise $\sigma n = 0.2 \ K$. 98

Figure 3-23: Relative Front Length (FLI $_{ m detected}$ /FLI $_{ m actual}$) of the Cayula algorithm Synthetic SST scenes suffer from a Gaussian noise $\sigma n=0.3~K$.	
Figure 3-24: Relative Front Length (FLl _{detected} /FLl _{actual}) of the Cayula algorithm. The synthetic SST scenes are filtered by a 3 by 3 pixels median filter.	n
Figure 3-25: Relative Front Length (FLI _{detected} /FLI _{actual}) of the Cayula algorithm. The synthetic SST scenes are filtered by a 9 by 9 pixels median filter	n
Figure 3-26: Front Width as a function of the front's gradient and temperature difference	
Figure 3-27: Example of the Cayula algorithm not being able to detect a from whose sinuosity is too high	
Figure 3-28: Detected relative front length as a function of the orientation of the front, for the Cayula and the Canny algorithms	
Figure 3-29: Two frontal orientations with non-similar cohesion as assessed by the Cayula algorithm	08
Figure 3-30: Example of the Canny algorithm being strongly impacted by missing data	10
Figure 3-31: Comparison of the performances of the Cayula algorithm when dealing with different resolutions	
Figure 4-1: Typical example of the daily coverage of SST from six different S data products	
Figure 4-2: Percent coverage of SST measurements from the AMSRE and the AVHRR in 3-day composite average maps	24
Figure 4-3: Example of an AATSR swath SST plotted at full resolution 1	25
Figure 4-4: AMSR-E SST plotted at 0.25° resolution	25
Figure 4-5: Results of collating SST data with the ODYSSEA analysis with and	30 30

Figure 4-6: Example of Level-3 multi-sensor ODYSSEA product
Figure 4-7: Example of an error in the ODYSSEA output
Figure 4-8: SST gradient magnitude of 4 GHRSST products
Figure 4-9: Detected fronts on 4 GHRSST products
Figure 4-10: OSTIA background error standard deviation for 10 km mesoscale and 100 km synoptic scale features derived from three years of daily FOAM ocean model outputs
Figure 4-11: ODYSSEA spatial correlation length scale for the mesoscale 147
Figure 4-12: NCDC AMSR +AVHRR and AVHRR-only zonal and meridional error correlation scales
Figure 4-13: Radial correlation length scale in km, calculated for OSTIA/ODYSSEA/REMSS MW on 01/01/2008
Figure 4-14: Ratios of the autocorrelation length scales
Figure 4-15: Gradient magnitude of OSTIA, ODYSSEA and REMSS MW Level-4 analysis SST products, on 01/01/2009
Figure 4-16: Regional ratios of monthly average SST gradient over the month of January 2008 for the OSTIA, ODYSSEA and REMSS MW 158
Figure 4-17: Monthly zonal average SST gradient and ratios over the month of January 2008 for the OSTIA, ODYSSEA and REMSS MW 159
Figure 4-18: Monthly zonal average SST gradient ratios over the month of January 2008 for the OSTIA, ODYSSEA and REMSS MW with varying smoothing involved (σs =0 to 100 km)
Figure 4-19: FLI and FTDI of OSTIA, ODYSSEA and REMSS MW
Figure 4-20: FLI and FTDI ratios of OSTIA, ODYSSEA and REMSS MW 164
Figure 4-21: Zonally averaged FLI and FTDI ratios of OSTIA, ODYSSEA and REMSS MW

Figure 4-22: Zonally averaged FLI and FTDI ratios of OSTIA, ODYSSEA and REMSS MW	
Figure 5-1: General architecture of the frontal detection routines	180
Figure 5-2: De Boyer Montegut et al. (2004) climatology for mixed-layer on the North Atlantic	•
Figure 5-3: North Atlantic region	189
Figure 5-4: Percentage of the area of the North Atlantic region that has mixed layer depth shallower than 75 m	
Figure 5-5: Front Length Index processed on daily OSTIA over the North Atlantic region with $d=0~km,~Lf=0.5~km,$ and $\Delta s=25~km$	
Figure 5-6: Front Gradient Index processed on daily OSTIA over the Nor Atlantic region with $d=0~km, Lf=0.5~km$, and $\Delta s=25~k$	
Figure 5-7: Front Length Index processed on weekly OSTIA over the No Atlantic region with $d=0~km,~Lf=0.5~km,$ and $\Delta s=25~km$	
Figure 5-8: Front Gradient Index processed on weekly OSTIA over the N Atlantic region with $d=0~km, Lf=0.5~km$, and $\Delta s=25~k$	
Figure 5-9: Maps of average monthly Front Gradient Index processed of OSTIA over the North Atlantic region with $m{d} = m{0} \ m{km}$, $m{L} m{f} = m{a}$ and $\Delta m{s} = m{25} \ m{km}$.	0.5 km,
Figure 5-10: NOAA NCEP reanalysis daily percentage of cloud coverage the North Atlantic	
Figure 5-11: Front Length Index processed on weekly OSTIA over the N Atlantic region with $m{d}=m{0}$ $m{km}$, $m{L}m{f}=m{0}.m{5}$ $m{km}$, and $\Delta m{s}=m{50}$ $m{k}$	
Figure 5-12: Front Gradient Index processed on weekly OSTIA over the Atlantic region with $m{d}=m{0}$ $m{km}$, $m{L}m{f}=m{0}.m{5}$ $m{km}$, and $\Delta m{s}=m{5}m{0}$ $m{k}$	
Figure 5-13: Front Length Index processed on weekly OSTIA over the N Atlantic region with $d = 25 km$, $Lf = 0.5 km$, and $\Delta s = 25$.	

Figure 5-14: Front Gradient Index processed on weekly OSTIA over the North Atlantic region with $d=25~km$, $Lf=0.5~km$, and $\Delta s=25~km$ 197
Figure 5-15: Front Length Index processed on weekly OSTIA over the North Atlantic region with $d=50~km$, $Lf=0.5~km$, and $\Delta s=50~km$. 198
Figure 5-16: Front Gradient Index processed on weekly OSTIA over the North Atlantic region with $d=50~km$, $Lf=0.5~km$, and $\Delta s=50~km$. 198
Figure 5-17: Front Length Index processed on weekly OSTIA over the North Atlantic region with $d=25~km$, $Lf=1~km$, and $\Delta s=25~km$ 199
Figure 5-18: Front Gradient Index processed on weekly OSTIA over the North Atlantic region with $d=25~km$, $Lf=1~km$, and $\Delta s=25~km$ 199
Figure 5-19: Front Length Index processed on weekly OSTIA over the North Atlantic region with $d=0~km,~Lf=1~km,~$ and $\Delta s=25~km.$ 200
Figure 5-20: Front Gradient Index processed on weekly OSTIA over the North Atlantic region with $d=0$ km , $Lf=1$ km , and $\Delta s=25$ km 200
Figure 5-21: Average OSTIA SST over the North Atlantic
Figure 5-22: Average OSTIA SST un-scaled gradient magnitude over the North Atlantic
Figure 5-23: Average OSTIA SST (low-pass 50 km) gradient magnitude over the North Atlantic
Figure 5-24: Average OSTIA SST (high-pass 50 km) gradient magnitude over the North Atlantic
Figure 5-25: Average OSTIA SST (high-pass 100 km) gradient magnitude over the North Atlantic
Figure 5-26: Front Length Index processed on daily ODYSSEA over the North Atlantic region with $d=0~km,~Lf=0.5~km,~$ and $\Delta s=25~km.$. 206
Figure 5-27: Front Gradient Index processed on daily ODYSSEA over the North Atlantic region with $d=0~km,~Lf=0.5~km,~$ and $\Delta s=25~km.$. 207
Figure 5-28: Sequence of un-scaled ODYSSEA SST gradient magnitude 208

Figure 5-29: Front Length Index processed on weekly ODYSSEA over the North Atlantic region with $d = 50 km$, $Lf = 0.5 km$, and $\Delta s = 50 km$. 209
Figure 5-30: Front Gradient Index processed on daily ODYSSEA over the North Atlantic region with $d=50~km$, $Lf=0.5~km$, and $\Delta s=50~km$ 209
Figure 5-31: Average ODYSSEA SST gradient magnitude over the North Atlantic
Figure 5-32: Average ODYSSEA SST (low-pass 50 km) gradient magnitude over the North Atlantic
Figure 5-33: Un-scaled OSTIA SST gradient magnitude212
Figure 5-34: Un-scaled ODYSSEA SST gradient magnitude212
Figure 5-35: Front Length Index processed on weekly REMSS_MW over the North Atlantic region with $d=0$ km , $Lf=0.5$ km , and $\Delta s=25$ km .
Figure 5-36: Front Gradient Index processed on weekly REMSS_MW over the North Atlantic region with $d=0$ km , $Lf=0.5$ km , and $\Delta s=25$ km .
Figure 5-37: Front Length Index processed on weekly REMSS_MW over the North Atlantic region with $d=0$ km , $Lf=0.5$ km , and $\Delta s=50$ km .
Figure 5-38: Front Gradient Index processed on weekly REMSS_MW over the North Atlantic region with $d=0$ km , $Lf=0.5$ km , and $\Delta s=50$ km .
Figure 5-39: Average un-scaled REMSS_MW SST gradient magnitude over the North Atlantic
Figure 5-40: Average un-scaled REMSS_MW SST (low-pass 50 km) gradient magnitude over the North Atlantic216
Figure 5-41: Front Length Index processed on weekly IFREMER_L3_IR over the North Atlantic region with $d=0$ km , $Lf=0.5$ km , and $\Delta s=$

Figure 5-42:	Front Gradient Index processed on weekly IFREMER_L3_IR over	
	the North Atlantic region with $d=0~km, Lf=0.5~km$, and	
	$\Delta s = 10 \ km.$	218
Figure F 42.	Front Longth Inday processed on weakly IEDEMED 12 ID over the	. .
rigure 5-45:	Front Length Index processed on weekly IFREMER_L3_IR over the	ie
	North Atlantic region with $d = 25 km$, $Lf = 0.5 km$, and	
	$\Delta s = 25 \ km. $	219
Figure 5-44:	Front Gradient Index processed on weekly IFREMER_L3_IR over	
	the North Atlantic region with $d=25~km$, $Lf=0.5~km$, and	
	$\Delta s = 25 \ km$	219
Figuro F 15:	Front Length Index processed on weekly IFREMER_L3_IR over the	20
rigule 5-45.		ie
	North Atlantic region with $d = 50 \text{ km}$, $Lf = 0.5 \text{ km}$, and	
	$\Delta s = 50 \ km. $	220
Figure 5-46:	Front Gradient Index processed on weekly IFREMER_L3_IR over	
	the North Atlantic region with $d = 50 \ km$, $Lf = 0.5 \ km$, and	
	$\Delta s = 50 \ km$.	20
Figure 5-47:	Front Length Index processed on weekly IFREMER_L3_IR over the second control of the seco	ne
	NA1 region with $d=0$ km , $Lf=0.5$ km , and $\Delta s=10$ km 2	221
Figure 5-48:	Front Gradient Index processed on weekly IFREMER_L3_IR over	
	the NA1 region with $d=0$ km, $Lf=0.5$ km, and $\Delta s=10$ km. 2	221
Figure 5-49:	Average un-scaled IFREMER_L3_IR SST gradient magnitude over	
	the North Atlantic	222
Figure 5-50:	Average un-scaled IFREMER_L3_IR SST (low-pass 50 km) gradie	nt
	magnitude over the North Atlantic	
Figure 5-51:	Spall (1995) index processed on OSTIA over the North Atlantic	
	region with d=0 km, Lf=0.5 km, and Δ s=25 km	225
Figure 5-52:	Maps of average monthly Spall95_Subduction index processed	or
rigule 5-52:		UII
	daily OSTIA over the North Atlantic region with $d=0 \ km$,	
	$Lf = 0.5 km$, and $\Delta s = 25 km$.	226

Figure 5-53: Spall (1995) index of permanent subduction processed on weekly OSTIA over the North Atlantic region with $d=0$ km , $Lf=1$ km , and $\Delta s=25$ km .
Figure 5-54: Front Length Index processed on daily IFREMER_L3_IR over the Sargasso Sea region with $d=0$ km, $Lf=1$ km, $\Delta s=10$ km 231
Figure 5-55: Lapeyre_Klein_SSH index of frontogenesis induced upwelling in $m.day - 1$ processed on daily IFREMER_L3_IR over the Sargasso Sea region with $d = 0$ km , $Lf = 1$ km , $\Delta s = 10$ km ,
Figure 5-56: Monthly composite of the Lapeyre_Klein_SSH index of frontogenesis induced upwelling processed on daily IFREMER_L3_IR over the Sargasso Sea region with $d=0~km$, $Lf=1~km$, $\Delta s=10~km$
Figure 5-57: Front Length Index processed on daily IFREMER_L3_IR over the Mediterranean Sea region with $d=0$ km, $Lf=1$ km and $\Delta s=10$ km
Figure 5-58: Lapeyre_Klein index of frontogenesis induced upwelling processed on daily IFREMER_L3_IR over the Mediterranean Sea region with $d=0$ km, $Lf=1$ km, $\Delta s=10$ km
Figure 5-59: Monthly composite of the Lapeyre_Klein index of frontogenesis induced upwelling processed on daily IFREMER_L3_IR over the Mediterranean Sea region with $d=0$ km, $Lf=1$ km, $\Delta s=10$ km, and $T=10-3$ kg $m-3$ km -1 .
Figure 5-60: IFREMER Level-3 SST of the California Current upwelling 238
Figure 5-61: Density gradient magnitude
Figure 5-62: Frontogenesis function FS in $kg2m-8s-1$ calculated from the density gradient magnitude shown on Figure 5-61 and altimetry data239
Figure 5-63: California Current region
Figure 5-64: Cloud coverage over the California Current region

(rontogenesis funtion FS calculated on OSTIA in the California Current Region, plotted on the fronts detected with $d=25~km$, $Lf=0.5~km$, and $\Delta s=25~km$
	ront Length Index processed on daily OSTIA over the California Current region with $d=25~km, Lf=0.5~km$, and $\Delta s=25~km.241$
i	apet_Fs index of frontogenesis calculated on daily OSTIA SST images over the California Current region with $d=25~km$, $Lf=0.5~km$, and $\Delta s=25~km$
Figure 5-68: N	Nonthly-averaged FLI and Capet_Fs index calculated on OSTIA
\	with $d = 25 km$, $Lf = 0.5 km$, and $\Delta s = 25 km$
1	ront Length Index processed on daily IFREMER_L3_IR over the North Atlantic region with $d=0$ km , $Lf=0.5$ km , and $\Delta s=10$ km .
ı	ox_kemper index of restratification at fronts on daily IFREMER_L3_IR over the North Atlantic region with $d=0~km$, $Lf=0.5~km$, and $\Delta s=10~km$
	Ionthly average of Fox_kemper index processed on daily IFREMER_L3_IR with $d=0$ km , $Lf=0.5$ km , and $\Delta s=10$ km . 248
(quivalent vertical heat flux due to submesoscale restratification of the mixed layer as estimated by Fox-Kemper and Ferrari (2008)
_	TIA_RAN zonal wavenumber spectrum over the Tropical Pacific
•	ng term mean Front Gradient Index (FGI) processed on weekly OSTIA_RAN with $d=0$ km , $Lf=0.5$ km , and $\Delta s=25$ km 261
`	ng term standard deviation Front Gradient Index processed on weekly OSTIA_RAN with $d=0$ km , $Lf=0.5$ km , and $\Delta s=$

Figure 6-4: Front Gradient Index processed on weekly OSTIA_RANand OSTIA
over the North Atlantic region with $d = 0 km$, $Lf = 0.5 km$, and
$\Delta s = 25 \text{ km.}$
Figure 6-5: Front Gradient Index processed on weekly OSTIA_RAN and OSTIA
over the Tropical Atlantic North region with $d=0~km$, $Lf=$
0.5 km , and $\Delta s = 25 km$
20 101111111111111111111111111111111111
Figure 6-6: Front Gradient Index processed on weekly OSTIA_RAN and OSTIA
over the Equatorial Atlantic region with $d=0$ km , $Lf=0.5$ km ,
and $\Delta s = 25 km$
and 15 = 20 km.
Figure 6-7: Front Gradient Index processed on weekly OSTIA_RAN and OSTIA
over the Tropical Atlantic South region with $oldsymbol{d} = oldsymbol{0} oldsymbol{km},$
$Lf = 0.5 km$, and $\Delta s = 25 km$
<i>Lj = 0.5 km</i> , and 25 = 25 km204
Figure 6-8: Front Gradient Index processed on weekly OSTIA_RAN and OSTIA
over the South Atlantic region with $d = 0 km$, $Lf = 0.5 km$, and
$\Delta s = 25 \ km \dots 265$
Δ5 – 25 km 200
Figure 6-9: Front Gradient Index processed on weekly OSTIA_RAN and OSTIA
over the Mediterranean Sea with $d = 0 km$, $Lf = 0.5 km$, and
$\Delta s = 25 \ km.$
45 – 25 km200
Figure 6-10: Front Gradient Index processed on weekly OSTIA_RAN and OSTIA
over the North Atlantic region with $d = 25 km$, $Lf = 0.5 km$, and
$\Delta s = 25 \text{ km}. \qquad 267$
Δ5 – 25 km 207
Figure 6-11: Front Gradient Index processed on weekly OSTIA_RAN and OSTIA
over the North Atlantic region with $d = 50 \ km$, $Lf = 0.5 \ km$, and
$\Delta s = 25 \text{ km}. \qquad 268$
Figure 6-12: 2007 annual mean Front Gradient Index difference between
OSTIA_RAN and OSTIA, both calculated with $d = 25 km$,
$Lf = 0.5 km$, and $\Delta s = 25 km$
Lj — υ. 3 κπι, απα Δδ — Δ3 κπι200
Figure 6-13: High Spatial Resolution monthly mean of Front Gradient Index
processed on weekly OSTIA_RAN with $d = 0 km$, $Lf = 0.5 km$,
and $\Delta s = 25 \text{ km}$

•	processed on weekly OSTIA with $m{d} = m{0} \ m{km}$, $m{L} m{f} = m{0}$. $m{5} \ m{km}$, and $\Delta m{s} = m{25} \ m{km}$
_	Climatology of Front Gradient Index processed on weekly OSTIA_RAN over the North Atlantic region with $m{d} = m{0} \ m{km}$, $m{L} m{f} = m{0} . m{5} \ m{km}$, and $\Delta m{s} = m{25} \ m{km}$, for several latitude bands 270
_	Climatology of Front Gradient Index processed on weekly OSTIA_RAN over the Tropical Atlantic region with $d=0~km$, $Lf=0.5~km$, and $\Delta s=25~km$, for several latitude bands 271
•	Elimatology of Front Gradient Index processed on weekly OSTIA_RAN over the South Atlantic region with $d=0~km$, $Lf=0.5~km$, and $\Delta s=25~km$, for several latitude bands 271
-	eak to peak of seasonal cycle of Front Gradient Index (FGI processed on weekly OSTIA_RAN with $d=0~km, Lf=0.5~Km,$ and $\Delta s=25~km$
-	Pate of minimum climatology of Front Gradient Index processed on weekly OSTIA_RAN with $d=0~km,~Lf=0.5~km$, and $\Delta s=25~km$.
_	Pate of maximum climatology of Front Gradient Index processed on weekly OSTIA_RAN with $d=0$ km , $Lf=0.5$ km , and $\Delta s=25$ km .
_	Correlation between Front Gradient Index processed on weekly OSTIA_RAN with $d=0~km$, $Lf=0.5~km$, and $\Delta s=25~km$ and monthly Boyer Montegut et al. (2004) Mixed Layer Depth 275
_	Monthly average Front Gradient Index processed on weekly OSTIA_RAN with $m{d} = m{0} \ m{km}$, $m{L} m{f} = m{0}.m{5} \ m{km}$, and $\Delta m{s} = m{25} \ m{km}$ 276
_	lovmöller plot of the Front Gradient Index processed on weekly OSTIA_RAN with $m{d} = m{0} \ m{km}$, $m{L} m{f} = m{0}. m{5} \ m{km}$, and $\Delta m{s} = m{25} \ m{km}$ 277
_	Oaily trend of Front Gradient Index processed on weekly OSTIA RAN with $d=0$ km , $Lf=0.5$ km , and $\Delta s=25$ km 278

_	ormalized trend of Front Gradient Index processed on weekly OSTIA_RAN with $d=0$ km, $Lf=0.5$ km, and $\Delta s=25$ km2	
•	vaily trend of Front Gradient Index processed on weekly OSTIA_RAN with $m{d} = m{0} \ m{km}$, $m{L} m{f} = m{0}$. $m{5} \ m{km}$, and $\Delta m{s} = m{25} \ m{km}$ 2	80
_	nnual mean, annual minimum and annual maximum, date of annual minimum and date of annual maximum OF FGI2	81
Figure 6-28: A	s for Figure 6-27 but for box 3 and box 4 on Figure 6-262	82
Figure 6-29: A	s for Figure 6-27 but for box 5 and box 6 on Figure 6-262	82
Figure 6-30: A	s for Figure 6-27 but for box 7 on Figure 6-262	83
	ront Gradient Index processed on weekly OSTIA_RAN and OSTI over the whole oceans with $m{d} = m{0} \ m{km}$, $m{L} m{f} = m{0}$. $m{5} \ m{km}$, and $\Delta m{s} = m{25} \ m{km}$	
1	ront Gradient Index processed on weekly OSTIA_RAN and OSTI for latitudes between 45 $^{\circ}$ S and 45 $^{\circ}$ N with $d=0$ km , $Lf=0.5$ km , and $\Delta s=25$ km 2	
Figure 6-33: N	IINO 3.4 index2	85
	agged correlation of the monthly anomaly of Front Gradient Index with NINO 3.4. The FGI is processed on weekly OSTIA_RAN with $d=0~km$, $Lf=0.5~km$, and $\Delta s=25~km$ 2	87
;	ag corresponding to the maximum correlation of the monthly anomaly of Front Gradient Index with NINO 3.4. The FGI is processed on weekly OSTIA_RAN with $d=0~km, Lf=0.5~km$, and $\Delta s=25~km$.	
	Ionthly averages of High Spatial Resolution monthly mean of Front Gradient Index processed on weekly OSTIA_RAN with $d=0~km,~Lf=0.5~km,~$ and $\Delta s=25~km.$ El Niño event of end of 1997	
_	Ionthly averages of High Spatial Resolution monthly mean of Front Gradient Index processed on weekly OSTIA_RAN with	

	$d=0~km,~Lf=0.5~km,$ and $\Delta s=25~km.$ La Niña event of end of
	1998
•	ong term mean Front Gradient Index processed on weekly OSTIA_RAN with $m{d} = m{0} \ m{km}$, $m{Lf} = m{0}.m{5} \ m{km}$, and $\Delta m{s} = m{25} \ m{km}$ 292
•	Annual mean, annual minimum and annual maximum of FGI, date of annual minimum of FGI and date of annual maximum of FGI. The FGI is extracted from the boxes 1 to 4 shown on Figure
	6-38

DECLARATION OF AUTHORSHIP

I, Mounir Lekouara declare that the thesis entitled Exploring Frontogenesis Processes in New Satellite Sea Surface **Temperature Data Sets** and the work presented in the thesis are both my own, and have been generated by me as the result of my own original research. I confirm that: · this work was done wholly or mainly while in candidature for a research degree at this University; · where any part of this thesis has previously been submitted for a degree or any other qualification at this University or any other institution, this has been clearly stated; · where I have consulted the published work of others, this is always clearly attributed: where I have quoted from the work of others, the source is always given. With the exception of such quotations, this thesis is entirely my own work; I have acknowledged all main sources of help; · where the thesis is based on work done by myself jointly with others, I have made clear exactly what was done by others and what I have contributed myself; none of this work has been published before submission.

xxi

Acknowledgements

This PhD thesis was a very personal journey, it would nevertheless not have been possible without the help and support from many people. I would first and foremost like to thank my supervisor Prof Ian S. Robinson. Working with Ian was a fantastic source of inspiration and I have gained greatly from Ian's creativity and profound knowledge in oceanography. Ian was never short of a motivation trick and his human skills were instrumental in my achievements. Thorough my post-graduate studies, Ian gave me the freedom to pursue my ideas and always supported me along the way, for this I am very grateful. I would also like to thank my supervisors Dr Christine Gommenginger and Marc Bouvet as well as my panel chair Dr Alberto Naveira Garabato for their advice and the useful scientific discussions we had. I would also very much like to thank my two examiners Dr Adrian Martin and Dr Peter Miller for their careful review and constructive comments.

This work was made possible by the funding of my two co-sponsors: the European Space Agency through the Network/Partnering Activity and the Graduate School of the National Oceanography Centre, Southampton. I am thankful to them for providing me with the opportunity to work on cutting-edge research problems at the intersection of satellite data engineering and oceanography. I am also grateful to la Fondation des Ponts et Chaussées for their loan towards my MSc in Satellite Oceanography which was one of the seeds that grew into this PhD thesis.

My gratitude goes to the scientists and engineers I have exchanged with during this thesis and whose insights were of great help: Dr Pierre Leborgne, Dr Marina Lévy, Dr Jean-Paul Huot, Dr Craig Donlon and Dr John Allen. I would also like to thank the people working at Ifremer and the Met-Office in the development and production of the OSYSSEA and OSTIA products: Jean-François Piolle, Dr Matthew Martin and Jonah Roberts-Jones. They always were eager to answer my questions and to provide detailed information on their products.

I would like to extend my thanks to the faculty, students and staff of the School of Ocean and Earth Science at the National Oceanography Centre who have provided a wonderful and enjoyable environment for my MSc and PhD studies. I am also thankful to Nicolas Floury and the TEC-EEP section at ESTEC (ESA) for having hosted me in good conditions during 6 months in total. I would like to thank the IT support teams in both NOCS and ESTEC for their fantastic work, as well as the security people in these two centres for their recurrent kind words late at night.

I feel very fortunate to have had the opportunity to take part of the D357 Geotraces research cruise on-board the RSS Discovery around the Cape of Good Hope and the South-Atlantic. Although this cruise was not directly related to my PhD, I am delighted to have shared, for 6 weeks, the life at sea of my fellow oceanographers who do not spend their whole working hours at a desk in an office as satellite oceanography scientists often do. For this I am grateful to Dr Gideon Henderson, Dr Brian King and Dr Loic Jullion.

I would like to warmly thank all my teachers and professors for having transmitted me the knowledge and skills necessary to achieve this research effort. I would also like to thank a few persons who had an important role in my decisions to start studying oceanography with my MSc in Southampton and later to engage myself in this PhD: Dr Morgan Mangeas who was my supervisor during my internship at the Institut de Recherche pour le Développement in New-Caledonia, as well as Bernardo Carnicero Dominguez and Miguel Aguirre who were my managers during my Young Graduate Trainee at ESTEC.

I would like to thank my fellow PhD students for making this journey interesting and fun, in particular Dr Nadia Suarez-Bosche, Dr Heleen Vanneste, Dr Eleonora Manca, Konstantina Rizopoulou and Dr Ibrahim Muhammed. This work was made possible thanks to the active moral support of my friends. Not only did they help me go through the painful two years of writing up this thesis after work on the evenings and on the week-ends but they also understood that this meant I had little time to spend with them until this day. Therefore I would really like to thank Matthias Renard, Laurent Despoisse, Pierre-Antoine Frugier, Guillaume Dirberg, Carolina Dopico Gonzalez, Manuel León Urrutia, Xavier Barbier, Benjamin Favetto, Annick Cros, Céline Chauvin, Luigi Orlandi, Willemijn van Enk, Hugues Renaudineau, Sebastien Gadou, Cyril Barnier, Mickael Basset, Robert Montabone, Alessandro Zuccharo Marchi and

Christoph Goetz. I would also like to send a very special thank you to Bastien Latargere, Benjamin Masia, Brice Helene, Guilhem Renaudie, Guillaume Levrey, Olivier Françoise and Yann Jacob.

My gratitude also goes to the MTG engineers and scientists at ESTEC with whom I have been working for two years. The very simple kind words of encouragement I received on a regular basis from many of them helped me go through this delicate moment of my life. I would like to specially thank Andreu Mora for teaching me the configuration control standards which I adapted to my routines.

Je remercie tout particulièrement mes parents qui m'ont élevé dans la culture du travail et du dépassement de soi, mais aussi de la curiosité et de la passion. Ils ont construit les fondations qui m'ont donné l'envie d'étudier et leur appui permanent m'a permis d'atteindre ce doctorat. Je souhaite également remercier ma soeur Amel pour ses précieux encouragements ainsi que pour la joie de vivre qu'elle me communique. Je remercie chaleureusement mon oncle Miloud de m'avoir supporté durant mes études et ainsi d'avoir participé à la réussite de ce doctorat. Je remercie aussi mes cousins, oncles, tantes et ma grand-mère Jacqueline Ruffier pour leur soutien moral. Enfin, mes remerciement les plus tendres sont adressés à Maria dont l'attention, les encouragements, le réconfort et la patience permanents m'ont porté durant ces deux dernières années.

Abbreviations

AATSR Advanced along track scanning radiometer

ATSR Along track scanning radiometer
ACC Antarctic circumpolar current

AMSRE Advanced microwave scanning radiometer-EOS

ARC AATSR re-processing for climate
ASC Ageostrophic secondary circulation

AVHRR Advanced very high resolution radiometer

AVISO Archiving, validation and interpretation of satellite

oceanographic data

CDR Climate data record

CNES Centre national d'études spatiales

ECMWF European centre for medium-range weather forecasts

ENSO El Niño-southern oscillation

EOS Earth observing system
ESA European Space Agency

ERS European remote-sensing satellites

EUMETSAT European organisation for the exploitation of meteorological

satellites

FLI Frontal length index
FGI Frontal strength index

FTDI Frontal temperature difference index
FOAM Forecasting ocean assimilation model

GHRSST GODAE high resolution SST

GHRSST-PP GHRSST pilot project

GMES Global monitoring for environment and security

GODAE Global ocean data assimilation experiment

GOES Geostationary operational environmental satellite

GSW Gibbs-seawater oceanographic toolbox

HSR High spatial resolution

HTR High temporal resolution

IFOV Instantaneous field of view

IFREMER Institut français de recherché pour l'exploitation de la

mer

IFREMER_L3_IR Infrared pixels of IFREMER Level-3 SST

JAXA Japan aerospace exploration agency

MADT Mean absolute dynamic topography

MERSEA Marine environment and security for the european area

MLD Mixed layer depth
MLE Mixed layer eddies

MLI Mixed layer instabilities

MSG Meteosat second generation

NASA National aeronautics and space administration

NCDC National climatic data center

NOAA National oceanic and atmospheric administration

NRT Near real-time

OGCM Ocean global circulation models

ODYSSEA Ocean data analysis system for MERSEA

OI Optimal interpolation

OSTIA Operational SST and sea ice analysis

OSTIA_RAN OSTIA re-analysis

PDF Probability of detecting a front

PE Primitive equations
PV Potential vorticity
QG Quasi-geostrophic

REMSS Remote sensing systems

SEVIRI Spinning enhanced visible and infrared radiometer

SG Semi-geostrophic

SIED Single-image edge detector

SLSTR Sea and land surface temperature radiometer

SQG Surface quasi-geostrophic

SMOS Soil moisture and ocean salinity

SNR Signal to noise ratio
SSH Sea surface height

SSHA Sea surface height anomaly

SSS Sea surface salinity

SST Sea surface temperature
TMI TRMM microwave imager

TRMM Tropical rainfall mapping mission

WS Window size

xxviii

Symbols

b	buoyancy
c_p	water specific heat
D	width of the front
d	width of the running mean filter
f	Coriolis frequency
g	acceleration due to gravity
Н	characteristic vertical length scale of the flow, mixed layer depth
\vec{k}	unitary vertical vector
L	filament width scale
L_f	local front width
L_{min}	minimum front length
N	Brunt-Väisälä (or buoyancy) frequency
R	density ratio
R_i	Richardson number
R_0	Rossby number
S	sea surface salinity
t	time
T, T_1, T_2	Canny thresholds
\vec{u}	velocity
$ec{u}_g$	geostrophic component of the velocity

\vec{u}_a	ageostrophic component of the velocity
и	horizontal (eastward) component of the velocity
u_a	ageostrophic horizontal (eastward) component of the velocity
u_g	geostrophic horizontal (eastward) component of the velocity
v	horizontal (northward) component of the velocity
v_g	geostrophic horizontal (northward) component of the velocity
v_a	ageostrophic horizontal (northward) component of the velocity
w	vertical component of the velocity
x	horizontal (along-front or eastward) length coordinate
у	horizontal (across-front or northward) length coordinate
Z	depth below the surface
α	expansion coefficient of temperature
β	expansion coefficient of salinity
ρ	density
$ ho_0$	typical water density
Δs	model grid-scale dimension
Δs	SST feature resolution
ΔT_{min}	minimum temperature difference across front
$ au_0$	along-front wind-stress
σ	surface strain
σ_n	temperature noise
$\sigma_{_S}$	length scale of the Gaussian smoothing filter
ψ	stream function

sea surface temperature θ gradient operator ∇ horizontal gradient operator ∇_H $()^T$ transpose operator $()^z$ vertical average over the mixed layer $\overline{()}$ along-front average operator $\overline{\overline{()}}$ coarse 2D horizontal average operator O'submesoscale perturbation from the coarsened average

1. Chapter 1: Introduction

1.1 General introduction

1.1.1 Climate science context

Most of the analyses performed to explore changes in the Earth's climate involve data that were averaged over a large region, such as the entire globe or the tropics. The IPCC Fourth Assessment Report details studies which look for trends in the time series of Sea Surface Temperature (SST) anomalies, ocean heat content, precipitations, sea-ice extent, salinity, sea level and basin-scale ocean circulation patterns (Pachauri & Reisinger 2007). Temperature increase is a very straightforward signature of the shift in the climate system as a consequence of increasing anthropogenic emissions of CO₂. Satellite and insitu measurements of SST as well as in-situ deep temperatures have been compiled into long Climate Data Records (CDR) from which regional and global rates of increase have been quantified. For instance the global ocean temperature was shown to have risen by 0.10°C averaged from surface to a depth of 700 m over the period 1961 to 2003 (Bindoff et al. 2007).

Satellite sensors however have the potential to resolve quite fine horizontal details of SST. Cloud free very high-resolution SST images have revealed ubiquitous complex flow structures at the surface of the oceans, which are the signature of a wide range of underlying dynamical processes. A new generation of global, multi-sensor, high-resolution SST products is being produced in the framework of the Global Ocean Data Assimilation Experiment (GODAE) High-resolution Sea Surface Temperature (GHRSST) project (Donlon et al. 2002). These products advantageously combine the high-resolution and high accuracy infrared measurements with the high coverage of the microwave sensors through an optimal interpolation method. They are the results of an optimized combination of the strengths of the different components of the SST observing systems. They have the potential to resolve small-scale dynamical activity at the surface of the ocean, globally and daily over a long period of time (up to 25 years).

This study's underlying motivation is to examine potential climate signals in satellite SST data at finer spatial detail than the regional averages of SST

anomalies which have been measured so far. To facilitate this, the information extraction from SST data has been pushed to its limits in order to explore local and transient small-scale processes and their spatial and temporal variability. The broad idea is to quantify these processes by frontal analysis of satellite SST data in order to generate global, spatially-detailed time series that have the potential to be analysed for climatic signals. This is in agreement with the U.S. Climate Change Science Program (Karl et al. 2006) recommendations to make better use of observational data and to develop data sets for a range of variables other than large-scale temperature, capable of supporting climate quality analysis. By constructing estimates of the changes in the internal dynamical variables of the ocean, the aim eventually is to build a better comprehension of the climate system. This is intended both to explain with a higher confidence the observed changes in the Earth system and to improve the characterization of small-scale ocean dynamics, and ultimately their parameterization, in numerical climate models, which would work towards better predictions of future climate evolutions.

1.1.2 Rationale for the small scales exploration

This focus on oceanic small-scale processes was driven by recent research efforts which are starting to unfold the importance of these processes in ocean surface dynamics. It is now accepted that local mesoscale (10-100 km) and submesoscale (1-10 km) processes in the surface mixed layer have a significant integrated impact on the ocean's primary production budget and on the carbon fluxes between the atmosphere and the ocean. Theoretical studies in geophysical fluid dynamics, mesoscale ocean general circulation and biogeochemical models, regional sub-mesoscale physical and bio-physical models, mesoscale in-situ measurements and satellite observations have considerably advanced the understanding of the small-scale dynamics in the last 20 years. They have shown that a substantial proportion of upwelling, subduction, stratification and lateral stirring in the upper-ocean occurs at the small scales.

Physical oceanographers started focusing on these small-scales dynamics when it became clear that the analytical and numerical studies of large-scale dynamics cannot account for all the variance of observed parameters in the mixed layer. The questions raised by this discrepancy are challenging because

these processes are embedded in a larger and energetic flow and hence are difficult to resolve from non-synoptic measurements. At these scales, the Rossby number is close to 1, therefore the geostrophic balance is lost and ageostrophic non-linear 3-dimensional turbulence tends to dominate. This makes these dynamics very difficult to simulate in numerical models. Nevertheless it is fundamental to understand the vertical motions associated with small-scale upper ocean dynamics because they play an important role in the global carbon cycle. Indeed, they are involved in the transport of deep nutrients into the euphotic zone, which enables primary production to occur. They also convey heat, salt and momentum fluxes below the mixed layer, as well as affecting the exchanges of gases between the ocean and the atmosphere. Since satellite capabilities and computing power available to scientists have recently considerably improved, it is a good time to combine the up-to-date satellite datasets with the most advanced results on the small-scale dynamics obtained from very high-resolution numerical simulations.

1.1.3 Focus on surface density fronts

In order to observe and quantify the mesoscale and sub-mesoscale processes of the mixed layer, we have chosen to use sea surface density fronts. They are defined as regions of enhanced horizontal gradient of density. The choice of surface density fronts was easy because they are observable on SST satellite images and because they are a signature of upper-ocean dynamics. Generally speaking, if a surface density front is present, it means that two water masses of different density are side by side. This situation can be the consequence of either internal dynamics of the mixed layer (i.e. horizontal advection, straining, upwelling, etc.) or inhomogeneous external forcing (wind-induced mixing, irregular solar heating due to clouds, etc.). Once two water masses of different density are made to coexist side by side, a pressure gradient force is exerted between them. The pressure gradient pushes the denser water underneath the lighter water, and when this slumping happens vertical mixing and restratification are in effect generated locally at the front. If the pressure gradient is countered by the Coriolis effect of a down-front flow in a geostrophic balance, the front can be maintained. The occurrence of a front

implies that some sort of dynamical activity is present on its surrounding waters.

Conversely, when dynamical activity occurs in the upper-ocean, it has a signature at the surface in the form of density fronts. If the ocean was perfectly stratified with a mixed-layer of globally uniform density, horizontal advection would have no effect on the surface density, because water masses of equal densities would be mixed. However, the real ocean is more complex, and its mixed layer is under the effect of heterogeneous forcing: meridionally variable solar heating, currents, storms, fresh water discharges and so on. As a result of this, the surface density is not homogeneous at the mesoscale and below, which makes it a good tracer of surface dynamics. Indeed, for instance, when water is advected horizontally by western-boundary currents and strained by eddies and turbulence, it comes into contact with different water masses which are likely to be of different density. In effect, the large-scale background density gradient from the latitudinally varying solar heating is enhanced in areas where energetic horizontal flows converge. On top of this, various mesoscale processes such as eddies and wind-induced coastal upwellings transport water from below the mixed-layer which is denser and colder, and this also generates surface density fronts. Surface density fronts are therefore a good indicator of mesoscale and submesoscale activity in the mixed layer.

Obviously, this view has an important limitation: the density fronts are associated with very diverse physical processes. Thus their effect on the mixed layer, and ultimately on the climate system, are variable as well. It will be shown that different processes can have similar signatures in term of density fronts. Our approach tackles this issue from two directions. Firstly, although in this work the exploration of fronts has been centred on measuring fronts revealed in SST data fields, we choose to make the most of additional knowledge and parameters in a combined approach to push the resolving of the dynamical features as far as possible. Secondly, only processes that are inherent to the presence of a front are considered. We focus more on dynamics induced by the presence of a front in its environment and less on the processes that have generated the front. The scope of this thesis is not to measure the variability of the vertical circulations generated at the mesoscale by eddy-pumping fluxes, wind-induced coastal upwelling or wind-induced

mixing. It is rather to focus on the smaller scale processes occurring at fronts, whether these fronts are those marking the boundary of a strong jet or those defining an eddy. The raw indices of detected fronts certainly include the larger scale processes, and the spatial and temporal variability and trends of these indices are an important result of this thesis. However, the dynamical parameters of the small-scale activity generated at the fronts recovered by our novel techniques are independent from the processes initiating these fronts (eddy, jet, upwelling...), because each front, may it be marking the border of an eddy, is simply treated as a front subject to an external forcing (straining, wind stress...).

1.1.4 From SST images to surface density fronts

SST images have the potential to resolve the 2-dimensional structure of the ocean surface dynamics. Like surface density, surface temperature can be used as a tracer to detect small-scale activity. However one needs the surface density to understand and quantify the underlying dynamics involved. The pressure gradient at a front is proportional to the horizontal gradient of density (or buoyancy), and the same is true for the potential energy stored in the front that is available for a forward energy cascade. It will be shown that several dynamical parameters can be inferred from the information of the surface horizontal density gradient.

However one needs to take into consideration the limits of the SST data. Firstly, it will be shown that multi-sensor satellite products have the advantage of the best conceivable coverage, but they are the result of an averaging of non-synoptic measurements and an optimal interpolation in space or time to fill gaps where data are not available. For this an autocorrelation matrix is applied in the production process which has the effect of smoothing to some extent the resulting SST field. In these conditions the capacity of these products to reveal mesoscale and submesoscale frontal variability needs to be assessed and accounted for in the interpretation of the results. Secondly, the satellite sensors measure the temperature of the top few millimetres of the ocean surface. When relating this temperature to the mixed-layer dynamics, one needs to make sure that this temperature is dominated by the temperature

of the mixed-layer rather than the temperature of the atmosphere. Thirdly, there is often a degree of compensation between the salinity and the temperature at the fronts. This happens when the temperature gradient is partly (or almost completely) counteracted by the salinity gradient in its effect on density. Effectively, this means that when translating a temperature gradient into a density gradient, while assuming the salinity to be constant, one may overestimate the density gradient, because the salinity is often slightly correlated to the temperature in the mixed-layer. Steps must be taken to minimize the errors induced by these three limitations. Similarly, a density front can be completely dominated by the salinity, with little or no thermal signature. In this case the density gradient is underestimated when calculated from the SST alone. It should be stressed that this work does not contribute to the understanding of this type of front.

1.1.5 Scope of the research

The first objective of the research activity presented in this thesis is to develop, test and validate front detection algorithms and software tools suitable for the new multi-sensor SST data sets. Strengths and weaknesses of the various existing algorithms and data sets are analysed and discussed, in order to propose a methodology for measuring and monitoring oceanic frontal variability, adapted to the future generation of SST data sets. To compare the ability of various algorithms and data sets to detect temperature fronts, a quantitative frontal index is defined based on the strength and the length of the detected fronts. This simple index is a first-level proxy to measure smallscale upper ocean dynamics. The work on the detection algorithm is based on existing techniques but it pushes them further as it validates them and rates their performances. The aspect on using the multi-sensor SST data sets is innovative as it is the first attempt to quantify the ability of such products to resolve small-scale features. The achievement of this first objective constitutes a substantial body of new work with the potential for publication in the literature on image analysis techniques. At the same time it has delivered analytical techniques enabling more penetrative research on dynamical applications and climate change indicators which are the ultimate goals of the thesis.

The second objective is to critically assess recent results of theoretical research by others on frontal dynamics, in the light of the observations that can be made from SST images. The idea is to derive information about oceanographic dynamical parameters from observations of the surface SST frontal field. This effort is based on a large and recent fluid dynamics literature (analytical and numerical), and additional parameters from other satellite sensors (altimeters for the background straining mesoscale field) and climatologies (salinity, mixed-layer depth) that are used in synergy with the SST. The intended outcome is first to conceive, and then to create. observational dynamical indices derived from SST fields in this synergetic context. The focus is mainly on frontogenesis mechanisms and their theoretical effects in term of vertical mixing and restratification. Observations of external forcing such as the surface ocean current field are combined with the SST to calculate consequences of these fronts in the upper ocean dynamics. These dynamical indices are intended to provide a more advanced insight into the ocean system than the first-level frontal indices because they quantify dynamical processes such as vertical transport or restratification, rather than simply quantifying fronts at the surface.

The final objective is to apply these methods to long time series of satellite measurements. These methods have the potential, not only to contribute to numerous oceanographic debates about the present state of the oceans, but also to improve predictions of the future state of the ocean in a changing climate. The first reason is that they can allow a better characterization of the small-scale dynamics variability in the climate models. The second reason is that the sensitivity of these new frontal dynamical indices to climatic signals can be explored, and conclusions may be drawn about the likely evolution of the ocean small-scale dynamics.

An additional underlying motivation of this work is to demonstrate that more can be done with satellite observations to comprehend oceanic processes. Although parts of the study strongly rely on analytical and numerical fluid dynamics results based on idealized situations as well as on detailed physical observations of a localized phenomenon, an approach has been developed which is systematic, objective and global. The new methodology is intended to be applied to global datasets, and to make use of additional parameters in an objective manner in order to produce a set of physical indices that are

consistent in both time and space. Regional peculiarities and heterogeneities in the data are dealt with as much as possible by the algorithms so that the resulting indices are robust in time and space, allowing comparison of their values on reliable maps or time series.

Ultimately, the question must be faced as to whether these indices meet climate accuracy and stability requirements so that they can be used as climate change indicators. This study is a step towards the creation of such climate change indicators based on the frontal dynamics as observed from SST satellite images, in synergy with other measurements. This is consistent with the spirit of the on-going ESA Initiative in Support of Climate Change, which defines Essential Climate Variables (ECV) to be processed from regionally averaged satellite measurement.

1.1.6 Summary of the objectives

The logical flow of the thesis can be summarized in a few questions, each one of them constitutes the objective of a chapter.

- Q1. What front detection algorithm is most suited to identify fronts on SST images?
- Q2. Which SST dataset is the most effective for front detection on a global scale?
- Q3. What aspects of the mixed-layer dynamics can be identified from the fronts detected on SST data fields?
- Q4. What is the spatial and temporal variability of the frontal quantities? How does it evolve on a climatic time scale?

1.2 The scientific context

1.2.1 Generalities about ocean fronts

Ocean fronts have always attracted the attention of fishermen who noticed much higher concentrations of pelagic species in their vicinity which marked them out as a preferred location for fishing. Fronts have also been searched for and mapped by the naval military forces as submarines hide behind them to avoid being detected by sonars. They have always been of strong interest to oceanographers who have observed them over a large range of scales: from

100m to 10,000 km along-front; from 10 m to 100 km across-front; from 1 m to 1 km down-front; their lifetime varies from hours to millions of years (Belkin 2002). A picture of a homogeneous surface mixed-layer with narrow zones of enhanced gradients of water properties has emerged. Fronts have been the subject of a large and multi-disciplinary research effort and are now understood to be a "pathway" between large scale 2-dimensional horizontal oceanic/atmospheric forces and small-scale 3-dimensional vertical phenomena. The dynamic tendency for the large-scale flow in frontal zones to lose its geostrophic balance and become hydrodynamically unstable allows the transfer of energy from large scales to small scales and enhances the vertical exchanges between the ocean interior and the surface layer. This section reviews the current knowledge on the dynamics associated with the oceanic surface fronts and their consequences for the biological and climate systems.

A sustained front is generally associated with a current, in which the Coriolis acceleration balances the pressure gradient created by the difference in density between either side of the front. The fronts are zones of high vertical shear coupled with the strong horizontal density gradient that marks them. This coupling is known as the thermal wind and is a fundamental manifestation of the geostrophic balance. The current flows along the contours of density, and may not destroy nor deform the frontal structure (Olson et al. 1994). The detailed structure of geostrophically balanced fronts is thoroughly described in Robinson (2010). Fronts that are sustained long enough to reach geostrophic balance fill the ocean over a wide range of scales. On the large scale (up to thousands of kilometres), fronts are encountered on the frontal flows of the major ocean currents such as the Gulf Stream in the Atlantic Ocean, the Kuroshio in the Pacific and the Antarctic circumpolar current around the Southern Ocean. On a smaller spatial and temporal scale, mesoscale turbulence of the ocean stirs large-scale density gradients into transient concentrated filaments and fronts (Mann & Lazier 2006, Robinson 2010).

This basic ideal view represents the first order of steady state dynamical description of a front. A front interacts with destabilising environmental forces such as mesoscale current strain and wind. This triggers its intrinsic dynamics and causes departures from balance and an evolution in time. For example, oscillations and baroclinic instabilities can arise along a front undergoing an

adjustment after its creation. This can result in an active restratification of the mixed layer through an energy cascade from the mesoscale to the submesoscale. Also mesoscale strain on some parts of the front can have a frontogenetic effect and develop localized strong upwelling/subduction of water masses. As the geostrophic balance is lost, non-linear small-scale secondary flows are created that work towards recovering the lost balance, sometimes by mixing and destroying the front, other times by developing large lateral oscillations and breaking the flow into meanders and eddies. Because these effects have a significant integrated impact on the dynamics of the mixed layer and the biological activity, it is fundamental to understand how fronts are created, how they are destroyed, how they evolve under different forcing and what physical phenomena are associated with their presence.

A more substantial review of recent theoretical studies of frontal processes is provided in Chapter 2.

1.2.2 Satellite observations of fronts

Most of the time, ocean fronts have a signature at the surface on the temperature field. SST datasets have been searched for fronts ever since the first datasets were released, they have shown to be capable of resolving spatial scales and temperature differences necessary to observe mesoscale fronts. In the 1980s, during the early stages of satellite SST acquisitions, temperature fronts were detected and monitored manually by operators. This was done in the context of fisheries, submarine military applications or weather prediction. In order to reduce the subjectivity in the front detection introduced by a human operator, objective automatic front detection methods were introduced. The design of such methods is a challenging task as fronts consist of complex horizontal structures embedded in the turbulence of the flow, and exhibit a wide variety of space and time scales. The instrument acquisition errors increase the complexity of the automatic detection algorithm which should be robust to noise, cloud-induced missing data and errors introduced by the atmospheric correction.

The issue of edge detection on SST was tackled in a variety of ways (see Hopkins et al. 2010 for a detailed review). Some algorithms based on image processing techniques were suggested, they rely on the computation of the temperature gradient. A high SST gradient is a signature of a sharp transition between water masses of different temperatures. Applying a gradient operator (Prewitt, Sobel etc...) on a SST image reveals the areas of transitions that mark the fronts (Simpson 1990). Fronts can then be mapped by setting a SST gradient magnitude threshold (Belkin & Gordon 1996). The precise location of fronts can be obtained following the method suggested by Canny (1986), which locates the fronts on the crests of the SST gradient, in other words on the local maxima of SST gradient in the gradient direction. The derivativebased edge detection methods present the advantage to relate the fronts it detects to a simple definition in terms of horizontal temperature gradient, which can subsequently be linked to dynamics of the mixed layer. On the other hand, the gradient computation is very sensitive to noise in the data, and these methods generally apply a preliminary smoothing filter to the data, which blurs away the fine features and underestimates the absolute value of horizontal SST gradient.

Other edge detection methods have been designed specifically for front detection on SST data suffering from noise and missing data. These methods divide the SST image into windows and apply statistical analysis on the pixels they contain to determine the presence of a front. The main algorithm following this approach is the histogram-based single-image edge detector (SIED) of Cayula and Cornillon (1992, 1995). This method was proven to be fairly robust to noise and missing data. However, it needs to be subjectively tuned and detects fronts that are strongly dependent on the chosen parameters. Yet, the SIED's advantages are widely recognized and this algorithm was used to detect fronts in numerous studies. Regional climatologies of SST fronts detected with the SIED on AVHRR time series were produced by Belkin and Cornillon (2003, 2004, 2005). It was also applied to detect satellite-derived chlorophyll a concentration fronts in the Long Island (Stegmann & Ullman 2004), and to examine fronts of normalized water-leaving radiance in the South Atlantic Bight (Bontempi & Yoder 2004). Miller (2004) built five-days composite SST, chlorophyll and sediment maps of fronts with

the SIED method, and combined them to derive statistics on the relationship between these properties.

Several studies explored the temporal variability of frontal indexes. Belkin and Cornillon (2005) detected fronts on Level-2 Pathfinder satellite fields between 1985 and 1996 using the Cayula method over the Bering Sea. Time-series of frontal frequencies were computed for each pixel which allowed the authors to explore the fronts' spatial structure and seasonal and inter-annual variability. The frontal probability index they defined exhibited a very strong seasonal variability, with a ten-fold increase from spring to summer and an abrupt drop in September. The annual mean monthly frontal index increased approximately 50% from 1985 through 1996, apparently signalling a concomitant intensification of some yet unidentified frontogenetic processes. Ullman et al. (2007) have explored the spatial and temporal variability of subtropical fronts in the subtropical frontal zone (STCZ). They used a modified version of the multi-image method described by Cayula and Cornillon (1996) to detect the fronts. They also found that the variability of the front probability is dominated by the seasonal cycle. They observed that the western part of the STCZ region has the largest seasonal variation with maximum probability in the spring, while the eastern part of the region has a more intermittent seasonal signal with peak probability during early summer. Cornillon and Obenour (talk, 2012) have explored the long-term temporal trends of fronts detected with the Cayula algorithm on the AATSR re-processing for climate dataset (ARC) and on the AVHRR Pathfinder one. The authors reported an increase of their frontal index of 0.47% per year with the day SST and 0.59% per year with the night data between 45°S and 45°N despite a global negative trend of temperature gradient magnitude of 0.4% per year.

All the methods mentioned above produce maps of fronts, and as they are applied to a time sequence of SST images over which the turbulence evolves, different fronts are detected in different places. Another family of front detection techniques was developed to study a single permanent front and observe how it moves and changes strength over time. Shaw and Vennell (2001) use a surface fitting technique to follow an ocean front on SST. Their algorithm records not only the position of the front's steepest gradient but also its width and the temperature difference across the front. Time series of the parameters of a front can therefore be constructed from a series of SST

images. This approach is suitable for the study of a specific front which should be permanent, as is the Southland front in New Zealand coastal waters. In this context the method was shown to be extremely useful since it allows one to explore the evolving history of a front and relate the frontal parameters to oceanographic quantities such as large scale forcing or local primary production. Hopkins et al. (2010) subsequently suggest a weighted local likelihood approach that is robust to noise and missing data and estimates the uncertainty associated with each parameter.

1.2.3 Previous efforts to combine observations with theory

Very few studies derive quantitative estimates of dynamical parameters of the mixed-layer from satellite observations. Most studies with this objective combine satellite observations with in-situ observations from an oceanographic campaign or a numerical model that assimilates them. Altimetry products are notorious for allowing relative values of horizontal geostrophic currents and eddy kinetic energy to be derived.

However most studies based on satellite data sets are either built on statistics of the measured parameters, which are not linked to dynamics, or draw only qualitative conclusions on the dynamics observed. This is especially true for what concerns vertical exchanges and small-scale physics. This section presents the handful of studies that attempt to bridge the satellite oceanography community to that of physical oceanography.

Siegel et al. (1999) paved the way in this domain by calculating the contribution of eddy pumping to the vertical flux of nutrients in the Sargasso Sea with satellite altimetry. Altimetry products are limited by their spatial and temporal resolutions, so they are unable to resolve small-scale dynamics. Nevertheless Klein et al. (2009) show that the Surface Quasi-Geostrophy (SQG – see section 2.2.4) framework should be efficient at diagnosing the vertical velocities in the upper ocean once the high resolution sea surface height product become available.

SST data appear to be more suited to the diagnosis of small-scale vertical circulation. For example Lehahn et al. (2007) make use of the parameterization of vertical velocity circulation at horizontal density gradients suggested by Legal et al. (2007). This parameterization is applied on submesoscale filaments stirred by eddies observed on SST images of the North-East Atlantic. The authors calculate a vertical velocity in the range of 25 m/day that corresponds to an energetic vertical cell capable of nutrient upwelling. In the meantime researches are being conducted to derive the full 3-dimensional circulation from surface temperature under the SQG assumption (Isern-Fontanet et al. 2008 and LaCasce and Mahadevan 2006). According to SQG, the 3D stream function can be well approximated, at least on some regions and under appropriate conditions, by a dominant mode obtained after assuming constant stratification and vanishing relative potential vorticity at surface (Turiel et al. 2008). In spite of the coarse simplification, SQG velocity fields derived from microwave SST images have been shown to acceptably describe the surface horizontal velocity field (as derived from altimetry maps), at least over open sea areas and for regions of strong SST gradients (Isern-Fontanet et al. 2006). Turiel et al. (2008) show that, under more relaxed, self-consistently verifiable conditions it is possible to describe surface streamlines at any location and time from microwave SST. Fox-Kemper and Ferrari (2008) study the climate implication of the parameterization suggested by Fox-Kemper et al. (2008) which relates horizontal buoyancy gradients and mixed layer depth to the restratification by MLIs that develop from baroclinic instabilities of ocean fronts. The mixed layer depth is estimated from a climatology, and the buoyancy gradients from altimetry. The choice of altimetry for estimation of the buoyancy gradient is made by the authors out of fear of an overestimation of the density gradient calculated from temperature gradients alone, because of the possible presence of compensated fronts. The result is that the restratification by MLIs is a leading mechanism in the upper ocean.

1.3 Outline of the thesis content

1.3.1 The approach: bridging between scientific communities

This study should be seen as an attempt to bridge two oceanographic disciplines. On one side, the physical oceanography community has achieved tremendous advancements on the understanding of submesoscale dynamics. On the other side, the satellite oceanography community has managed to build new observation products that maximize both quality and availability. The underlying objective of this thesis is to send a message to both communities. We would like to convince the physical oceanography and climate science communities that the satellite data sets have reached a level of maturity that allows one to answer dynamical questions on the small-scale activity of the real ocean. We would also like to demonstrate to the satellite oceanography community that recent dynamical results make it possible to relate remote surface measurements to the underlying dynamics of the mixed layer, when an appropriate methodology is applied.

As recognized by Chapron et al. (2010), "research efforts are highly needed to better understand the different sensor physics and capabilities, to demonstrate and explore in more details the combined uses of the different observations, to propose and test improved dynamical and statistical integration strategies to be used to guide the developments for innovative, efficient and thematically-driven data-mining methodologies". This study is a step toward the development of a new generation of algorithms that combine various satellite products with in-situ climatologies in a way that is consistent with the current knowledge of the small-scale dynamics in order to extract oceanographic dynamical variables. It is the belief of the author of this thesis that this approach is original in the sense that it is systematic, objective and global. The intention is to provide a methodology for optimal and automatic use of satellite data, recovering as much information as possible, in a way that would allow the construction of long time series of the recovered parameters, which means that the calculated indexes should be coherent in both space and time.

This study is also new with regard to the SST datasets on which it is based on. Indeed the newly available multi-sensor Global High Resolution SST products

(GHRSST) offer an unprecedented high spatial and temporal coverage. However the ability of these blended data sets to reveal small-scale features has not hitherto been explored and quantified. The methodology that is proposed in this thesis therefore seeks to assess the characteristics of the input data from which the algorithms extract the information. This study also includes the innovative inter-comparison of existing front detection methods and quantification of their ability to detect frontal features in various conditions.

An important objective of this study is to bring forward a new generation of frontal indexes that are dynamically more meaningful than the historical ones. The suggested frontal indicators should facilitate new applications of satellite products with potential for answering questions related to the influence of small-scale frontal dynamics on the vertical exchanges in the mixed layer. Finally, the ground is set for a potential use of frontal indexes as a climate change indicator, which is something completely new.

1.3.2 Road map for the thesis

This thesis is organized in six further chapters, each of the substantive chapters 3 to 6 being aimed at answering one question from the list in 1.1.6. Chapter 2 provides a review of physical oceanography knowledge of fronts and is an essential input for addressing Q3. Chapter 3 explores which front detection algorithm is the most suited to the satellite SST images (Q1). It describes and discusses several existing front detection techniques and edge detection algorithms based on the image processing literature. The different methods are compared and their performances are quantified, as a function of the characteristics of the SST data used as an input. Chapter 4 asks the question of which SST product is the most efficient for the detection of fronts on the global scale (Q2). It assesses the ability of different global SST products to resolve fronts at various scales. Chapter 5 presents an automatic and optimized methodology to detect fronts on SST datasets. It builds on the dynamical results presented in chapter 2, and discusses their practical implementation. The outcome of this chapter, in response to Q3, is a set of frontal indexes based on the physical understanding of the dynamics associated with fronts and a methodology to compute them. In chapter 6, the

spatial and temporal variability of some of the basic frontal indexes is explored and characterized in response to Q4. Long time series of the indexes are constructed and analysed with a climate perspective. Finally, Chapter 7 summarises the achievements and identifies ways to take the work forward.

2. Chapter 2: Dynamics of ocean fronts

This chapter presents a review of the current understanding of mesoscale and sub-mesoscale fluid dynamics in the vicinity of ocean surface fronts. It penetrates further into the theoretical study of frontal dynamics than the rest of the thesis, the primary focus of which is to develop methodologies for extracting information about frontal conditions from observational data. That being the case it may not be strictly essential to read this chapter in order to follow in general the methods and achievements of the work described in subsequent chapters. Nonetheless, the motivation of the thesis is to develop data analysis tools that eventually will become useful to provide observational evidence that can validate or challenge theoretical models of frontal processes. Thus the formulation of tools such as frontal indexes should, as far as possible, be informed by the current concerns of ocean frontal dynamicists. The author of this thesis also believes that it is important for remote sensing specialists to get acquainted with the results of dynamicists on the frontal dynamics presented here. Therefore a chapter like this, which explores the state-of-the-art of the underpinning dynamical theory, is considered to be an essential element to ground the thesis in its oceanographic context. In places throughout the chapter cross-references are made to later chapters to identify particular elements of frontal theory which have informed some of the design choices for the data analysis methods that comprise the main substance of the thesis.

2.1 Fronts within the wider context of upper ocean processes

The oceanic mixed layer was long characterized in terms of small-scale vertical processes that reduce the vertical gradients of tracers and momentum, and large-scale horizontal motions that stir and mix the lateral gradients. In this characterization, 3-dimensional processes are thought to occur only at the very small-scale (0.1 m to 100m). For instance, Langmuir cells driven by wind

and convection cells driven by surface buoyancy fluxes have been investigated for their contribution to mixing and energy dissipation. At the other end of the scale spectrum, (10km to 100km), large scale ocean currents and mesoscale eddies have been studied extensively and are believed to dominate the horizontal stirring and the lateral transport of heat, momentum and tracers (Boccaletti et al. 2007). Dynamics at scales between 100 m and 10 km (submesoscales) are assumed to be subdominant. However recent observational (Ferrari & Rudnick 2000), modelling and analytical studies (Capet et al. 2008b, Lévy et al. 2001, Spall 1997) have challenged this view: motions in this intermediate range of scales are often leading order in the vertical flux of mass, buoyancy and tracers in the upper ocean. In addition, they are thought to be instrumental in transferring energy and properties from the largely adiabatic mesoscale flow field, to a scale where mixing can occur (Thomas et al. 2008).

These recent studies have been motivated by the crucial search for missed physical mechanisms that could close the budget of phytoplankton production through additional nutrient supply. There is a debate on the spatial and temporal scales involved in the physical supply of nutrients in the euphotic layer through vertical mixing. It is understood that on the global/annual scale, nutrients are controlled by the thermohaline circulation and the wind mixing. Yet the geochemical estimates of new production surpass this rate of nutrient supply by a factor of two. Nutrient supply by mesoscale eddies is estimated to account for 20-30% of the global annual primary production budget (McGillicuddy et al. 1998, McGillicuddy Jr et al. 2003). The most likely mechanism which is able to explain this discrepancy seems to be related to the underestimation of the dynamics at small scales because of the lack of resolution of both the models and the in-situ measurements. Indeed very high resolution Ocean Colour satellite images have revealed that submesoscales can account for approximately 50% of the total resolved variance of Chlorophyll (Glover et al. 2008). This highlights the issue of nutrient distribution at small scales.

The biogeochemical studies on the vertical exchange of tracers are divided into two conceptual views. The first view assumes that the vertical exchanges occur principally in the interior of mesoscale eddies, and relate the time evolution of the eddy anomaly to the vertical transport through a linear

relationship. This view includes the eddy pumping paradigm (McGillicuddy et al. 1998). Observed and modelled submesoscale structures are usually interpreted in terms of horizontal dispersion driven by the two-dimensional turbulence dynamics, therefore having no impact on the vertical exchanges. This conceptual view has contributed to significant advances for the estimation of the vertical exchanges due to mesoscale eddies, but it is based on two questionable assumptions. First, it implicitly assumes that nutrients or tracers are well mixed on isopycnals. Second, it assumes that the space between the mesoscale eddies is a dynamical desert in term of the vertical pump (Klein et al. 2008). On the other hand, the second view allows the possibility of vertical exchanges directly at small scales, within the submesoscale structures, through frontal and ageostrophic processes. In this scenario, eddies contribute in an indirect way to the vertical transport because submesoscale structures are produced by the mesoscale eddy-eddy interactions and straining of the mesoscale current. This study focuses on dynamics inherent to fronts, hence it is based on the scientific literature related to the second view. The eddy-pumping mechanism is not taken into account by the developed indices, eddies are rather seen as fronts in their radial direction.

Ocean surface fronts are ubiquitous across the ocean, and are found at scales varying from the mesoscale to the submesoscale. Whether fronts are large or small, submesoscale dynamics can be triggered by their presence. This chapter reviews the proposed mechanisms for the development of submesoscale structure and vertical circulation in the presence of horizontal density gradients. They can be classified into three main groups of dynamics:

- 1. The theory of frontogenesis driven by lateral strain (Hoskins & Bretherton 1972).
- 2. The occurrence of unforced submesoscale baroclinic instabilities on fronts losing their geostrophic balance, which has the potential to restratify the mixed-layer (Boccaletti et al. 2007).
- 3. The generation of intense downwelling at fronts by down-front wind stress due to cross-front Ekman transport at the surface (Thomas & Lee 2005).

The rest of this chapter gives an overview of the present understanding of the dynamics that occur at surface fronts. It summarizes the observational studies, the analytical models based on a variety of assumptions, and the results from numerical models of increasing complexity and resolution. It aims to give the reader a first understanding of the parameters involved in these dynamics. In particular, it will be noticeable how the value of the horizontal gradient of density emerges as a recurrent and important parameter in the quantification of the dynamics involved at front. This is the primary link between theoretical models of frontal processes and the capacity of satellite remote sensing of SST to detect and measure those processes.

Section 2.2 reviews theories of frontogenesis driven by the straining field of a larger scale phenomenon. Section 2.3 explores the role of frontal instabilities in re-stratifying the mixed layer, and section 2.4 considers basin-wide numerical models capable of simulating mesoscale frontal dynamics. Finally section 2.5 seeks to identify some of the current questions being asked by ocean dynamicists, and to which satellite-retrieved SST fields may have a contribution to make. It should be noted that some of the theoretical ideas described in this chapter are picked up again in Chapter 5 which explores in greater detail the existing parameterisations for submesoscale processes that attempt to capture their contribution to vertical velocities and restratification at fronts. Such cases are cross-referenced later in this chapter.

2.2 Frontogenesis

The understanding of fronts has been the subject of a long-standing scientific effort. Physicists have explored the dynamics of turbulent fields for decades to gain insights on the mechanisms that are involved in the creation, sustaining, intensification and destruction of large horizontal buoyancy gradients in the troposphere and in the ocean surface layer. The rotation of the Earth is understood to be instrumental in the presence of the fronts, as they are approximately in a geostrophic balance. The understanding of oceanic turbulence is a difficult task and it remains one of the main sources of uncertainty within climate models. Indeed, the turbulence is the result of a mix of physical mechanisms interacting at a variety of scales. There are different ways to investigate the turbulence. Oceanographers can perform in-situ measurements, but they can sample only punctual stations at sea. They often run a transect through the region of interest, but the non-synopticity of the

measurements combined with the low resolution of the transect limit their conclusions on fast evolving phenomena (Allen et al. 2001). Also the features of interest are often embedded in a larger and more energetic flow, which makes it difficult to measure them. Faced with these difficulties, dynamicists have confronted the issue with purely theoretical and mathematical approaches. As early as in 1928, physicists designed analytical models to describe the formation of fronts in the atmosphere (Bergeron 1928). The analytical models of turbulence require assumptions and approximations concerning the physics at play. This is usually done by assuming that in particular conditions, certain scales and forces are dominant and the phenomena not taken into account are considered negligible. This allows the turbulent field to be modelled by a set of assumptions and equations, called a regime, and conclusions to be drawn from the consequences of the equations.

Obviously the realism of these analytical models is limited by the representativeness of the approximations they are based upon. Different approximations lead to different results and part of the remaining uncertainty is due to questions on the applicability of these regimes. Nevertheless the analytical models have tremendously advanced the understanding of the atmospheric and oceanic turbulence. As computer capabilities advanced from the 1980s, two-dimensional simplified numerical models of fronts were developed to explore their time evolution. Later three-dimensional numerical models based on less restrictive approximations gave more insights on the interaction of scales and mechanisms in the ocean mixed-layer. It has been possible for the last ten years to run basin-wide simulations of oceanic turbulence based on Primitive Equations (PE). The PE imply no assumption on the balance of forces involved, the only limitation being the resolution of the simulation. Dynamicists are making some great progress by pushing the resolution of these models to a computational limit (about 1km for a basinwide simulation), which reveals non-linear behaviour associated with submesoscale activity. Because fewer assumptions are made in the design of PE models, more realistic results are obtained. However the interpretation of these results remains a tricky task as it is not always clear to what extent a particular mechanism is responsible for an observation.

2.2.1 Time evolution of the horizontal density gradient

Although much of the interesting theory about frontogenesis is concerned with nonlinear feedback, it is useful to consider the density as a passive tracer conserved in the Lagrangian sense. Lapeyre et al. (2006) show that the evolution of frontogenesis (frontolysis), which is the process that leads to formation (destruction) of the horizontal density gradient is governed by the following equation:

$$\frac{D\nabla_{H}\rho}{Dt} = -(\nabla_{H}\vec{u})^{T} \cdot \nabla_{H}\rho - \frac{\partial\rho}{\partial z} \cdot \nabla_{H}w$$
(2-1)

Where $\vec{u}=(u,v,w)$ is the velocity. u and v are the horizontal components of the velocity and w is the vertical one. $(\nabla_H \vec{u})^T$ is the transposed velocity horizontal gradient tensor.

The first term on the rhs of (2-1) is the straining of the density field by the horizontal velocity field, whereas the second term is the flattening (or steepening) of the isopycnals by the vertical velocity that develops in response. As eddies stir, fold and stretch the fronts, the density gradient evolution is driven by the competition between the strain, which can "compress" the density gradient, and the vertical velocity, which can modify the slope of the isopycnals. The two terms on the rhs are linked by the fact that the density is not exactly a passive tracer, and non-linear effects are generated as a front is being strained. This is developed in the next paragraphs.

2.2.2 The theory of strain driven frontogenesis in the Quasi-Geostrophic (QG) regime

Many studies have explored the mesoscale eddies and submesoscale turbulence within the framework of quasi-geostrophic theory (QG) based on a small Rossby number approximation (Charney 1948). The Rossby number can be defined as the RMS value of the relative vorticity divided by the Coriolis parameter f. This regime which accurately describes the mesoscale phenomena associated with eddies, predicts vertical velocities (w) of the order of 1-10 m/day. The typical w distribution in the QG approximation is a

multipolar structure with alternate upwellings and downwellings along meandering fronts (with upwelling occurring downstream of the trough and downwelling occurring downstream of the ridge) (Woods 1988). These patterns, which extend vertically down to the zero-crossing of the first baroclinic mode (i.e. approximately 1000m), are induced by the curvature and by eddy-eddy interactions (Lévy et al. 2001).

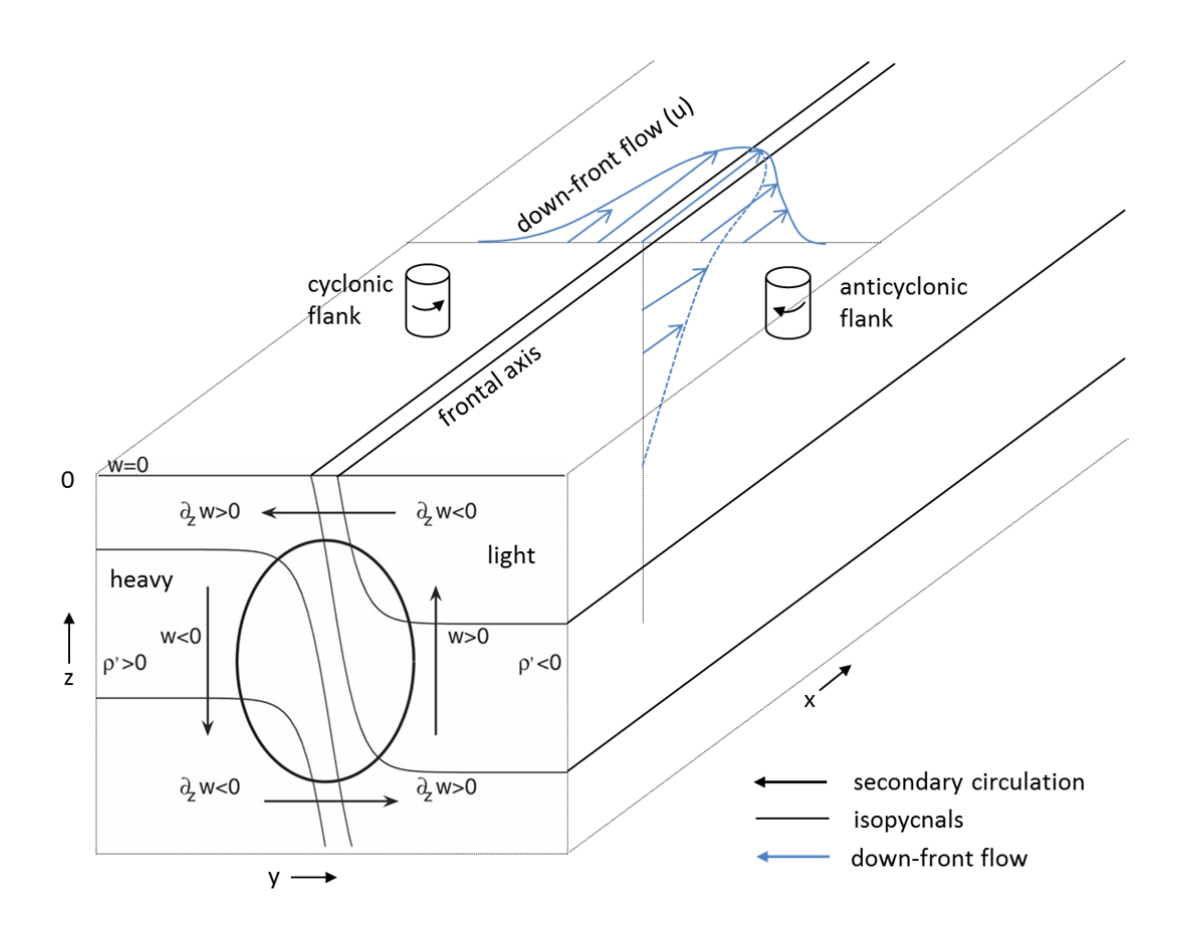


Figure 2-1: Schematic configuration for an intensifying straight horizontal density front with f > 0. The front is close to the geostrophic balance. Also shown is the ageostrophic circulation that develops in response to strengthening of the front. The lines are isopycnals, the black arrows correspond to the ageostrophic circulation, the blue arrows correspond to the down-front flow. Light fluid is on the right of the figure and dense fluid is on the left. Adapted from Lapeyre et al. (2006), Capet et al. (2008b) and Williams and Follows (2003).

The theory of frontogenesis aims at explaining how fronts are formed and intensified by two-dimensional turbulence and identifying the mechanisms triggered when this happens. The main papers describing the way cross-front density gradient intensifies are Stone (1966), Hoskins and Bretherton (1972) (hereby HB72) and Hoskins (1982) (hereafter H82). The mechanism described by the authors is an initiation by larger-scale straining (performed by mesoscale eddies, a meandering jet or wind-induced straining), which disrupts the geostrophic balance for the along-front flow and generates an ageostrophic secondary circulation in the cross-front plane. The secondary circulation acts to restore geostrophic balance by advectively tilting isopycnals towards the horizontal, which is equivalent to restratifying the front and accelerating the geostrophic flow, hence resisting horizontal density gradient strengthening (Capet et al. 2008b). The geostrophic flow is accelerated by means of an horizontal ageostrophic circulation, whose divergence on each side of the jet explains the large values of $\partial_z w$ observed near the surface (where w = 0) (See Figure 2-1). This divergence has the effect to increase the magnitude of the relative vorticity (Spall 1995). The ageostrophic circulation that develops on each side of the density front has a systematic bias that favours the upwelling (downwelling) of light (dense) fluid to release the potential energy associated with the front (Hakim et al. 2002). This argument is not only valid at the scale of the large-scale front but, more importantly, at the scale of the sub-mesoscale density gradients that are present in large number in the mixed-layer (Lapeyre et al. 2006).

This circulation was observed at sea by Pollard and Regier (1992), and explained in the following way: as the convergence in the flow intensifies the surveyed front, the high strain rates generate large shear and high vorticity. As water moves toward the front on the anticyclonic side, its absolute vorticity decreases, and the thickness between pairs of isopycnals must also decrease to conserve potential vorticity (PV). Since the surface cannot rise or fall, a vertically upward velocity must result. The presence of a boundary, such as the ocean surface, is instrumental in the process of frontogenesis. Similarly, on the cyclonic side of the front, the velocity must be downward. The magnitude of the velocity must increase with depth from zero at the surface. Below some level the confluence decreases and the vertical velocities also decrease. A closed ageostrophic circulation results, in which water from the anticyclonic

side of the front crosses toward the cyclonic side near the surface, with a deeper return flow (see Figure 2-2).

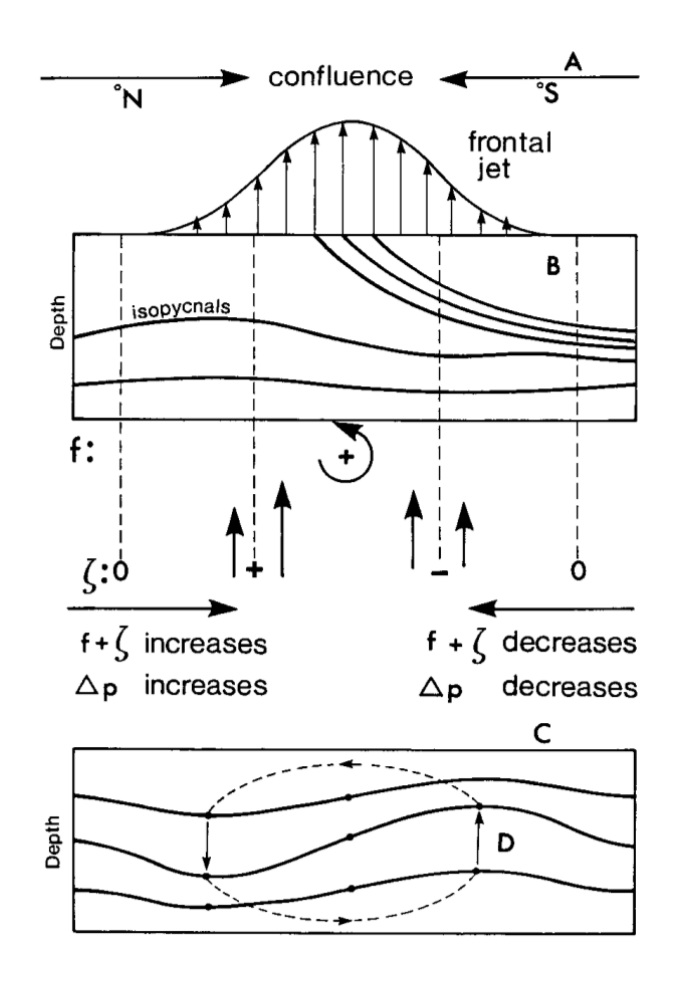


Figure 2-2: Overall confluence A moves water into an area of increasing (decreasing) vorticity on the cyclonic (anticyclonic) flank of a front B causing the separation of isopycnals to increase (decrease). Since the surface is fixed, a vertical circulation D is set up in the sense shown. From Pollard and Regier (1992).

Hoskins et al. (1978) (hereafter H78) derived the now famous QG "omega" equation in its Q-vector formulation:

$$\nabla_H^2(N^2w) + f^2 \frac{\partial^2 w}{\partial z^2} = -\frac{2g}{\rho_0} \nabla_H \cdot Q_g, \tag{2-2}$$

where w is the vertical velocity, f is the Coriolis frequency and N is the Brunt-Väisälä (or buoyancy) frequency,

$$N^2 = -\frac{g}{\rho_0} \frac{\partial \rho}{\partial z},\tag{2-3}$$

 N^2 is assumed to be constant across the front.

The Q-vector is defined as

$$Q_g = \left(\nabla_H \vec{u}_g\right)^T \nabla_H \rho = \left(\frac{\partial \vec{u}_g}{\partial x} \cdot \nabla_H \rho, \frac{\partial \vec{u}_g}{\partial y} \cdot \nabla_H \rho\right) = \left(Q_1^g, Q_2^g\right), \tag{2-4}$$

Following the QG theory, the flow is decomposed into geostrophic and ageostrophic components $\vec{u} = \vec{u}_g + \vec{u}_a$, where the geostrophic velocity is $\vec{u}_g \equiv \vec{k} \times \nabla_H \rho / f$, p is the pressure and \vec{k} is the unitary vertical vector. We have by definition $\vec{u}_g = (u_g, v_g, 0)$ and $\vec{u}_a = (u_a, v_a, w)$.

The Q-vector is a measure of the rate of increase for the horizontal density gradient arising from the straining by the horizontal geostrophic velocity field. Equation (2-2) relates the velocity divergence and vertical velocity fields to the frontogenesis of the geostrophic velocity field. It states that the vertical velocity field is triggered by the creation of a density gradient by the straining action of the eddies, through the Q-vector that intervenes in (2-1). Its net effect is to oppose the creation of density gradients in (2-1). In this consequence of the QG assumption, the role of the ageostrophic vertical velocity w is to maintain thermal wind balance, as the geostrophic velocity field acting through the Q-vector attempts to destroy it.

The QG omega equation is a representation of the balanced dynamics associated with fronts and it is valid in most situations, even with high Rossby number (Klein & Lapeyre 2009). The QG omega equation can be solved in w by defining an ageostrophic stream function such that $(u_a,w)=\left(-\frac{\partial\psi}{\partial z},\frac{\partial\psi}{\partial x}\right)$ where u_a is the ageostrophic flow in the x direction, and giving suitable boundaries conditions (w=0 at the surface and at a given depth). Significant further simplifications can be made by assuming the ageostrophic circulation to be purely two-dimensional in the cross-front plane. This leads to the following equation (Hoskins 1982):

$$N^2 \frac{\partial^2 \psi}{\partial x^2} + f^2 \frac{\partial^2 \psi}{\partial z^2} = -\frac{2g}{\rho_0} Q_2^g, \tag{2-5}$$

The solution for the stream-function is elliptic. This methodology is employed in the majority of the oceanic field studies to derive the vertical velocity, which is difficult to measure, from the high resolution hydrographic and velocity observations in the upper ocean (Pollard & Regier 1992), (Allen et al. 2001), (Martin & Richards 2001). Figure 2-3 presents the derived ageostrophic circulation at a front surveyed with ADCP during the FASINEX experiment, using the omega equation (Pollard & Regier 1992). Vertical velocities of up to 40 m/day at 200 m are found.

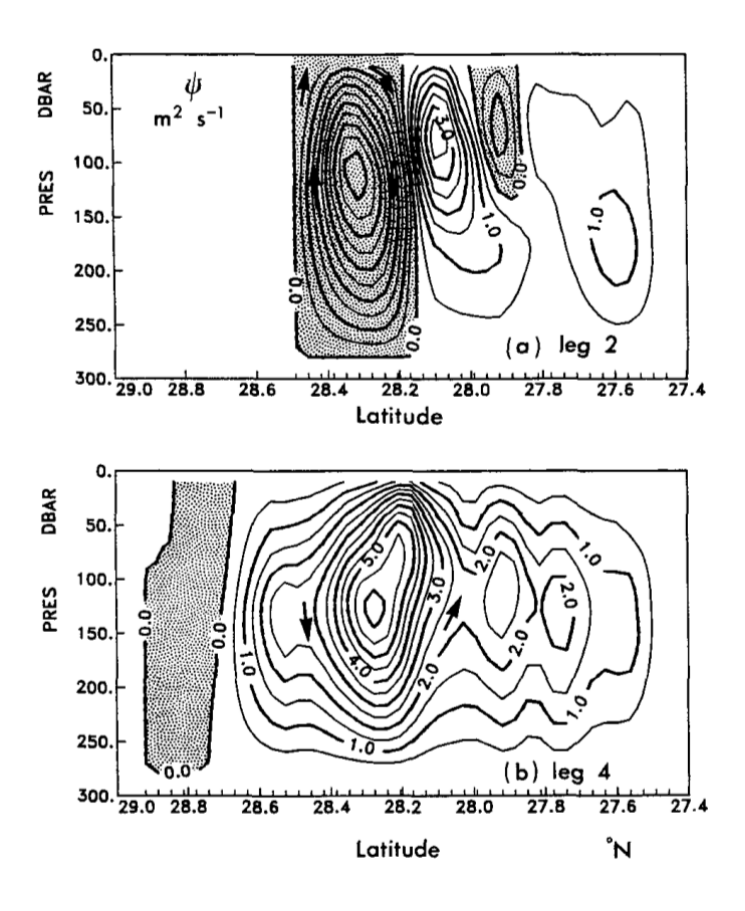


Figure 2-3: Ageostrophic streamfunctions ψ for two legs across a surveyed front. Regions of negative values are stippled. Arrows indicate the sense of circulation, such that high values of ψ are on the left of the direction of travel. From Pollard and Regier (1992).

These studies assume that the geostrophic forcing dominates the creation of ageostrophic circulation. This means that vertically varying frictional forces or laterally varying buoyancy sources and sinks are supposed not to disrupt the

thermal-wind balance, which would drive ageostrophic circulation to restore it. The validity of these assumptions comes into question for submesoscale flows, especially if the flow is exposed to atmospheric forcing (Thomas & Ferrari 2008). Mahadevan and Tandon (2006) use a high-resolution numerical simulation that generates Rossby numbers of the order of 1 to show that the QG omega equation misdiagnoses the position and sign of the most intense vertical velocities near the surface. It is able to explain the mesoscale vertical motion at depth (50-100 m), but not the submesoscale motions closer to the surface (0-50 m). The authors suggest that unbalanced dynamics and ageostrophic instabilities may have a role in the submesoscale up- and downwelling observed in the model. The fact that important frictional effects near the surface are not represented in the omega equation could also explain the discrepancy between the model and the omega equation. Finally this equation does not allow variations of stratification, nor does it integrate the advection of geostrophic momentum by the ageostrophic motion. The semigeostrophic (SG) form of the omega equation relaxes these last two restrictions.

2.2.3 The theory of strain driven frontogenesis in the Semi-Geostrophic (SG) regime

The QG theory places severe restrictions on the Rossby and Richardson numbers. It assumes that $R_0 \ll 1$ and $1/R_i \ll 1$, consequently it is not designed to accurately describe the dynamics of submesoscale phenomena. High-resolution numerical models of the mixed-layer based on the PE have shown that high strain is associated with large relative vorticity and large vertical velocity. However the regions where vertical velocities are triggered by strain are also regions of a high Rossby number (Mahadevan & Tandon 2006). Therefore the QG approximation is not valid in these areas where submesoscale dynamics occur. [HB72] have produced a frontogenesis theory that is less restrictive than QG theory and that includes ageostrophic effects highlighted in the previous paragraph. The SG regime is a more complex set of equations and scaling assumptions, which take into account critical nonlinear interactions with large Rossby numbers. These nonlinear interactions involve advection of the geostrophic quantities not only by the geostrophic motions

but also by ageostrophic motions, which is not allowed by the QG theory (Klein et al. 2008). The inviscid and adiabatic frontal model of HB72 describes the manner in which a confluent geostrophic flow (for example on the large scale a collision of western boundary currents at gyre boundaries or, on the mesoscale a confluence by eddy circulations) intensifies an initially weak baroclinic zone via its horizontal deformation field. This process involves the formation of an ageostrophic secondary circulation (ASC) whose convergent flow augments the confluence and leads to the formation of an infinitely strong front in a finite time. In this representation, the ASC is responsible for both vertical exchanges and frontogenesis. ASCs arise at fronts to keep the along-front flow in geostrophic balance as is required by the SG approximation (Hoskins 1982). The advection of density and momentum by confluent flow tends to push the jet out of thermal-wind balance and hence induces an ASC whose spatial structure is governed by the omega equation (H78). Like confluent flow, redistribution of momentum or buoyancy by small-scale turbulent mixing disrupts the geostrophic balance and, therefore, drives a geostrophy-restoring ASC (Thomas & Lee 2005). The QG omega equation (2-2) is still valid in the SG regime, but the forcing appearing in the Q-vector is not assumed to be the result of geostrophic flow only. Indeed the strain is generated by both geostrophic and ageostrophic velocities. Numerical models of meandering fronts have proven the QG omega equation to be very accurate in predicting the vertical velocity (Pinot et al. 1996, Strass 1994). However in the particular case of strong fronts or submesoscale fronts, where the Rossby number becomes high, the Semi-Geostrophic (SG) "omega" equation describes the ageostrophic circulation more accurately (Naveira Gabarato et al. 2001). Hoskins and Draghici (1977) express the SG "omega" equation in the same terms as its QG counterpart (density and horizontal geostrophic velocity), but the authors do so in the geostrophic coordinate system, following a transformation. Naveira Gabarato et al. (2001) use this equation to derive ageostrophic vertical circulations from hydrographic and ADCP in-situ measurements at the Antarctic Polar Front.

Following Eliassen (1948), Thomas et al. (2008) considers a front in the y-z plane, with no density gradient along-front and an along-front velocity purely geostrophic ($u = u_g$) and in thermal wind balance.

The two-dimensional ageostrophic circulation can be described by an across-front overturning stream function ψ where $(v_a, w) = \left(\frac{\partial \psi}{\partial z}, -\frac{\partial \psi}{\partial y}\right)$.

The SG equivalent of (2-5) is derived by Thomas et al. (2008):

$$F_2^2 \frac{\partial^2 \psi}{\partial z^2} + 2 S_2^2 \frac{\partial^2 \psi}{\partial z \partial y} + N^2 \frac{\partial^2 \psi}{\partial y^2} = -\frac{2g}{\rho_0} Q_2^g, \tag{2-6}$$

 Q_2^g , the y-component of the Q-vector, is defined by (2-4).

$$S_2^2 = -\frac{g}{\rho_0} \frac{\partial \rho}{\partial y} = f \frac{\partial u_g}{\partial z}$$
 and $F_2^2 = f \left(f - \frac{\partial u_g}{\partial y} \right)$. Under the assumptions that these coefficients and N^2 are constant, Thomas et al. (2008) were able to solve (2-6). The solution for the ageostrophic function is elliptic, as in the QG approximation. Figure 2-4 illustrates one solution for (2-6).

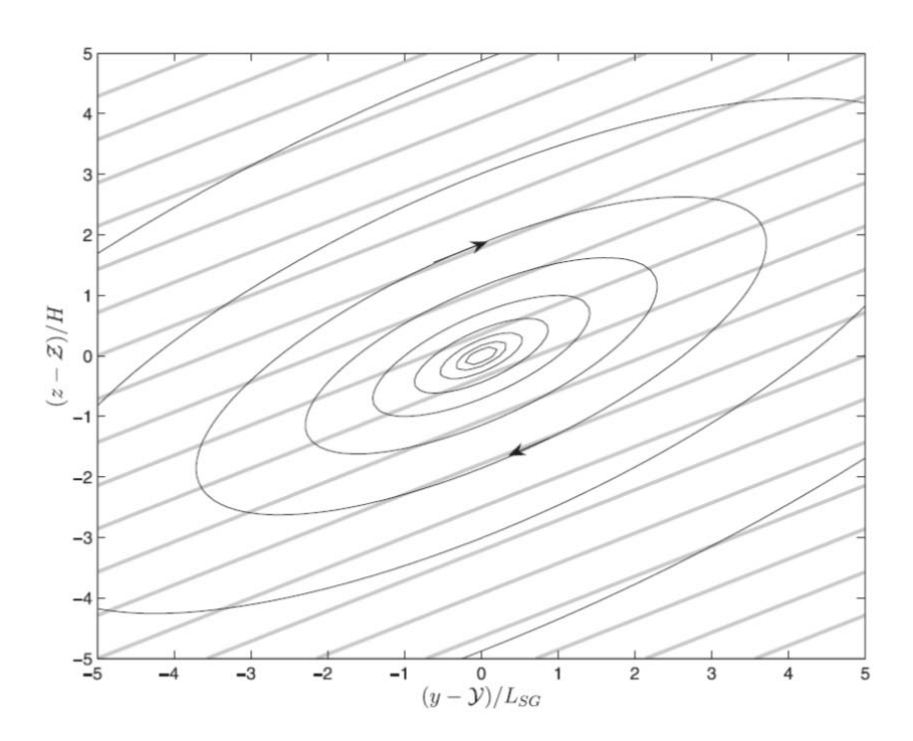


Figure 2-4: Ageostrophic circulation driven by a negative point-source Q-vector, $Q_2^g < 0$, at y = Y and z = Z. Isopycnals (gray contours) slant upward to the North due to a southward buoyancy gradient. For this frontogenetic forcing, $Q^g \cdot \nabla_h b > 0$, where b is the buoyancy, the circulation is thermally direct and tends to restratify the fluid. From Thomas et al. (2008).

The vertical velocity associated with the stream function is given by

$$w = -\frac{F_2^4}{2\pi (fq_{2D})^{3/2}H^2} \frac{(y-Y)}{Arg},$$
(2-7)

with

$$Arg = \frac{\left[(y-Y) - (z-Z)S_2^2/F_2^2 \right]^2}{L_{SG}^2} + \frac{(z-Z)^2}{H^2},$$
(2-8)

and where

 $L_{SG}=Hrac{\sqrt{fq_{2D}}}{F_2^2}$ is the SG Rossby radius of deformation, H is a characteristic vertical lengthscale of the flow, and $q_{2D}=rac{1}{f}(F_2^2N^2-S_2^4)$ is the potential vorticity (PV) of the two-dimensional geostrophic flow. One can deduce from this that at depth z=Z one finds

$$w = -\frac{1}{2\pi f H^2} \frac{1}{(y-Y)} \underbrace{\left(\left(f - \frac{\partial u_g}{\partial y} \right)^2 N^2 - \left(\frac{g}{\rho_0 \partial y} \frac{\partial \rho}{\partial y} \right)^2 \right)^{3/2}}_{A}.$$
 (2-9)

Under the assumption that f and H are constant in the vicinity of the front, one can say that the SG assumption leads to a vertical velocity which is proportional to the value of A (on the rhs of (2-9)). If one further assumes that N^2 and $\frac{\partial u_g}{\partial y}$ are constant on a side of the front, w becomes a direct function of the density gradient across the front. It is clear that the absolute value of the vertical velocity anywhere at the front is increasing as a function of the density gradient. There is no such simple conclusion when considering $\frac{\partial u_g}{\partial y}$, instead the effect of an increase of this term on the vertical velocity depends on the magnitude of the horizontal density gradient. This is coherent with the omega equation (2-2), which stresses that the vertical velocity depends on the configuration of the horizontal geostrophic strain with regard to the orientation of the front.

The SG analytical model of HB72 showed that a barotropic external deformation field applied to a uniform density gradient causes a finite discontinuity to develop at the surface in a finite time. This result is in contrast to a purely QG model in which the surface discontinuity forms as time goes to infinity. HB72 explains that, in reality, mixing or friction and three-dimensional

effects, which are ignored in the model, would eventually take over to smooth out discontinuities. Intense submesoscale structures can be described by the dynamics contained in the PE or the SG regime. Associated with the strong submesoscale vorticity gradients, the vertical velocities are one order of magnitude stronger than the vertical velocities of QG dynamics (Pollard & Regier 1992), (Spall 1997). Numerical simulations suggest that submesoscale vertical velocities are maximum at around 100 m depth where they overtake mesoscale QG vertical velocities, which are maximum at around 1000 m depth (Lévy et al. 2001).

2.2.4 The theory of frontogenesis in the SQG regime

Another set of dynamics, the Surface Quasi Geostrophic regime (SQG), has been suggested to describe the oceanic eddy field in the surface layers (Blumen 1978). The SQG system involves the same assumptions as the QG system. In particular, the Rossby number is assumed to be small. In addition, the SQG regime considers a nonzero surface density anomaly and assumes a uniform potential vorticity (PV) in the interior. Essentially, the surface density is a Dirac delta of potential vorticity, as first recognized by Bretherton (1966).

Mesoscale eddies stir the nonzero surface density anomalies, which leads to a cascade of energy to small scales and strong density gradients at submesoscale, through the process of frontogenesis. The consequence is that the three-dimensional dynamics, and in particular the vertical structure of surface fronts, are entirely driven by the time evolution of the density at the surface.

Like the QG approximation, the SQG regime is used by ocean and atmosphere dynamicists to study the properties of the turbulence, because it facilitates the computations of the simulations. Indeed, in contrast to the Primitive Equation models, SQG models have only two dimensions, which makes it possible to run a numerical model with a much higher spatial resolution. The SQG regime is the counterpart of the regime of interior QG turbulence, which assumes that motions are not influenced by vertical boundary conditions on the streamfunction and behaves as though these conditions were homogeneous. Consequently, the interior QG regime assumes surface density anomalies to be

zero (Klein & Lapeyre 2009). The interior QG regime exhibits a steep velocity spectrum (close to k⁻³ or k⁻⁴), and its turbulence does not produce small-scale features, independently from the spatial resolution of the simulation. In this regime, the vertical velocity field is located mostly with the mesoscale eddies because large vorticity amplitudes are found principally in the eddy cores. In contrast, the SQG regime involves a shallow surface velocity spectrum (k^{-5/3}), with more energetic small scales, identical to the density spectrum (Klein et al. 2008). The vertical pump in this regime is essentially at small scales and appears to be evenly partitioned between mesoscale eddies and small-scale elongated filaments between the eddies (Lapeyre & Klein 2006a).

These authors have used PE simulations to show that the ocean dynamics can be decomposed in terms of a solution forced by the potential vorticity in the interior (QG mode) and a competing solution forced by the surface density (SQG mode). One of their results was the dominance of the latter mode in the first 500 meters. As a consequence, the dynamics in these layers can be recovered with analytical relations. Using SQG equations, a complete determination of the stream-function in the upper-layer of the ocean can be obtained from a unique snapshot of the surface density anomaly. This follows Held (1995) and Hakim (2002), who deduced winds associated with temperature anomalies in the tropopause, using the SQG assumptions. Lapeyre and Klein (2006) have shown that the SQG model allows one to reconstruct the 3-D dynamics of submesoscale and mesoscale from just the horizontal surface density field using a constant Brunt-Väisälä frequency. LaCasce and Mahadevan (2006) have also demonstrated the relevance of this model for the upper oceanic layers using in-situ data and comparing with SQG reconstruction using SST. Isern-Fontanet et al. (2006) explored the potential use of microwave SST for the estimation of ocean currents. The authors showed a good correlation between the horizontal current recovered from the SST by the SQG model and the current obtained from altimetric measurements.

Isern-Fontanet et al. (2008) showed that an effective version of SQG (eSQG) is quite successful in reconstructing the velocity field at the ocean surface for scales between 30 and 300 km. Their approach consists of inverting the QG potential vorticity generated by surface density only, assuming that temperature anomalies fully represent surface density anomalies. This method only requires a single snapshot of SST and two parameters: the mean Brunt-

Väisälä frequency and a parameter that determines the energy level at the ocean surface. They tested the performance of the approach using an Ocean General Circulation Model simulation representing the North Atlantic in Winter. They concluded that results are reasonably good in the first 500 m and that the success of the method mainly depends on the quality of the SST as a proxy of the density anomaly at the base of the mixed layer. The ideal situation for the application of this method is after strong wind events, because the mixed layer is deep.

2.2.5 Scaling of the Omega equation

The SQG model is very energetic in the small scales, and filaments are created and stirred by the straining action of eddies. These filaments are bounded by fronts, which are strengthened whenever the filaments are elongated. The resulting thermal-wind imbalance generates vertical motions that are governed by the omega equation. Lapeyre and Klein (2006) calculate a scaling of this equation, based on SQG regime characteristics. They obtain

$$w(z) = \frac{g\sigma}{N^2} \frac{\Delta \rho}{\rho_0} \frac{z}{D} \exp\left(\frac{z}{D}\right),\tag{2-10}$$

where σ is a scale for the surface large-scale strain field, with a classical value $\sigma = 2.5 \times 10^{-6} \, s^{-1}$. $\Delta \rho$ is the density variation across the fronts that bound the filament. D = fL/N is the vertical length scale to which the density decays exponentially, which is a SQG consequence. L is the width scale of the filament.

This parameterization of the vertical velocity is a function of the stratification, the width of the filament, the magnitude of the strain applied to it and the density difference across the fronts bounding the filament. The authors calculate an average $w(100m)\approx 0.85~m.~d^{-1}$ at filaments produced by a typical fully turbulent eddy field in free decay simulation. This parameterization is adapted to be used on satellite SST and altimetry in section 5.4.

Legal et al. (2007) derive another parameterization of the vertical velocity from a scaling of the omega equation:

$$\left(1 + \frac{N^2 D^2}{f^2 L^2}\right) w = -2 \frac{g D^2}{\rho_0 f^2 L^2} \sigma \Delta \rho,$$
(2-11)

The authors apply this formula to the appropriate values related to an in-situ high resolution survey in a region of the northeast Atlantic Ocean characterized by a large number of strongly interacting eddies. Equation (2-11) translates into

$$w \approx -250\Delta\rho,\tag{2-12}$$

where w is in meters per day and $\Delta \rho$ is in kg/m^3 .

This linear relationship is checked by calculating the correlation between the small-scale density anomalies across the field (after removing the large-scale meridional density gradient) and the diagnosed vertical velocities obtained using in-situ SeaSoar data combined with the analysis of altimeter data. The anticorrelation between the two quantities is remarkable, and the regression calculation leads to a factor of -300, a value close to the estimation (-250) deduced from the scaling (2-12). Thus, the strong anticorrelation between the vertical velocity field and the small-scale density anomalies is easily explained by the elongation of the small-scale density filaments by the large-scale strain field, whose effects are described by the omega equation.

2.3 Restratification effect of frontal submesoscale instabilities

The previous section shows how a large scale straining field acting to intensify a front can trigger ageostrophic vertical circulations which counteract the frontogenesis so that the thermal wind balance is maintained. This mechanism was explored under the perspective of the vertical exchanges occurring in the vicinity of fronts. The principal objective behind these studies is to improve the understanding of vertical exchange of properties between the atmosphere and the ocean, as well as the upwelling of nutrients from the deep, the subduction of plankton under the thermocline and their effects on the oceanic carbon pump. Another class of studies has emerged in the last decade which focuses on how the front affects the mixed layer stratification. Horizontal buoyancy gradients store available potential energy, which gets released

whenever the fronts become unstable and slump. As a front slumps, the density gradient is rotated from the vertical to the horizontal, and the consequence is an increase of the stratification. It is now understood that unforced submesoscale baroclinic frontal instabilities play a leading role in the release of frontal potential energy. They currently focus the attention of dynamicists who seek to parameterize their contribution to the restratification for use in coarse resolution ocean models.

Traditionally, the processes affecting the stratification and the mixed layer depth (MLD) were seen as purely one-dimensional. In this view, the stratification is reduced (MLD deepens) through turbulent mixing produced by winds or cooling and evaporation at the surface, which makes surface water denser. Conversely, the stratification is increased (MLD gets shallower) when heating and precipitation reduce the surface density. This view is now challenged and the role of lateral instabilities in the restratification of the mixed layer was proven to be significant whenever there are horizontal density gradients (Boccaletti et al. 2007). The authors illustrate their theory with the following scenario. A winter storm hits the open ocean, mixing the top 100 m of the water column over a patch of a few hundred square kilometres. Once subsided, the storm leaves behind a homogenized layer in which horizontal variations of salinity and temperature have survived, yet vertical variations have been virtually erased by vertical mixing. The horizontal gradient of density is the surface signature of nearly vertical isopycnals produced by localized mixing. After the storm, a dynamical adjustment process begins that restratifies the surface layer by slumping of the fronts. This slumping, initially a simple gravitational overturning, is subsequently modified by rotation leading to a geostrophic adjustment. This geostrophic adjustment limits the release of energy and prevents further slumping where a Coriolis force develops with an along-front flow to balance a cross-front pressure gradient. Tandon and Garrett (1995) predicted that this adjustment takes a few day during which the initially vertical isopycnals oscillate around the geostrophically adjusted state with

$$N^2 = \left(\frac{\partial b}{\partial y}\right)^2 / f^2,\tag{2-13}$$

Chapter 2

where $\frac{\partial b}{\partial y}$ is the cross-front buoyancy gradient. This formula was validated by Boccaletti et al. (2007) with a high-resolution numerical model of a front undergoing dynamical adjustment. However Boccaletti et al. (2007) show that the geostrophically adjusted state can be further unstable to submesoscale baroclinic instabilities that continue restratification. Their simulation demonstrates that the bulk of the restratification happens after the baroclinic instabilities set in. These instabilities, which are referred to as mixed layer instabilities (MLI), differ from instabilities in the ocean interior because of the weak surface stratification. They have a small vertical scale, are submesoscale in the horizontal (of the order of 1-10 km), and a growth time scale of the order of a day.

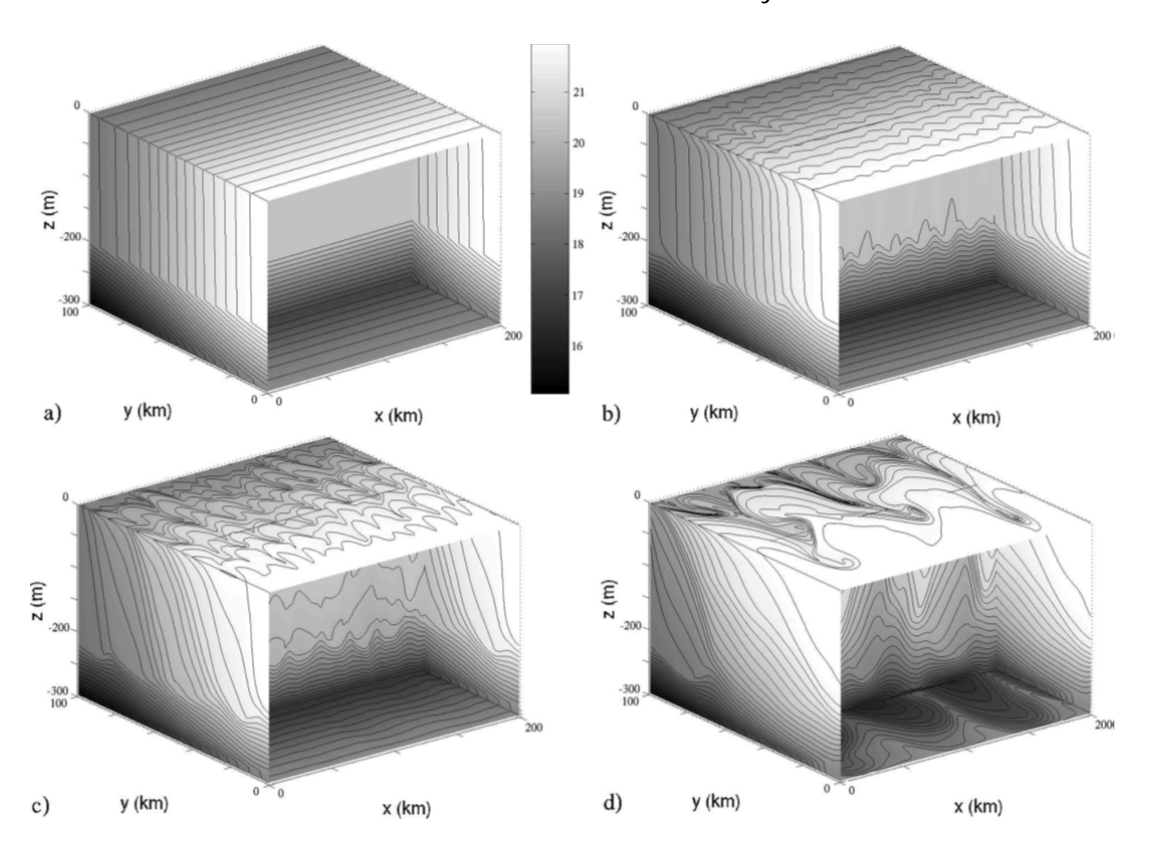


Figure 2-5: Development of mixed layer baroclinic instabilities along a temperature front undergoing geostrophic adjustment. (a) The initial configuration consists of a lateral temperature front in a well-mixed surface layer on top of stable density stratification. (b) After 10 days the front has tilted from the vertical to the horizontal and wavelike disturbances appear along the front. The tilt of the wave disturbances in the along-channel direction is such as to release the potential energy stored in the horizontal stratification much like in the Eady problem. (c) By day 12 the disturbances are fully nonlinear and start growing in scale as a result of an inverse cascade of energy. (d) At day 17 the disturbances have wrapped up into eddies and frontogenesis develops along the rim of the eddies. The colour bar is in degrees Celsius, and the contour interval is 0.25°C. From Boccaletti et al. (2007).

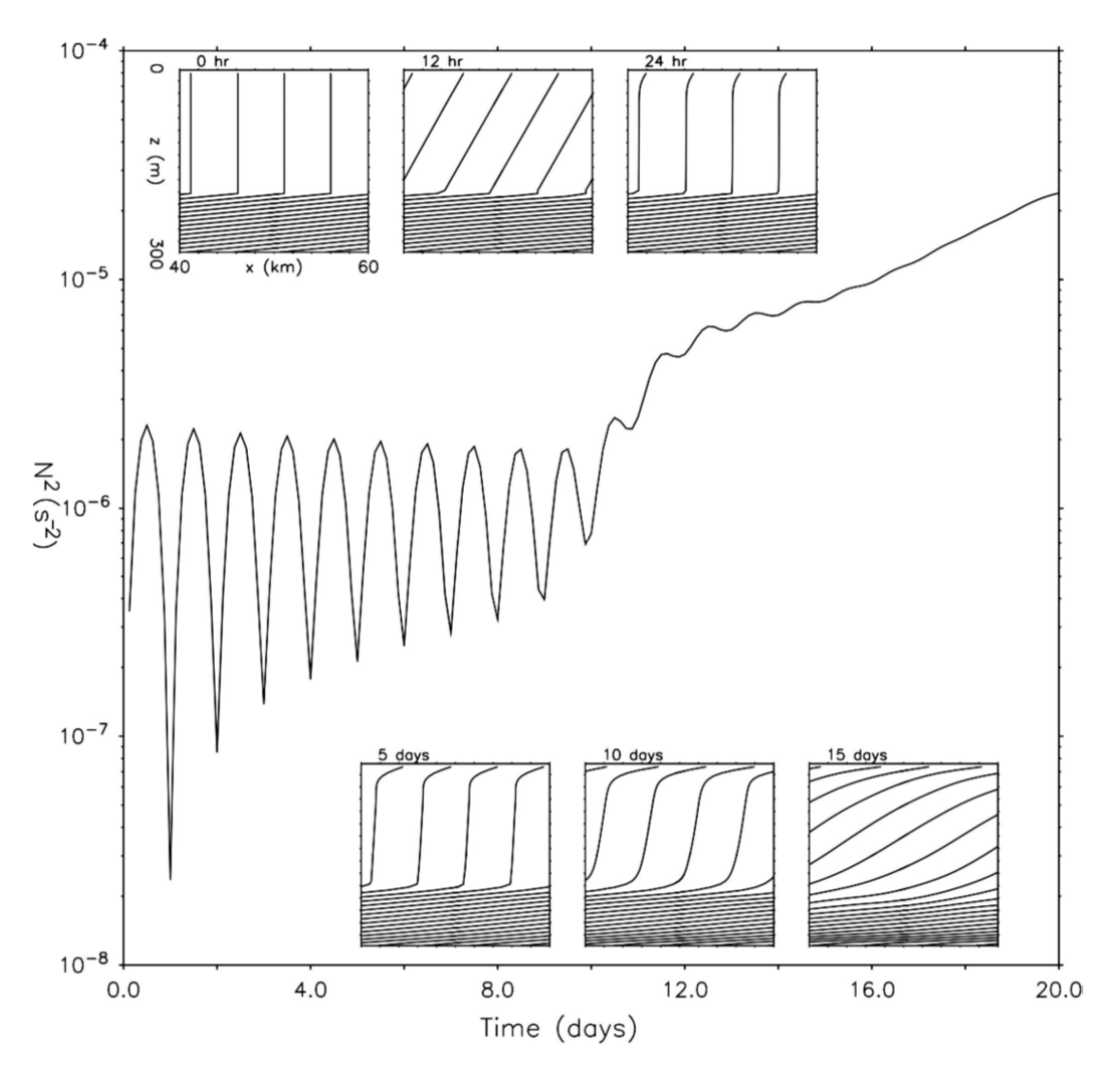


Figure 2-6: Increase in domain-averaged buoyancy frequency N^2 as a result of slumping of the mixed layer front shown in Figure 2-5. The initial vertical stratification is 0. The insets show snapshots of the various stages of the along-channel average of buoyancy. The initial slumping oscillates on the inertial period (h 0–24). It is followed by a restratification due primarily to the growth of baroclinic MLIs (days 2–10) and then by the eddies resulting from the nonlinear interaction of the MLIs (day 10 onward). MLI perturbations are infinitesimal until day 10 and thus N^2 is seen to simply oscillate around the geostrophic adjusted state. Only once MLIs reach finite amplitude does the increase in N^2 become significant. From Boccaletti et al. (2007).

Figure 2-5 presents a series of 3D snapshots of the front during the adjustment, and Figure 2-6 displays the stratification of the scene against time. Tandon and Garrett (1994) argue that mesoscale restratification acts on time scales too slow to compete with vertical mixing, hence its role in the mixed layer restratification should be ignored. Boccaletti et al. (2007), on the

contrary, show that MLIs develop at the mesoscale and are fast enough to restratify between mixing events. MLIs inject high potential vorticity thermocline waters into the mixed layer and drive substantial restratification despite the action of vertical mixing. They constitute a leading-order process in the mixed layer heat budget for fronts stronger than about $1 \times 10^{-3} \ K/km$ and play an important role in determining the depth, temperature and salinity of the mixed layer. MLIs have been observed and proven ubiquitous by a few observational studies such as Flament et al. (1985) and Munk et al. (2000).

Fox-Kemper and Ferrari (2008) note that ocean models that do not resolve the submesoscale, which require a grid of the order of 100m, have a bias toward weak near-surface stratification. This is a consequence of the fact that they typically ignore dynamical restratification by slumping of horizontal density gradients within the mixed layer. They propose a parameterization for the restratification driven by finite-amplitude baroclinic instabilities of the mixed layer in term of an overturning streamfunction that tilts isopycnals from the vertical to the horizontal. The streamfunction (ψ_e) is proportional to the product of the horizontal buoyancy gradient $(\frac{\bar{\partial}b}{\partial y})$ the mixed layer depth (H) squared, and the inertial period (f):

$$\psi_e \approx 0.06 \cdot H^2 \frac{\overline{\partial b}}{\partial y} / f. \tag{2-14}$$

Where the overbar denotes an average along-front. Therefore, restratification proceeds faster at strong fronts in deep mixed layers with a weak latitude dependence. Fox-Kemper and Ferrari (2008) compare the parameterization with submesoscale-resolving simulations and estimate the importance of MLI restratification from data. Fox-Kemper et al. (2010) explore the numerical implementation of the parameterization and its effect in realistic global simulations. This parameterization is tested on satellite SST data in section 5.6.

Questions remain on the interaction between mesoscale eddies ands MLI and how they affect the restratification. Lapeyre et al. (2006) suggest that mesoscale instabilities can also act to restratify the upper ocean through frontogenesis. However that study used coarse-resolution numerical simulations that do not allow for the development of MLIs. Boccaletti et al. (2007) speculate that mesoscale eddies dominate in regions of strong

convergence, where MLIs are suppressed according to Spall (1997), while MLIs compete and often dominate over mesoscale restratification elsewhere.

Another question under investigation is the role of wind above fronts in the restratification. Depending on the orientation of the wind with regard to the front, its consequence can be an intensification or a destruction of the stratification. When the wind stress has a component up front, the surface Ekman flow will advect lighter water over denser, thereby restratifying the mixed layer. On the other hand, down-front winds advect denser water over lighter, giving rise to an ageostrophic circulation which destroys the mixed layer stratification and leads to the intensification of the front. The latter mechanism was described by Thomas and Lee (2005). Thomas and Ferrari (2008) show that restratification ensuing from frontogenesis can be of comparable magnitude with the wind destruction of stratification, which means that the latter can easily overcome the former. Mahadevan et al. (2010) study the competition between down-front wind action to maintain the isopycnals vertical at the front and the enhancement of the stratification by the MLIs. An equilibrium between the two processes can be found over long periods, where the potential energy input by the wind is extracted by strengthened MLIs. The authors suggest a scaling diagnostic to determine whether the effect of MLIs or wind dominates under different conditions.

$$r = \tau_0 / \left(0.06 \rho H^2 \frac{\overline{\delta b}}{\partial y} \right), \tag{2-15}$$

where τ_0 is the along-front wind stress. Their simulations show that though the cross-front transport of buoyancy induced by the down-front component of the wind opposes restratification by MLIs, it becomes diminished as the eddies and growth of the frontal instability disrupt alignment between the wind and frontal axis.

2.4 Basin-wide models combining several mechanisms

The previous sections have presented researches on frontal dynamics based on analytical equations and numerical models of a single front. The models have increased in complexity over the past 30 years, starting from two-

dimensional simplified simulations to three-dimensional high-resolution non-linear numerical simulations of one front undergoing the forcing from mesoscale strain and wind. This evolution was made possible by the continuous improvement in computer performances. Since the 2000s, scientists have started to use the most advanced super-computers, which were more commonly used to perform global climate models runs, to simulate mixed layer dynamics at the regional/basin scale, over a long time scale, and with a spatial resolution high enough to resolve the submesoscale. Biophysical models of eddy fields showed consequent increases of primary productivity (PP) as the resolution of the models was increased.

Mahadevan and Archer (2000) explored the range of resolution from 40 to 10km in a model representing an area of the ocean where PP is limited by the availability of nutrients. They observed an increase of a factor of three of PP as a consequence of the appearance of small-scale fronts at high resolution. Similarly, Levy et al. (2001) reported a factor 2 change in PP when changing the resolution from 10 to 2 km. The latter resolution allowed the model to resolve small fronts surrounding or ejected by the eddies. Intense vertical velocities of up to 40 m/day were observed in the vicinity of the fronts. Capet et al. (2008b) continued this work and simulated an idealized subtropical eastern boundary upwelling current system similar to the California Current (about 700 by 700 km). They observe that pushing the resolution to O(1 km) creates a complex flow structure with mesoscale eddies and fronts. In addition, instabilities arise along the wind-driven alongshore currents and significant energy is transferred into submesoscale fronts and vortices in the upper ocean (see Figure 2-7).

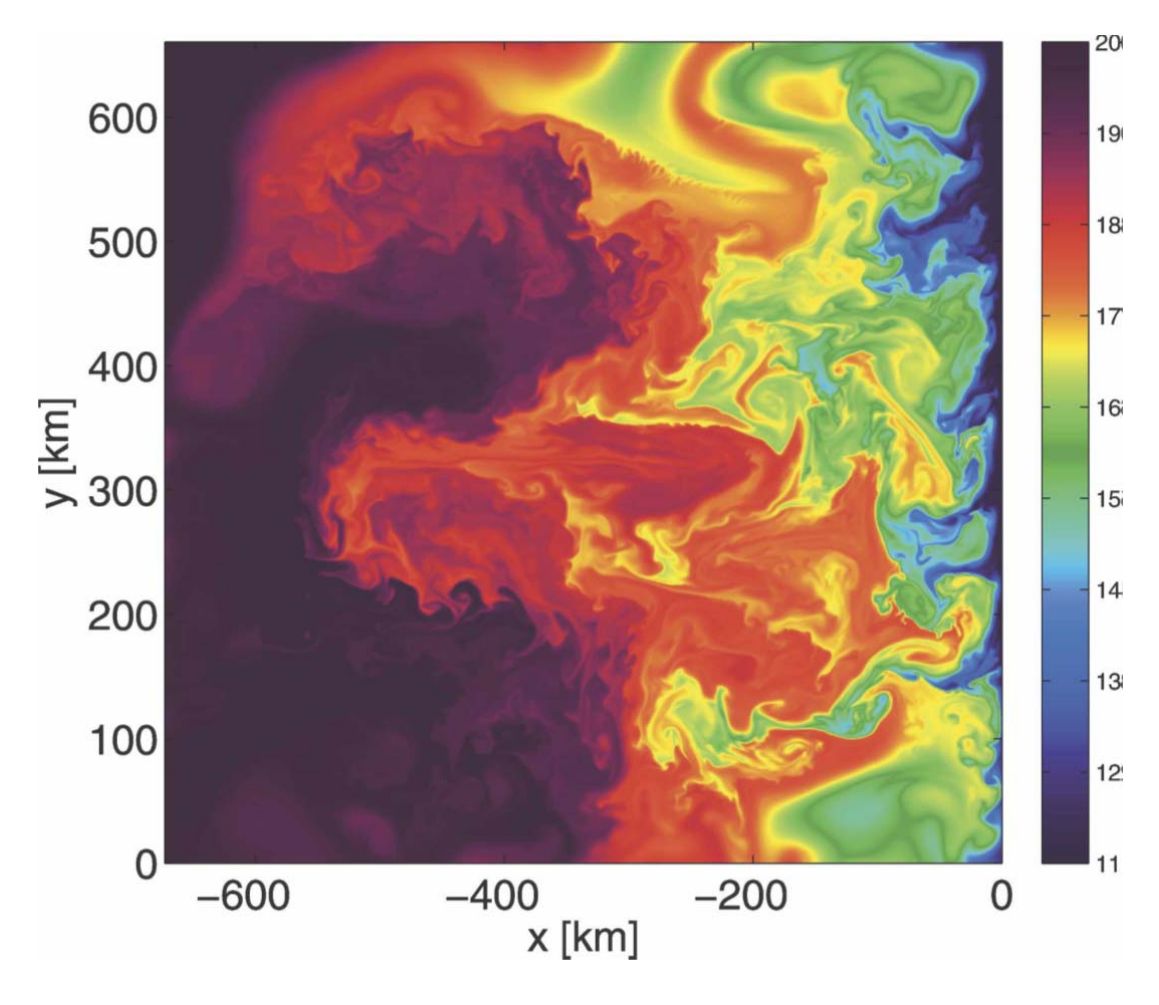


Figure 2-7: Simulated instantaneous surface temperature field. Note the string of meanders and filaments in $17^{\circ}-19^{\circ}$ C water with wavelength ≈ 50 km running along the edges of the offshore eddies (MLIs). From Capet et al. (2008b).

The submesoscale arises through surface frontogenesis growing off upwelled cold filaments that are pulled offshore and strained in between the mesoscale eddies. In turn, some submesoscale fronts become unstable and develop submesoscale meanders and fragment into roll-up vortices. Associated with this phenomenon are a large vertical velocity (up to 50 m/day) and Rossby number and a large vertical buoyancy flux acting to restratify the upper ocean. The authors developed a combination of composite averaging and separation of distinctive subregions of the flow in order to analyse the submesoscale fronts from a phenomenological and dynamical perspective. To investigate the frontogenesis driven by the horizontal strain, they used

$$F_S = Q_S \cdot \nabla_H \rho, \tag{2-16}$$

where

$$Q_S = -\left(\frac{\partial u}{\partial x}\frac{\partial \rho}{\partial x} + \frac{\partial v}{\partial x}\frac{\partial \rho}{\partial y}, \frac{\partial u}{\partial y}\frac{\partial \rho}{\partial x} + \frac{\partial v}{\partial y}\frac{\partial \rho}{\partial y}\right),\tag{2-17}$$

 F_S is a measure of the rate of increase for the horizontal density gradient arising from the straining by the horizontal velocity field. F_S is computed from satellite SST data and altimetry in section 5.5. Note that equation (2-17) is close to the Q-vector defined in (2-4) except for the sign and the fact that it represents the straining from the total horizontal field, rather than only its geostrophic component in (2-4). Hoskins (1982) states

$$\frac{D|\nabla_H \rho|^2}{Dt} = F, \tag{2-18}$$

where F is the addition of the straining by the horizontal density field (F_S) with the straining deformation by vertical velocity, the vertical mixing and the horizontal diffusion. Typical horizontal patterns of the frontally concentrated quantities $|\nabla_h \rho|$, w, w''T'' and F_S are shown in Figure 2-8. (Herein " refers to a spatial and temporal high-pass filtering). These quantities are mutually related in a way that is suggestive of on-going frontogenesis. As predicted by Hoskins and Bretherton (1972), the extrema of vertical velocity and vertical flux of temperature are localized in regions where the velocity field is conducive to frontogenesis, that is, where F_S is large.

Chapter 2

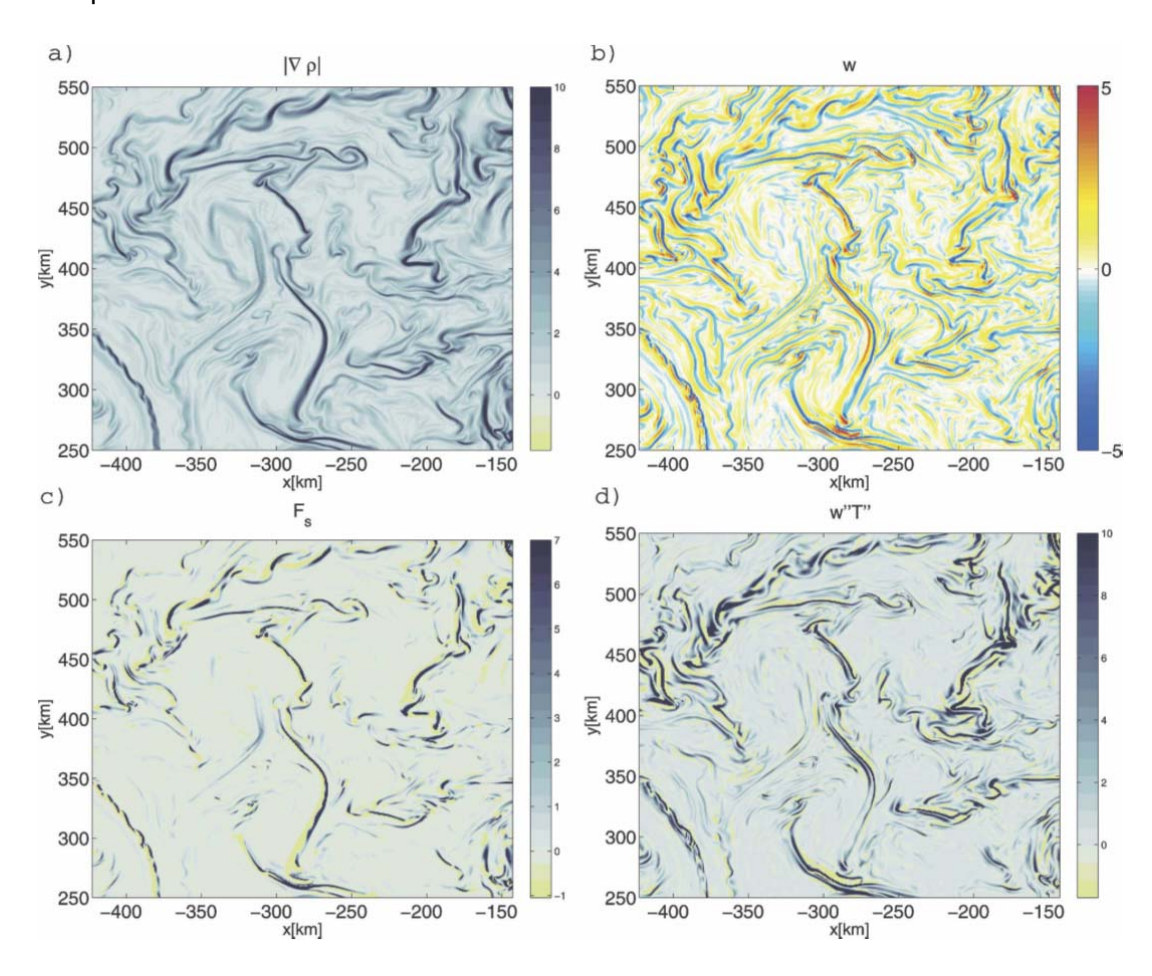


Figure 2-8: Instantaneous horizontal patterns for frontal quantities simulated at t=160 days and 10-m depth in a 270 km \times 300 km subdomain: (a) $|\nabla_h \rho|$ ($\mathbf{10^{-5}} kg.m^{-4}$), (b) |w| ($\mathbf{10^{-4}} m.s^{-1}$), (c) F_S ($\mathbf{10^{-14}} kg^2m^{-8}s^{-1}$), and (d) $w''T''(\mathbf{10^{-5}} m.^{\circ}C.s^{-1})$. From Capet et al. (2008b).

The authors also process composite vertical profiles of these quantities over frontal regions within the domain and from 50 independent times. These profiles clearly show a general positive tendency of $F_{\rm S}$ in the top 20 meters. Upward velocities on the light side of fronts reach 20 m/day at 10 meters depth, whereas the maximum downward velocities on the heavy side are -50 m/day at the same depth.

These series of three publications are remarkable in the sense that they are the first to simulate such a large region while resolving such small features. The authors observed mesoscale jets, submesoscale fronts, frontogenesis, ageostrophic secondary circulation, frontal instability across a range of scales and coherent vortices, which typically occur simultaneously. The flow remains

close to satisfying a geostrophic or gradient-wind force balance most of the time. The main departure from balance are found in the vicinity of both stable and unstable fronts, and the unbalance patterns most strongly reflect the ageostrophic secondary circulation (ASC) associated with frontogenesis. These ASCs are confined to the surface boundary layer and efficiently release potential energy and effectively act to restratify the upper ocean, even though only a small fraction of the domain is actively frontal at any given time.

The results from Levy et al. (2010) suggest that submesoscale dynamics have an impact on the large scale circulation. Their simulation took advantage of one of the most advanced super computers to compute 100 years duration of a dynamic scene characteristic of mid-latitude oceanic gyres. As the resolution of the model is increased from 1/9°to 1/54° (about 2 km), major changes on the circulation occur with submesoscale physics having an integrated and cumulative effect on the large-scale oceanic circulation. These changes ensue from the emergence of a denser and more energetic vortex population at 1/54°, occupying most of the basin and sustained by submesoscale physics. Non-linear effects of this turbulence strongly intensify the jet that separates the two gyres, and a regime of energetic secondary zonal jets emerges, associated with complex recirculation. In parallel, submesoscales restratify both the seasonal and main thermocline, inducing a particular reduction of deep convection and the modification of the water masses involved in the meridional overturning circulation. This suggests that submesoscale processes play an important role on the mean circulation and the mean transports at the scale of oceanic basins.

2.5 Questions that are left to be answered

The oceanographic community is putting a lot of efforts into understanding the dynamics associated with ocean surface fronts. It is now clear that the vertical exchanges that occur in their vicinity play a major role in the transfer of momentum, heat and tracers between the mixed layer and the atmosphere on one side, and the deep water on the other side. Therefore the presence of fronts is instrumental in the setting of the mixed layer stratification and composition. The general processes and interactions that happen at the fronts

and their consequences in term of vertical velocity or restratification are fairly well understood from a qualitative perspective. They were indeed predicted by analytical studies, linked to atmospheric science, several decades ago. Since these early publications, numerous in-situ observations and constantly improving numerical models have confirmed these predictions.

The issue of the quantification and prediction of the dynamics associated with fronts is being tackled. Significant conclusions were reached in the previous decade, and further important results should be published in the coming one. The challenge is to improve the understanding of the physical processes at fronts, how fronts are created, destroyed or maintained and how they interact with their environment. The main focus point at the moment is the role of the submesoscale within these processes. The objective of the dynamicists involved in these studies is eventually to be able to parameterize the small-scale physics occurring at fronts. This would dramatically improve the quality of the prediction of the ocean global circulation models (OGCM), which do not resolve the submesoscales and will most probably not do so for a very long time.

It is the opinion of the author of this thesis that satellite observations of the ocean are being underestimated in this context, whereas they have the potential to bring answers to some of the questions the dynamicists are asking themselves. Similarly, dynamical research is being overlooked by the satellite oceanography community when it provides results that have the power to increase the oceanographic observation capabilities of satellites. This section presents currently open dynamical questions for which satellite observations have the potential to provide answers or at least advance the understanding. Some of these questions will be tackled by this thesis, the others will be left open but could benefit from the methodology established here.

The main question is the issue of the frequency of the fronts on the ocean. Many dynamical studies derive values of subduction, upwelling or restratification, expressed as a vertical flux of heat, occurring in the vicinity of a front under certain conditions. However a greater understanding of the frequency of such features in the ocean surface is required to estimate the integrated, cumulative, overall impact on the mixed layer dynamics and on the global ocean properties. Spall (1995, 1997) and Boccaletti (2007) recognize the

need for such analyses. Global data sets of SST have the capability to quantify the occurrence and variability of the fronts that respect certain conditions assumed in the physical studies.

The frontal statistics hidden in the SST data sets can be refined if one uses in synergy other observational data sets such as the mesoscale geostrophic straining field (from altimetry), the wind stress (from scatterometers) or the mixed layer depth (from Argo floats). A methodology integrating the various observation data sets while making the most up to date of dynamical knowledge could lead to a comprehensive description of some surface dynamics at the global scale. Moreover, parameterization of small-scale dynamics have been suggested (Fox-Kemper et al. 2008, Mahadevan et al. 2010) for use in global ocean circulation models but are believed by the author of this thesis to be also useful when applied on real satellite data. The frontal statistics, eventually combining several parameters, have also the potential to assess the quality of the numerical simulations with respect to observations.

As was discussed in the previous sections, the main driver for front creation, also called frontogenesis, is horizontal convergence. A mesoscale convergence under the form of strain can intensify a weak meridional gradient of temperature by pushing different water masses toward each other. It was shown that ageostrophic secondary circulations respond to the intensification of a front by strain in order to maintain the thermal-wind balance. These ASCs, in turn, have a frontogenetic effect due to their divergence at the surface boundary. Other studies have demonstrated that a front can be destroyed, a process called frontolysis, if it goes baroclinically unstable, meanders and the isopycnals slump toward the horizontal. The mixed layer instabilities (MLI) develop along the front and act to destroy the front and restratify the mixed layer. However, little is known about the competition between instability and active frontogenesis in a baroclinic flow (Capet et al. 2008b). Spall (1997) observed in numerical simulations that frontogenesis provided by the deformation field counteracts the frontolysis of the baroclinic instabilities such that strong coherent time-dependent meandering jets are maintained for as long as the deformation field persists. Satellite data sets are suitable to explore this competition and to provide answers since high resolution SST products resolve the frontal instabilities while altimetry products provide a good insight into the straining field applied to the surface fronts.

Chapter 2

Turbulence research has achieved major results, and the phenomenology and physical mechanisms of the separate regimes of two- and three-dimensional, geostrophic, stratified, gravity-wave, and boundary-layer are now fairly well established (see Muller et al. 2005, Ferrari and Wunsch 2009, Ferrari and Wunsch 2010 for a review on these studies). These regimes describe well the nature of geophysical turbulence at various space and time scales and at various locations on the ocean. However a fundamental question remains: how do these regimes of turbulence coexist and connect in the ocean? It is not fully understood how the energy of the general circulation, generated at the large climatic scale, cascades to the small scales where most of it is dissipated. In particular, scientists are trying to explain the dynamical transition from the anisotropic, overwhelmingly two-dimensional, large-scale geostrophic to the more isotropic, 3D-like, small-scale (Müller et al. 2005).

Submesoscale processes in the vicinity of fronts are understood to play an important role in the energy budget of the ocean. For instance, when a front is created by a large scale horizontal straining, it stores available potential energy in the baroclinic current it forms. This energy is dissipated in smallscale three-dimensional kinetic energy as the MLIs set in, slump the front and act to restratify the mixed layer. The energy distribution in the mixed layer is often characterized in terms of length scale by the power spectrum of kinetic energy. General three-dimensional turbulence spectra show a characteristic -5/3 power law, which means a -5/3 slope of spectral density of variance plotted against wave number in log-log scale, and a cascade of energy to smaller scales. On the other hand geostrophic mesoscale flow spectra have a -3 slope and a reverse energy cascade (Thomas et al. 2008). Little energy is found at small scales in this regime. Capet et al. (2008b) observed that the spectrum slope of their primitive equation model depends on its spatial resolution, it is -3 for a resolution resolving mesoscales and -2 for the resolution resolving submesoscales. Boccaletti et al. (2007) and Fox-Kemper and Ferrari (2008) show that the energy peak triggered by MLIs is transferred to both larger and smaller scales. The reverse cascade occurs as MLIs evolve and merge into mesoscale eddies. The forward cascade is intimately tied to frontogenesis and frontal instabilities, especially through the advection by the horizontally divergent, ageostrophic component of the flow (Capet et al. 2008c). Today, global satellite observations of SST resolve fine

spatial scales (up to 1km for AATSR) and the combination of various sensors resolve a temporal scale of one day. This is sufficient to answer questions on the validity of the different turbulence regime and how they interact with each other. Spectrums of currents derived by altimetry products and chlorophyll content from ocean colour instruments have been measured and compared (see Levy and Klein 2004 for a review). However the author of this thesis is not aware of any such study based on SST datasets with a global, systematic perspective.

3. Chapter 3: SATELLITE-BASED FRONT DETECTION TECHNIQUES

This chapter focuses on front detection algorithms that can be applied to a spatial field of SST to extract frontal quantities. Two recently developed automated front detection techniques are reviewed. The details of the algorithms as suggested by their respective authors are explored, and practical implementations of each approach, adapted to the objectives of this thesis, are described.

These automated front detection techniques have significantly improved the study of ocean fronts on satellite images. They offer objectivity in the quantitative analysis of ocean fronts that was out of reach when detection was performed subjectively by human operators. Large quantities of satellite data can now be processed and the results can be analysed with spatial and temporal consistency. The fact that the algorithms can deal with 2-dimensional snapshots of SST allows composites of front maps to be created from a time series of individual frontal maps from high-resolution SST images. These composites are different from the result when the front detection algorithm is applied to the composite of SST images over the same period, because any high spatial and temporal variability of mesoscale and submesoscale frontal activity is already blurred and reduced in the averaged SST image before any frontal analysis is performed. When an operator observes a map of SST and marks fronts on it, the operation is tedious and the result is not objective. The same SST map analysed twice by an operator may produce different front positions depending on the operator's instantaneous mood, not to mention inconsistencies between the results of two different operators! If one wants to analyse the variation of frontal quantities in time and space, it is absolutely necessary to apply an automatic computational method. The two algorithms presented in this chapter comply with this requirement.

However, what is missing in the scientific literature is an understanding of the performance of these techniques. These techniques can so far be compared to black boxes which return consistent results in the sense that they seem to

detect fronts and deliver the same results when provided with the same inputs. However, if the objective is to derive physical parameters from the detected fronts, as in the context of this thesis, it is necessary to explicitly quantify the relation between the input scenes and the fronts detected by the algorithms. One should be able to predict which fronts are detected and which are not in order to carry out a dynamical interpretation of the detected fronts.

The last objective of this chapter is to evaluate and compare the performances of the two algorithms, which are required to function in a wide range of conditions. Indeed, these algorithms should detect fronts of various scales and intensity that are embedded in a complex turbulent flow. They should be able to do so from satellite data which suffer from limitations in term of data availability, resolution, noise and atmospheric artefacts. This chapter will lead to the appropriate selection, in chapters 5 and 6, of an algorithm and its associated parameters in relation to the characteristics of the data field on which the fronts are detected.

It should be noted that this chapter does not explicitly consider the capacity for front detection of SST fields derived from different data sources, an issue which is explored in the subsequent chapter. Chapter 4 will show that satellite SST observations and products have the potential to resolve density fronts in the mesoscale (10-100 km) and sometimes in the sub-mesoscale (1-10 km). It will also present a study on the ability of various SST data sets to resolve density fronts.

3.1 Front detection methods based on local statistics of the SST field

When looking at a SST image, fronts appear as the boundary between water masses of different temperatures around eddies, jets, upwellings or other mesoscale features. It is possible to enhance them by applying a filter to the image that would show where the SST is changing rapidly in space. Simple filters based on local statistics of the SST field are competent for this task: these are the operators that compute the spatial variance, the skewness, the gradient and the Laplacian (second spatial derivative) (Cornillon & Watts 1987).

Figure 3-1 shows how SST gradient processed by Burls and Reason (2006) from interpolated microwave data in the South Atlantic can resolve frontal features. It reveals high frontal activity around the Antarctic Circumpolar Current (ACC), the retroflection of the Agulhas Current and at the convergence zone where the Brazil Current meets the Malvinas Current. Strong fronts are encountered, with magnitudes of SST gradient reaching over 0.035 K/km. It is notable that even rather coarse daily SST images (resolution of 25 km) can reveal some mesoscale variability in the meanderings of the ACC jets. The authors measured a substantial inter-annual variability in the strength and latitudinal location of the Northern and Southern Subtropical Front, simply by taking meridional transects in the SST gradient.

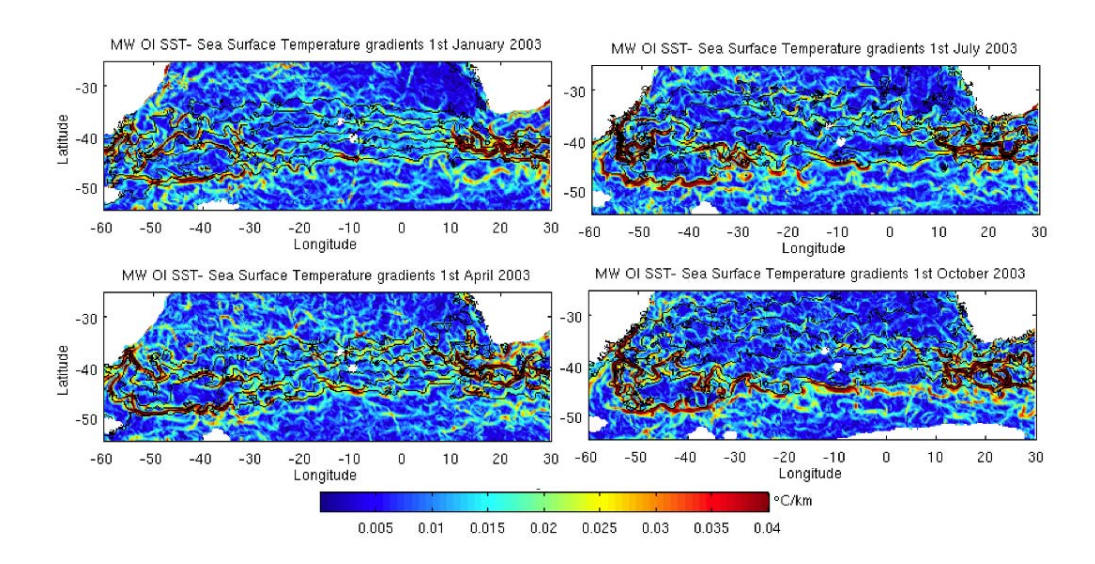


Figure 3-1: Daily SST gradient for January 1, April 1, July 1 and October 1, 2003, derived from a 25 km resolution Optimal Interpolation of Microwave SST dataset. Isotherms are overlaid in black. From Burls and Reason (2006).

Improved methods also exist that take advantage of new image processing techniques to enhance edges (Holyer & Peckinpaugh 1989). These methods have the advantage of being simple to apply to satellite images, but are very sensitive to noise. The way to deal with this limitation is initially to filter the data to eliminate the spatial noise, although this makes it more difficult to detect finer-scale frontal features in the end.

3.2 The Canny method

Figure 3-1 shows that calculating the SST gradient is a good way to enhance fronts and to make them obvious to a human eye. One can define a front as a region where the SST gradient is higher than a defined threshold as Belkin and Gordon (1996) did. This is an objective and automated method to detect fronts. It isolates fronts from the rest of the SST values but does not extract them in the form of vector structures. Detected fronts should however be defined as individual spatially defined objects that can be integrated temporally rather than as a block of flagged pixels in a raster image of a geophysical parameter in order to record and analyse the fronts consistently in terms of characteristics such as their length or their strength (Shimada et al. 2005).

The precise location and length of the fronts can be obtained following the method suggested by Canny (1986), which locates the fronts on the crests of the SST gradient. The Canny algorithm first estimates the gradient magnitude and searches for local maxima of gradient in the gradient direction. It then looks for pixels with gradient magnitude larger than a threshold T_2 . These pixels are flagged as frontal pixels. Finally the algorithm tracks along the front crests, i.e. perpendicularly to the gradient, flagging pixels as frontal pixels until the gradient magnitude falls below a smaller threshold T_1 . It does not, in its native form, link the flagged pixels together as a vector-defined independent object. The Canny algorithm was developed for automatic edge detection in the field of image processing, but Castelao et al. (2006) had the idea to apply it on SST data for front detection. The authors applied this technique on geostationary infrared SST data (GOES-10) over the California Current system, with the following thresholds: $T_2 = 0.006 \, K/km$ and $T_1 = 0.0015 \, K/km$.

3.2.1 A new implementation of the Canny method

To support the analytical work in subsequent chapters of this thesis a new implementation was coded in Matlab of an algorithm based on the Canny concept to detect fronts on SST data. It was possible to take advantage of a built-in Matlab Canny function for image processing. The core of this function was extracted because it is coded in a very optimized way, but it was adapted so that it can set thresholds with meaningful geophysical values of SST gradient instead of using image processing generic thresholds based on relative image brightness values. The main difficulty was to code a realistic estimation of the 2-dimensional gradient of an SST image. A simplistic way of estimating the SST gradient is to divide the SST increment of adjacent pixels by the horizontal distance that separates them as:

$$\nabla SST(i,j) \approx \begin{pmatrix} \frac{SST(i+1,j) - SST(i,j)}{d_i} \\ \frac{SST(i,j+1) - SST(i,j)}{d_j} \end{pmatrix}$$
(3-1)

where d_i and d_j are the zonal and meridional distances in km between 2 pixels in the SST image, respectively.

This is the first order SST gradient; it is only an estimation since the gradient of a discrete image does not exist mathematically speaking. It is in practice defined as the gradient of a continuous underlying function. The underlying function is the interpolation of the discrete image, hence it is not unique. There are several ways of interpolating the discrete SST data and therefore the SST gradient can only be an estimation. Of course, the higher the resolution of the SST data, the better quality the estimation of the SST, and hence of the SST gradient, will be. The first order SST gradient detailed above is in fact the gradient of a very coarse interpolation of the SST field: the interval between each pixel is filled uni-dimensionally by interpolating linearly the SST. This gradient estimation is not the most accurate if the SST is not considered to vary linearly, it is also extremely sensitive to spatial noise. Due to measurement noise, very high gradient values can be estimated in regions of low actual SST variations. This limitation can be overcome by estimating the second order SST gradient.

Chapter 3

The second order SST gradient is obtained by convoluting the SST image with the derivative of the Gaussian function. The second order gradient presents the advantage of being more robust to measurements containing spatial noise, but it is based on some smoothing of the data, which implies a loss of high frequency spatial variability. In fact this process is strictly equivalent to the initial smoothing of the SST by a running Gaussian mean, followed by the estimation of the first order SST gradient. The level of smoothing applied depends on the shape of the smoothing filter. The smoothing filter applied in this thesis is a two-dimensional Gaussian filter parameterized by a characteristic length scale, its standard deviation σ_s given in km.

$$g(x,y) = \frac{1}{2\pi\sigma_s^2} e^{-\frac{x^2 + y^2}{2\sigma_s^2}}$$
(3-2)

Where x and y are the zonal and meridional distances in km from the origin of the filter. Note that the expression "standard deviation" is not completely accurate as there is no statistical distribution involved. However the Gaussian filter is similar in shape to a zero-mean Gaussian distribution of standard deviation σ_s . The derivative of g(x,y) against each direction is convoluted on the SST image to estimate the zonal and meridional SST gradient. When dealing with SST data, care has to be taken to account for the geographical projection on which the data are provided. Global SST products are usually given on a grid whose steps in latitude and longitude are constant. This projection is called cylindrical. In this projection meridians are mapped to equally spaced vertical lines and circles of latitude (parallels) are mapped to horizontal lines. By the geometry of its construction, the projection stretches distances East-West. The amount of stretch is the same at any chosen latitude and increases towards the Poles. If the Earth is approximated to a sphere, the relationship between a step in latitude (at constant longitude) and the distance in km is constant. It is

$$D_{meridional} = 111.12 * \Delta lat$$
 (3-3)

Where $D_{meridional}$ is the distance in km equivalent to a shift in latitude of Δlat in degrees at constant longitude. Conversely, the relationship between a step in longitude (at constant latitude) and the distance in km is a function of latitude:

$$D_{zonal} = 111.12 * \cos(lat) * \Delta lon$$
 (3-4)

where D_{zonal} is the distance in km equivalent to a shift in longitude of Δlon in degrees at a constant latitude lat. Therefore a SST image projected on a cylindrical projection is distorted and its pixels have varying horizontal (zonal) sizes in km depending on their latitude. Yet, the filter needs to be be circular when projected onto the ground, i.e. it should be circular in term of distance but not on the SST grid. If this is not ensured, the data are smoothed unevenly and anisotropically, which would introduce smoothing filter artefacts. To correct this effect it was decided to define a well-chosen shape to the running Gaussian derivative, as a function of the pixels $D_{zonal}/D_{meridional}$ ratio. The SST data are then convoluted with a filter whose shape is changing for every latitude row. The Gaussian filter was also normalized with care to obtain correct values of SST gradient even over the high latitudes where the pixels are not square in kilometres.

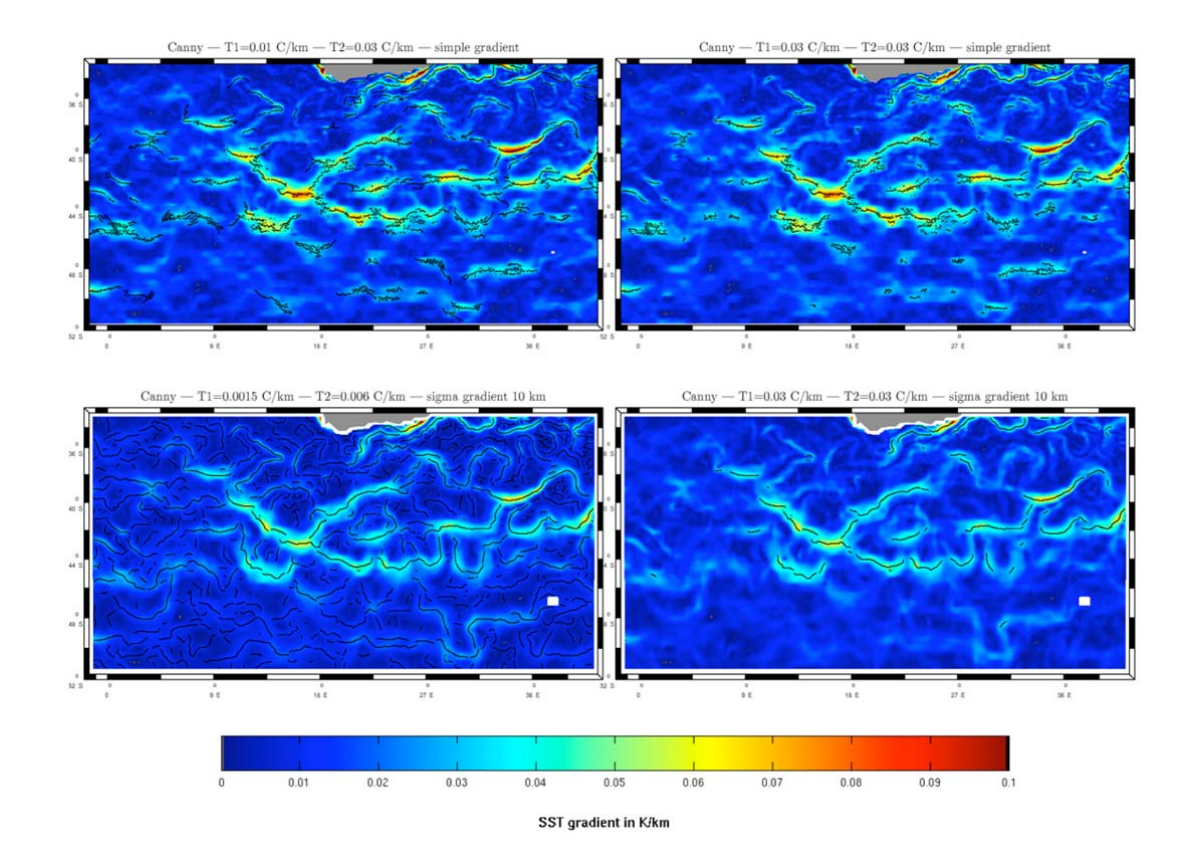


Figure 3-2: Canny front detection algorithm applied to an OSTIA SST image (31/12/2008). The initial resolution is 0.05°. A gradient is estimated to a first order, taking into account only adjacent pixels (top) and by convoluting the derivative of a Gaussian function whose standard deviation is 10 km (bottom). The fronts are displayed in black and the SST gradient magnitude is mapped on the background.

Four examples of fronts detected by the Canny method over the Agulhas Retroflection are presented in Figure 3-2. The SST data are extracted from a Level 4 product, the OSTIA dataset (SST data sets are discussed in Chapter 4). Two parameters have been varied in the examples shown: the SST gradient magnitude thresholds T_1 and T_2 along with the smoothing filter length scale σ_s . The plots show the detected fronts on the local maxima of SST gradient in the gradient direction. This shows that the quantity and shape of fronts detected is strongly dependent on the choice of parameters used in the Canny algorithm. A minimum level of smoothing seems necessary to avoid getting fronts that are meandering unrealistically as shown on the top (unfiltered) row of Figure 3-2. The level of the thresholds defines what fronts are detected and how far

they expand. It is worth noting also that the SST gradient magnitude is lowered by the application of a smoothing filter.

To summarise, this modified implementation of the Canny method relies on the preliminary definition of the following parameters that control the way the algorithm detects fronts:

- The SST gradient magnitude thresholds T_1 and T_2 .
- The standard deviation σ_s (in km) of the Gaussian filter applied, if any, for the smoothing of the input SST scene for the estimation of the SST gradient magnitude. If no filter is applied as in the top row of **Figure 3-2**, σ_s is set to 0 km.
- An optional minimum front length L_{min} in km, to avoid extremely small fronts.

3.3 The Cayula method

Front detection algorithms based on the computation of the gradient suffer from a high-sensitivity to noise. Hence an initial step of smoothing is required to reduce the amount of noise, which also removes high spatial frequencies and fades fine-scale features. Another limitation of these filters is that they do not behave well when some data are missing, in general due to cloud cover which prevents infrared radiometers from sampling the SST. Of course no front detection technique can work on a large missing patch of the SST image. However level-2 (single sensor snapshot) images are sometimes corrupted by patchy clouds which prevent unobstructed views over wide areas even though only a few percent of pixels are flagged as cloud. In these conditions it is still possible for a human operator to detect visually a front but the gradient cannot be estimated in the vicinity of missing data. This implies that there is a need for a better automatic method able to deal with a small percentage of missing data. This was the rationale for developing the Cayula approach.

3.3.1 Description of the Cayula method

Cayula and Cornillon (1992) developed an edge detection algorithm (also called the histogram method or the SIED: Single Image Edge Detector) that is able to deal advantageously with fine features, noise and missing data due to cloud cover, but which is also objective and automatic, and returns fronts as geometric vectors. This approach was new in the way it defined the temperature fronts as the (usually thin) region of separation between two regions of largely uniform temperature. This algorithm works at 2 different spatial levels: the window and the image levels. The image is first segmented into overlapping windows (32x32 pixels for images of 1 or 2 km resolution).

At the window level, for each of those windows a statistical test decides the existence or not of two distinct populations through a histogram analysis of the SST values of the window pixels. For each temperature threshold τ , two populations of pixels within the window are identified:

- P_1 is the ensemble of pixels whose SST is lower than τ P_2 is the ensemble of pixels whose SST is higher than τ

The optimal threshold τ_{opt} is computed such that $J_b(\tau)$, the contribution to the total variance resulting from the separation in two clusters P_1 and P_2 , is maximized.

Where

$$J_b(\tau) = \frac{N_1 N_2}{(N_1 + N_2)^2} [\mu_1(\tau) - \mu_2(\tau)]^2$$
 (3-5)

Where N_1 is the number of pixels in P_1 , and N_2 is the number of pixels in P_2 , and $\mu_1(\tau)$ is the mean of P_1 , and $\mu_2(\tau)$ is the mean of P_2 .

The segmentation is considered sufficient if the proportion of the total variance due to the separation between clusters is high enough, i.e.:

$$\frac{J_b(\tau_{opt})}{J_b(\tau_{opt}) + J_e(\tau_{opt})} \ge 0.7 \tag{3-6}$$

Where $J_e(\tau)$ represents the sum of the variances within each of the two populations.

$$J_e(\tau) = \frac{N_1}{N_1 + N_2} S_1(\tau) + \frac{N_2}{N_1 + N_2} S_2(\tau)$$
 (3-7)

Where $S_1(\tau)$ is the variance of P_1 , and $S_2(\tau)$ is the variance of P_2 .

Another statistical test which, in contrast to the segmentation phase, takes into account the spatial distribution, assesses the compactness of these two populations. The populations are considered as compact when the three following inequalities are fulfilled:

$$C_1 = \frac{R_1}{T_1} \ge 0.90 \tag{3-8}$$

$$C_2 = \frac{R_2}{T_2} \ge 0.90 \tag{3-9}$$

$$C = \frac{R_1 + R_2}{T_1 + T_2} \ge 0.92 \tag{3-10}$$

Where T_1 (T_2) is the total number of neighbour pairs between pixels belonging to P_1 (P_2) and neighbour pixels belonging to either population:

$$T_1 = |\{(x,y), such \ that \ y \in [\mathcal{N}(x) \cap \mathcal{X}], \forall \ x \in P_1\}|$$

$$T_2 = |\{(x, y), such that y \in [\mathcal{N}(x) \cap \mathcal{X}], \forall x \in P_2\}|$$

 \mathcal{X} is the population of pixels in the window: $\mathcal{X} = P_1 \cup P_2$.

| | is defined as the cardinality of the set.

For reasons of computational economy and simplicity, only the first neighbours of a given pixel are used to evaluate the cohesion:

$$\mathcal{N}(x_{i,j}) = \{x_{i,j+1}, x_{i,j-1}, x_{i+1,j}, x_{i-1,j}\}$$
(3-11)

 R_1 (R_2) is the total number of neighbour pairs between pixels belonging to P_1 (P_2) and neighbour pixels belonging to P_1 (P_2) too.

$$R_1 = |\{(x, y), such that y \in [\mathcal{N}(x) \cap P_1], \forall x \in P_1\}|$$

$$R_2 = |\{(x, y), such that y \in [\mathcal{N}(x) \cap P_2], \forall x \in P_2\}|$$

If the populations are compact, and not scattered, the pixels that are neighbour to one of the other population's pixels are flagged as potential frontal pixels.

The algorithm then shifts to the image level to link the independent flagged pixels so that they form continuous frontal structures, trying to follow the isotherms and eliminating very short fronts (e.g. less than 15 pixels in length). This method allows the control of many parameters during the process and also offers as an output the full frontal structure with information on the length or the strength of these fronts. It is also an improvement because it is not based on the absolute strength of the front, but on the relative strength depending on the context, thus making the edge detection temperature-scale invariant. Figure 3-3 illustrates an output of the histogram method from an infrared satellite SST scene.



Figure 3-3: AVHRR/2 SST fields with clouds zeroed and detected edges overlaid in white. From Cayula and Cornillon (1992).

The Cayula method was later upgraded to a multi-image edge detection that is able to measure temporal behaviours of the detected fronts such as their persistence (Cayula & Cornillon 1995). The histogram method has been validated against in-situ front measurements, showing an error rate of 14% instead of 29% for a simple SST gradient threshold algorithm (Ullman & Cornillon 2000). Several studies have applied the histogram method for producing regional climatologies of fronts from SST data (Level-2 AVHRR) time series: Belkin and Cornillon (2003, 2004, 2005).

3.3.2 Implementation of the Cayula method

A new implementation has been coded in Matlab of the Cayula method for edge detection, adapted for the work in this thesis. The principles by which it operates are illustrated in Figure 3-4 and Figure 3-5. It is a complex algorithm whose implementation is made difficult when adapting it so that it can efficiently detect fronts on global high resolution SST maps. The process of

Chapter 3

linking the frontal pixels together into a coherent and continuous vector front (step f to step g in Figure 3-5) is very demanding in terms of computational power and memory because it has to be implemented by iteration: for each frontal pixel detected the routine must search through its neighbours for other frontal pixels, while trying to follow isotherms. The choice was made to divide the input SST scene into 10° by 10° boxes to ease this process, and the algorithm was adapted to make it link to the fronts detected on the borders of the boxes, in order not to create artefacts on the sides of the selected 10° boxes or else many detected fronts would end right at the window grid lines.

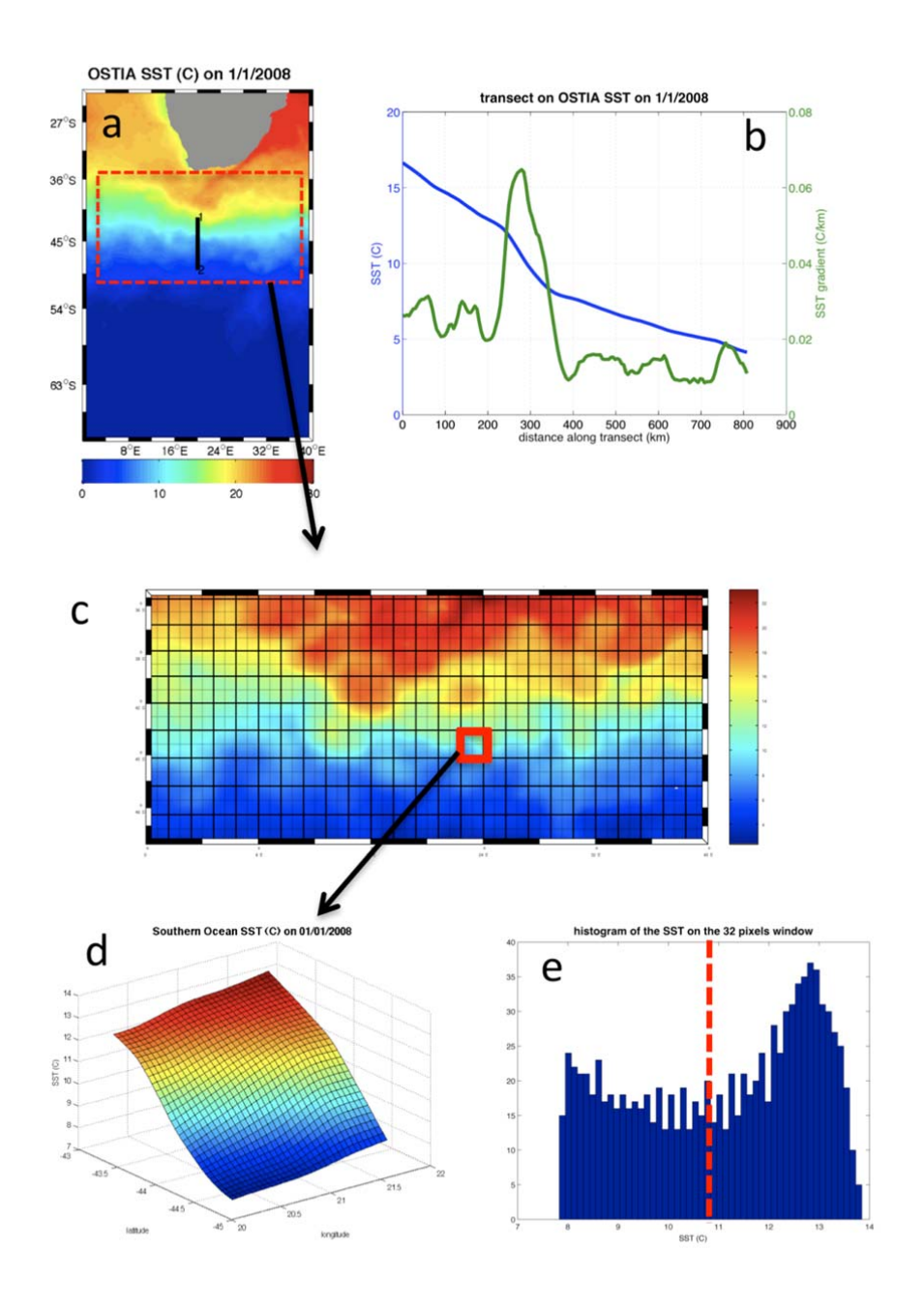


Figure 3-4: Illustration of the different levels in the Cayula algorithm. a) the initial OSTIA SST data, over the ACC South of Africa. b) transect of the SST and the SST gradient over the path displayed on the original data. c) SST over the red dashed box, with the window level grid overlaid. d) SST values of the 32x32 pixels window. e) histogram of the SST values of the window pixels, with the result of the segmentation overlaid as a red dashed line.

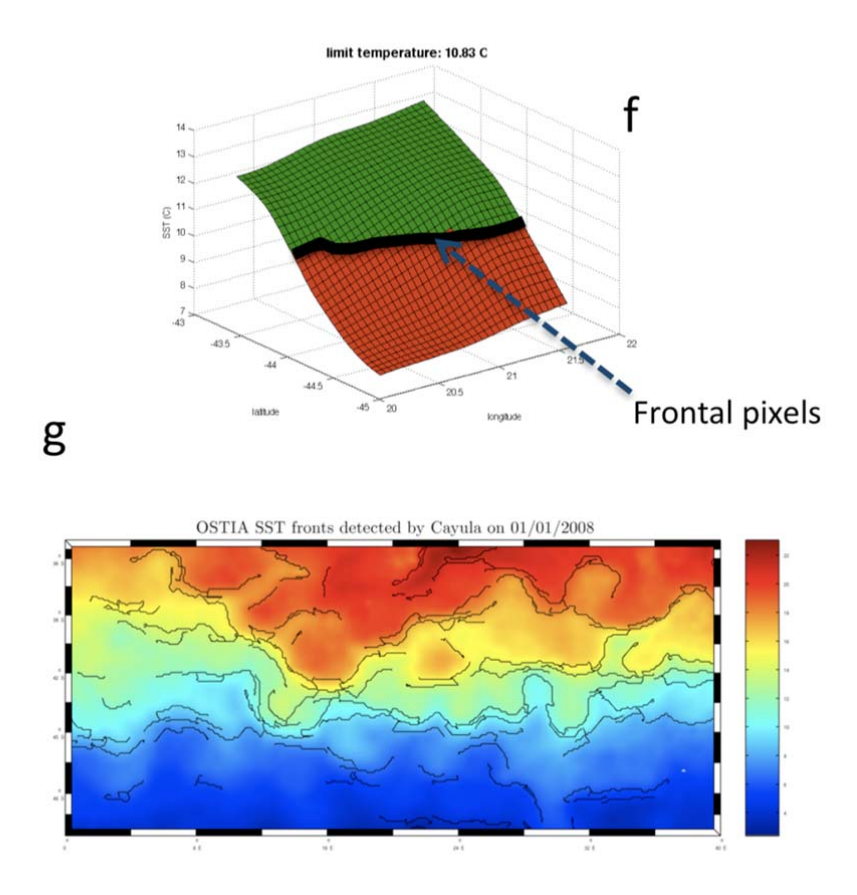


Figure 3-5: Illustration of the different levels in the Cayula algorithm. f) the window is divided into two populations of pixels following the result of the segmentation. g) the resulting detected fronts over the area after the window level and the local level processing are accomplished.

This implementation of the histogram method requires the assignment of several arbitrary input parameters that control the algorithm processes and hence the resulting detected fronts:

- The standard deviation σ_s (in km) of the Gaussian filter applied, if any, for the smoothing of the input SST scene for the estimation of the SST gradient magnitude. Alternatively the median smoothing filter size can be set.
- The window size (WS), in pixels, in the segmentation operation (Figure 3-4.c). This parameter is fundamental for the whole algorithm. The histogram method will only detect a front if a portion

of it is found to divide, one of the windows into 2 coherent groups of pixels of different SST. The routine that is applied on every window (Figure 3-4.e) searches which SST value, if any, is dividing the distribution of the window pixels SST values into two distinct distributions, whose individual variances explain a large part of the total distribution variance. This analysis only allows the detection of one front or none for each window. Consequently, on one hand, if the size of the windows is too big, the risk is to miss complex frontal features when two fronts are present on the window. The statistical test detects in this case only one front or sometimes no front at all. On the other hand, if the window is too small, the risk is to detect the same front several times in different windows. In that case, one window may not cover the whole width of a front, so it will detect a front over its slope, but the adjacent windows and the overlapping ones will also detect the same front, simply translated by a few pixels. This phenomenon is clearly visible on Figure 3-5.g: strong fronts surrounding the ACC jets are detected twice, and most of them are drawn with double lines. In this example the fronts were detected with a window size of 32 pixels (i.e. 1.6°), it seems that this parameter is too low for this region characterized by very strong and wide fronts.

• The grid on which the input SST scene is projected. The algorithm is able to resample the SST on a lower resolution grid, which has the effect of simplifying the frontal detection but also hides the fine front features. It can resample the data on a regular grid (also called equalarea grid, or local sinusoidal grid, or Mercator equal-area projection) too, where the resolution is not in degrees of latitude/longitude but in kilometres. This is particularly important over high-latitudes where 1° in latitude is much larger than 1° in longitude. The front detection method must not be biased by a strong asymmetry of the pixels shape when projected onto the ground. The regular grid can only be constructed locally to avoid direction biases and this complicates the coding of the whole algorithm.

- A minimum temperature difference ΔT_{min} : Ullman and Cornillon (2000) and Miller (2009) improved the histogram method statistical test by introducing a temperature difference threshold (between the SST means of the two populations at the window level) under which a front is not flagged, even if the segmentation process has succeeded. Those authors chose $\Delta T_{min} = 0.375~K$ (with a window size 32 pixels of 1.2 km) and $\Delta T_{min} = 0.4~K$ respectively to limit false detections caused by sensor noise inherent to standard level-2 SST fields. The implementation developed here allows the utilization of such a threshold.
- A minimum front length L_{min} . The fact that the fronts are constructed as vectors (as opposed to a raster of front pixels) makes possible the definition of a minimum threshold on the frontal length. Once all the fronts have been detected, a routine measures the length of the fronts and keeps only fronts longer than this threshold. This is to avoid the proliferation of very small fronts.

3.4 Definition of simple Frontal Indexes

After the fronts are detected by one of the two front detection algorithms, it is helpful to convert the geographical locations of the list of points that constitute a front position into a numerical value. For the qualitative analysis of frontal variability, spatial and temporal frontal indexes based on various characteristics of the fronts are defined:

- The total frontal length index (FLI) in km that takes into account only the length of the fronts. This is a measure of the cumulated length of the fronts detected in a given area, it is therefore normalised by the area in which it is integrated. Its units are km/km² or km¹.
- The frontal strength index (FSI): this is a measure of both the length and strength of the fronts. An estimation of the magnitude of the front is integrated over the whole length of the fronts. The frontal strength can be estimated in several ways. It can be defined as the mean SST difference ($|\overline{SST_1} \overline{SST_2}|$) between the means of the two

populations of pixels dividing a window in the first steps of the Cayula algorithm. This index is called **Frontal Temperature Difference Index (FTDI)**, its unit is km.K/km². The frontal strength can also be estimated by the SST gradient magnitude on the front, which is a local maximum in the gradient direction when the front is detected by the Canny method. This index is called the **Frontal Gradient Index (FGI)**, its unit is (K/km).km/km² =K/km². It should be stressed that the Canny algorithm is only able to return the FGI while the Cayula method can return either the FTDI or the FGI.

Any of these Frontal Indexes can be processed from a global daily SST scene. They can be plotted as the result of a single day's processing (Figure 3-6), integrated over different regions and plotted against time, or averaged over time and plotted as a map (Figure 3-7). The latter was obtained by adding daily frontal position maps of the California Current system and dividing the sum by the number of days processed to get a monthly **Probability of Detecting a Front (PDF)**. The PDF is the time-averaged frontal position, it is presented on a map like Figure 3-7, while the FTDI is the time series of the geographically averaged frontal length and strength.

This kind of analysis can resolve the seasonal variability of many mesoscale features to a significant extent. For instance, over the California Current System, fronts reveal the coastal upwellings within about 50 km of the coast during spring and fall. In September, the upwelling jet appears to be separating from the coast at 42° N for a few hundred kilometres. In December, the frontal features are shifted offshore with long filaments occurring at 33° N that separate the California Current System from warmer subtropical water. During the winter the frontal activity is sharply decreasing, probably because of a weakening of upwelling favourable winds. These results are consistent with the thermal fronts analysis of Castelao et al. (2006).

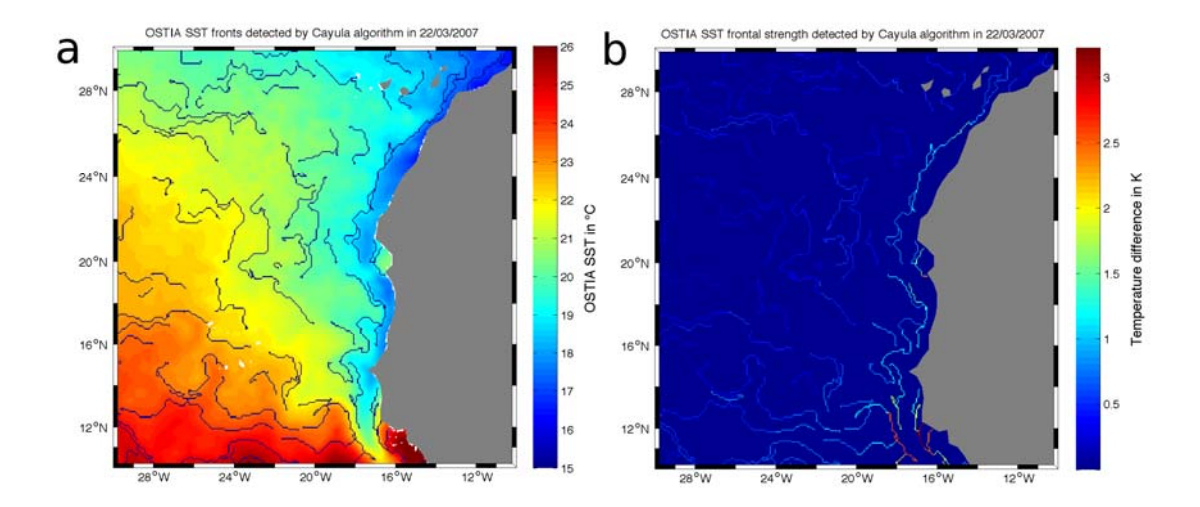


Figure 3-6: a) OSTIA SST data on 22 March 2007, East Atlantic next to West-Africa, with the fronts detected by the Cayula algorithm superimposed. b) the frontal strength FTDI of the fronts detected by the Cayula algorithm. The frontal strength is calculated as the difference between the mean SST of the two populations separated at the window level. The window size is 32 pixels (1.6°).

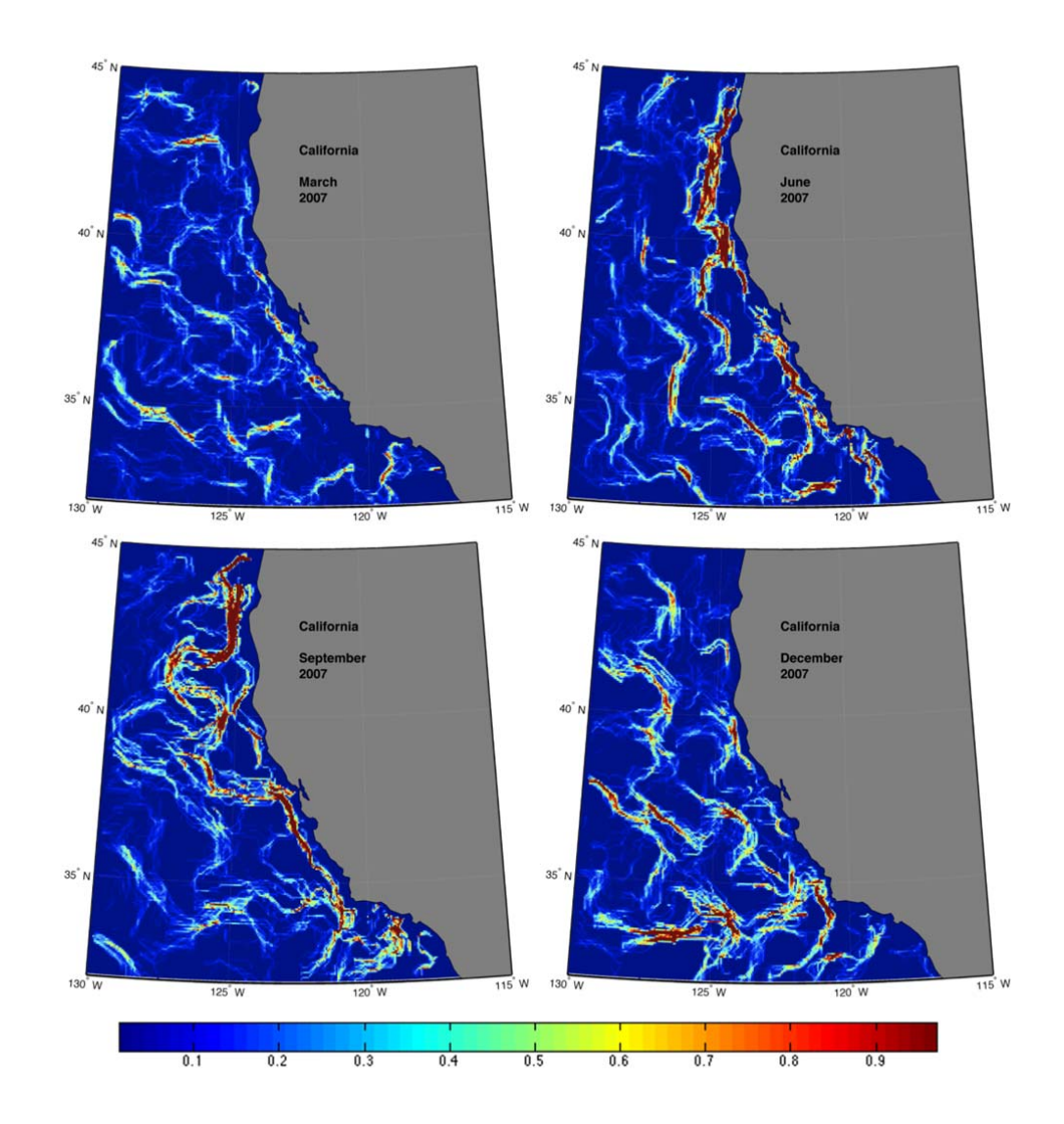


Figure 3-7: Probability of detecting a front (PDF) over the California Current System averaged monthly over March, June, September and December 2007. Fronts are detected following the algorithm detailed in Cayula and Cornillon (1992), with a window size of 32 pixels (1.6°), on OSTIA products.

3.5 A critical analysis of frontal detection techniques

The advantages of the automatic front detection methods over a human-based front detection process are obvious: they are faster and objective. They are objective because each of them will detect the same fronts every time when applied to the same SST scene, and their outputs are qualitatively comparable. For example it is relevant to compare the fronts detected by the same

technique over the same region but from different dates. However, it is not a simple task to compare frontal indexes processed by two different methods, because the detected fronts are the resulting combination of both the initial SST scene and the methodologies inherent in the algorithms. The earlier sections of this chapter describe the methodology adopted by the two frontal detection techniques. In order to interpret the detected fronts in a dynamical context and to compare results obtained by the two methods, it is necessary to explicitly quantify their behaviours. It is not enough to know what processing is applied to the input SST field, because it is complex, but one should be able to "characterise" what fronts will be detected as a function of their size or strength and with which accuracy. Published studies making use of these algorithms have used them as "black boxes" that can be applied over a time-series of SST products and whose resulting variability gives an indication of the frontal variability. This section aims at "opening the black boxes" and shedding light on the relationship between the inputs and the outputs of these algorithms. It is easy to express in simple words the definition of a front as implied by the Canny method, especially if $T_1 = T_2$ (that is the fronts are the locations of local maximum of SST gradient magnitude in the SST gradient direction, where the SST gradient magnitude is larger than T_1). However the smoothing filter initially applied to reduce the effect of noise on the gradient estimation has an effect on small scales that can be quantified. In the case of the Cayula method, it is not obvious how to describe quantitatively the effect on the output frontal indexes of the decomposition into windows in the first steps of the algorithm and the statistical test applied to estimate the segmentation and cohesion within the windows.

3.5.1 Characterization of the Canny algorithm

The limitations of the Canny algorithm are inherent to the data it uses as input. The fronts it returns are of course restricted to those present in the SST image. Depending on the resolution of the SST image, small fronts are or are not detectable. This statement is true for any method as no algorithm can detect features that are not present in the input image. The high sensitivity to noise of the gradient computation also limits the minimum scale that can be resolved by the Canny algorithm. It is absolutely necessary to eliminate spatial

noise in the data before the calculation of the gradient can be performed. If the noise is not smoothed out, very high values of SST gradient will be observed that have no link to the underlying mixed layer SST field that is an indicator of upper ocean dynamics. The elimination of spatial noise is achieved by means of spatial filters, which are in effect low-pass filters: they cancel small scale variations. The two filters considered in this study are the following:

· The running Gaussian filter:

$$SST_{filt}(x_i, y_i) = \sum_{n=-N}^{N} \sum_{m=-M}^{M} SST(x_i + n, y_i + m) \cdot N_{\sigma_S}(n \cdot \delta_x, m \cdot \delta_y)$$

Where $SST_{filt}(x_i,y_i)$ is the value of the filtered SST image on row x_i and column y_i . N_{σ} is the two-dimensional Normal function of zero mean and standard deviation σ in km.

$$N_{\sigma}(x, y) = \frac{1}{2\pi\sigma^2} e^{-\frac{x^2 + y^2}{2\sigma^2}}$$

 δ_x and δ_y are the resolutions of the grid in the row and column directions respectively. M and N are the sizes of the Gaussian filter in the row and column directions respectively.

• The running mean filter:

$$SST_{filt}(x_i, y_i) = \sum_{n=-N}^{N} \sum_{m=-M}^{M} SST(x_i + n, y_i + m) \cdot \frac{1}{(2N+1)(2M+1)}$$

These two filters are applied for each pixel of the SST image, this is done by convolution of the two-dimensional filter.

The gradient in the x direction, in the case of the Gaussian filter, is calculated the following way:

$$\nabla_{x} SST_{filt}(x_i, y_i) = \frac{1}{\delta_{x}} \left(SST_{filt}(x_i + 1, y_i) - SST_{filt}(x_i, y_i) \right)$$
(3-12)

One can show that

$$\nabla_{x}SST_{filt}(x_{i}, y_{i}) = \sum_{n=N}^{N} \sum_{m=-M}^{M} \nabla_{x}SST(x_{i} + n, y_{i} + m) \cdot N_{\sigma_{s}}(n \cdot \delta_{x}, m \cdot \delta_{y})$$
(3-13)

Which means that the gradient of the filtered SST is the filtered gradient of the SST.

The effect of a running Gaussian filter on a front is shown on Figure 3-8. One can see that as the standard deviation of the filter increases, so does the extent of the front, which decreases the gradient in the middle of the front. The effect on the gradient is shown on Figure 3-9. It is noticeable that the gradient of a front whose width is smaller than $3\sigma_s$ is significantly reduced by the application of the filter.

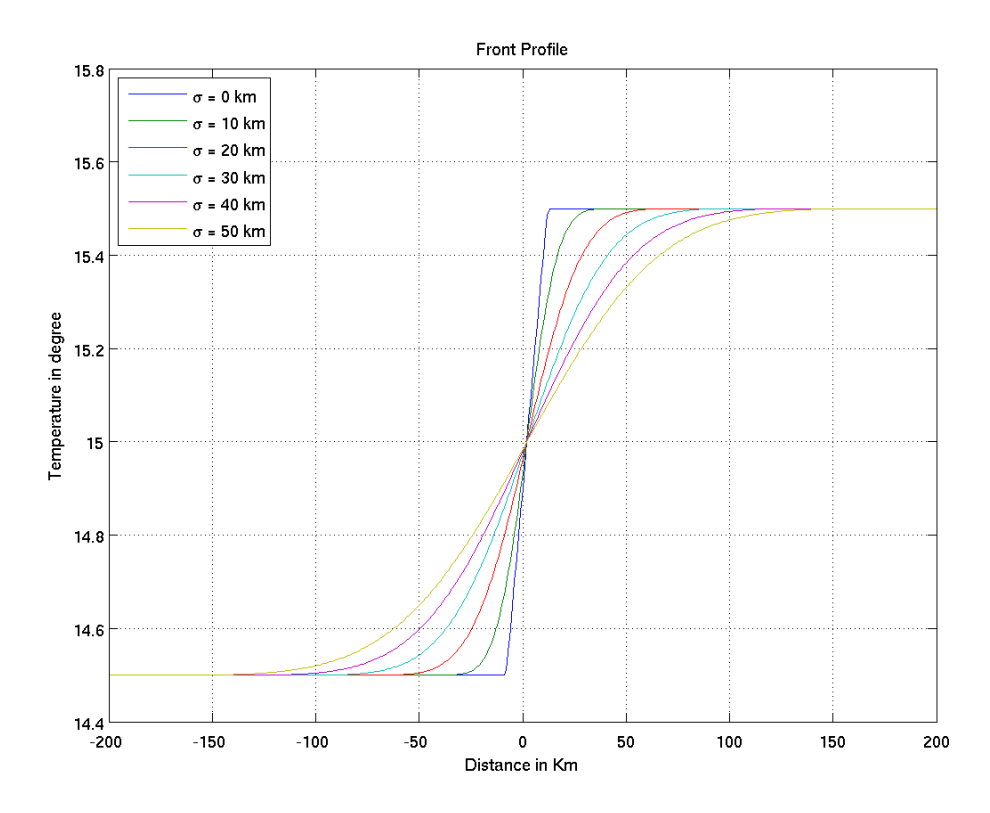


Figure 3-8: Smoothing effect of Gaussian filters on a simple front. In blue is the profile of an initial front which is modelled by a SST gradient of 0.05 K/km over 20 km. Running Gaussian Filters of various standard deviations are applied to the SST scene before the profile is taken. A filter of 0 standard deviation is by convention returning the input data.

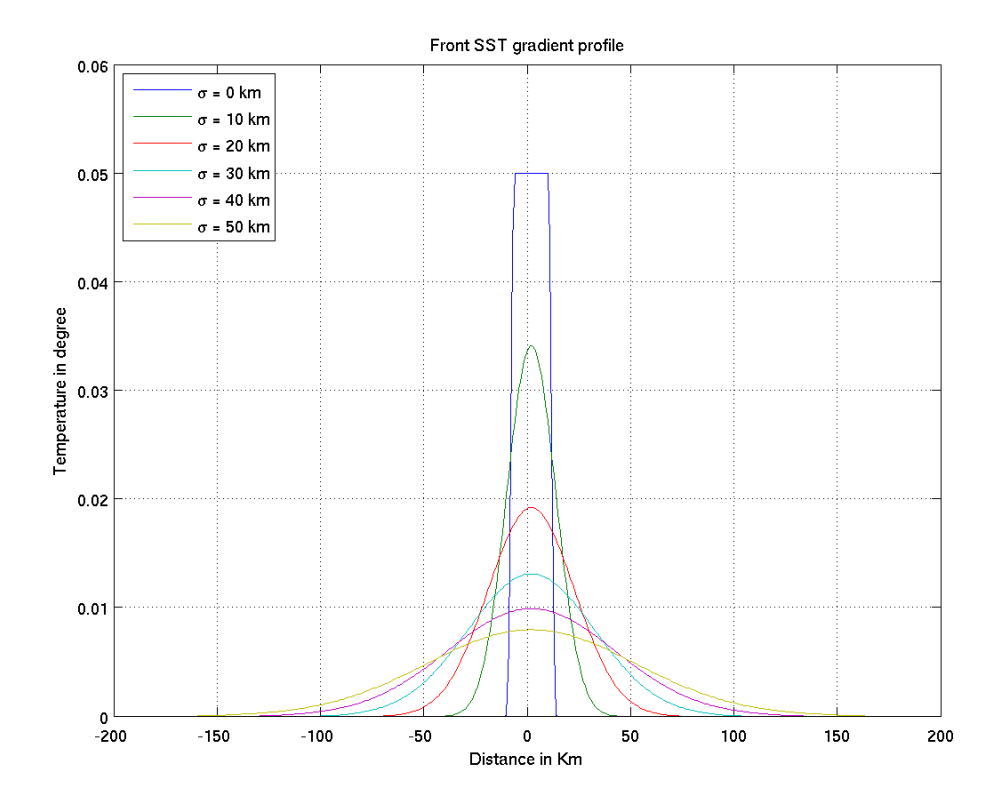


Figure 3-9: Smoothing effect of Gaussian filters on the Gradient on a simple front. In blue is the profile of an initial front which is modelled by a SST gradient of 0.05 K/km over 20 km. Running Gaussian Filters of various standard deviations are applied to the SST scene before the gradient is calculated and the profile is taken. A filter of 0 standard deviation is by convention returning the input data.

The reduction of the gradient can be deduced in the following manner:

Firstly, let us notice that the maximum gradient is at x_{0} , the middle of the front. In the case where the front is along the x-axis, we can simplify the calculations by looking at the front profile in one dimension. We have

$$\nabla_{x}SST_{filt}(x_{0}) = \sum_{n=-N}^{N} \nabla_{x}SST(x_{i} + n) \cdot N_{\sigma_{S}}(n \cdot \delta_{x})$$
(3-14)

$$\nabla_x SST_{filt}(x_0) = \nabla_x SST(x_0) \cdot A \tag{3-15}$$

Where

- $A=erf\left(\frac{1}{2\sqrt{2}}\cdot\frac{D}{\sigma_s}\right)$ in the case of the running Gaussian filter with $erf(x)=\frac{2}{\sqrt{\pi}}\int_0^x e^{-t^2}dt$ is the error function. D is the width of the front, in the case of Figure 3-8 and Figure 3-9, $D=20~\mathrm{km}$.
- $A = \begin{cases} \frac{D}{d} & \text{if } D < d \\ 1 & \text{if } D > d \end{cases}$ in the case of the running Mean filter. $d = (2N+1)\delta_x$ is the size in km of the running mean filter.

This shows that the effect of the smoothing filters on the fronts is a direct function of the ratio between the width of the fronts and the length-scale of the filter:

$$R_{gauss} = \frac{D}{\sigma}$$

$$R_{mean} = \frac{D}{d}$$

Figure 3-10 and Figure 3-11 display the scaling factor A as a function of these ratios. This quantifies the scaling of the gradient on all fronts by the smoothing filters applied in the Canny method.

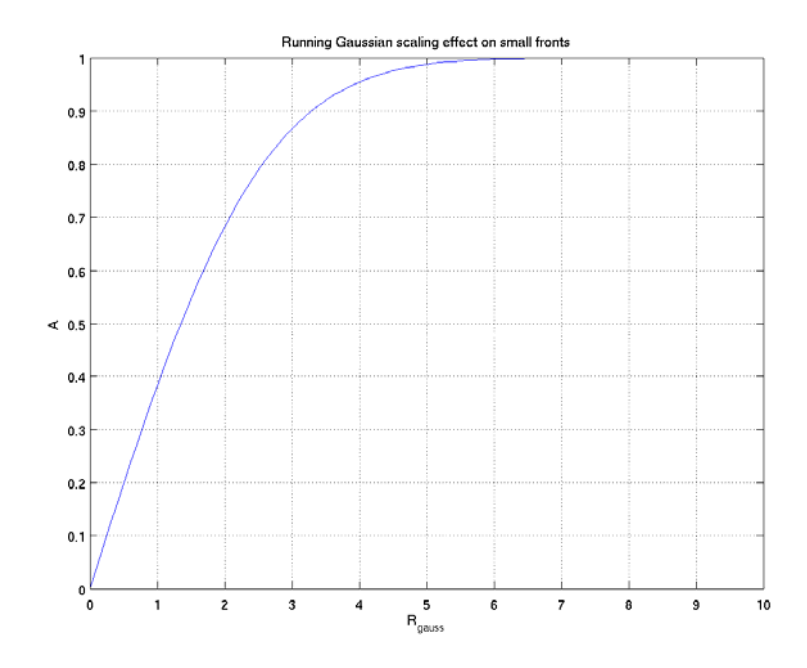


Figure 3-10: In the case of the Gaussian filter, scaling factor of the front maximum gradient as a function of R_{gauss}

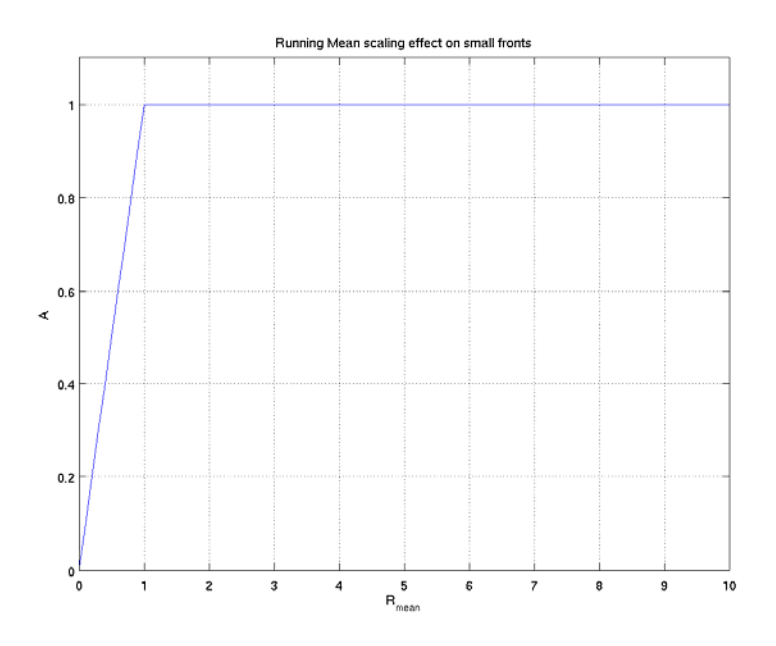


Figure 3-11: In the case of the running mean filter, scaling factor of the front maximum gradient as a function of R_{mean}

One can see that the smaller the R_{gauss} or R_{mean} ratio, i.e. the larger the filter and/or the smaller the gradient scale, the more the gradient is reduced by the filter. These filters are in effect low-pass filters, they erase small scale spatial variability. This filtering step is necessary when it is assumed that the highfrequency part of the SST spectrum is not trustworthy, because it contains more measurement noise and atmospheric artefacts than actual surface temperature variations. The more smoothing is applied, i.e. the larger the filter, the more noise is cancelled out. However, the filter is not only taking out noise but also real small scale variability in the SST. In order to optimize the algorithm, one should choose a filter size that is the smallest one able to cancel the noise in order to leave the biggest part of the spectrum resolvable by the algorithm. The choice of filter size to use for the frontal analyses presented in the rest of this thesis is made by exploring results of the Canny method applied with different smoothing filter and retaining the one that resolves the smallest scales without appearing to detect fronts that are meandering unrealistically or in a way that seems not linked to the dynamics of the scene. This is illustrated on Figure 3-2. The size of the filter depends on the characteristics of the input product in terms of spatial noise.

Chapter 5 will discuss a methodology that makes *a-priori* assumptions on the SST spatial spectrum to estimate and recover the amount of actual SST small scale gradient smoothed out by a spatial filter or by a sampling at low resolution. This methodology relies on this SST spectrum assumption and on the larger scale gradient measured after the application of the filter.

3.5.2 Characterization of the Cayula algorithm

The Cayula algorithm is always taken as a black box. The author of this thesis is not aware of any publication describing its behaviour and predicting what type of fronts it detects. The parameters of this algorithm, listed in section 2.3.2, are not mathematically related to the outputs of the processing in a theoretical way. In other words, the Cayula algorithm is used as a black box which detects fronts automatically. The uncertainty inherent in the Cayula method, but not always appreciated, lies in the statistical tests applied at the window level. These steps are the measurement of the segmentation, i.e. the

division of the window pixels values into two distinct populations, and the cohesion, which is the compactness of these two populations. The Cayula algorithm can be applied with or without an initial smoothing of the SST data. The following subsections within 3.5.2 characterise the Cayula algorithm behaviour without any consideration of initial smoothing: section 3.5.2.1 assumes a noise-free input SST scene while section 3.5.2.2 considers a noisy image. They deal only with the steps of the Cayula algorithm that occur after any potential initial smoothing. The amount of noise present on the input scenes analysed in section 3.5.2.2 can be thought of either as the original noise on the SST image, in the case where no initial smoothing filter is applied, or as the remaining noise after pre-filtering. In the case where pre-smoothing is performed, the overall assessment of the Cayula method for detecting fronts must combine both the analysis in section 3.5.2.2 and the impact of presmoothing (using a running mean or Gaussian filter) as already explored in 3.5.1. The full Cayula algorithm including the initial filtering is characterized in section 3.5.3.1.

3.5.2.1 The Cayula algorithm at the window level on a noise-free scene

Let us consider the segmentation test on a zero noise window SST scene. If the window is seeing a perfectly uniform scene, i.e. no front is present, no segmentation is detected by the segmentation test. There are two simplified configurations under which a window can observe a front as illustrated in Figure 3-12. Depending on the width of the front and the size of the window, the whole front can be captured by a window (case 1), or a fraction of it only can be seen by a window (case 2). In both cases, if a front is present, even though it is extremely low in intensity, tests showed that a segmentation is detected within the window. This means that two distinct populations are detected in the window, and the difference between their average temperatures is calculated. This difference is the basis of the FTDI (Frontal Temperature Difference Index), it is a measure of the intensity of a detected front. When a front is detected, this temperature difference is used in the Cayula algorithm in two instances. Firstly, it is compared to the parameter ΔT_{min} , the minimum temperature difference for a front to be retained. If the front is too weak, the difference between the average temperatures of the two

populations is lower than ΔT_{min} and the algorithm concludes that there is no front over the window being explored. Secondly, if the temperature difference is greater than ΔT_{min} , the segmentation test is fully successful and the algorithm continues by assessing the cohesion. If the detected front is compact enough and, once reconstructed at the image level, long enough to be kept, i.e. longer than L_{min} , it will be accounted within the frontal index FTDI. The contribution of the front to the FTDI index is equal to its strength integrated along the whole length of the front. The strength is measured in this case by the temperature difference at the window level. The temperature difference calculated by the Cayula algorithm at the window level during the segmentation test is thus a fundamental quantity that is instrumental in the decision to keep a detected front or not and in the way its strength is stored in the frontal index.

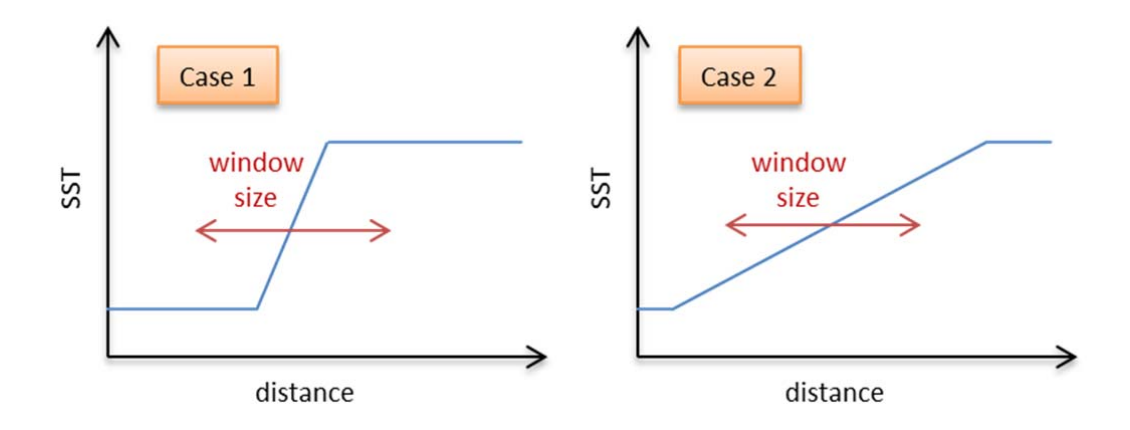


Figure 3-12: Two simplified configurations under which a window of the Cayula algorithm can see a front. Transects across the front and the size of the window are plotted. In case 1, the totality of the front is captured by the window, whereas in case 2, a portion of the front only is captured.

To characterize the Cayula algorithm, one needs to understand the relationship between the properties of a front and this temperature difference at the window level. Tests showed that, in the idealized case of very sharp fronts with no noise, that are so sharp that the window is seeing two populations of homogeneous temperature, the measured temperature difference is by design equal to the real temperature step across the front. This situation is a

particular situation under case 1 in Figure 3-12. Let us now consider a very large front with a constant temperature gradient across it. The window is seeing only a portion of it, as in case 2 of Figure 3-12. In this situation, a segmentation is always detected and the temperature difference is a linear function of the temperature gradient on the front. Figure 3-13 shows the temperature difference measured as a function of the gradient on the front, in the case of a window size of 32 pixels of 0.05° resolution.

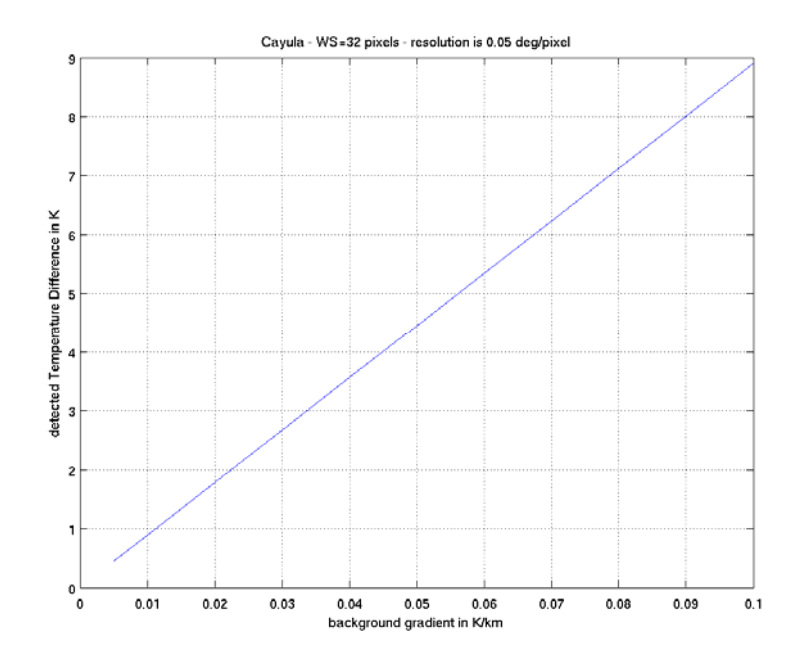


Figure 3-13: Temperature difference measured by the Cayula algorithm at the window level during the segmentation test, in case 2, as a function of the gradient on the front.

This function is linear:

$$\Delta T = 89 * \nabla SST$$

With ΔT in K and ∇SST in K/km. The total temperature step across the window is equal to

$$\Delta T_{tot} = WS * \nabla SST \tag{3-16}$$

With WS the size of the window in km. In this case

$$\Delta T_{tot} = 178 * \nabla SST$$

Hence

$$\Delta T = \Delta T_{tot}/2 \tag{3-17}$$

This means that the recovered temperature difference across a front within a window is equal to half the total temperature variation across the whole window in the case 2.

This result is important as it allows one to choose the appropriate value for parameter ΔT_{min} , so that unwanted fronts are not detected. For example, the Cayula algorithm tends to detect fronts in most of the windows when run with the $\Delta T_{min} = 0$ K. This is due to the presence of low background temperature gradient, mostly meridional, everywhere on the ocean surface. As a consequence weak fronts are detected all over the ocean with a regular step due to the window decomposition grid of the Cayula algorithm. The Figure 3-5 shows an example of this effect. For this reason, scientists have introduced the parameter ΔT_{min} to limit the detection of weak fronts on this background gradient which is not fundamentally linked to the mesoscale dynamics. However no justification was provided to explain the choice of the the parameter ΔT_{min} . Equation (3-16) allows one to set the parameter ΔT_{min} as a function of the minimum background gradient to be detected and the size of the window.

This result also helps to understand the measured strength of a front. One can see that the way the strength of a front is recovered depends on its width when compared to the window size. For a very sharp front, the whole temperature step across it is added up in the FTDI. For a front larger than the window, only half of the temperature step across the window is measured. However in this case, the front is likely to be detected several time by adjacent windows, hence the recovered frontal strength will add up when integrated in the index.

3.5.2.2 The Cayula algorithm at the window level on a noisy scene

The previous section describes the behaviour of the Cayula algorithm in the idealized situations of case 1 and case 2 (Figure 3-12) when the SST scene is noise-free. In reality, the window decomposition of the algorithm isolates fronts of all scales and intensities. Noise is present on the SST image due to measurement errors and atmospheric effects on the ocean surface. Moreover, the fronts do not appear perfectly because of the turbulence, which mixes temperature variations of all scales. So the fronts observed are embedded in a complex turbulent flow which tends to blur it. Noise affects the stages of segmentation test and cohesion test, since it tends to blur a front. This makes a noisy front less likely to be detected. In order to quantify this effect, the Cayula algorithm window level stages were tested on a wide range of scenes.

Synthetic SST gradient scenes were simulated and parameterized through their gradients and their temperature differences. A gradual amount of noise was then added to the scenes. These scenes were used as inputs to the Cayula algorithm at the window level so that both the segmentation and the cohesion were tested. When no noise was added to the scenes, even for very low nonzero gradients, a front was always detected between two segmented and coherent populations. As the noise was increased, the fronts needed to be sharper (greater temperature difference and steeper gradient) to be detected. Figure 3-14 presents the maximum noise that is allowed on the synthetic scenes for the segmentation and cohesion tests to be positive, for a window of 32 pixels with a typical resolution of 0.05°. One can see that, as most of the ocean fronts lie over a gradient of less than 0.05K/km, for a temperature difference of less than 3K, the segmentation and the cohesion is positive over the fronts if the spatial noise is less than 0.5K. Note that the spatial noise modelled here is a Gaussian and added for each pixel, this is a simplified model of the different types of noise mentioned above.

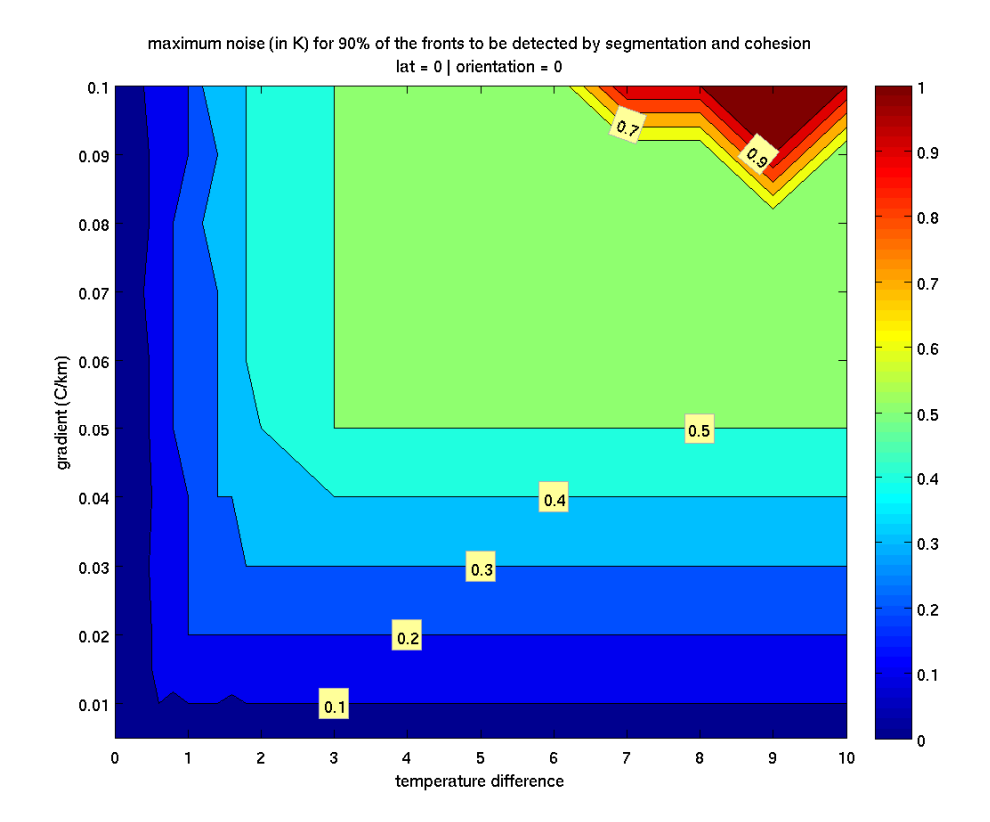


Figure 3-14: Maximum noise (in K) allowed on top of synthetic SST frontal scenes (parameterized through their gradients and the temperature differences) for both the segmentation and cohesion tests to be positive in the histogram algorithm. Window size is 32 pixels and the resolution is 0.05°, the minimum temperature difference is set to 0K.

3.5.3 Cross-comparisons of the front detection techniques

The previous sections have characterized separately the behaviour of the Canny and Cayula algorithms in relation to the features that are specific to each of them. The theoretical effect of the smoothing filters on the small scale in the Canny method was calculated and the behaviour and the robustness to noise of the Cayula algorithm at the window level was assessed. This section aims to compare the performances of these algorithms in various practical situations, as they are applied on imperfect images representative of the variety of fronts present on the ocean surface. Large synthetic images are generated and subjected to both algorithms in order to compare the detected fronts against common criteria.

3.5.3.1 Detection of fronts of all scales and strength on potentially noisy images

An ideal front detection method should be able to detect fronts of all scales and strength generated by the turbulent flow at the surface. It should also be able to do so on satellite SST images that suffer from noise. These capabilities are assessed for the Canny and Cayula algorithms by generating a large volume of synthetic scenes on which they are applied. Each synthetic scene is characterized by the presence of a single front that is parameterized by a temperature difference and an average gradient across it. The profile of the front is generated following a fitted Sinusoid function. The position of the front on the scene is recorded for the assessment of the front detection results. A random Gaussian noise is also added on each pixel, characterized by its standard deviation σ_n expressed in K. This noise is a simplification that accounts for measurement noise, small-scale atmospheric effects and small-scale turbulence which tends to blur fronts on SST images by creating meanders along them.

After the synthetic scenes are produced, the detection algorithms are applied on them. Frontal position and strength are estimated by the algorithms. The algorithm performances are rated against two success criteria:

- The accurate resolution of the actual front length
- The accurate resolution of the actual front strength

The first criteria is compared directly from each method, the second criteria is assessed theoretically and discussed as it is calculated via different indexes on each algorithm.

To allow a fair comparison between the two front detection algorithms, both of them are tested after the same amount of smoothing is applied: the smoothing is achieved by the convolution of a running Gaussian filter whose standard deviation is $\sigma_s = 5$ or 10 or 20 km. Figure 3-24 and Figure 3-25 show the performances of the Cayula algorithm after a 3 by 3 and 9 by 9 pixels median filter is applied to lower the noise, since this is commonly used in reported implementations of Cayula.

3.5.3.1.1 Resolution of front length on noise-free images

Figure 3-15 shows the relative front length detected by the Canny algorithm with various parameters, for a wide range of fronts, on noise-free scenes. The relative front length is the ratio of the length of fronts (FLI) detected with the actual length of fronts present on the scene. Ideally, this ratio should be equal to 1. One can observe that as the parameters T1 and T2 are set to higher values, fewer fronts of small gradient or small temperature difference are detected. Small scale fronts are characterized by a high gradient and/or a small temperature difference. Moreover, it was also found that the detected fronts are always at the right position, this means that the Canny method is efficient at locating the front on a noise-free image. Figure 3-15 also shows that the larger the smoothing filter, the stronger the fronts need to be in order to be detected by the Canny algorithm. This result is consistent with the explanation that the smoothing lowers the gradient at small scales. When the gradient on a front is lowered below the detection thresholds the front is not detected. One can conclude from this that the Canny algorithm with low threshold parameters and little smoothing is very suitable for detecting fronts on a noise-free scene.

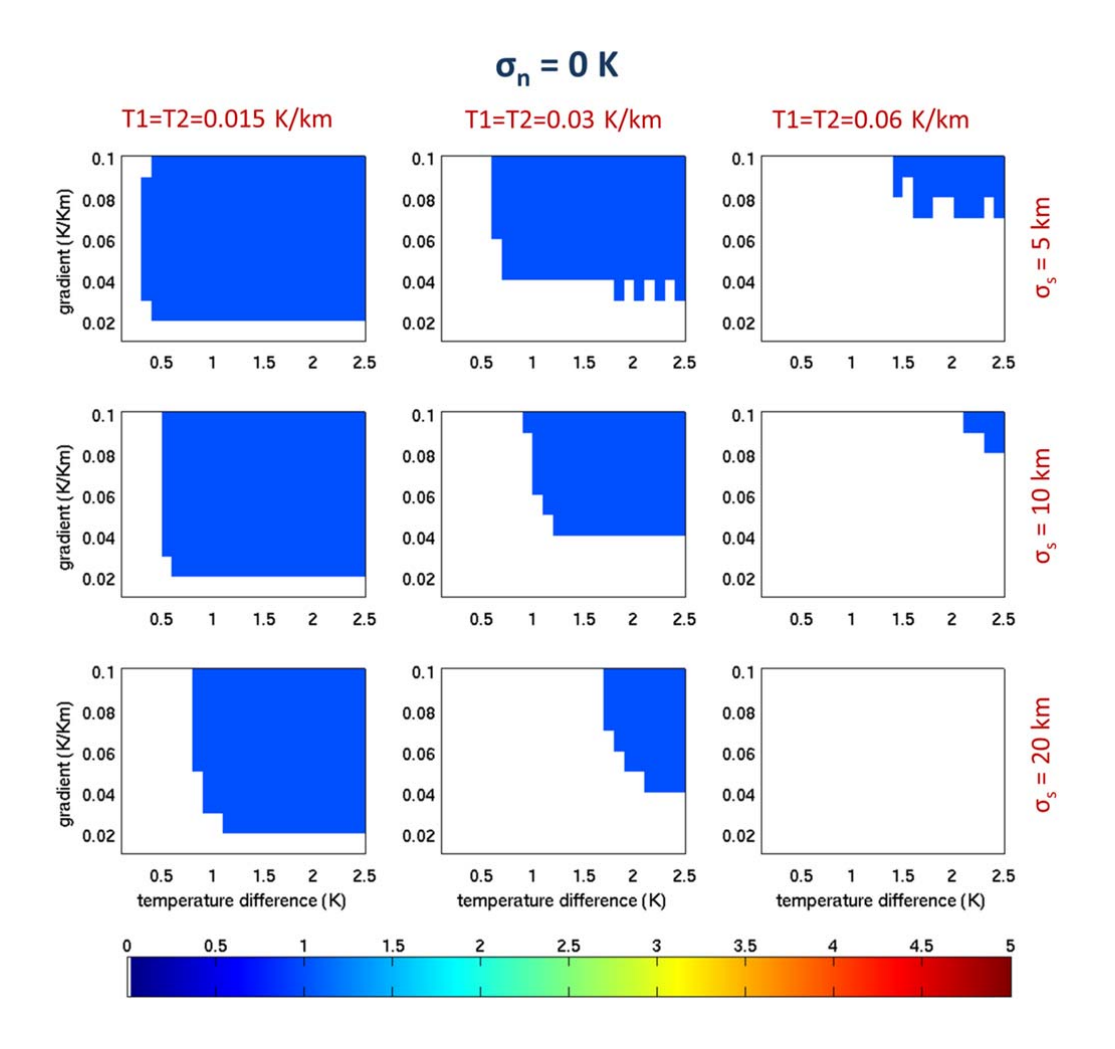


Figure 3-15: Relative Front Length ($FLI_{detected}/FLI_{actual}$) of the Canny algorithm. The input SST scene resolution is 0.05°. The latitude is 0 and the front is oriented zonally. The results are presented for three values of σ_s and for three values of T1=T2. The gradient is calculated after the SST is convoluted with a running Gaussian filter. The synthetic SST images are **noise-free**.

Figure 3-16 shows the results of the same experience with the Cayula algorithm. It displays the relative front length detected on a noise-free scene, with the minimum temperature difference set to 0 K or 0.4K. Apart from very small and very sharp fronts, most of the fronts are detected. However the length is not resolved properly as most fronts are detected twice, and the very wide ones are even detected up to five times. This is due to the window decomposition in the Cayula method, when several windows see the same front at several places across it. Setting the minimum temperature difference (ΔT_{min}) to 0.4K reduces the number of fronts detected on an original wide

front, but it also prevents the detection of fronts whose temperature step is lower than ΔT_{min} . In this case of noise-free inputs, increasing the smoothing does not affect the number of detected fronts, contrary to the Canny case discussed before.

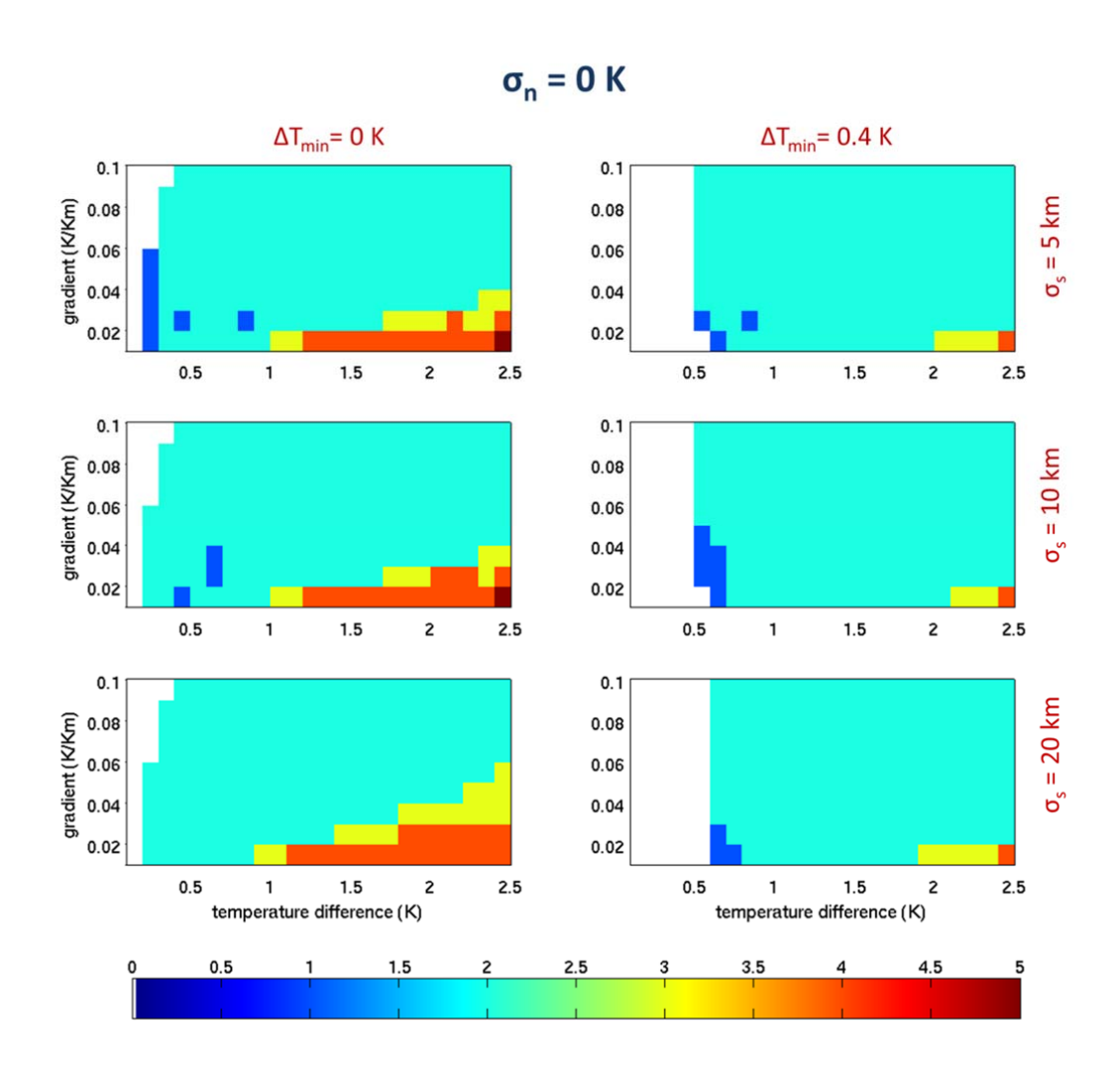


Figure 3-16: Relative Front Length ($FLl_{detected}/FLl_{actual}$) of the Cayula algorithm. The input SST scene resolution is 0.05°. The latitude is 0 and the front is oriented zonally. The results are presented for three values of σ_s and for two minimum temperature difference ΔT_{min} . The gradient is calculated after the SST is convoluted with a running Gaussian filter. The synthetic SST images are **noise-free**.

3.5.3.1.2 Resolution of front length on noisy images

The situation with no noise present is not a realistic one. In practice, the detection method has to perform with some level of noise present on the image. Figure 3-17, Figure 3-18 and Figure 3-19 present the relative front length detected on SST scenes suffering from a noise of 0.1K, 0.2K and 0.3K respectively. Each shows the response to the same combinations of parameters as shown in Figure 3-15 for the noise-free Canny behaviour. It is striking that the parameters suited to the noise-free images (σ_s =5 km and low T1=T2=0.015 K/km) are not suitable for noisy situations. As illustrated in Figure 3-20, if the scene is not smoothed enough by the filter and if the detection thresholds are set too low, fronts are detected all over the image, whether or not there is an actual front. This results in high relative front length of up to 16 with a noise of 0.3K.

From Figure 3-17, Figure 3-18 and Figure 3-19, one can deduce that two sets of parameters for the Canny method seem to be capable of detecting fronts of a wide range of scales and to do so with a relative front length close to 1:

- a) σ_s =5 km and T1=T2=0.03 K/km
- b) $\sigma_s = 10 \text{ km}$ and low T1=T2=0.015 K/km

Parameter set **b** is able to detect fronts of smaller scale and is more robust to noise. Its relative front length stays close to 1 even for a noise of 0.3K, while parameter set **a** behaves less well at 0.3K noise. Figure 3-19 indeed shows that it detects 2 to 3 times too many fronts when the input images feature low gradient fronts with a high temperature step (i.e. wide fronts) and a 0.3 K noise. Although set **a** detects more noise-induced fronts, it will be shown in the next section that this set of parameters is better at resolving the frontal strength because the smoothing filter is narrower.

Figure 3-21, Figure 3-22, and Figure 3-23 show the performances of the Cayula algorithm when facing an increasing noise contamination. It is noticeable that, as noise increases, the small scale fronts are less detected. This is due to the fact that the segmentation and cohesion tests fail in those cases for which the noise is too high with regard to the temperature step measurable at the window level.

Comparing the performances of the Canny parameter set **b** with the Cayula method, one can conclude that the Canny algorithm is superior to the Cayula one for accurately resolving the frontal length, even in the presence of noise. The Canny method detects the right amount of fronts in the well-defined ensemble of fronts that it is able to detect. Conversely, the comparison of Figure 3-21, Figure 3-22, and Figure 3-23 shows that, for a given set of parameters (initial smoothing and minimum temperature difference), an increase in the input noise results in a decrease of the number of detected fronts. The Cayula algorithm is more sensitive to the image noise. This dependency is also observed on Figure 3-24 which shows the effect of an increasing input noise with a fixed 3 x 3 pixels median filter. Figure 3-25 shows the results of the same analysis but with a 9 x 9 pixels median filter. One can notice that the dependency on noise is reduced as the filtering stage is able to reduce it to a larger extent. As a consequence more weak fronts are detected but the detected frontal length remains less accurate than with the Canny.

It is striking on Figure 3-16, Figure 3-21, Figure 3-22, Figure 3-23, Figure 3-24 and Figure 3-25 that the Cayula algorithm detects fronts down to much lower gradients and temperature differences than Canny. However due to the overlapping window approach, Cayula detects most fronts twice, and some at the limit of the detectability are detected up to 5 times their actual length. So it is clear that the choice of algorithm involves a trade-off of more reliable detection against a wider range of detectability.

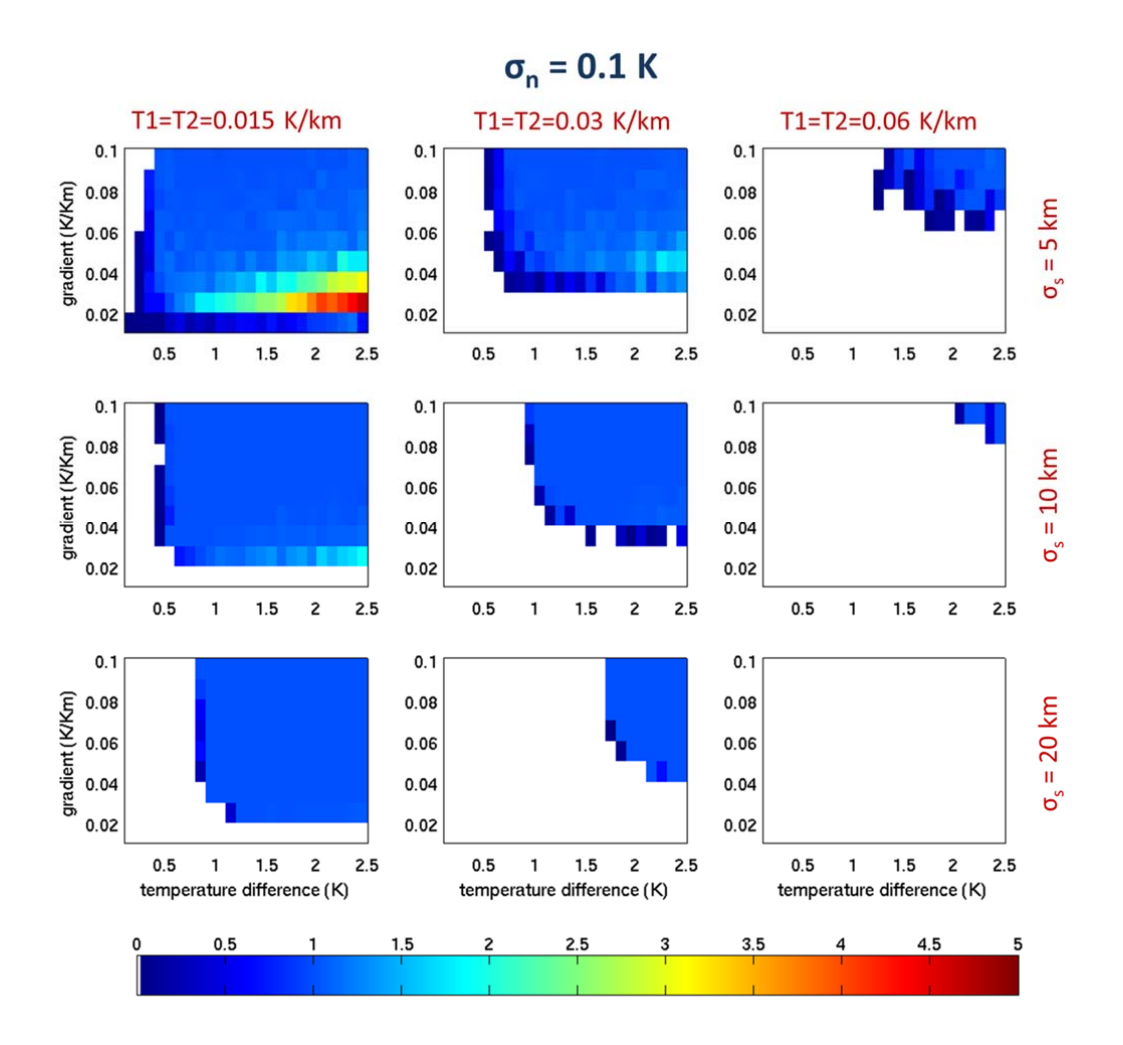


Figure 3-17: Relative Front Length ($FLI_{detected}/FLI_{actual}$) of the Canny algorithm. The input SST scene resolution is 0.05°. The latitude is 0 and the front is oriented zonally. The results are presented for three σ_s and for three T1=T2. The gradient is calculated with a running gaussian filter. The synthetic SST suffer from a Gaussian noise of $\sigma_n = 0.1K$.

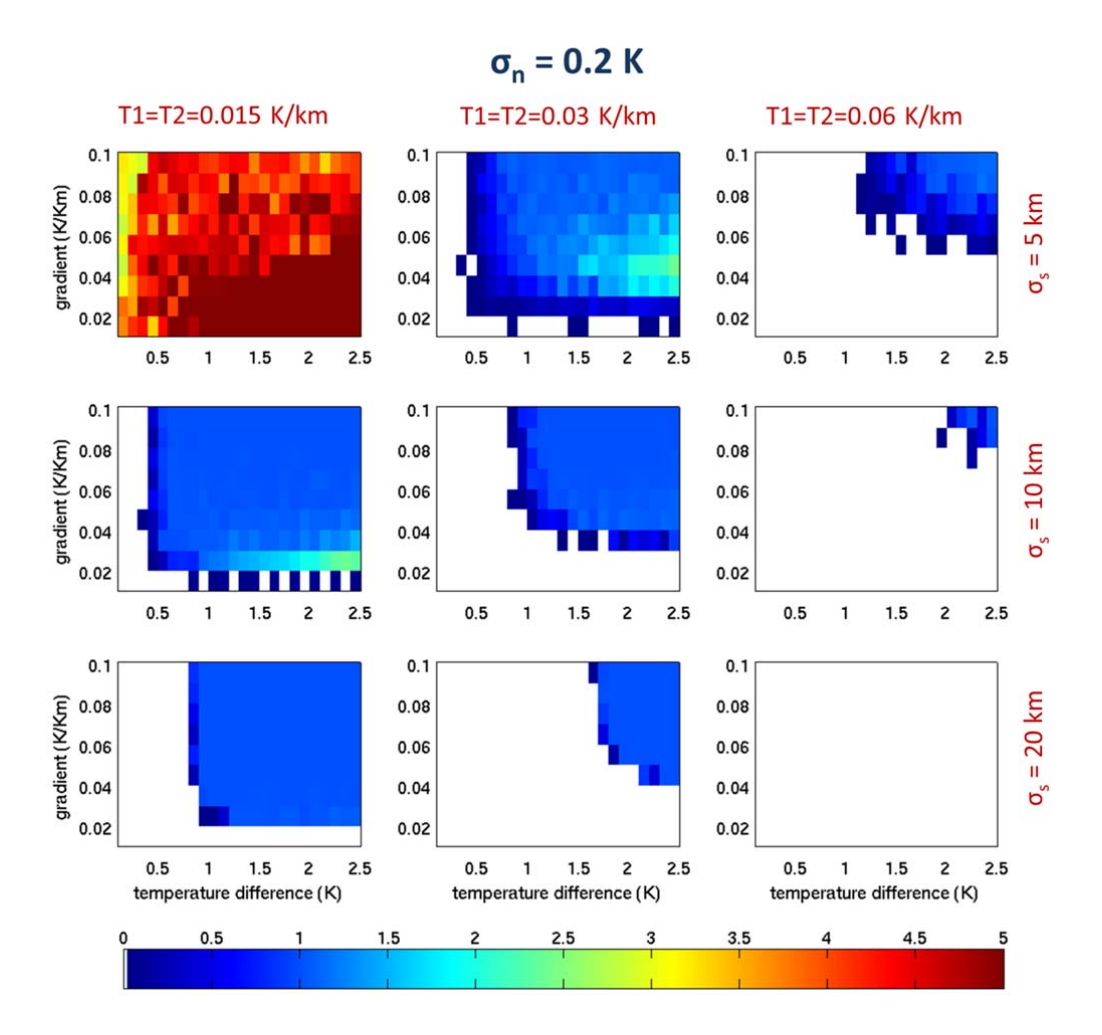


Figure 3-18: Relative Front Length (FLI_{detected}/FLI_{actual}) of the Canny algorithm. The input SST scene resolution is 0.05° . The latitude is 0 and the front is oriented zonally. The results are presented for three σ_s and for three T1=T2. The gradient is calculated with a running gaussian filter. The synthetic SST suffer from a Gaussian noise of $\sigma_n = 0.2K$.

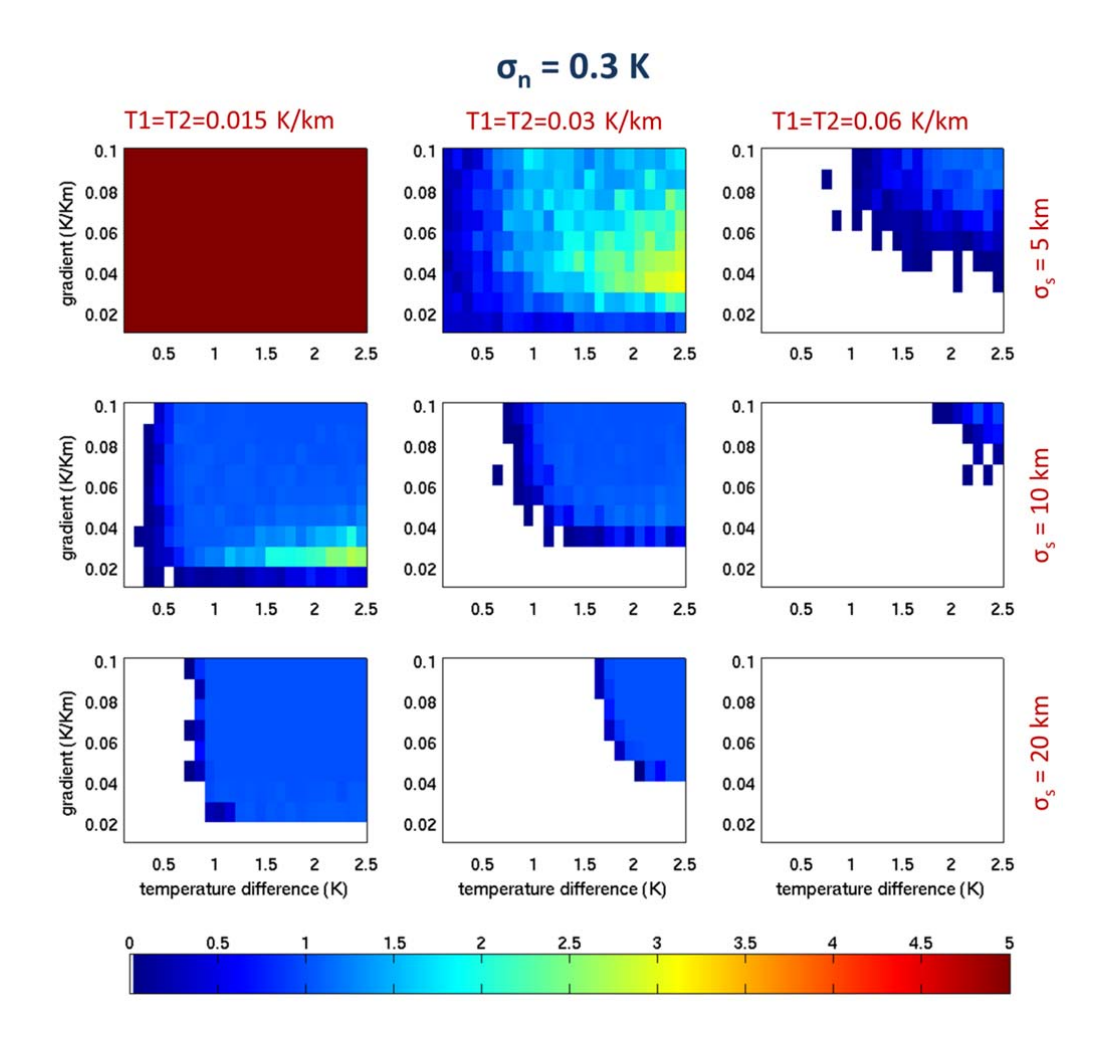


Figure 3-19: Relative Front Length (FLI_{detected}/FLI_{actual}) of the Canny algorithm. The input SST scene resolution is 0.05° . The latitude is 0 and the front is oriented zonally. The results are presented for three σ_s and for three T1=T2. The gradient is calculated with a running gaussian filter. The synthetic SST suffer from a Gaussian noise of $\sigma_n = 0.3K$.

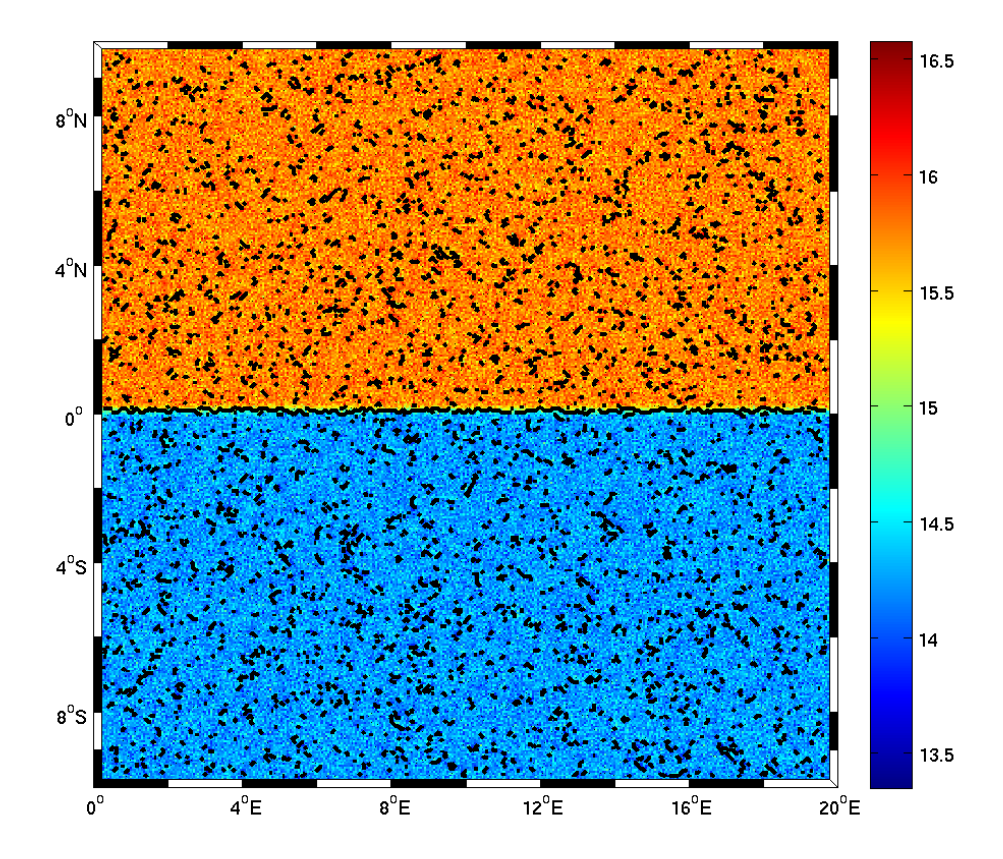


Figure 3-20: Example of the Canny algorithm detecting too many fronts because of the presence of noise. The original front is defined by a temperature step of 1.5 K and a North-South temperature gradient of 0.05 K/km. On top of it, the source image suffers from a Gaussian noise of 0.2K. Its resolution is 0.05 °. The fronts are detected with the Canny algorithm whose parameters are set to: $\sigma_s = 5 \ km$ and $T_1 = T_2 = 0.015 \ K/km$.

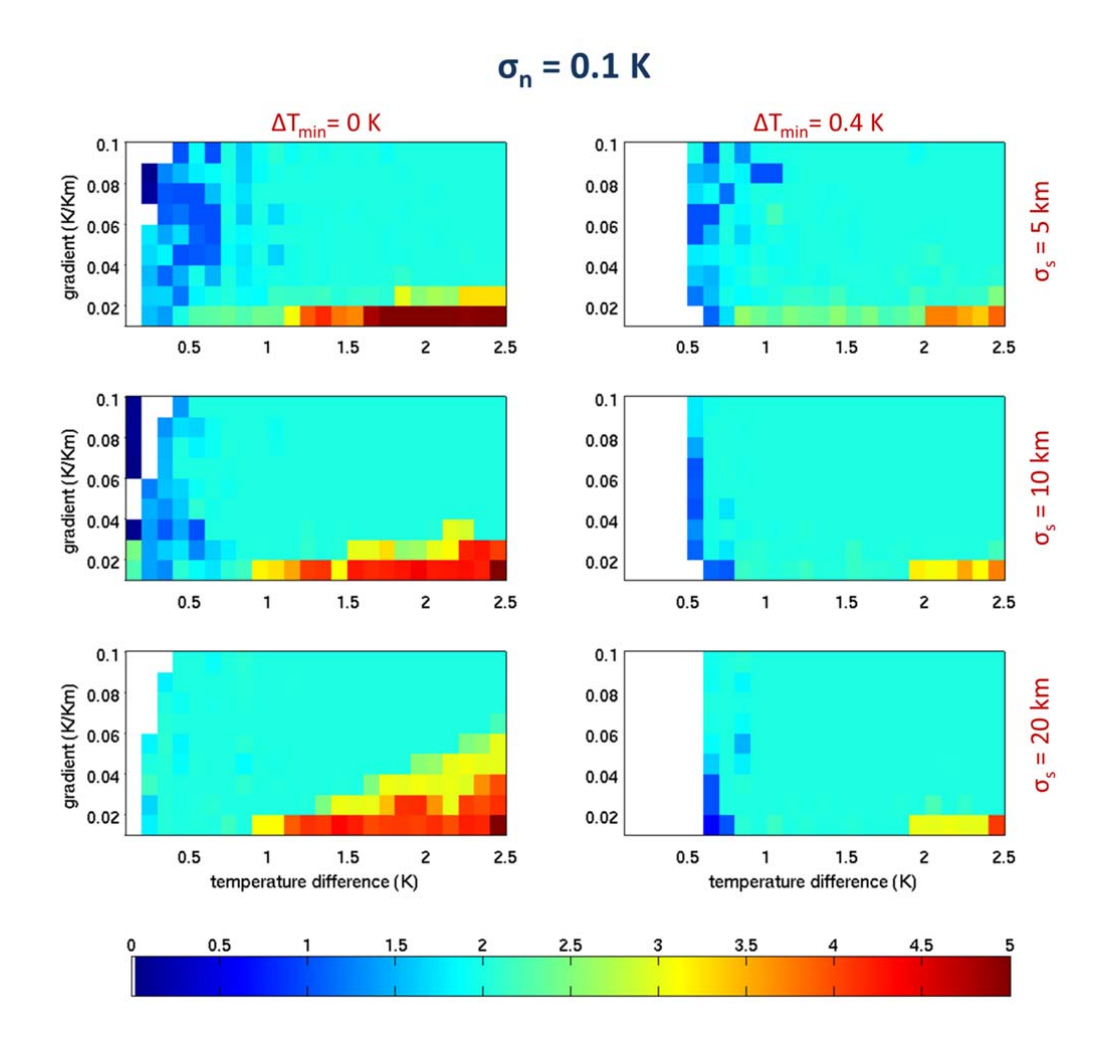


Figure 3-21: Relative Front Length (FLI_{detected}/FLI_{actual}) of the Cayula algorithm. The input SST scene resolution is 0.05°. The latitude is 0 and the front is oriented zonally. The results are presented for three values of σ_s and for two minimum temperature difference ΔT_{min} . Synthetic SST scenes suffer from a Gaussian noise $\sigma_n = 0.1 \ K$.

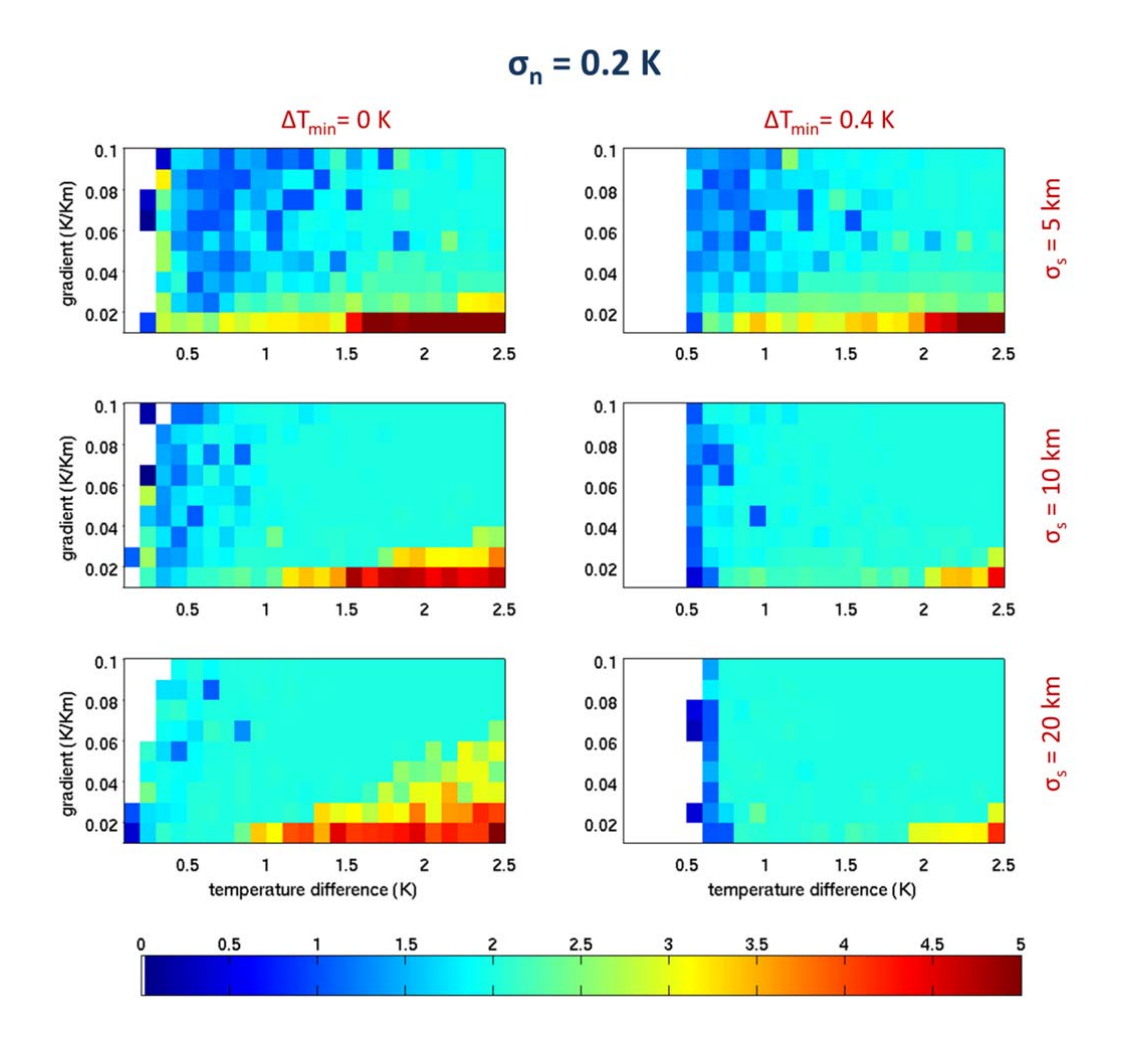


Figure 3-22: Relative Front Length (FLI_{detected}/FLI_{actual}) of the Cayula algorithm. The input SST scene resolution is 0.05° . The latitude is 0 and the front is oriented zonally. The results are presented for three values of σ_s and for two minimum temperature difference ΔT_{min} . Synthetic SST scenes suffer from a Gaussian noise $\sigma_n = 0.2~K$.

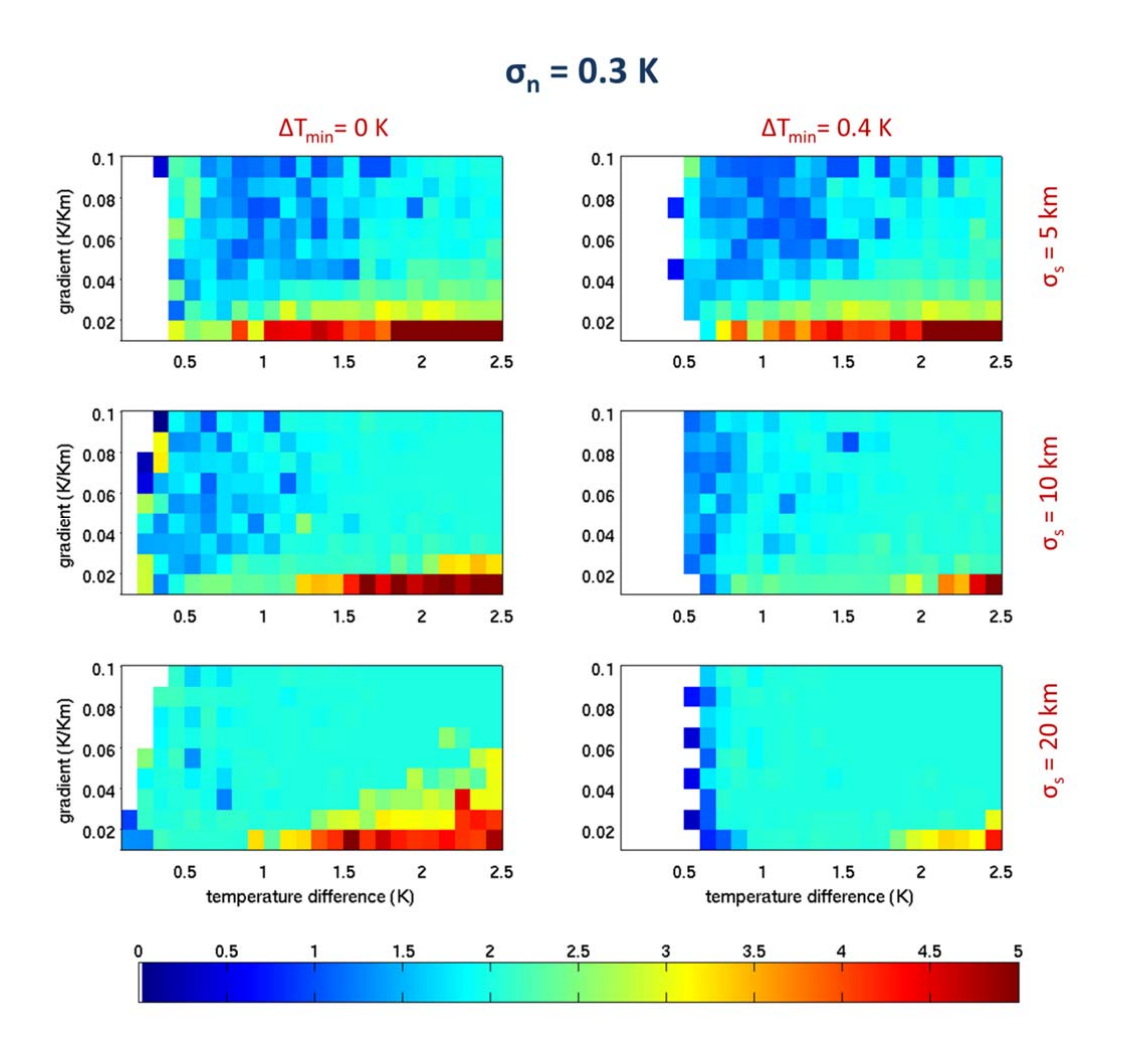


Figure 3-23: Relative Front Length (FLI_{detected}/FLI_{actual}) of the Cayula algorithm. The input SST scene resolution is 0.05°. The latitude is 0 and the front is oriented zonally. The results are presented for three values of σ_s and for two minimum temperature difference ΔT_{min} . Synthetic SST scenes suffer from a Gaussian noise $\sigma_n = 0.3~K$.

3x3 median filter

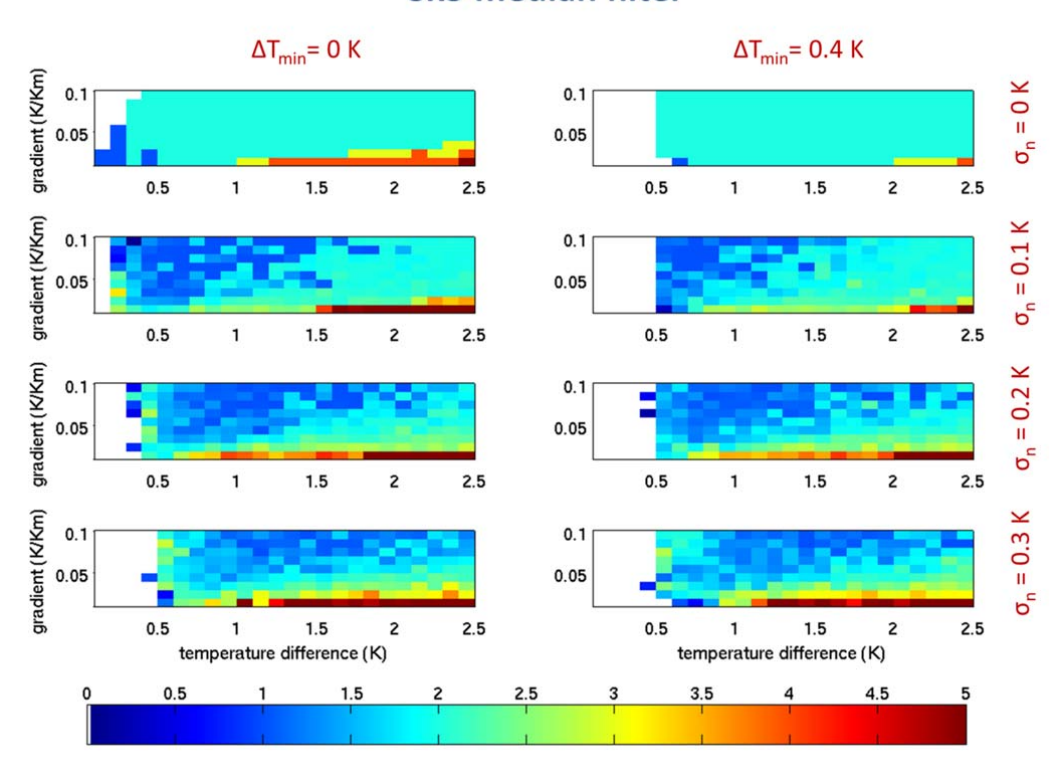


Figure 3-24: Relative Front Length (FLI_{detected}/FLI_{actual}) of the Cayula algorithm. The input SST scene resolution is 0.05°. The latitude is 0 and the front is oriented zonally. The results are presented for four values of σ_n (Gaussian noise) and for two minimum temperature difference ΔT_{min} . The synthetic SST scenes are filtered by a 3 by 3 pixels median filter.

9x9 median filter

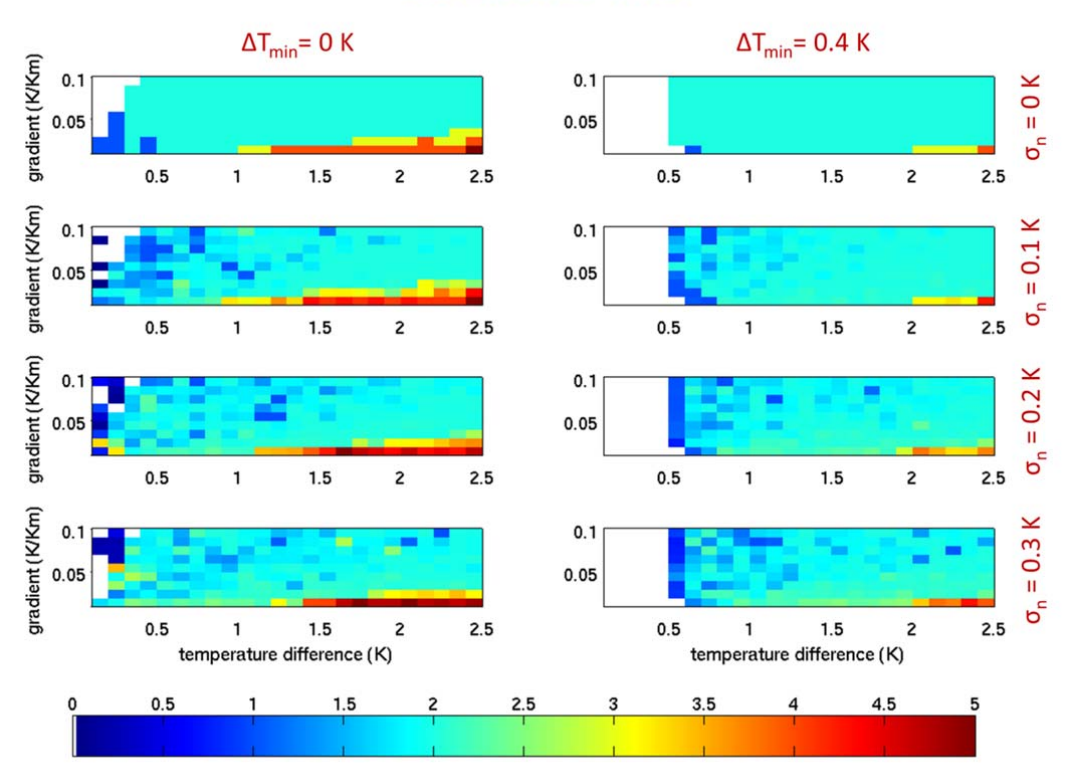


Figure 3-25: Relative Front Length (FLI_{detected}/FLI_{actual}) of the Cayula algorithm. The input SST scene resolution is 0.05° . The latitude is 0 and the front is oriented zonally. The results are presented for four values of σ_n (Gaussian noise) and for two minimum temperature difference ΔT_{min} . The synthetic SST scenes are filtered by a 9 by 9 pixels median filter.

3.5.3.1.3 Resolution of front strength on noise-free images

On noise-free images, the Canny algorithm can be applied with low σ_s and low T1 and T2. In this situation the algorithm potentially resolves the gradient at the fronts perfectly. The returned frontal strength is the SST gradient magnitude integrated along the fronts which are detected along the crests of SST gradient magnitude. It is important to note that the frontal strength index is not linked to the front width. This is a limit of the Canny algorithm, because it does not differentiate fronts according to their width but only to their maximum gradient magnitude at their centre.

Section 3.5.2 describes the behaviour of the Cayula algorithm at the window level. It is relevant here because the front strength is estimated by the

temperature difference between the two populations of pixels on each side of the front within one window. If the front width is very small, this value corresponds to the temperature step across the front. If the front's width covers a significant portion of the window (case 1 of Figure 3-12), the temperature step across the front is underestimated by the measured temperature difference. If the front width is larger than the window size (case 2 of Figure 3-12), the actual temperature step is even more underestimated. However, in case 1 the front may be detected several times and this may compensate to some extent the underestimation of the temperature step.

A fundamental difference between the two algorithms is the way each estimates the frontal strength. The Canny algorithm estimates the FGI (Frontal Gradient Index), which is a measure of the gradient magnitude at the front's centre. Conversely, the Cayula algorithm estimates the FTDI (Frontal Temperature Difference Index), which is a measure of the temperature step across the front. These two indexes are linked, but their relationship depends on the front's width as shown in Figure 3-26. The Canny method estimates perfectly the FGI on noise-free images, while the FTDI is imperfectly measured by the Cayula algorithm even on noise-free scenes. On the other hand, the FGI estimation is very much impacted by the presence of noise when the FTDI is more robust to it, provided a front is detected.

It should be stressed that the Cayula method is also able to estimate the FGI. Indeed it is possible to estimate the SST gradient magnitude and return it at the locations where the Cayula algorithm detects fronts. Of course, the estimation of the gradient is what is challenging in the Canny method. In this case the performances are equivalent, except that the Cayula method detects fewer fronts as shown in section 3.5.3.1.2.

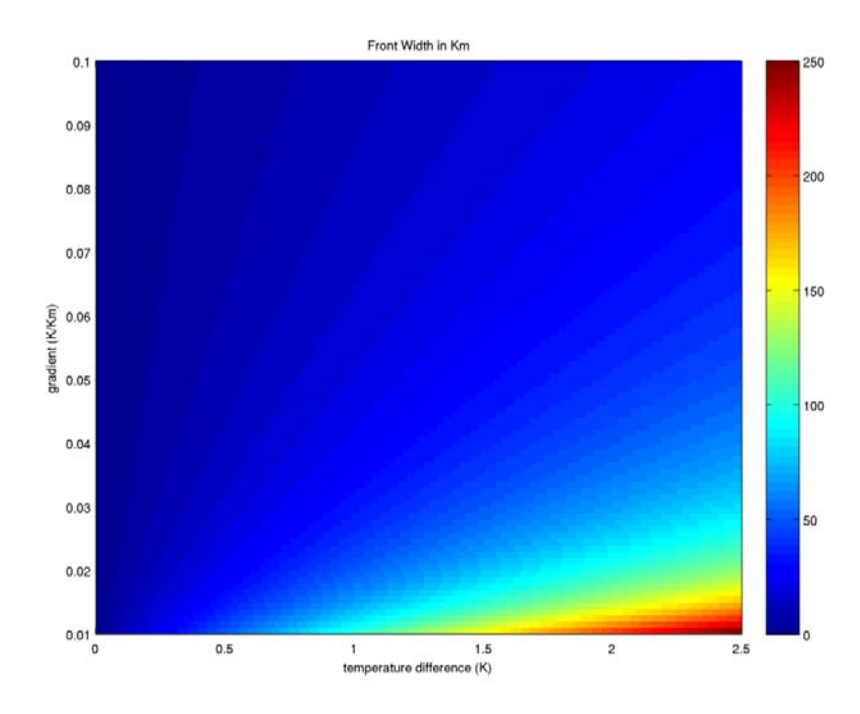


Figure 3-26: Front Width as a function of the front's gradient and temperature difference.

3.5.3.1.4 Resolution of front strength on noisy images

When dealing with noisy scenes input to the Canny algorithm, a trade-off is needed between the ability to detect small fronts, and the ability to resolve the frontal strength. It is a trade-off between an accurate recovered frontal length and an accurate recovered frontal strength. For instance, parameter set $\bf b$ (σ_s =10 km and low T1=T2=0.015 K/km) introduced above is better than set $\bf a$ (σ_s =5 km and T1=T2=0.03 K/km) because it detects smaller fronts by smoothing the noise more and it detects them only once (as seen in Figure 3-17, Figure 3-18 and Figure 3-19). However set $\bf b$ has a larger smoothing filter, whose consequence is to underestimate the gradient at small scales. This effect is described and characterized in section 3.5.1. For a gradient to be retrieved with a 90% accuracy after a Gaussian filter, it should be 3.29 times larger than the smoothing filter standard deviation (σ_s). This is illustrated in Figure 3-10. Thus the set of parameters $\bf a$ is able to estimate with precision the FGI on fronts of width larger than 16.45 km. The set $\bf B$ is able to do so on fronts wider than 32.9 km.

The level of smoothing necessary to resolve the frontal length depends on the properties of the SST data used as input. It is difficult to have a precise estimation of the noise present on the images. The preferred approach adopted in this thesis is to test the behaviour of the Canny method on a particular SST dataset with a variety of σ_s and judge which is the minimum amount of smoothing necessary to avoid detecting fronts linked to noise. This step may be considered as being subjective, in that it depends on the scientist's eye. However it is unavoidable and its effect is well characterized, so that it is well understood what scales are recovered. Obviously, the same filter should be applied across space and time so that consistent indexes can be constructed. Keeping the level of smoothing minimum is important to allow the accurate recovery of the frontal strength.

3.5.3.2 Detection of intricate fronts and fronts of high sinuosity

The scale of the fronts detected by the Cayula method is strongly dependent on the chosen window size (WS) parameter. It was shown that if the window size is too small with regard to the front's width, the same front can be detected several times. On the other hand, if WS is too large, small fronts and intricate fronts may not be detected. It is worth recalling that a front is detected by the Cayula algorithm if and only if it divides one of the windows into two populations of pixels whose average temperatures are significantly different and that are compact enough. It is important to note that the Cayula method is not able to detect two fronts or more within one window. The presence of two or more fronts in a window generally fails the tests of segmentation and cohesion, which ends up with no front at all being detected.

Figure 3-27 illustrates this limit by showing the results of detection tests on synthetic fronts of varying sinuosity. The sinuosity is a measure of the deviation of a path between two points (the front) from the shortest path (a line) between the extremities. It is given by the ratio of the actual front length to the shortest path length. For a sinuosity of 5, the window size is still small enough to detect the front everywhere. As the sinuosity is increased to 8, the window is never able to see a unique front and no front is detected at all. This shows that the Cayula algorithm is very dependent on the parameterized size

of the window, as its ability to detect fronts is limited by their sinuosity and the length scale of the sinuous pattern relative to the window size.

Conversely, even though the Canny algorithm is limited in the small scales due to the initial step of smoothing, it is able to detect fronts of all scales. It is an important advantage of the Canny algorithm that it is able to detect fronts of a wide range of scales, provided the noise has been smoothed out.

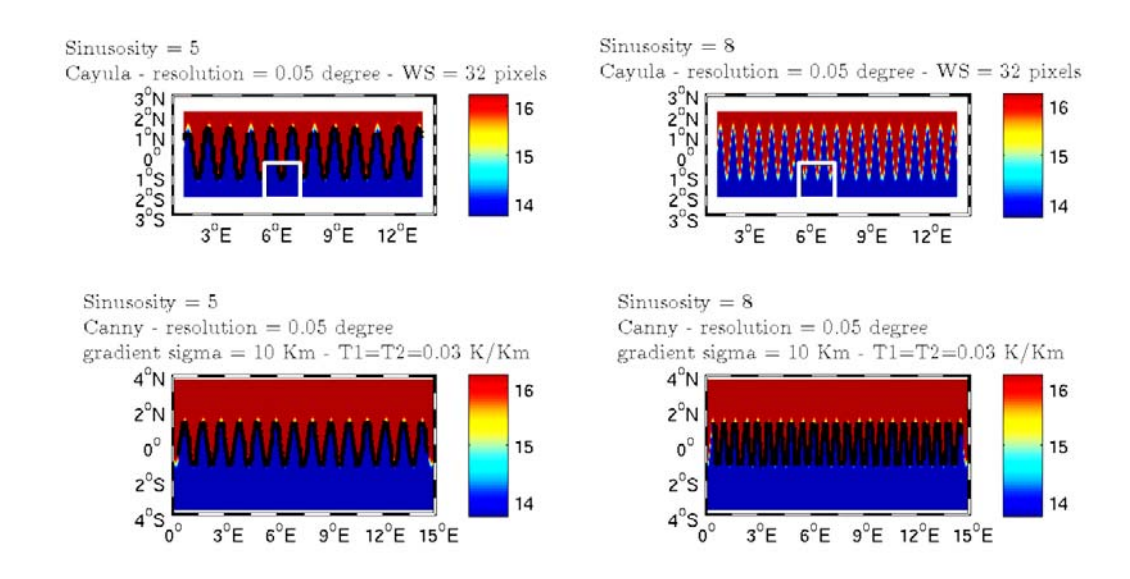


Figure 3-27: Example of the Cayula algorithm not being able to detect a front whose sinuosity is too high. The background is a noise-free synthetic scene of a meandering front, with a low sinuosity (left) and a high sinuosity (right). The top row shows the front detected by the Cayula algorithm. A black line is plotted where a front is found. No front is detected over the front of high sinuosity by the Cayula algorithm (top right). A Cayula window is displayed for indication. On the contrary, the Canny algorithm is able to detect the fronts of low (bottom left) or high (bottom right) sinuosity.

3.5.3.3 Detection of fronts of all orientations

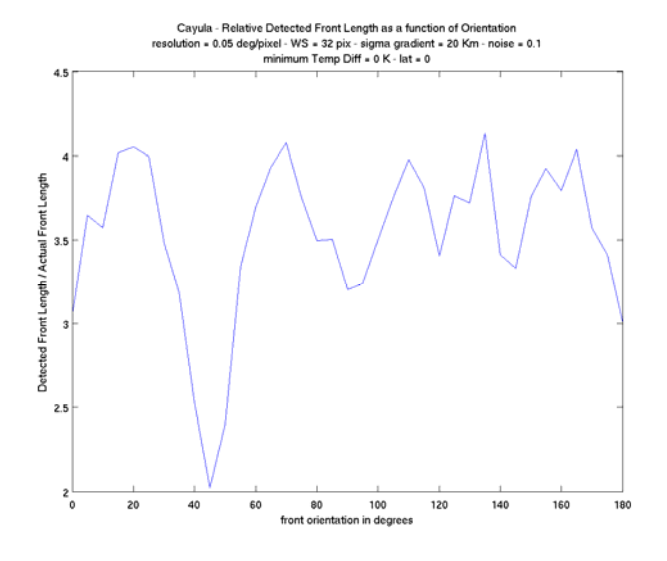
An ideal front detection method should detect equally fronts of all orientations. This is necessary in order not to introduce systematic biases in the detected frontal indexes based on the orientation of the front. One can assume that the fronts are isotropic in the open ocean, however strong fronts linked to jets tend to follow the direction of the current, hence they will have a preferred direction in some parts of the world. Fronts associated with

upwellings tend to be parallel to the coast, and they ought to be detected with the same accuracy as fronts along the ACC which tend to be more zonal. Figure 3-28 presents a case where the Cayula algorithm behaves very differently when presented with the same front but rotated at different angles. When the front is at 45°, it is not detected at all, whereas at 70° it is detected on average 4 times. Conversely, the Canny algorithm is very robust to the front orientation and the relative front length stays close to 1 whatever the front orientation.

The reason for which the Cayula algorithm appears inconsistent for different front orientation is the limited ability of the cohesion test to perform uniformly and independently of the front orientation. As illustrated in **Figure 3-29**, the conditions (3-8) and (3-9) are harder to meet in case the front is oriented in diagonal with regard to the pixel grid (case b of **Figure 3-29**) because R_1 and R_2 are lower than in the case where the front is aligned to the grid (case a of **Figure 3-29**). Indeed, the pixels at the border between the populations have only 2 neighbours within their population in the case b, when they have 3 of them in case a. One could think of a potential improvement of the Cayula algorithm which would be to calculate the neighbouring pairs to include the "diagonal neighbours" by replacing (3-11) by (3-18):

$$\mathcal{N}_{improved}(x_{i,j}) = \{x_{i,j+1}, x_{i,j-1}, x_{i+1,j}, x_{i-1,j}, x_{i+1,j+1}, x_{i-1,j-1}, x_{i+1,j-1}, x_{i-1,j+1}\}$$
(3-18)

This potential improvement would be implemented at the expense of computation time. The author believes that it could improve the robustness of the Cayula algorithm against front orientation. This suggested improvement was not tested nor implemented in the scope of this thesis.



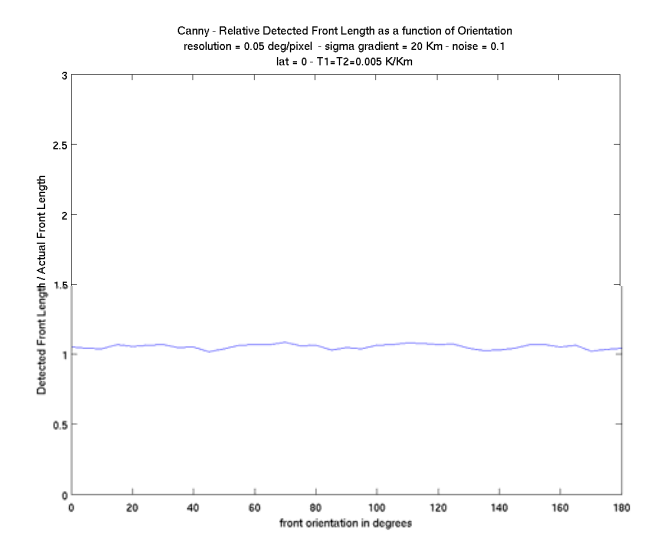


Figure 3-28: Detected relative front length as a function of the orientation of the front, for the Cayula algorithm (top) and the Canny algorithm (bottom). The synthetic front is characterized by a gradient of 0.01 K/km and a temperature difference of 1 K. Both algorithms are run after the same 20 km running Gaussian filter is applied to the temperature images.

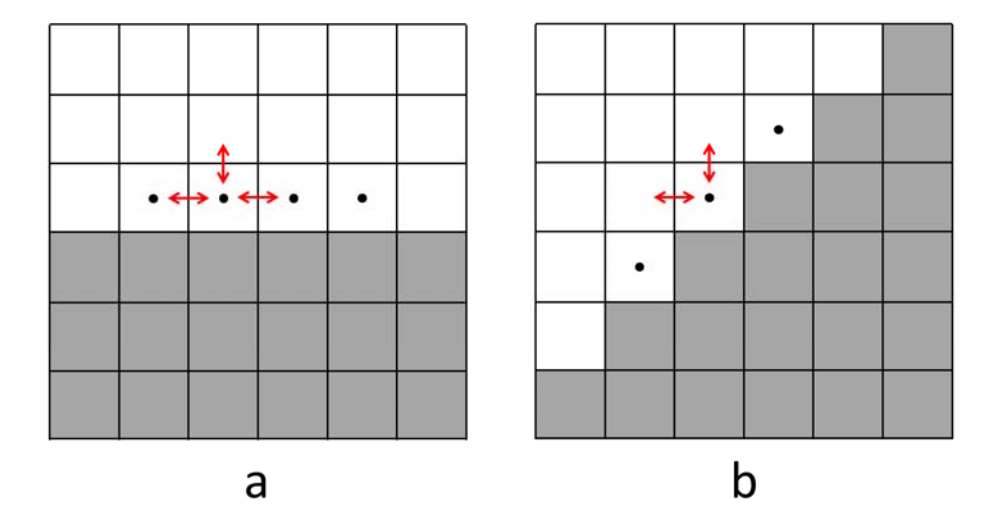


Figure 3-29: Two frontal orientations with non-similar cohesion as assessed by the Cayula algorithm. The pixels of the window (non-representative window size of 6 pixels) are divided into two populations following the segmentation step depending on the orientation of the underlying front with regard to the grid. The dotted pixels are the ones which cause the cohesion step to return different results in a) and b). The red arrows show the neighbouring pairs involving one of the dotted pixels at the border between the populations.

3.5.3.4 Detection of fronts on images that suffer from missing pixels

Level-2 SST data are single-sensor products. They generally suffer from a certain extent of missing samples. Data are missing wherever the sensor is not able to make an accurate measurement. For infrared sensors, this happens over cloudy areas, whereas for microwave instruments it occurs over rainy spots and close to land. When a large patch of data is unavailable because of such a situation, no algorithm is able to detect anything. However the clouds are often scattered and cover a small portion of the overall scene integration. A front detection adapted to Level-2 products should be able to deal with a small amount of missing data, disseminated over the image. Figure 3-30 shows that the Cayula algorithm (applied without initial filtering) is much better at detecting the front than the Canny one in these conditions. The reason why the Canny method fails is that the application of the smoothing filter enlarges each missing data spot by the size of the filter. In the case of Figure 3-30, each original missing pixel is about 5.5 km wide, but after the smoothing filter is applied the missing patch grows to 3 times $\sigma_{\rm s}$: 30 km (not

shown in the figure). The smoothing filter strategy is that if one of the pixels is missing, every pixel that shall be smoothed taking into account the missing pixel ends up as missing too. One way to deal with this issue is to interpolate first on the missing samples, and this is what is done in Level-4 SST products. However the interpolation can result in the underestimation of a gradient and it could be preferable to just ignore a missing spot.

The Cayula algorithm was developed for this very reason and it is extremely efficient in dealing with small missing patches, as seen in Figure 3-30. The segmentation and cohesion tests are not affected by a few missing pixels within a window.

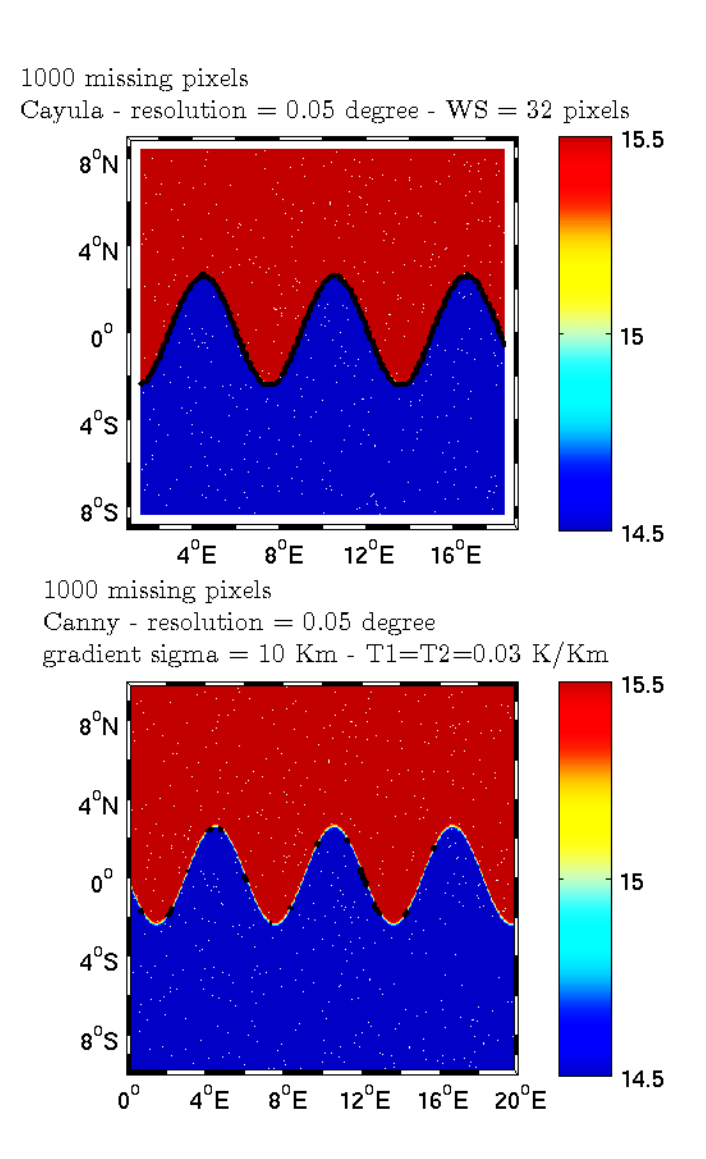


Figure 3-30: Example of the Canny algorithm being strongly impacted by missing data. A synthetic image of a front is created and 1000 pixel values are removed at random locations before the detection techniques are applied. The detected fronts by the Cayula (top) and the Canny (bottom) algorithms are shown as a black line. On the top panel, the Cayula algorithm is able to detect the front along its whole length despite the missing values in the input data (shown as white pixels). In contrast, the Canny algorithm is only able to detect very small portions of the front due to the missing pixels.

3.5.3.5 Detection of fronts on images projected on a cylindrical projection

Global SST products are usually provided on a cylindrical geographical projection. This means that a square image pixel is shorter in kilometres from east to west than north to south. It gets shorter as one gets closer to the pole, whereas the north-south size of a pixel remains uniform with latitude. One needs to ensure that this does not introduce biases in the detected fronts.

The Canny algorithm can deal with it by

- a) Applying a meridionally varying smoothing filter size, so that it always remains the same size in kilometres in the North-South and East-West directions, whatever the latitude.
- b) Accounting for the varying pixel size in kilometres when calculating the gradient.

These two steps ensure that no bias is introduced by the cylindrical projection in the detected fronts.

The Cayula algorithm needs to project the data on a latitude-dependent sinusoidal projection so that it can be applied on an image whose pixels are square in kilometres. This step is complex because the sinusoidal projection is only valid locally. This means that a global scene cannot be processed in one go; it needs first to be decomposed into local regions where the data are reinterpolated on an equal-area grid. The fronts are then detected on each region and care must be taken to ensure that the fronts laying at the intersection of two regions are linked properly on both sides. The Cayula method is much more complex to properly implement on a global scene.

3.5.3.6 Robustness to arbitrary parameters

One ambition of this chapter is to characterize the front techniques and adapt them so that they can be used in a way that carries a dynamical meaning. Its strategy is to shed light on the "black box" aspects of the algorithms by describing the relationship between the inputs (front and image properties) and the outputs (detected front length and strength). For this, the effect of

each parameter of the algorithms must be understood. The parameters that have a significant impact on the result should have their effect characterized so that it can be avoided, corrected or accounted for in the physical interpretation. If a parameter is shown to have no impact on the result, it may be chosen in a subjective manner.

An important parameter is the resolution of the grid onto which the image is projected. Of course, the higher the resolution, the smaller the scale potentially resolved on the image. However, the choice of the resolution is a subjective one, and different resolutions can also show exactly the same thing. In this case, a front detection algorithm should return the same results when fed with one resolution or the other. The Canny algorithm is able to do so, and it is not affected by the input data resolution at all. Obviously, this is true as long as the frontal structures are not at a length scale smaller than or comparable to the resolution of the image.

For the Cayula algorithm, this is not the case. It was shown that the choice of the size of the window is instrumental in deciding the scales of the detected fronts. WS (the window size) is parameterised in pixels, but its physical value is in kilometres. It is very important to keep WS constant in kilometres on the ground across the image, between images and between products. If two SST products are provided with different resolutions, then the size of WS in pixels should be adapted so that WS stays constant in kilometres. This is needed in order to compare with consistency the detected fronts on the two products. However, this impacts the behaviour of the Cayula algorithm as shown in Figure 3-31. The Cayula algorithm was presented with strictly the same scene, at three different resolutions, and applied with a constant WS in kilometres. No spatial filtering was applied prior to frontal detection. The results were different depending on the input resolution, even for a noise-free scene. This is due to the cohesion test, which is less likely to succeed when presented with a small number of pixels. In the case of the scene at 0.2° resolution, the WS is 180 km and 8 pixels. The exact same scene at 0.1° resolution, with a WS of 180 km and 16 pixels is considered compact. This means that it is important to apply the Cayula algorithm on scenes of equal resolution when comparing detected fronts of different SST products. For the characterization of the Cayula algorithm described above to be valid, WS should be 32 by 32 pixels. If one wishes to apply the Cayula method on various scales, it is recommended

to resample the input data so that WS can be user-defined in kilometres and remain 32 pixels wide.

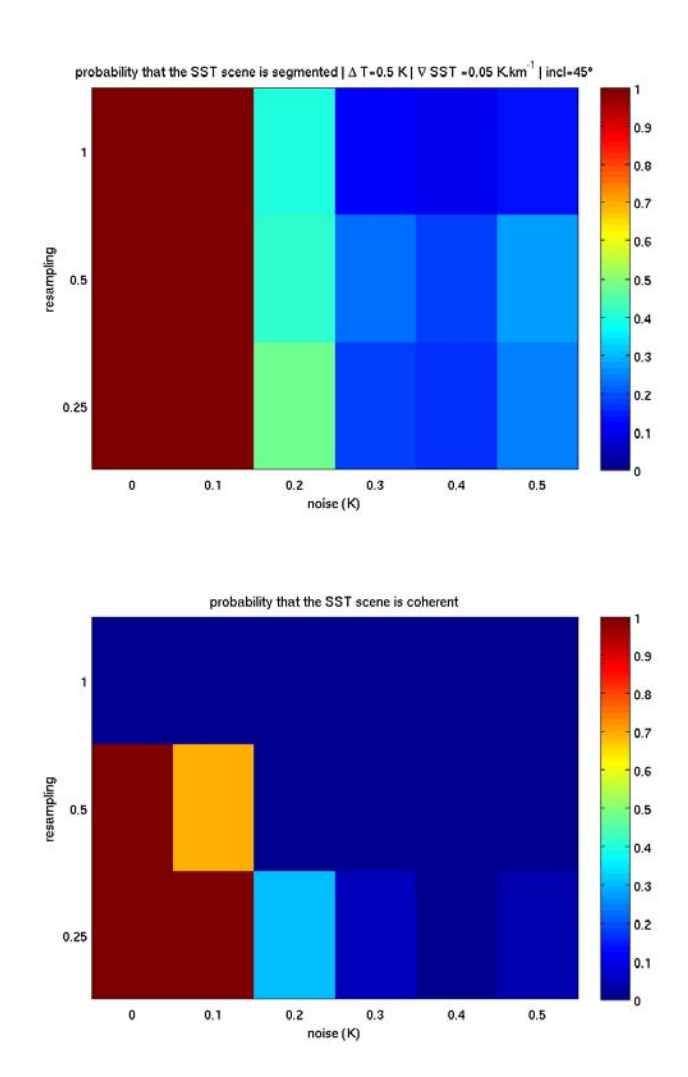


Figure 3-31: Comparison of the performances of the Cayula algorithm when dealing with the same scene, but input at different resolutions. An initial scene is produced at 0.2° resolution, and resampled to 0.1° and 0.05° by nearest neighbour interpolation. 0.2° corresponds to resampling 1, 0.1° to resampling 0.5 and 0.05° to resampling 0.25. The window size is kept constant to 180 km and is adapted in pixel number. The top panel is the probability that the SST scene is segmented and the bottom panel shows the probability that the SST scene is coherent. The studied front is defined by a temperature step of 0.5 K, a temperature gradient of 0.05 K/km and an inclination of 45° over the image.

There is one more parameter used in the Cayula algorithm, but not by Canny, the effect of which must be characterized. This is the origin of the grid that decomposes the SST scene into windows. Its origin is purely subjective but it could have an influence on the result. Usually this grid starts at the first row and first column of the SST image and is constructed from there following a step equal to the window size. Tests were run on real regional SST scenes on which fronts were detected by the Cayula algorithm but with decomposition grids slightly shifted from each other. Fronts were detected at slightly different places, but the frontal indexes (FLI and FTDI) were only modified by less than 0.5%. This is in fact natural because the window grid is composed of two overlapping grids. As a consequence, fronts are spatially well covered by overlapping windows and a window that does not see a front after the shift of the grid origin is likely to be compensated by one of the windows that are overlapping and seeing the involved region. The Cayula algorithm is hence robust to the origin of the decomposition grid.

3.5.3.7 Computational efficiency

The Canny method is much more efficient in term of computational efficiency. It was possible to implement it by making use of compiled Matlab libraries that need to be called in a specific way in order to be geophysically meaningful. The smoothing filter and gradient computation can also be optimized with Matlab built-in functions. The step that requires the most processing time is the linking of the potential frontal pixels. This step is long because it is incremental, pixel by pixel and front by front until all the pixels are linked to each other.

This step of frontal construction from potential frontal pixels is also necessary in the Cayula method. The latter algorithm is also very demanding in its previous stages. The detection of potential frontal pixels by the statistical tests at the window level is very incremental. For each window, the segmentation is tested by running a statistical test at a series of increasing temperatures. The temperature that divides the window in two populations in the clearest way is potentially retained. This processing cannot be optimized and had to be coded in Matlab with the use of many loops. The Cayula detection method is

therefore not as optimized as the Canny and demands more computation power.

3.6 Algorithm selection in relation to ocean dynamics objectives

To build frontal indexes that have a dynamical meaning, it is important to use a method that is well understood and that returns measurements that are related to ocean dynamics. It was shown that the Canny algorithm is much more accurate for detecting the right amount of fronts. It is also more consistent against noise since its behaviour is not as dependent on the noise of the input data as compared to the Cayula. However, it should also be recognised that Cayula does allow the detection of weaker fronts than Canny, which may be an important criterion for other studies.

It was also shown that the Canny algorithm is more mathematically precise. One can say that the fronts that the Canny algorithm returns are the locations where the SST gradient magnitude is higher than a user-defined threshold. In contrast, the frontal temperature difference index (FTDI) returned by the Cayula method is linked to the gradient at the front in a slightly uncertain way because it depends on the width of the front

Moreover, the first chapter shows that if surface density gradients can be estimated from satellite SST fields they may be used to parameterize dynamical processes occurring at fronts. Retrieval of density gradients implies that reliable estimates of frontal temperature gradient are required rather than simply whether or not a front is present. For this reason the precision and robustness of the Canny algorithm, as explored and discussed in this chapter, makes it the preferred frontal analysis method, provided the image noise level and the amount of unbroken coverage allows its use.

4. Chapter 4: SST datasets for front detection

The broad objective of this thesis, as discussed in chapter 1, is to explore the knowledge of ocean dynamics that can be derived from observations of sea surface temperature fields. Having considered methods for detecting fronts on satellite SST images, our attention turns now to review and assess the various SST products available today, and to analyse their capacity for resolving frontal features. The underlying objective is to develop a more informed understanding of the types of useable ocean information that can be obtained when the various frontal detection methods explored and developed in chapter 3 are applied to the different classes of observed SST datasets to be discussed in this chapter.

SST datasets have a wide span of applications which range from Numerical Weather Prediction (NWP) (Chelton & Wentz 2005) to the estimation of flux of heat, momentum and gases between the ocean and the atmosphere. SST is also an essential climate variable because its absolute time series can reveal the role of the ocean in short and long term climate variability (Reynolds et al. 2002). Different applications imply different requirements on the SST datasets. For instance, the NWPs need a mesoscale temperature field with no missing data, whereas the priority of the climate time-series inputs is the absolute accuracy and the availability of well-defined error estimates associated to each measurement. In the context of front detection, the requirement on SST inputs is not so much on absolute accuracy but on the ability to resolve gradients of all scales. The ideal SST dataset for front detection hence should be able to resolve small scale and large scale gradients. It was shown in chapter 3 that a low level of noise is also critical for the precise detection of small scale features which are often associated with a weak signal. This ideal dataset should also resolve high time frequencies by being produced on a daily basis. In order to build meaningful statistics of temperature fronts and their associated dynamics, it is important that the SST dataset offers a good spatial coverage. The temporal coverage of as many years as possible is also desirable since this allows conclusions to be drawn about climatic scales. Finally, to be consistent with the objectives of this thesis, the SST products

from which fronts are to be extracted should broadly reflect the temperature of the mixed layer rather than the atmosphere temperature and the ocean skin temperature dynamics.

4.1 Introduction to the SST products

4.1.1 Level-2 SST

In order to detect fronts over a certain region at a certain time, the best one can hope for is a clear-sky high-resolution infrared SST image. This scene is ideally acquired by a very accurate satellite infrared radiometer such as AATSR. The AATSR (Advanced Along-Track Scanning Radiometer) is the last of the ATSR class of sensors flown on near-polar orbits by ESA. ATSR, ATSR-2 and AATSR were flown respectively on ERS-1 (1991-1996), ERS-2 (1995-2008) and Envisat (2002-2012). These sensors operate in the infrared and scan conically, making two independent observations of each part of the sea surface within the narrow swath, through different atmospheric path lengths. For each pixel viewed at night, 6 independent measurements of brightness temperature are made with the double-view, and with two spectral windows within the 10.0-12.5 µm atmospheric window plus another centred on 3.7 µm. During the day, the 3.7 µm channel cannot be used so 4 independent measurements are made over each pixel. The extra channels from the dual view yield additional information about atmospheric transmission effects leading to an improved atmospheric correction procedure. This allows the ATSR sensors to be robust to the effect of water vapour and atmospheric aerosols (Robinson et al. 2012). These sensors were designed to provide SST observations to the levels of accuracy (close to 0.3 K), coverage and stability required for climate research. On top of this positive attributes, AATSR offers the finest satellite SST resolution of 1 km at nadir. AATSR's major weakness is however its narrow swath width of 512 km which limits its coverage. AATSR suffers from a minimum 3 days revisit time at the Equator, which is typically increased by the cloud contamination inherent to infrared acquisitions. ESA is developing a follow-up instrument with a somewhat wider swath called the Sea and Land Surface Temperature Radiometer (SLSTR) as part of the European Global

Monitoring for Environment and Security (GMES or Copernicus) initiative. SLSTR will fly aboard the first GMES satellite expected in 2014 (Aguirre et al. 2009) and will continue the dual view capability which has given the ATSR class of sensors their improved capacity for atmospheric correction.

The Advanced Very High Resolution Radiometer (AVHRR) is another class of SST sensors that follows a meteorological mission, with a lower absolute accuracy but a higher coverage. AVHRR is a National Oceanographic and Atmospheric Administration (NOAA) instrument. It is a six channel scanning radiometer with three channels in the visible/near infrared region and three thermal infrared channels. NOAA has maintained two polar orbiting satellites in complementary near polar orbits since 1983 (with morning and afternoon Equator crossing times) providing day and night global coverage by each satellite. The instrument swath width is approximately 2500 km and the Instantaneous Field Of View (IFOV) at nadir is 1.1 km (Donlon et al. 2012). The AVHRR instrument also flies on the MetOp series of satellites that are part of the EUMETSAT Polar System. See Goodwin et al. (2000) for a complete description of the instrument.

Infrared SST is also acquired by geostationary missions such as Meteosat Second Generation (MSG) and Geostastionary Operational Environment Satellites (GOES). The Spinning Enhanced Visible and Infrared Radiometer (SEVIRI) is the imaging radiometer that operates on the Meteosat 8 (MSG-1) located at 3.8°W. SEVIRI uses 11 and 12 µm channels for SST retrieval with an IFOV of about 3 km at nadir (Aminou 2002). Full disk images are acquired every 15 minutes. The United-States operate several GOES that monitor North-America and the Pacific Ocean. These satellites are equipped with a thermal imager that has 3 channels for SST: 3.9, 11, and 12 µm. Its spatial resolution at nadir is 4 km.

Whereas infrared SST instruments are hindered by the presence of clouds, passive satellite microwave radiometry is achievable in all weather conditions except heavy rainfall. The brightness temperature measured at 6-10 GHz depends primarily on the SST and surface roughness of the ocean. The roughness effect is largely removed from the measured signal using information in both the horizontally and vertically polarized channels providing a unique relation between the measured brightness temperature and

SST. At 6-10 GHz microwave radiation penetrates clouds with little attenuation and is insensitive to atmospheric water vapour and aerosols (Donlon et al. 2012). The Tropical Rainfall Mapping Mission (TRMM) Microwave Imager (TMI) is a NASA and JAXA joint mission. It was launched in November 1997 and is still operating today. It measures SST with the 10.7 GHz frequency, providing 25 km gridded data based on an oversampled IFOV of about 55 km. TMI is on a circular low earth orbit with a coverage between 40°S and 40°N. TMI SST retrievals are sometimes of poor quality close at the northern and southern limits of its coverage because the sensitivity of the channel 10.7 GHz to SST is lost for SST below 12 °C. TMI suffers from side-lobe contamination when islands or coastline reach into the antenna footprint and during rainfall events. Data within 100 km of land and during rainfall are removed from the measured record (Donlon et al. 2012). NASA's Earth Observing System (EOS) Agua mission was launched in May 2002 and carries the Advanced Microwave Scanning Radiometer for EOS (AMSRE) provided by JAXA. AMSRE extends passive microwave SST capability into high latitudes using a 6.9 GHz channel. Its very large swath width (1445 km) ensures a near global daily coverage at 25 km grid resolution (based on an oversampled IFOV of about 76 km). As for TMI, side-lobe contamination is a problem for AMSRE SST retrievals in coastal areas and regions less than 100 km from shore are excluded (Donlon et al. 2012). AMSR ceased to function on October 2011 due to a faulty mechanism on its rotating antenna.

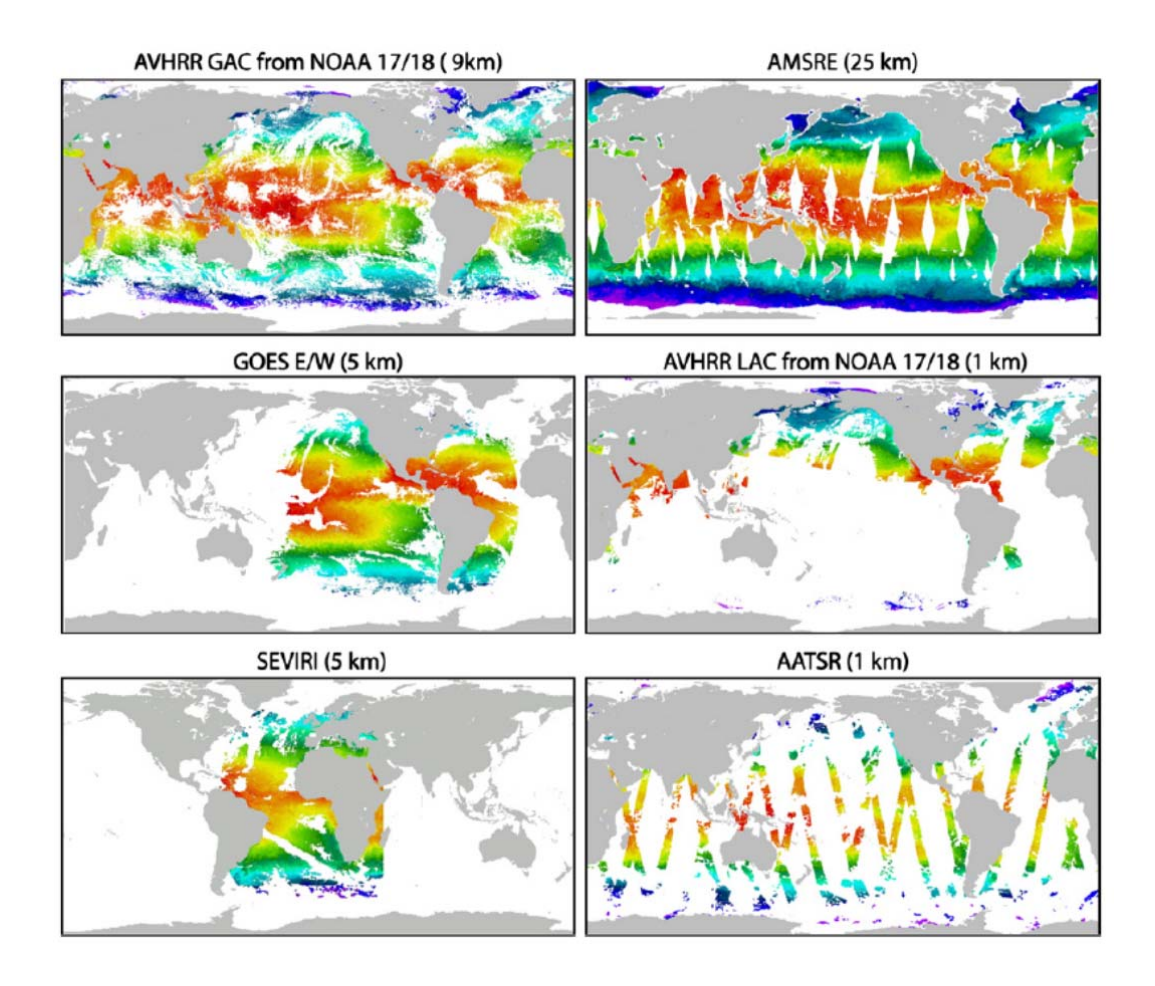


Figure 4-1: Typical example of the daily coverage of SST from six different SST data products, at different spatial resolutions, all from the same day. From Robinson et al. (2012).

Figure 4-1 presents the typical daily coverage of some of the above-mentioned satellite SST sensors. It highlights how infrared measurements are impaired by clouds. Geostationary infrared instruments can offer an increased coverage because they observe the same area every 30 minutes and the chances to see a cloud-free pixel at least once in the day are higher. On the other hand they offer a lower spatial resolution and are limited to a fixed region, visible by the satellite in its geostationary orbit. It is worth stressing that AATSR suffers from both a cloud contamination and a narrow swath and offers a very limited coverage each day.

To detect fronts on AATSR data, a solution could be to construct a level-3 AATSR product. This consists of a time-composite of AATSR data created by averaging acquisitions made on several consecutive days or weeks. The

rational is to increase the spatial coverage by reducing the temporal resolution. Missing cloudy data and the long revisit time of AATSR can be balanced by the averaging over a longer time period, for instance 10 days or a month. While this strategy improves the spatial coverage, it compromises the accuracy and spatial coherence of the scene. Indeed, the association of non-synoptic patches in a mosaic of SST scenes from different days representing a dynamic region in different states leads to spatially inconsistent SST images. If the SST samples are averaged rather than mosaicked the risk is to oversample a dynamic region which results in fuzziness and smoothing of the fine features. This is due to the fact that high frequencies in space and time are linked, so a low-pass filter in time results in a low-pass filter in space as well. The trade-off between the coverage and the accuracy is a difficult one in this case because some regions in the Tropics and at mid-latitudes suffer from a seasonal cloud coverage, and very few infrared measurements are available during the cloud season.

Figure 4-2 shows the averaged percentage of coverage one can hope for with 3-day Level-3 composites of AMSRE and AVHRR. AMSRE composite covers nearly the whole oceans, to the exception of the regions close to shore and tropical regions that suffer from persistent rainfalls. The figure also shows that a 3-day composite is far from being sufficient to achieve a global AVHRR coverage, because of persistent cloud coverage in the Tropics and at midlatitudes. Reynolds et al. (2007) partitioned the oceans in 1/4° grid boxes and measured the proportion of the boxes with at least one acquisition of AMSRE and AVHRR independently. They show that the average day and night operational AVHRR coverage is 8%, while it is 40% and 46% for AMSRE day and night measurements respectively. If day and night are combined, the operational AVHRR and AMSRE coverage increases to 16% and 86% respectively.

The inability of infrared satellite measurements to penetrate clouds severely limits their temporal and spatial continuity and the study of important mesoscale dynamics. On top of this, cloudy regions are often associated with strong ocean frontal boundaries and substantially enhanced cloud presence probabilities are found on the downwind side of Gulf Stream warm core rings (Park et al. 2006). Enhanced convection and clouds are often found at

mesoscale frontal boundaries which limit infrared sensors' ability to sample fronts. Clouds may also be overestimated and falsely detected above SST fronts because some cloud filters are based on a threshold for SST gradient. Figure 4-3 illustrates this issue, while AATSR is able to resolve very fine scale temperature features, some fronts are hidden by thin clouds possibly due to erroneous cloud flagging. In contrast, Figure 4-4 shows the microwave acquisition over the same day and same region by AMSR-E. It is striking how much information is lost when sampling the SST at 0.25° resolution. In addition, one can also notice that a lot of information is lost within 100 km of the coast.

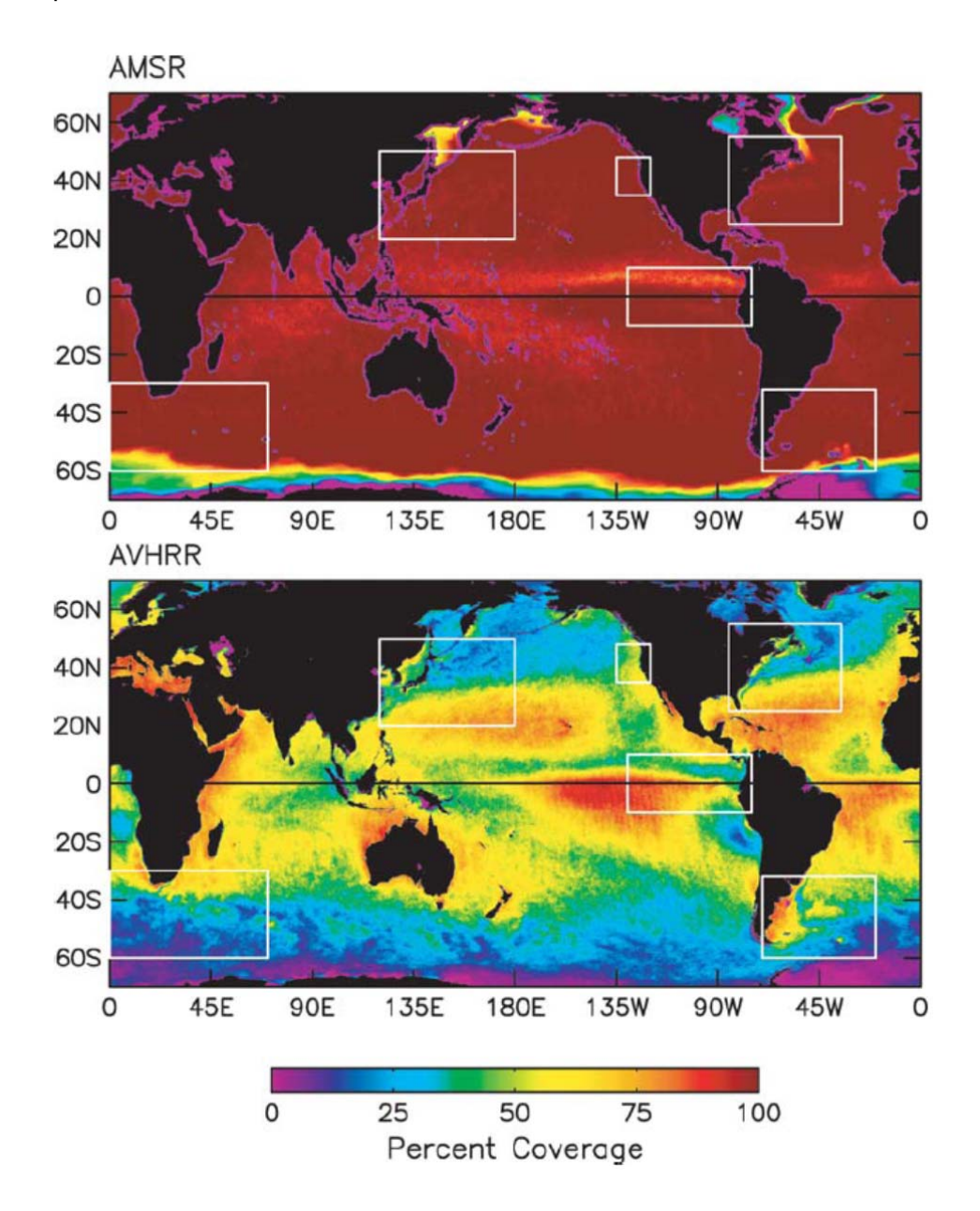


Figure 4-2: Percent coverage of SST measurements from (top) the AMSRE and (bottom) the AVHRR in 3-day composite average maps during the 12-month period Oct 2002 through Sep 2003. From Chelton and Wentz (2005).

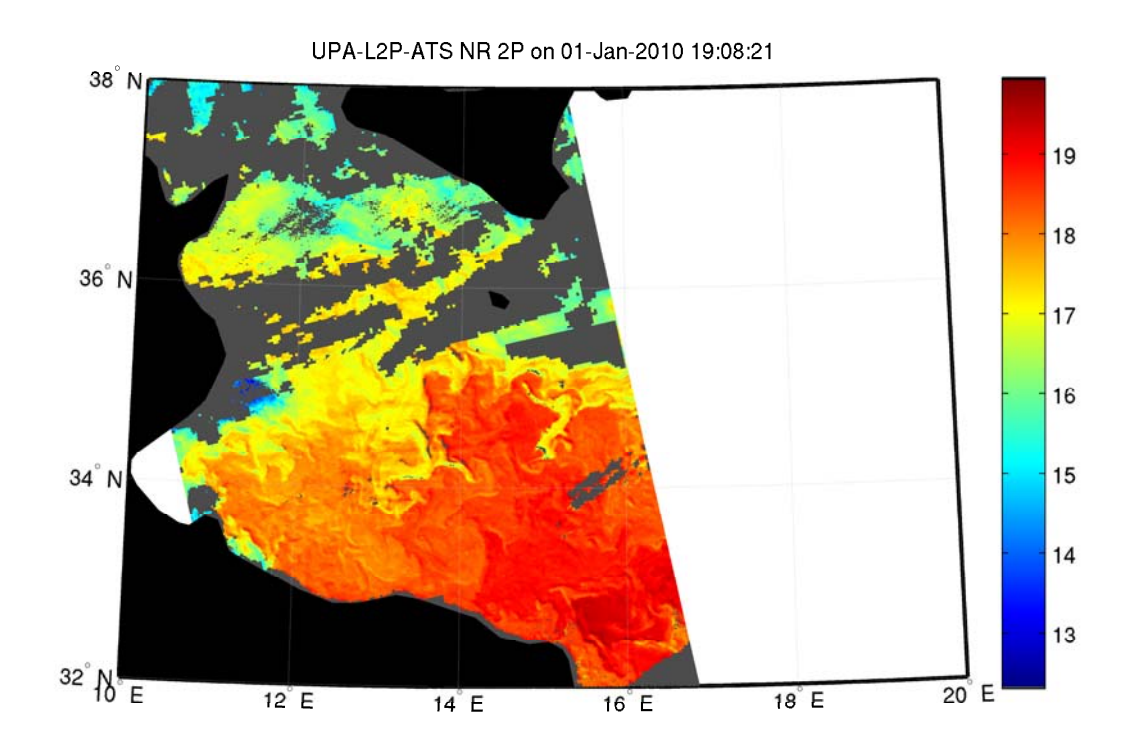


Figure 4-3: Example of an AATSR swath SST plotted at full resolution (1 km) off the coast of Lybia on 01 January 2010.

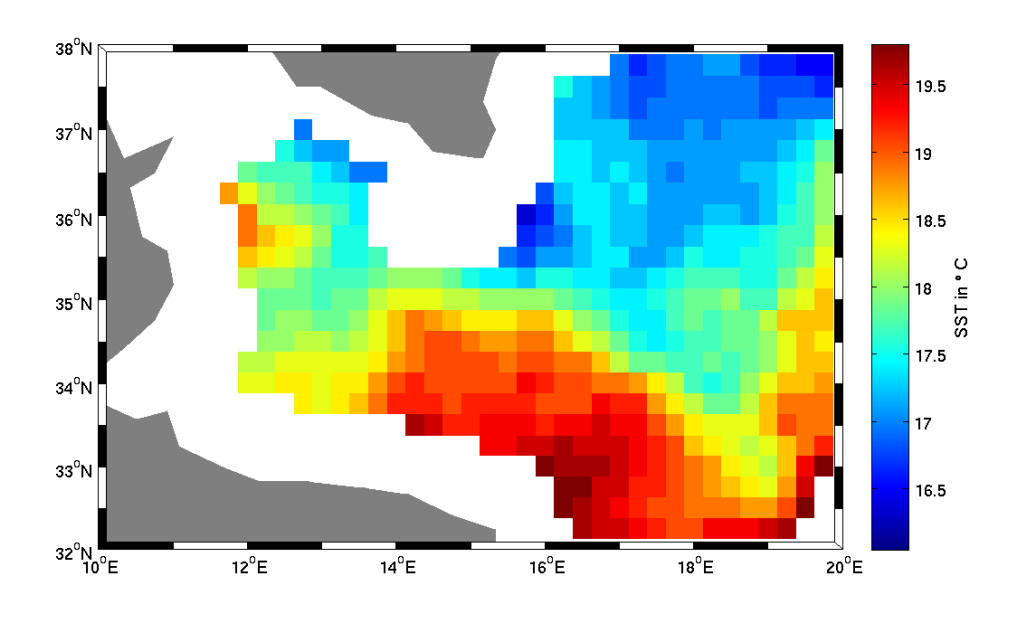


Figure 4-4: AMSR-E SST plotted at 0.25° resolution off the coast of Lybia on 01 January 2010.

4.1.2 Level-4 SST

In 2000 the Global Ocean Data Assimilation Experiment (GODAE) recognized that no SST measurements available at that time could meet the stringent accuracy, timeliness and spatial-temporal coverage criteria required for operational ocean prediction (Smith & Koblinsky 2001). The GODAE High-Resolution SST Pilot Project (GHRSST-PP) was initiated to address this need and has been superseded by the Group for High Resolution SST (Donlon et al. 2007). GHRSST achievements are the development and coordination of a highly successful framework in which satellite SST measurements are exchanged in a common format with uncertainty estimates and supporting ancillary fields used to control the quality of the data (Donlon et al. 2002). GHRSST now presents the user community with an unprecedented choice of SST products from a wide variety of complementary sensors. GHRSST products are delivered in an operational near-real time (NRT) context, in a common format for all data sets, which greatly facilitates their exploitation by the users (Donlon et al. 2012). For instance, all the Level-2 SST products mentioned in the previous section are distributed on FTP servers. Any user is now able to download the archive or the NRT SST products from the wide range of international agencies producing them, in L2P format. This common format consists in NetCDF files with the same fields for each product.

On top of this, GHRSST coordinated the development, creation and dissemination of Level-4 SST products, also called SST analysis products. These are multi-sensor gap-free SST products that result from the combination of measurements from a variety of instruments and some level of interpolation in space and time to fill in the gaps. SST analyses are designed to produce the best estimates of SST for a given time and location, over a regular grid based on irregularly gridded sparse measurement data sets. GHRSST SST analyses are derived from statistical methods rather than the assimilation of SST measurements into a numerical ocean model. The analysis products are based on Optimum Interpolation (OI) techniques, which were initially developed for meteorology in the 1960s. The OI was introduced in the SST context by Reynolds and Smith (1994) who produced analysis products based on AVHRR and in-situ data from ships and buoys. The analyses are performed weekly on a 1° spatial grid from November 1981 to present by OI with a separate step to

correct any large-scale satellite biases relative to the in-situ data. At the time this technique was developed, only AVHRR was available, thus the spatial scales of the OI were designed conservatively. However, since the late 1990s, more satellite SST datasets have become available and this has allowed the development of analysis products with improved spatial and temporal scales.

GHRSST Level-4 SST products exploit the complementary nature of the different Level-2 SST datasets, and combine them in a way that offsets the strengths and weaknesses of each system against the others to produce a more complete, frequent and accurate SST analysis. The strategy is to take advantage of both the spatial and radiometric accuracy of infrared radiometers and the spatial and temporal coverage of the microwave sensors in the same product. The OI is fed by a selection of SST data from near-polar or geostationary satellites together with in-situ measurements. It is designed to calculate the best estimate of SST over regions that are sampled by several instruments, based on quality information associated to each measurement or on a pre-defined priority order of the input data sets. In this way, where high spatial resolution high accuracy infrared measurements in cloud-free conditions are available, the output Level-4 SST can reflect the observed infrared fine features. Where the cloud cover dominates, the available microwave measurements at a coarser resolution govern the output of the SST analysis. Regions where no satellite measurement is available for the given day are filled by spatial interpolation if measurements are present close enough or by temporal interpolation if data are available from not too long ago during the previous days at the same location. In the case that no observation has been available for some time, the analysis decays back to a climatological mean reference field after a certain period defined by the analysis design.

GHRSST Level-4 SST products are being produced by a variety of organizations in multiple ways. The details of the design of each analysis vary as a function of their objectives. Analyses designed for the exploration of SST anomaly on climatic scales require as input excellent absolute accuracy satellite SST data sets, most probably from well calibrated and bias-corrected infrared radiometers. Conversely, analyses used as boundary layer in NWP require the best coverage achievable, hence need as input as many Level-2 SST products as possible. In the first example, little or no interpolation is acceptable, as climate analysis is based on measured samples only. In the second example, a

gap-free image is needed every day, for the NWP model to function. In this case it is better to interpolate in space and time, or even to relax gradually to a climatology.

The design of an analysis involves a series of choices that are driven by the priorities assigned to it. The first choice is whether the analysis is covering the whole globe or just a region of interest. Another important choice is which SST data should be used in the analysis procedure and this decision constrains the achievable temporal coverage of the analysis data set. Then choices have to be made on the spatial grid spacing and the update frequency. The GHRSST Level-4 SST analyses are produced daily, at a resolution of 1/20° or coarser (6 km at the Equator) for the global products and 1 km for the regional ones. The bias correction scheme varies among the various products, and so do other analysis parameters such as the temporal and spatial error correlation scales. The speed at which an analysis should relax to a climatology when no data are available is also an important decision. Reynolds and Chelton (2010) show that these and other choices that must be considered in the design of an analysis procedure may lead to very different results.

The main motivation behind the development of analysis products is the improved coverage achieved by combining several SST Level-2 data sets. Many analyses use as many input files as possible to obtain the most accurate product at a given time (Kawai et al. 2006). However, this choice complicates the analysis procedure as the integrated SST system is very dynamic. Each system is prone to errors that vary across time and space. Infrared satellite data suffer from poor cloud clearing which is the biggest source of error in most infrared satellite SST retrievals, poor pre-launch characterization, sensor degradation and failure of SST retrieval algorithms under anomalous atmospheric conditions, aerosol contamination following a major volcanic eruption, or seasonal aerosol events such as the Saharan aerosol plumes. In the case of microwave sensors, errors are caused by poor rain flagging, ambiguity in surface emissivity due to incomplete knowledge of the surface wind vector, radio frequency interferences and side lobe contamination. On top of these error sources, all satellite measurements are subject to unforeseen problems related to instrument anomalies, spacecraft manoeuvres and spacecraft operations. In-situ SST data are affected by measurement sensor drift over time, poor pre-deployment characterization and calibration, physical

damage at sea and biological obstruction by birds and algae. Ship observations are subject to sensor warming due to poor sensor installation and lack of metadata describing the depth of observation (Donlon et al. 2012). As a consequence, all measurements suffer from random errors and systematic biases.

The OI is able to cope with the random errors in an efficient way. Indeed, a common technique is to weight the inputs with the known errors that characterize them, so that the measurements in which one has more confidence in are more influential in the estimation of the SST. Also, the errors from the various sources are often independent, so the weighted mean achieves a lower error than the input errors. However, the OI is unable to deal with the global and regional systematic biases of the input data. The blending of several SST datasets with non-uniform and different systematic bias can lead to spatial patchiness at the frontier of the input products on the analysis SST. This spatial patchiness is illustrated in Figure 4-5 which shows the consequence of the discrepancies in the SST biases in the resulting analysis output. It is important to point out that this spatial patchiness is an artefact that has severe consequences on the analysis SST gradient. Even small jumps in SST can create unwanted strong gradients because they occur over short distances. This effect would significantly depreciate the ability of Level-4 SST products to resolve fronts accurately if it is not corrected. Fortunately, the GHRSST analysis procedures include bias adjustment schemes. Before being fed to the OI, the input Level-2 SST images are automatically adjusted for systematic errors. This is done by comparing each of them to a common reference dataset, which can be in-situ measurements or a Level-2 product. AATSR is useful for this task because it is designed to minimize bias and sensitivity to atmospheric aerosols (Merchant & Harris 1999, Merchant et al. 1999). The reader is invited to refer to Leborgne et al. (2012) for a discussion on the optimization of the multi-sensor bias correction.

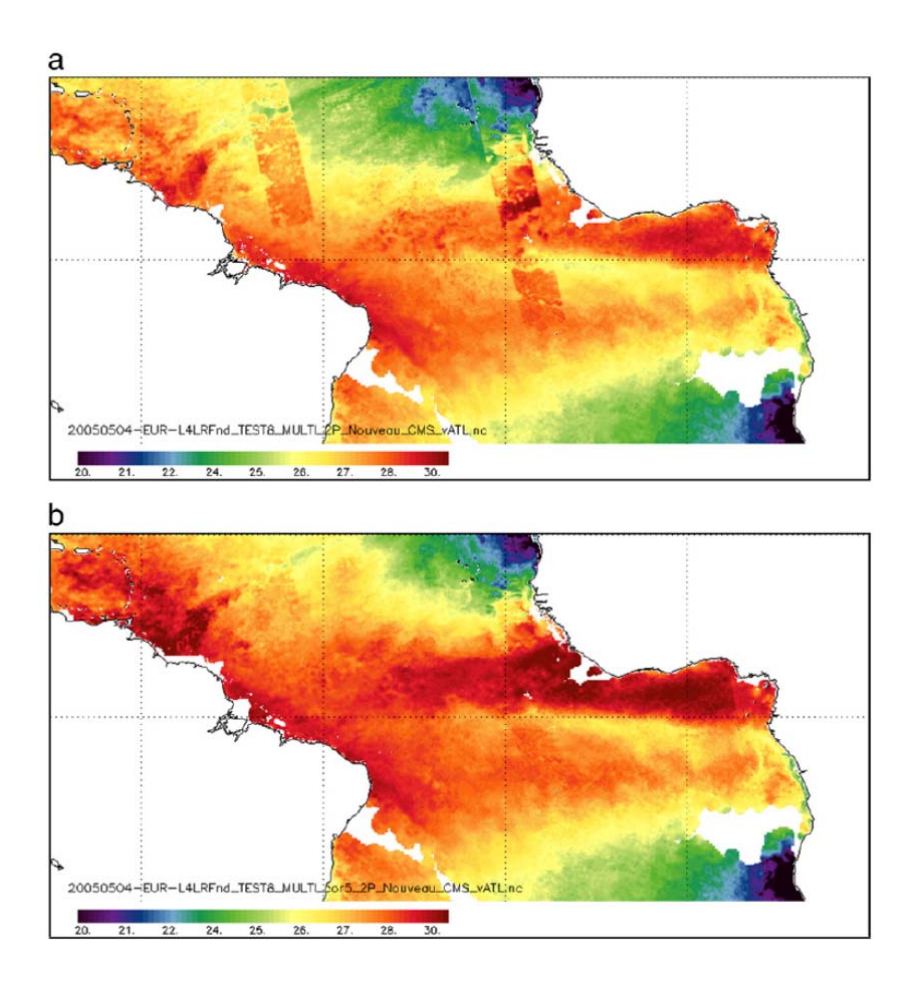


Figure 4-5: Results of collating SST data (scale units are °C) with the ODYSSEA analysis, (a) when no bias correction is applied (upper panel) and (b) when bias correction to AATSR as a reference standard is applied over a 5-day window (lower panel). From Robinson et al. (2012).

Merging several SST Level-2 data sets in the same product is challenging because the satellite sensors do not all measure the same parameters. Sea Surface Temperature is a general concept, and its definition depends on what one actually means by "Surface". The top few meters of the ocean surface do not have a vertically uniform temperature. In low wind conditions solar radiation tends to heat the top few meters of the sea during the day, but this stratification disappears at night as the surface loses heat, promoting gravitationally driven vertical mixing. This phenomenon is called diurnal warming. There is also a thin surface layer of water a few tens of microns thick that is cooler than the water beneath (Robinson & Donlon 2003). GHRSST

introduced definitions for the different measurements achieved by the SST sensors:

- The skin SST: the temperature in the upper 10 μm of the surface water as measured by the infrared radiometers.
- The sub-skin SST: the average temperature across a depth of a few mm as measured by microwave radiometers.
- The foundation SST: the temperature at the base of the diurnal thermocline, free of diurnal variability, if present (Donlon et al. 2007).

At dawn, if the diurnal thermocline from the previous day has collapsed during the night, the foundation SST is the same as the sub-skin SST. The GHRSST Level-4 analysis SST product approach is to deliver the estimation of the foundation SST. The Level-2 input SST images need to be "converted" to foundation SST before their ingestion in the OI. Since models of diurnal variability are still uncertain (Merchant et al. 2008), ancillary data are used to flag and then reject SST data with a high probability of being affected by the diurnal thermocline. In effect, this concerns daytime low wind situations. Additionally, a simple correction of the cool skin effect is applied on infrared data, this is done by adding 0.17 K to the SST measurements with a wind speed above 6 m/s (Donlon et al. 2002). This approach is well suited to the exploration of dynamics at fronts since the foundation SST broadly corresponds to the temperature of the ocean's upper mixed layer (Robinson et al. 2012). It is important to base the physical analysis on the temperature of the mixed layer because it is closely linked to the dynamics we are interested in. Diurnal variations in the top few millimetres are mostly controlled by solar heating and changes in the wind stress, and have little impact in the vertical circulation events. In the context of this thesis, diurnal variability of the surface temperature is an artefact that should be avoided.

Another attribute of the GHRSST products that makes them very useful for frontal detection is the fact that each analysis value should be accompanied by an uncertainty estimate. The uncertainty estimate is calculated with different techniques in the different products. These techniques are complex and allow the uncertainty estimate to reflect both the uncertainties in the input Level-2 data and the amount of interpolation involved at each grid point. Grid points

Chapter 4

where reliable data were averaged and little interpolation was necessary to obtain a value are given low uncertainty estimates. Users of a Level-4 product are free to decide which quality threshold is needed for their study, and this results from a trade-off between the coverage and the confidence in the data.

Table 4-1 summarizes the Level-4 and Level-3 products mentioned in this thesis. Additional multi-sensor SST products are listed on http://www.nodc.noaa.gov/SatelliteData/ghrsst/accessdata.html and https://www.ghrsst.org/data/data-descriptions/

The attributes of different L4 SST products, and particularly how these may impact on the detection of fronts, are discussed individually in the following subsections.

Product	Instruments	Data Source Agency	Spatial res.	Temporal res.	Coverage	Time Series	Parameter			
Level 4										
OSTIA	AVHRR, AMSRE, TMI, AATSR, SEVIRI, in situ	UK Met Office	6 km	daily	global	April 2006 - present	SST foundation			
OSTIA reanalysis	AVHRR, ATSR, AATSR	UK Met Office	6 km	daily	global	1985 - 2007	SST foundation			
ODYSSEA	AVHRR, AMSRE, TMI, AATSR, SEVIRI, GOES	CNES / Ifremer	12 km	daily	global	October 2007 – December 2009	SST foundation			
REMSS_MW	AMSRE, TMI, WindSAT	Remote Sensing Systems	25 km	daily	global	June 2002 - present	daily minimum SST			
REMSS_MW_IR	TMI, AMSR-E, WindSAT, MODIS	Remote Sensing Systems	9 km	daily	global	2006 - present	daily minimum SST			
AVHRR- only	AVHRR	NCDC	25 km	daily	global	1981 – present	SST			
AMSR+ AVHRR	AMSR, AVHRR	NCDC	25 km	daily	global	June 2002 - present	SST			
Level 3										
ODYSSEA	AVHRR, AMSRE, TMI, AATSR, SEVIRI, GOES	CNES / Ifremer	12 km	daily	global	October 2007 – December 2009	SST foundation			

Table 4-1: summary of the GHRSST Level-4 and Level-3 products mentioned in this thesis.

4.1.2.1 The Operational Sea Surface Temperature and Sea Ice Analysis (OSTIA)

OSTIA is a GHRSST Level-4 analysis produced by the Met Office as part of the GMES MyOcean project. It is produced operationally, daily, on a global 1/20° grid, using in-situ, AVHRR, AMSR, TMI, AATSR and SEVIRI data. The analysis is run with data from a 36-h period, using two error correlation scales, 10 km and 100 km, which vary depending on the region. All satellite data are adjusted for bias errors in comparison with a "background SST estimate" based on a combination of AATSR data and in-situ measurements from drifting buoys. Data are filtered, based on surface wind speed data, to remove diurnal

variability and AATSR data are adjusted to represent the SST at the same depth as drifting buoy measurements (0.2 to 1 m). OSTIA is designed for ocean prediction and NWP, it is used operationally as a boundary condition for all weather forecast models at the Met Office and European Centre for Mediumrange Weather Forecasting (ECMWF). OSTIA was shown to have a zero bias and an accuracy of ~0.57 K when compared to in-situ measurements. It positively impacts the accuracy of the Met Office NWP model (Donlon et al. 2012). In addition, an OSTIA re-analysis was produced by the Met-Office that uses the same procedure as operational OSTIA. It is based on Pathfinder from 1981 and reprocessed (A)ATSR data from 1991, bias corrected and quality controlled insitu data. The OSTIA reanalysis is based on fewer input products than operational OSTIA but offers a long and consistent long time series of more than 20 years that allows the exploration of seasonal and decadal variability. This dataset provides the input for the study of climatological variability of fronts presented in chapter 6.

4.1.2.2 The Ocean Data Analysis System for MERSEA (ODYSSEA) analysis

ODYSSEA is another real-time global analysis developed within the Marine Environment and Security for the European Area (MERSEA) project within IFREMER (Autret & Piollé 2007). It merges AVHRR, AMSR, TMI, AATSR, GOES and SEVIRI data into a daily 1/10° grid. All the Level-2 data sets are intercalibrated by the correction of the large-scale daily bias between themselves and the AATSR dataset used as reference. The analysis procedure of ODYSSEA is different from that of OSTIA. One important difference is the creation of the intermediate multi-sensor composite product. Each day, a global multi-sensor gridded product is computed by mosaicking data from inter-calibrated singlesensor composite products. Each pixel of the multi-sensor product is filled with the best SST measurement available on its location in a 3 days window centred on the estimation time of the analysis. The best observation is selected depending on the acquisition time (data closer to the centre time are given higher priority), the SST retrieval conditions such as SST range, wind, aerosols, sea ice, cloud proximity. The choice of the best measurement is also based on a classification of the respective sensor errors under each class of these criteria. Typically, a clear-sky night-time AATSR measurement obtained

during the right day will always be selected. Microwave data are used to fill in the gaps where persistent cloud coverage has prevented infrared measurements or where the infrared measurements are suspected to be contaminated by atmospheric artefacts. The multi-sensor composite product is produced at the same resolution as the analysis Level-4 output, i.e. 1/10°. It suffers from gaps but is only filled with real observations. It is named a Level-3 SST product and constitutes both an intermediate product for the ODYSSEA Level-4 analysis and an output product of the ODYSSEA processing chain. The last step of the ODYSSEA analysis processing chain is the estimation of the Level-4 SST output by OI, from the Level-3 SST and previous days of Level-4 SST. The covariance of the field is specified by a structure function modelled by the sum of two Gaussian functions each associated with specific time and space scales. The spatial length scales are isotropic and taken to 80 km and the Rossby radius (bounded by 20 km and 80 km) for the two functions respectively. The time length scales are set to 2 days and 1 day respectively, with a relaxation on the Pathfinder Version 5 climatology when no data are available at all. The ODYSSEA returns the foundation SST. It also runs regionally on a 1 km resolution for the Mediterranean Sea, the North West European Seas, the Galapagos region, Brazil, South-Africa and Australia. The regional ODYSSEA data sets are produced and distributed by Ifremer in the frame of the ESA Medspiration project.

4.1.2.3 The Remote Sensing Systems (RSS or REMSS) Microwave analysis

The REMSS MW analysis is computed daily on a 25 km grid using AMSR and TMI data. Before the ingestion of the data in the OI, the TMI's emissive Antenna correction is applied. The diurnal warming is also estimated and removed. All observations are adjusted to remove any diurnal signal based on the local time of day and wind speed. Using a diurnal model, all microwave SSTs are 'normalized' to a daily minimum SST, defined to occur at approximately 8 AM, local time (Gentemann et al. 2003). The measurement bias is corrected using in-situ data, and the errors associated to the single-sensor acquisitions are characterized. Then the SST samples are blended together using the OI scheme described in Reynolds and Smith (1994). A first-guess field, the previous day's OI SST, is employed to calculate data increments, which are all nearby data

minus the first-guess field. The new SST estimate is formed by a weighted sum of increments, with the weights calculated by the OI method, added to the first guess data. Correlation scales of 4 days and 100 km are used in determining the weights used in the REMSS methodology. Details on this analysis can be found at http://www.remss.com/sst/microwave oi sst data description.html. The particularity of the SST analysis is to be based on microwave measurements only; hence it is extremely useful for comparison when discussing the contribution of infrared sensors in global Level-4 SST products.

4.1.2.4 The NOAA's National Climatic Data Center (NCDC) AVHRR-only and AMSR+AVHRR analyses

NCDC is producing two daily analyses on a ¼° grid following the same procedure, as described by Reynolds et al. (2007). AVHRR-only uses in-situ and AVHRR data, while AMSR+AVHRR adds AMSR data. Large-scale bias is corrected using in-situ data from ships and buoys, separately during day-time and night-time. Then the in-situ and corrected satellite data are fed into an OI procedure, which uses error correlation scales that range from 50 to 200 km with smaller scales at higher latitudes, especially in western boundary current regions, and larger scales in the tropics. This analysis applies some temporal smoothing by using 3 consecutive days of data, with the middle day weighted higher than the other two days. Further smoothing is also caused by the temporal smoothing of the bias corrections. Additionally, the ship SSTs are corrected relative to buoy SSTs by subtracting 0.14°C from all ship observations before they are used to bias correct the satellite data. Thus, all observations are bias corrected with respect to buoy SSTs and there is no attempt made to adjust to foundation temperature (Reynolds & Chelton 2010).

4.1.3 Level-3 SST

As mentioned in the previous section, IFREMER produces the ODYSSEA Level-3 multi-sensor SST product daily on a 1/10° grid. This product shares some advantages with the Level-4 analysis products such as the spatial and temporal coverage, the bias correction, the adjustment to foundation SST and quality

estimates associated to each pixel. The high spatial and temporal coverage is achieved by the blending of AVHRR, AMSR, TMI, AATSR, GOES and SEVIRI data into a daily 1/10° grid. However the blending procedure is different from those involved in the production of Level-4 analysis products. In the case of Level-3, each output pixel comes from a real measurement of a unique instrument selected for its quality and proximity to the selected date. Because the Level-3 grid resolution is 1/10°, the several infrared independent samples of the chosen instrument that are made within a Level-3 pixel are averaged. Infrared Level-2 products are in effect down-sampled to construct Level-3 products. Level-3 products are produced by mosaicking Level-2 measurements of various sensors depending on their quality and availability at different places and times. Absolutely no interpolation is involved in the Level-3 products, each pixel's value coming from an actual SST measurement of one of the systems. In addition, there is no relaxation to a climatology in the case that no information is available for some time over a region. As a consequence, Level-3 products are not gap-free and do not cover the whole oceans, even though the high number of observing systems used in these products ensures a near-total coverage, especially because they are selected from a 3-days window. Another difference compared with Level-4 products is that Level-3 products provide the source SST instrument for each grid pixel and the time the acquisition was made as auxiliary data (Autret & Piollé 2007). Figure 4-6 presents a day of global Level-3 ODYSSEA SST, the time of the acquisition and the satellite source for each pixel.

Chapter 4

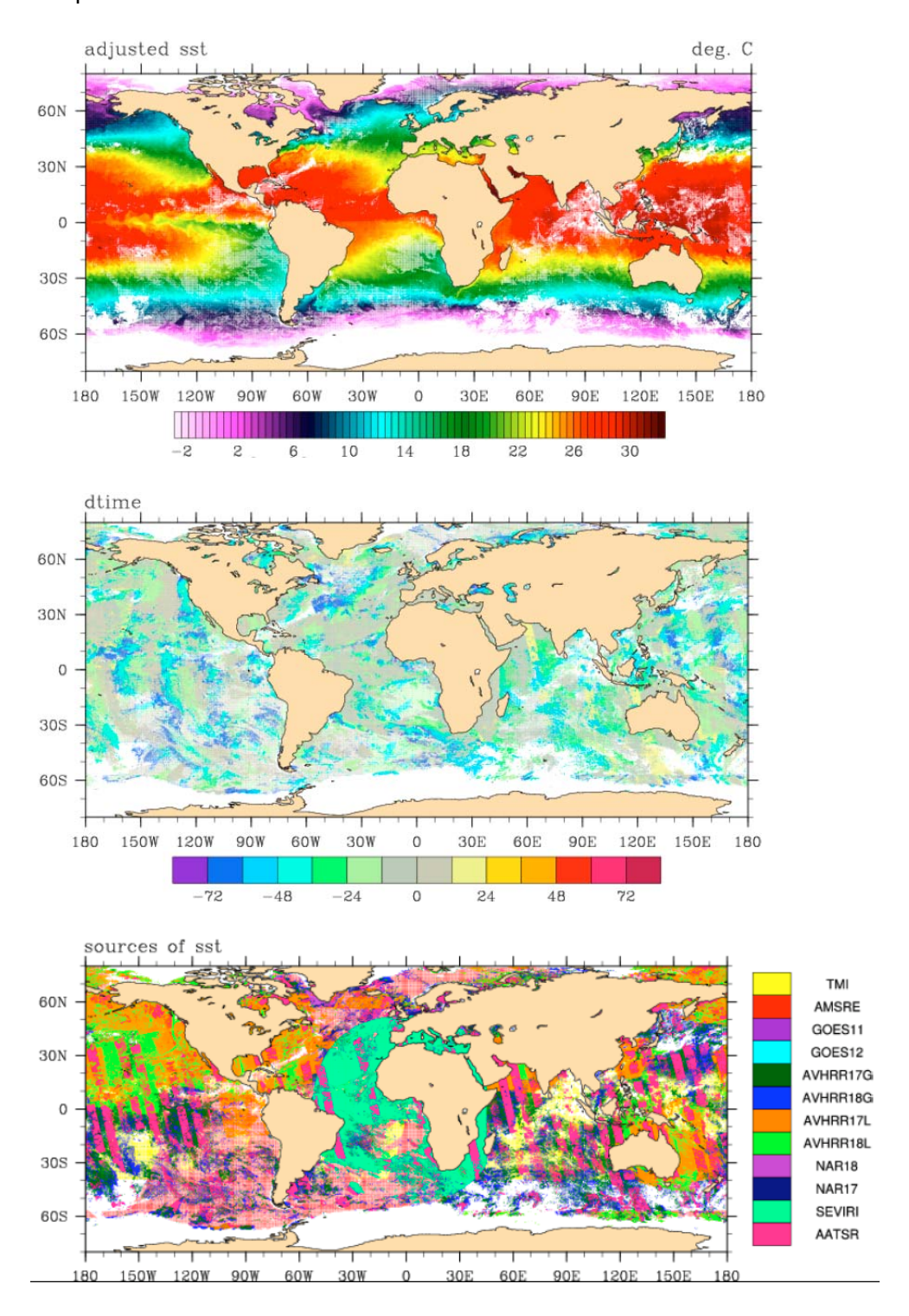


Figure 4-6: Example of Level-3 multi-sensor ODYSSEA product for 15/10/2007. Top: foundation SST. Middle: time difference. Bottom: sources of SST. From Autret and Piollé (2007)

4.2 Limitations of the Level-4 SST for front detection

4.2.1 General considerations

Level-4 analysis products are an important breakthrough in the field of SST because they pave the way to smarter and complementary uses of independent single-sensor Level-2 data sets. Many SST applications were previously limited by the restricted and intermittent coverage of individual SST sensors, or by the low resolution and accuracy of microwave ones. These limitations are tackled by the GHRRST Level-4 analyses. Hence the scientific potential of individual products is widened by their merging provided it is done properly. A lot of efforts were put by the GHRSST international science team in order to overcome challenges inherent to the combination of independent and irregular SST measurements in a way that minimizes the errors of the resulting SST field (Le Borgne et al. 2012, Robinson et al. 2012). Errors of the analysis field originate both from the errors of the input Level-2 data sets and the errors introduced by the analysis procedure. The estimation of SST from several single-sensor datasets is a very complex problem, and the GHRSST analyses are imperfect solutions to it. The procedures are statistical methods but they have to rely on a set of assumptions in order to deal with excesses and lacks of input data. The excess of data is dealt with by averaging or selection of data, the lack of data is tackled by interpolation in space and time that relies on assumptions of oceanic spatial and temporal variability. The OI is a complex statistical algorithm that requires a certain number of steps to converge and find a solution fitting best the possibly contradictive inputs it is fed with. It is also a very computationally demanding step of the processing chain, and the number of iterations allowed is generally bounded to limit the processing time. In some cases this results in a non-converged solution which can be far from the true SST. This is illustrated by Figure 4-7 which shows a very rare occurrence of an obvious artefact introduced by a probable faulty cloud detection in an infrared input of the ODYSSEA chain. This section explores some issues of the Level-4 analyses that limit their ability to reveal frontal variability.

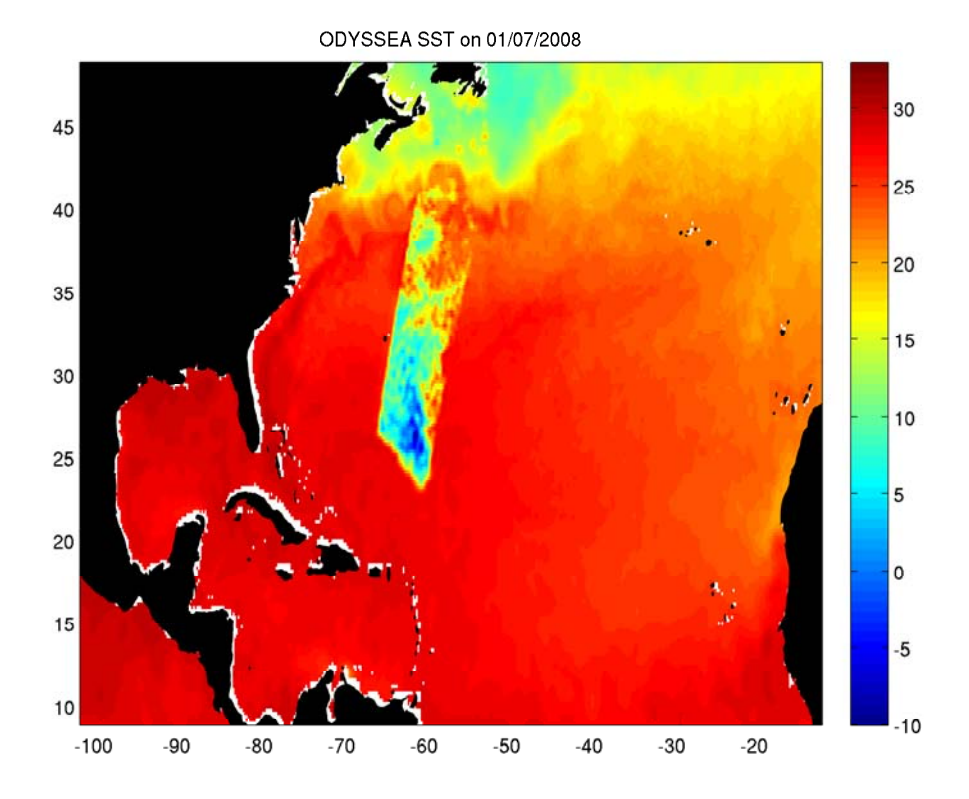


Figure 4-7: Example of an error in the ODYSSEA output. Note that this error is a rare occurrence and has been properly tackled by IFREMER.

4.2.2 Level-4 analyses are spatially smoothed

When searching for fronts in the data, the main drawback of Level-4 SST products is that they do not resolve very small scales. Even when a scene is spatially resolved by high resolution infrared sensors, the corresponding Level-4 analysis are much smoother than the Level-2 input images. All the OI schemes introduce a level of spatial smoothing which is governed by the specification of the background error covariances and the correlation length scales chosen in the analysis design (Donlon et al. 2012). The level of smoothing varies amongst the various Level-4 SST analyses. It is necessary to reduce the noise of the output SST image. As was explained in chapter 3, spatial smoothing reduces spatial noise in the data at the expense of actual small scale features. The level of smoothing and the resulting minimum resolved feature resolution that characterize an analysis product depend on the aims of each analysis and the signal-to-noise ratios (SNR) of the input data.

An analysis that applies little smoothing benefits from high resolution features and an increased signal at small-scales, it suffers however from a greater susceptibility to noise. The analysis procedures apply spatial smoothing to remove residual error of the bias correction and ensure a smooth transition between the pixels originating from different data sets. Also the OI is fed with SST acquisitions at different times in a day, even though there is a correction of the diurnal variability achieved through the foundation SST, there is a residual error to it plus there are other effects than solar warming that can change the SST at frequencies higher than once per day. These effects include the tidal advection of strong horizontal temperature gradients. The spatial smoothing is also intended to minimize these high temporal frequency variations of SST because they can make non-synoptic measurement spatially inconsistent. It is important to distinguish between the grid spacing and the feature resolution of an SST analysis. The grid spacing defines the smallest possible features that could be resolved in the analysis. It will be shown that OSTIA's feature resolution is coarser than the one of OSYSSEA, even though OSTIA's grid spacing is twice as fine.

The OI also introduces smoothing as it interpolates over patches of missing data. Spatial interpolation is a very simple way to fill a gap in the data while making little assumption on the estimated field. When a gap in the available input data is filled by interpolation, a smooth transition is created between available measurements. This gives a false impression of a region with little energy at small scales, whereas small-scale variability may have been present in reality. If one applies a front detection algorithm on a Level-4 SST image where some spatial interpolation was necessary, no front may be detected over the interpolated patches when a front may have been present. This effect would tend to underestimate the presence of fronts if not appropriately dealt with. Interpolation in time also smoothes the data because high frequencies in time and space are often linked. Hence the averaging of samples from different dates over a highly varying scene ends up in a scene on which high spatial frequencies have been reduced. Following the same principle, SST climatologies, which are produced by averaging a very large number of observations, are very flat. Therefore, when the OI decays back to a climatology, small scales are absent from the result and the occurrence of fronts is underestimated.

Figure 4-8 shows a regional example SST gradient magnitude of 4 different products: OSTIA, ODYSSEA, ODYSSEA L3 and REMSS MW. Because gradients are computed from spatial differences, they are useful in showing how well analyses can resolve strong coherent features such as the Agulhas Retroflexion Currents. Figure 4-8 shows that the SST gradient magnitude is the highest in the Level-3 image because no smoothing was applied to it. Note that the Level-3 pixels that are associated with microwave measurements are filled at the original resolution of 25 km (see Figure 4-9) with many pixels in between being left with missing data. The gradient cannot be calculated over missing samples therefore the missing regions of Figure 4-9 are expanded in Figure 4-8 over their neighbouring pixels. This phenomenon also occurs near land and its intensity increases with the size of the smoothing filter. As explained in chapter 3, whenever a pixel is missing, all the pixels that require the missing pixel's value in order to be smoothed are turned into missing values in the smoothed scene. The Level-3 image shows the finest details but suffers from the cloud coverage, microwave values being discarded by the gradient computation. It is notable also that ODYSSEA seems to resolve finer features than OSTIA. There also seems to be more energy at small and mesoscales in the ODYSSEA because the gradient magnitude is larger than OSTIA's. Both OSTIA and ODYSSEA resolve finer scale than REMSS MW which is based on microwave data only. REMSS MW is also unable to resolve SST gradient near land because microwave side-lobe contamination.

Figure 4-9 presents the fronts detected by the Canny algorithm on the same SST images. The original SST of the 4 products for which the gradient magnitude was displayed on Figure 4-8 is plotted on Figure 4-9, with the detected fronts overlaid. Note that the fronts were detected with a smoothing running Gaussian filter of σ_s =20km. The smoothing filter reduces the small scales of each product, bringing them closer to each other. Still, more fronts were detected on ODYSSEA than on OSTIA (FLI is larger) and they were stronger on ODYSSEA (FGI is larger). A very comparable amount of fronts were detected on REMSS MW and OSTIA, both in term of length and strength. However, OSTIA is able to resolve fronts close to land, such as the important Benguela upwelling front, whereas the microwave SST is unable to do so. Level-3 ODYSSEA data shows little amount of fronts because of the missing

pixels over microwave patches that prevent the Canny algorithm from functioning properly.

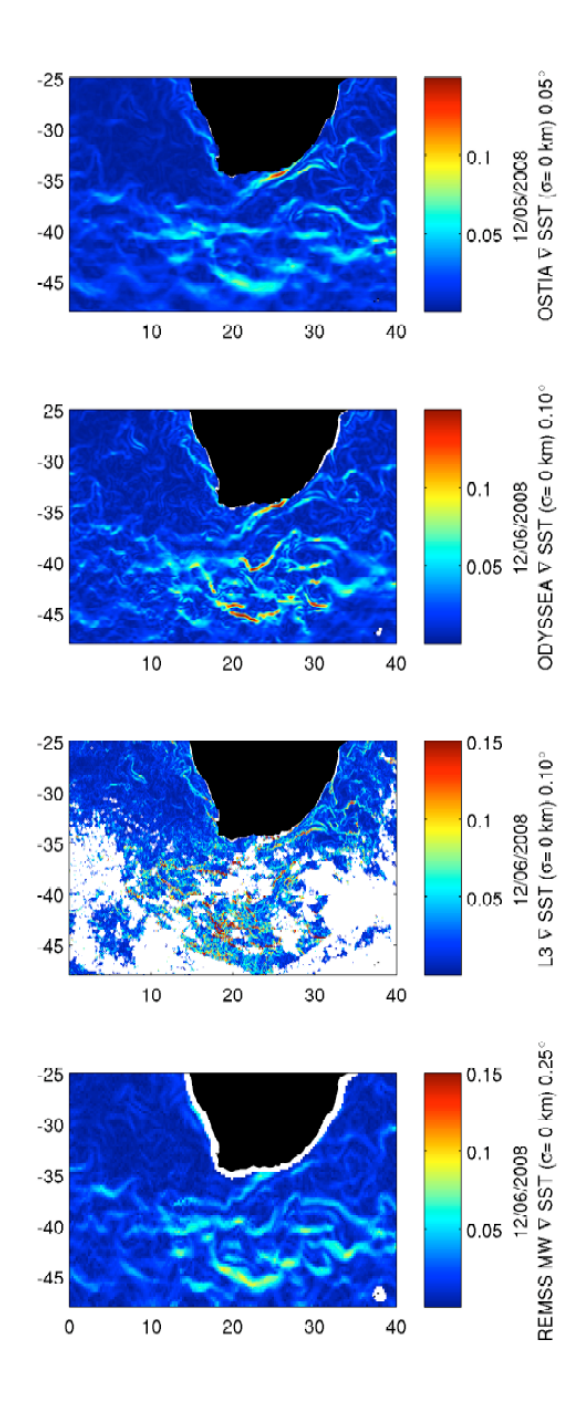


Figure 4-8: SST gradient magnitude of 4 GHRSST products (from top to bottom): OSTIA Level-4, ODYSSEA Level-4, ODYSSEA Level-3 and REMSS MV Level-4. The data are taken over the Agulhas region on 12/06/2008. The gradient is computed with no initial smoothing applied (σ_s =0 km).

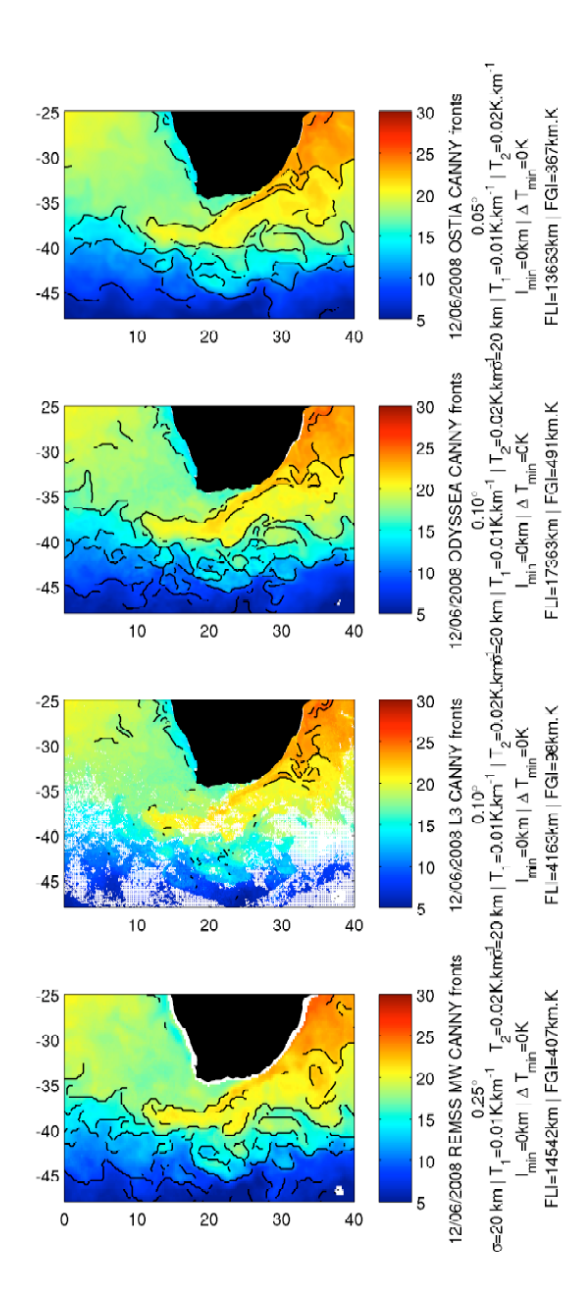


Figure 4-9: Detected fronts on 4 GHRSST products (from top to bottom): OSTIA Level-4, ODYSSEA Level-4, ODYSSEA Level-3 and REMSS MV Level-4. The data are taken over the Agulhas region on 12/06/2008. The fronts are detected with the Canny algorithm, with the threshold parameters T1=0.01 K/km and T2=0.02 K/km and the smoothing running Gaussian of σ_s =20 km.

4.2.3 Level-4 analysis smoothing scales vary spatially

Not only do the Level-4 analyses introduce some smoothing in the SST data, but they do not do so uniformly. The level of smoothing applied by an analysis

procedure is a complex combination of several factors. One of these factors is the error correlation scale. It is a parameter of the OI that controls the size of the smoothing filter and how far alternative measurements are looked for to substitute a missing one. The error correlation should be set carefully, if it is too small, the analysis can be too noisy where there is data and may decay too quickly to a climatology where there is none. If the error correlation scale is too large, the small gradients are unnecessary reduced. The error correlation scale is split into spatial and temporal components. It is involved in the systematic trade-off between interpolation in space, or in time, or a decay to a climatology. In some analyses, the three strategies may occur at the same time, with relative weights that are governed by the OI parameters and the quality and coverage of the input data sets. The REMSS MW analysis relies on isotropic error correlation scales of 100 km and 4 days. Other analyses allow the error correlation scale to vary with location so that the feature resolution of the analysis fits the local dominant scale of variability. The rationale of this approach is to increase the confidence in the results by means of physical assumptions in the generation of the product. In areas where small scales dominate, the smoothing and interpolation in space are reduced so that the OI result contains more energy at small scales. On the opposite, in areas where the larger scales dominate, it is possible to search for data a bit further to improve spatial coverage and diminish noise and yet still be confident about the result. Where it is assumed that larger scales are dominant, the analysis do not generate unrealistic small-scale features, even if some are present in the input data.

The OSTIA analysis is built on two error correlation length scales of 10 km, to account for mesoscale variability, and of 100 km to capture larger scale variations introduced by synoptic features in the atmosphere. These scales are derived from the output of a 3-year integration of the Met Office Forecasting Ocean Assimilation Model (FOAM, (Bell et al. 2003, Bell et al. 2000) . Spatially varying error variances derived from the FOAM run and associated with these scales are input to the analysis procedure and define the effective correlation scale (Figure 4-10). The effective correlation scale applied in the ODYSSEA procedure is governed by two isotropic length scales. The first scale is equal to 80 km. The second is set to Rossby Radius of Deformation, bounded by 20 km and 80 km, calculated on a 1° grid using the 1998 Levitus climatology.

This scale is presented on Figure 4-11, it is quite different from the one of OSTIA. The NCDC error correlation scales are not exactly isotropic, as shown on Figure 4-12. They have been calculated by Reynolds et al. (2007) on AVHRR and AMSR data sets by spatial lagged correlations following Reynolds and Smith (1994).

The spatially varying error correlation length scales used in the analysis procedures limit the spatial consistency of the frontal results that are derived from them. It was shown in chapter 3 that the frontal detection is strongly linked to spatial variability. The amount of fronts detected on the SST images depends on the amount of smoothing that was applied on the image. Spatial variability of the smoothing filter complicates the spatial comparison of frontal results. Therefore it is important to know whether a different quantity of detected fronts in two different locations is due to different local characteristics or simply different amount of smoothing. The analysis products that apply spatially variable filters do so with a scientific rational that derives either from a temporal averaging of observed correlation length scale or from a temporal averaging of a model output. This approach offers confidence in the fact that the smoothing is making the output realistic, so the observed spatial variations of scales are close to the real ocean ones. One can argue that the methodologies to calculate the scales are prone to errors. The validity of the OSTIA scale assumption is limited by the precision of the FOAM model, which is unequal and suffers from the scarcity of FOAM input observations in some regions. One should therefore account for the uncertainties in the error correlation assumptions in the interpretation of the front detection results. In addition, even if these assumptions were completely realistic, they are based on temporal averages and constrain the presence of small scales in a way that is constant in time. Hence an actual temporal signal in the amount of small scale would not propagate fully to the results. The design of these analysis procedures limits the exploration of such temporal variability in the presence of small scales, in some regions.

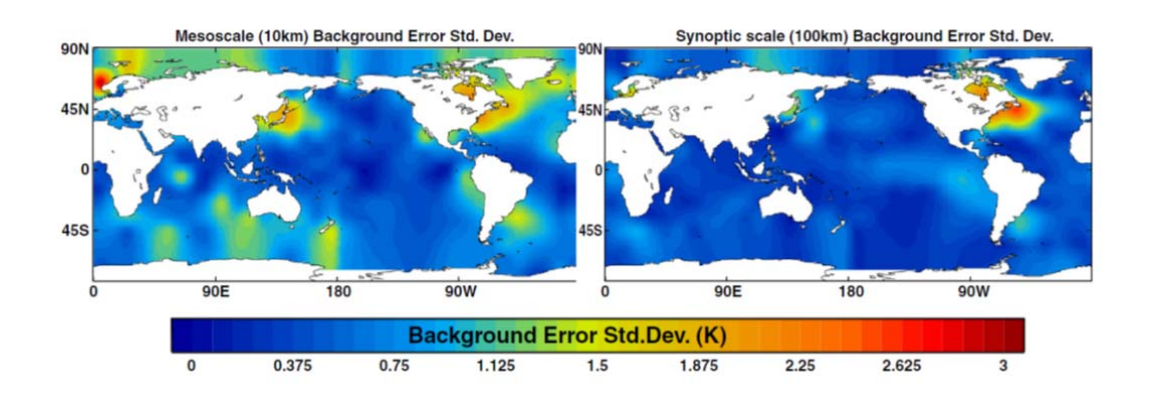


Figure 4-10: OSTIA background error standard deviation for (left) 10 km mesoscale and (right) 100 km synoptic scale features derived from three years of daily FOAM ocean model outputs. From Donlon et al. (2012).

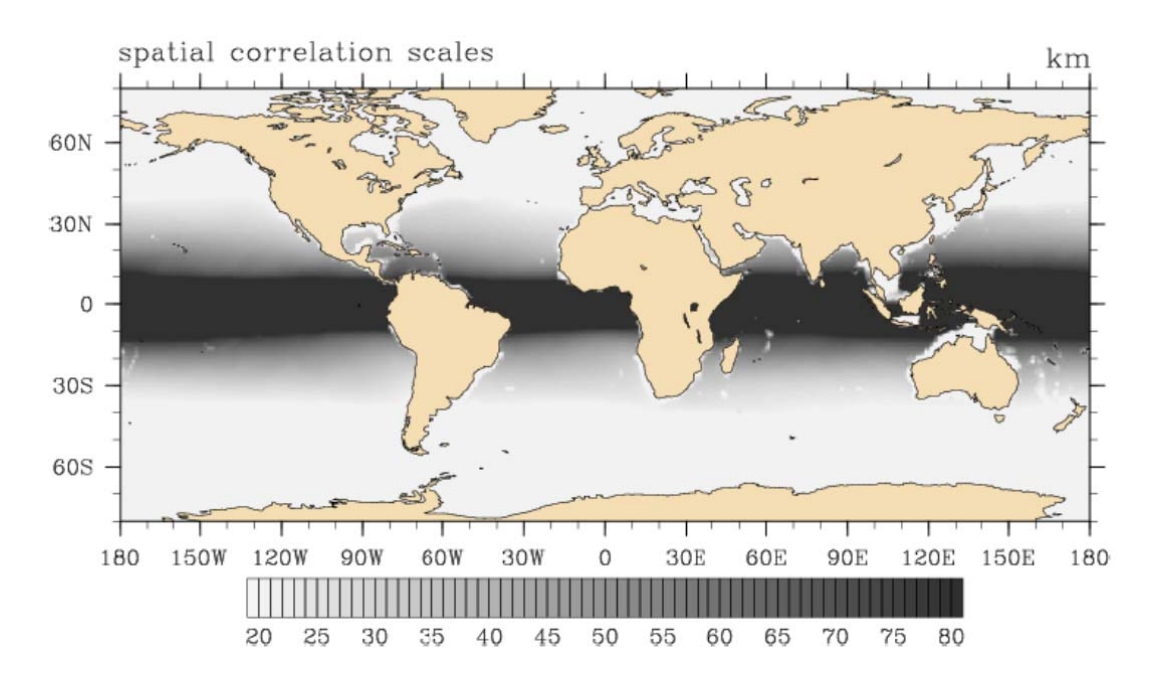


Figure 4-11: ODYSSEA spatial correlation length scale for the mesoscale. From Autret and Piollé (2007).

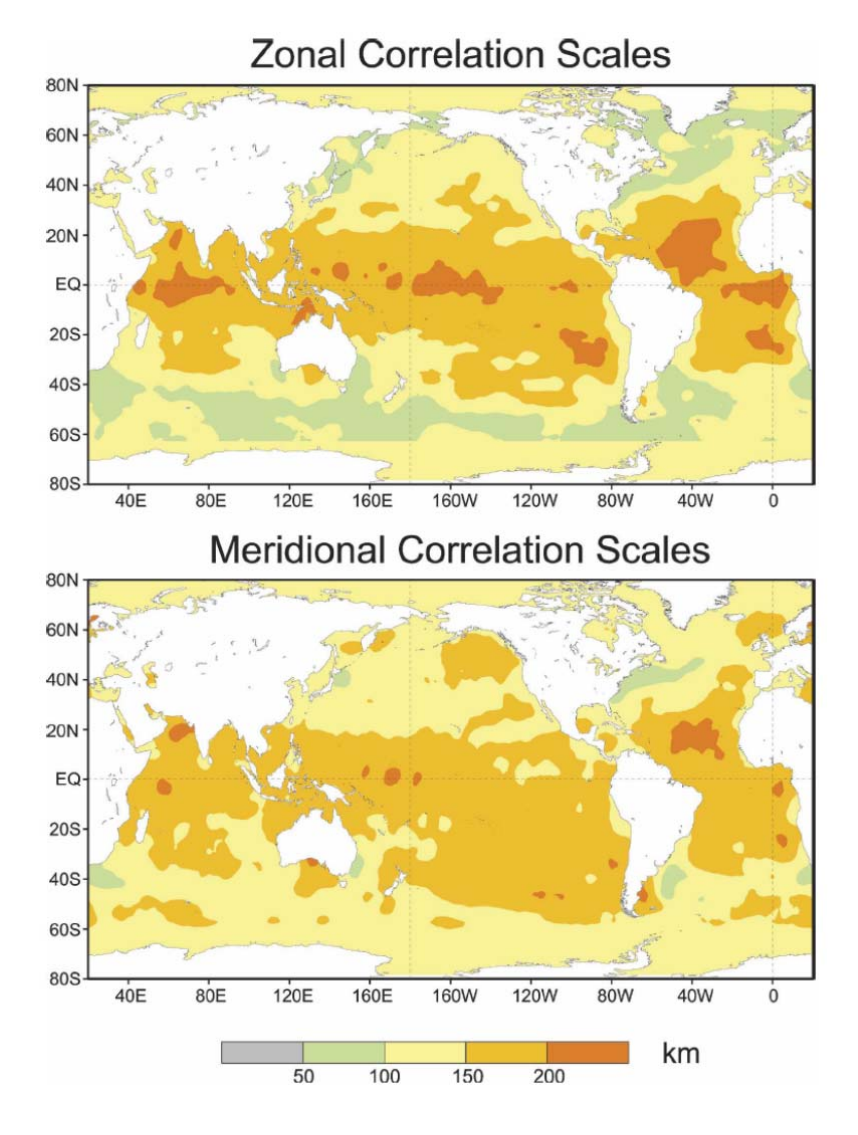
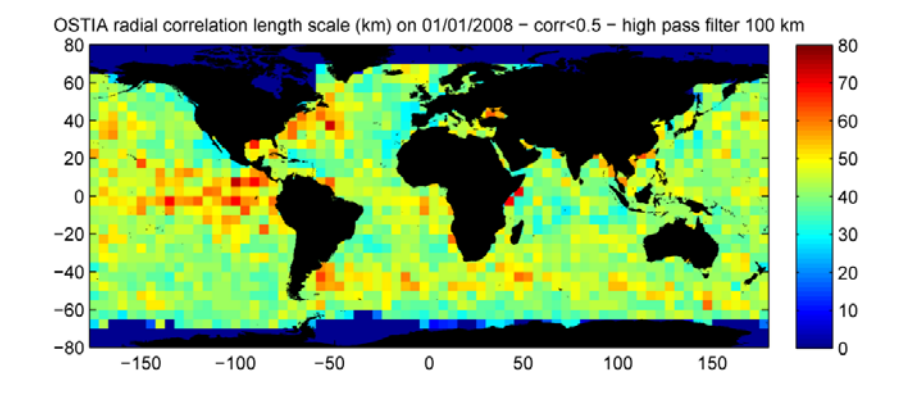


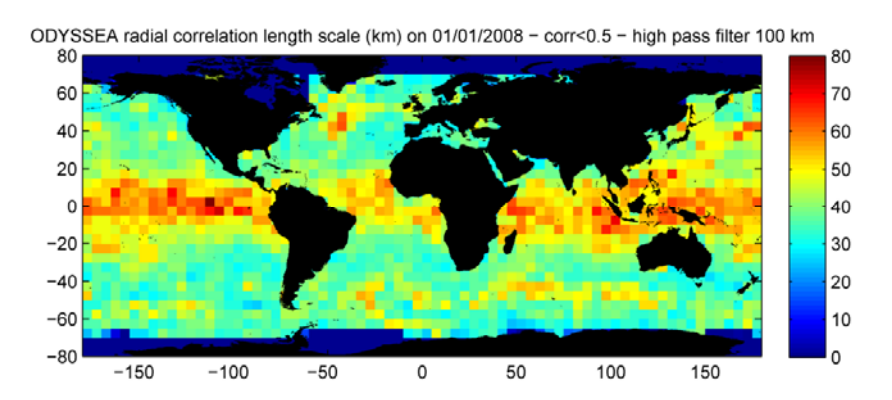
Figure 4-12: NCDC AMSR +AVHRR and AVHRR-only zonal and meridional error correlation scales. From Reynolds et al. (2007).

The error correlation length scales are described and implemented in different ways in the Level-4 analyses mentioned in this thesis. Other steps of the analysis procedures also introduce an unknown quantity of smoothing. Another way to compare the spatial smoothing applied by each procedure is to compare directly the autocorrelation length scales of the output images. The autocorrelation length scale was calculated on one day of OSTIA, ODYSSEA and REMSS MW. For this, the SST anomaly was computed and a high-pass filter with a cut-off frequency of 100 km was applied. This filter is critical since variations in the absolute SST value increases the autocorrelation. The autocorrelation was processed on a 1° grid. The autocorrelation function was

processed locally by shifting in every direction the filtered SST anomaly field and getting the correlation with the non-shifted field. When the shift is zero, the correlation is equal to one. As the shift increases, the correlation decreases. The correlation decreases faster when the studied field is varying quickly in space. The autocorrelation length scale is defined as the distance over which the autocorrelation drops below 0.5, following Isaaks and Srivastava (1989). The calculated autocorrelation length scales of the three analyses mentioned above are shown on Figure 4-13. It shall be stressed that the measured scales depend on the combination of the real oceanic scales and of the scale filtering applied by the analyses. In addition, the next section shows that the scales present on Level-4 SST images is also governed by the type of SST data used as input. It is still interesting to compare the three maps on Figure 4-13 because they estimate in different ways the same real scene. Hence the differences presented on Figure 4-14 depend on the differences in the analysis procedures only. The autocorrelation length scale on OSTIA vary from 30 to 80 km, with larger scales on and around the Gulf Stream, the tropical and equatorial East Pacific and around the Antarctic Circumpolar Current (ACC). ODYSSEA scales are distributed less evenly than OSTIA's. They are large everywhere between the Tropics, as well as on the Gulf Stream, the Kuroshio Current and the ACC but on narrower regions than on OSTIA. In contrast, mid- and high-latitude regions are characterized by a very small autocorrelation length scale of about 30 km. Figure 4-14 shows a clear pattern in the differences between OSTIA and OSYSSEA scales. The ODYSSEA scales of Figure 4-13 correspond closely to the theoretical spatial correlation length scale applied by ODYSSEA and shown on Figure 4-11. The larger scales observed on the ACC on ODYSSEA relative to its surroundings can be attributed to the scales of the real surface temperature since the theoretical ODYSSEA spatial correlation length scale do not vary in the involved region. The scales displayed on the REMSS MW dataset are assumed to be close to reality, however they are confined to scales that the microwave resolution can resolve. The rectification of microwave measurements on an oversampled grid is not straightforward but it does not result in a spatially varying amount of smoothing applied. It is striking that the autocorrelation length scale of the microwave-only product is not significantly larger than that of analyses which make use of high-resolution infrared data. REMSS MW show larger scales on the Kuroshio Current, the Gulf Stream and the ACC. However the Tropical

regions are not characterized by larger scales, except on a narrow Equatorial band in the Pacific. This comparative analysis is based on a single day used as an example; it is not sufficient to draw general conclusions about the genuine autocorrelation scales on the ocean. It is however a good illustration of the different scales produced by the Level-4 SST analyses when estimating the same scene.





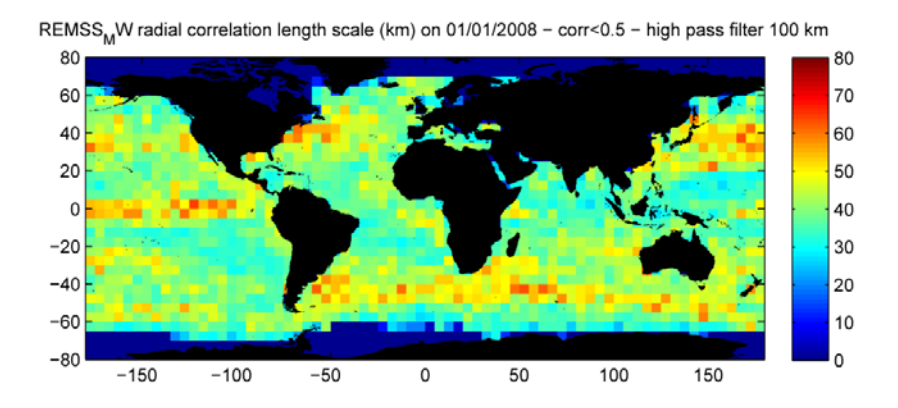


Figure 4-13: Radial correlation length scale in km, calculated for OSTIA/ODYSSEA/REMSS MW on 01/01/2008. The length scale is defined by the scale at which the autocorrelation drops below 0.5. A high pass filter of 100 km is applied before the autocorrelation is processed.

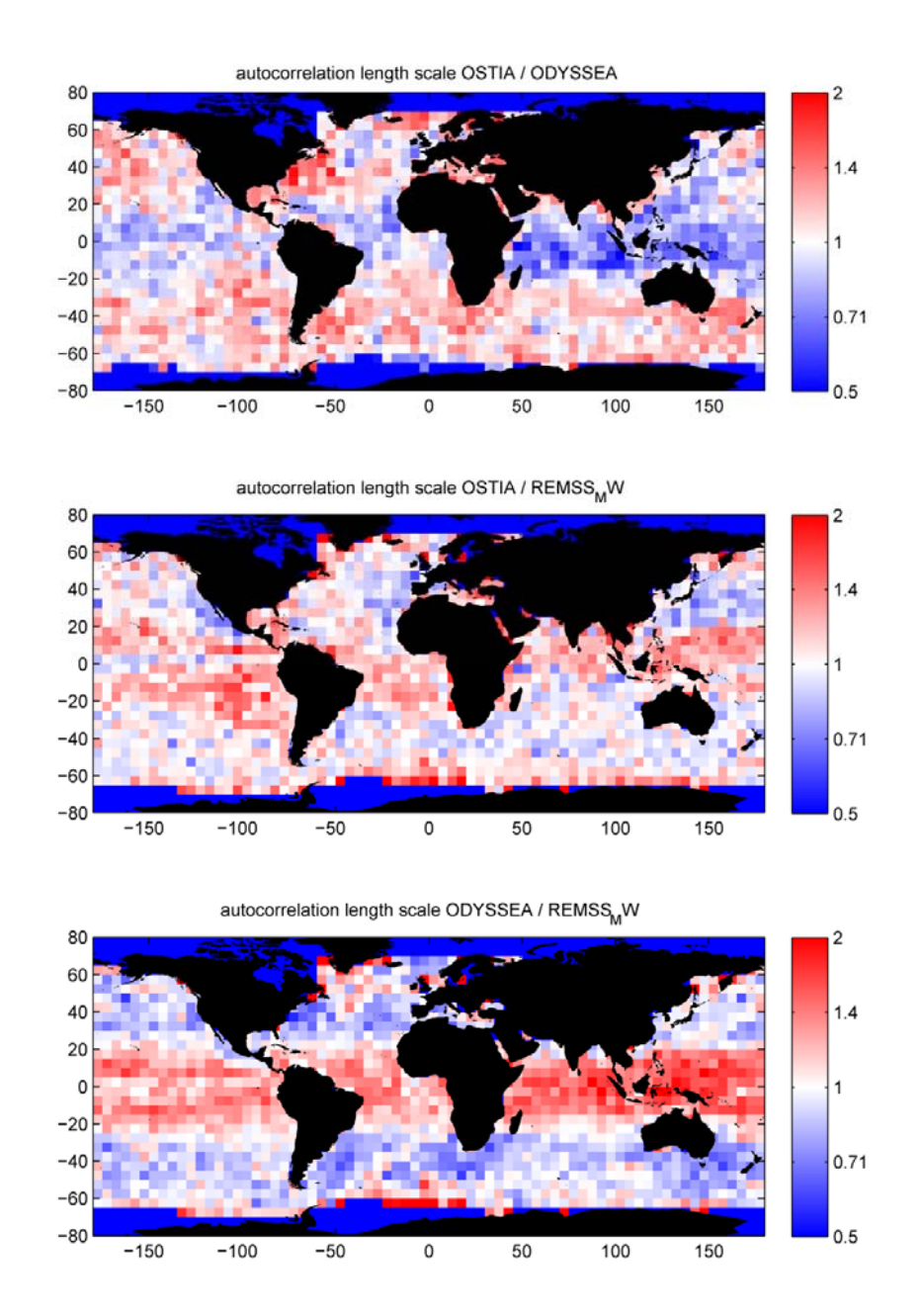


Figure 4-14: Ratios of the autocorrelation length scales shown on Figure 4-13.

4.2.4 Level-4 analysis smoothing scales vary in time

The previous section showed that some Level-4 analyses products are designed to return SST images whose feature resolution varies in space. When detecting fronts on these images, this effect should be accounted for in order not to misinterpret the portion of the spatial variability of fronts which is an artefact of the analysis procedure. A good understanding of the smoothing added by the OI and its variation in space helps to mitigate this limitation. The problem gets more complicated when the feature resolution varies also in time over the same location if it is due to processing artefacts rather than a natural signal. Changes in satellite SST instruments used as input to the analyses over time can impact the resulting feature resolution. These changes can be due to a variable cloud coverage which eliminate infrared measurements or rain events which also contaminate microwave inputs. They can also be the consequence of adding a newly available satellite instrument or terminating an old instrument. These changes can lead to artificial abrupt jumps in the resolution of the analyses (Reynolds et al. 2007). Consider, for example, an analysis product that blends infrared and microwave data sets. Cloud-free regions benefit from high-resolution infrared sampling as well as microwave sampling. If the analysis inherent smoothing is low enough, high-resolution features are transmitted to the output SST when infrared data are available. Suppose, now, that on a later day a persistent cloud cover appears on the same area. In these conditions, the analysis can only estimate the SST from low resolution microwave data sets. The resulting SST field feature resolution is bounded by the low resolution of the microwave images used as input. This example shows that an analysis that blends microwave and infrared data runs the risk that changes in infrared coverage because of cloud cover or narrow swath generate apparent temporal inhomogeneity in the small-scale variance. To explore this effect it is useful to consider analysis products that follow the same procedure but on different input data sets. Reynolds et al. (2007) discuss 3 products based on the same procedure. NCDC AVHRR that is based on infrared data only, NCDC AMSR that is based on microwave data only, and NCDC AMSR&AVHRR that blends infrared and microwave data. To quantify the cloud cover effect on small scales, the authors define a gradient index on the Gulf Stream region whose cloud coverage is characterized by a strong seasonal variability. They found that differences between the gradient index of AMSR

and AMSR and AVHRR combined OI are very small. This result can be the consequence of either the large smoothing and infrared spatial binning involved in the NCDC procedure or of the limitation of the gradient index as a small-scale quantification. The gradient index calculated by the authors could be too coarse to give a larger weight to small scales but it should also be stressed that a gradient magnitude is not directly proportional to the presence of small scales. Especially on highly dynamic jets like the Gulf Stream, the temperature gradient is very large even at scales resolved by the microwave. Reynolds and Chelton (2010) show by exploring the zonal wavenumber spectra of the SST of various products at various locations and times that AMSR data can degrade the combined AMSR and AVHRR resolution in cloudfree regions. This conclusion seems at first unnatural because, as illustrated in Table 4-2, the two products both benefit from high-resolution infrared data as input in clear-sky conditions. Yet, the NCDC OI is based on averaging available input data, hence the inclusion of the coarse 50-km resolution AMSR data at a time of prevalent AVHRR data results in a smoothing of the SST field that would otherwise be obtained from the 25-km (after spatial binning) AVHRR data alone. This observation clearly means that the NCDC AMSR&AVHRR product feature resolution is dependent on the cloud coverage and the availability of infrared data. This effect is likely to be accentuated in the OSTIA and ODYSSEA products because they rely on less smoothing and, at least in the case of OSTIA, make use of infrared data more effectively than NCDC OI (Reynolds & Chelton 2010).

Table 4-2 also shows that in case of persistent cloud cover, the NCDC AVHRR analysis product has no other alternative but to apply spatial and temporal interpolation, or to decay to a climatology. This can result in the absence of 50 km scales that are resolved by the microwave. Reynolds et al. (2007) establish that AMSR data significantly improve the resolution of the AMSR&AVHRR product under cloud-cover conditions when compared with AVHRR-only analysis. This effect is particularly important over the Gulf Stream region because of the seasonal cloud cover. The authors found that the gradient index of AMSR&AVHRR is nearly equivalent in the summer to that of AVHRR-only but is almost double in winter. This stresses the importance of microwave data in multi-sensor Level-4 products and raises questions about the

consequences of the failure of AMSR in October 2011 on the mid and high latitude winter Level-4 data since then.

	NCDC L4 SST	Climatology/ Interpolation	Microwave data	Infrared data
Clear sky	AVHRR			Х
	AMSR		Х	
	AMSR&AVHRR		Х	Х
	AVHRR	X		
Cloud cover	AMSR		Х	
	AMSR&AVHRR		Х	

Table 4-2: type of SST input data available for the 3 NCDC Level-4 SST products as a function of the cloud conditions.

4.3 Qualitative comparisons of the gradients

Another way to compare Level-4 SST products is to compare their gradient magnitude. Gradient magnitude is both a relevant dynamical index as shown in chapter 2 and a qualitative indicator, although not perfect, of how the smallscale are resolved by each product. If looking at the gradient of various products does not allow one to conclude which one is closest to reality, it nonetheless sheds light on processing artefacts and differences between the products. Figure 4-15 displays the gradient magnitude calculated on a single day of OSTIA, ODYSSEA and REMSS MW SST, with no smoothing applied (σ =0 km). The SST gradient magnitude reveals a great deal of mesoscale activity on the ocean surface. In the three products, the gradient resolves the western boundary currents and the activity in their surroundings, the ACC, Tropical Instability Waves in the East Pacific, coastal upwellings and smaller scale activity. A first glance gives the same impression on the three SST gradient maps of a higher gradient magnitude at mid-latitudes along the strong surface currents and a lower gradient in the Equatorial and Tropical regions. Yet it seems that OSTIA SST gradient drops quicker below the Gulf Stream where REMSS MW gradient is present and even going further to the South towards the

Equator. ODYSSEA seems to have a higher gradient than OSTIA where the gradient is low, but a lower gradient than REMSS MW. The later analysis resolves the stronger gradient in regions of low gradient but one can easily detect artefacts of the data merging as passes of AMSR seem to be characterized by a stronger gradient than the surrounding areas. It is important to add that these artefacts are a substantial obstacle for the front detection because they would trigger frontal detection on the edges of the passes.

This impression is confirmed by Figure 4-16 and Figure 4-17 which compare the gradient magnitude on the three products with regional and monthly ratios. The gradient magnitude was calculated for each day of the January 2008 for each of the three products, with no smoothing involved (σ =0 km). The monthly average gradient magnitude for each region shown on Figure 4-16 was calculated so that the ratios OSTIA/ODYSSEA, OSTIA/REMSS MW and ODYSSEA/ REMSS MW could be computed. Figure 4-16 and Figure 4-17 show that ODYSSEA gradient is everywhere higher than OSTIA gradient, especially in the 20°S-40°S and 20°N-40°N latitude regions. REMSS MW gradient is much stronger than OSTIA between 40°S and 40°N and much stronger than ODYSSEA between 20°S and 20°N. Note that REMSS MW seems to have both smaller scales and larger gradient than OSTIA and ODYSSEA in the Equatorial and Tropical regions. However it has a gradient equal to ODYSSEA at mid-latitudes but scales larger than ODYSSEA in these regions (Figure 4-14). Similarly, ODYSSEA has a higher gradient than OSTIA everywhere, but it has a larger feature resolution than OSTIA between 20°S and 20°N and a smaller elsewhere. This shows that the autocorrelation length scale and the gradient magnitude at σ =0 km are two different concepts which are not always correlated.

Figure 4-18 shows that the differences between the gradient magnitude of the products decreases as σ increases. This demonstrates that the differences between the products are at the small scales. As the scales grow bigger because the smoothing increases, the gradient magnitudes come closer to each other. It is a natural and expected result that the products agree on the very large scales, because they are fairly stationary and very well resolved by all the inputs.

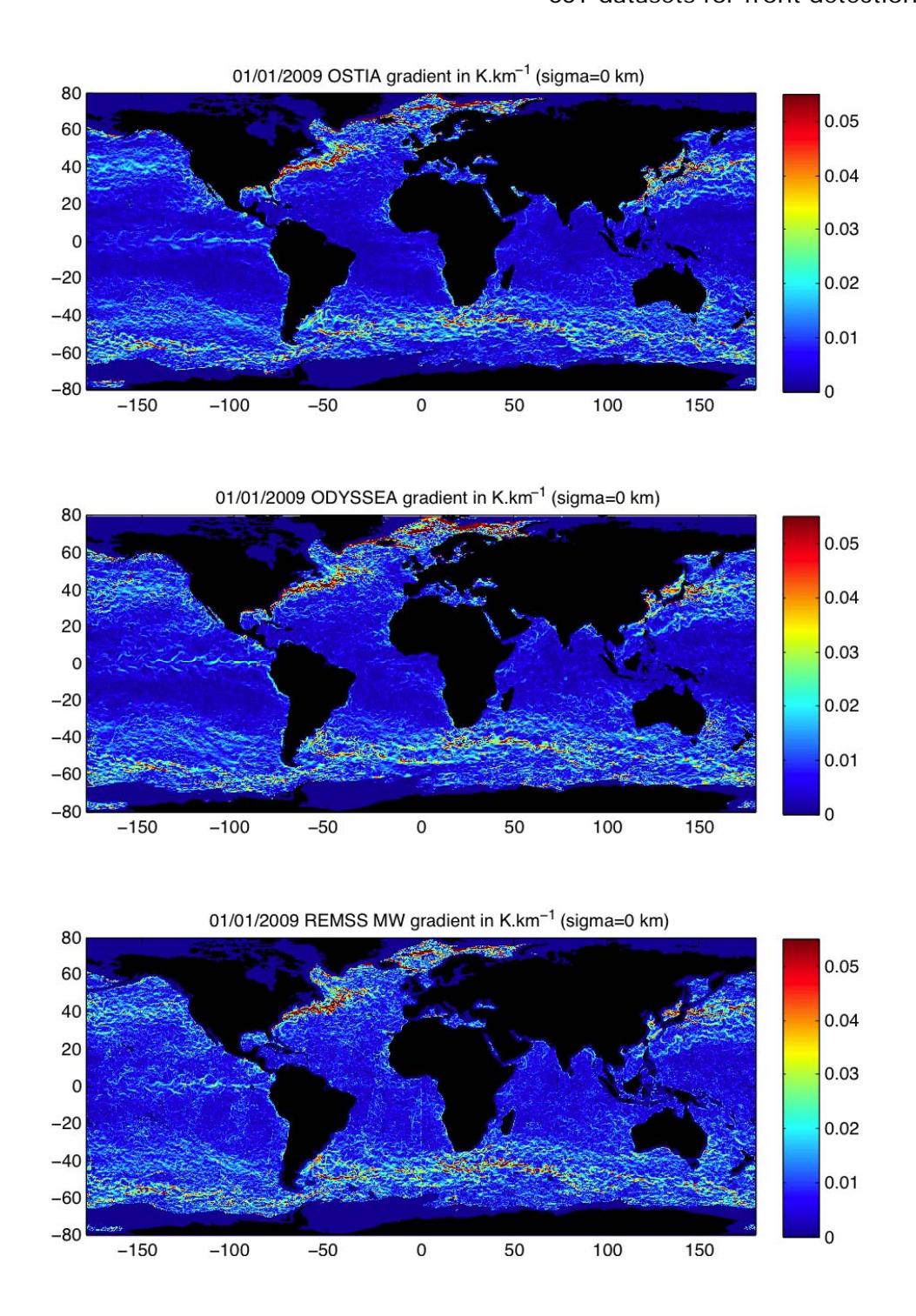


Figure 4-15: Gradient magnitude of OSTIA, ODYSSEA and REMSS MW Level-4 analysis SST products, on 01/01/2009. The gradient is calculated with a simple gradient operator, without any smoothing applied.

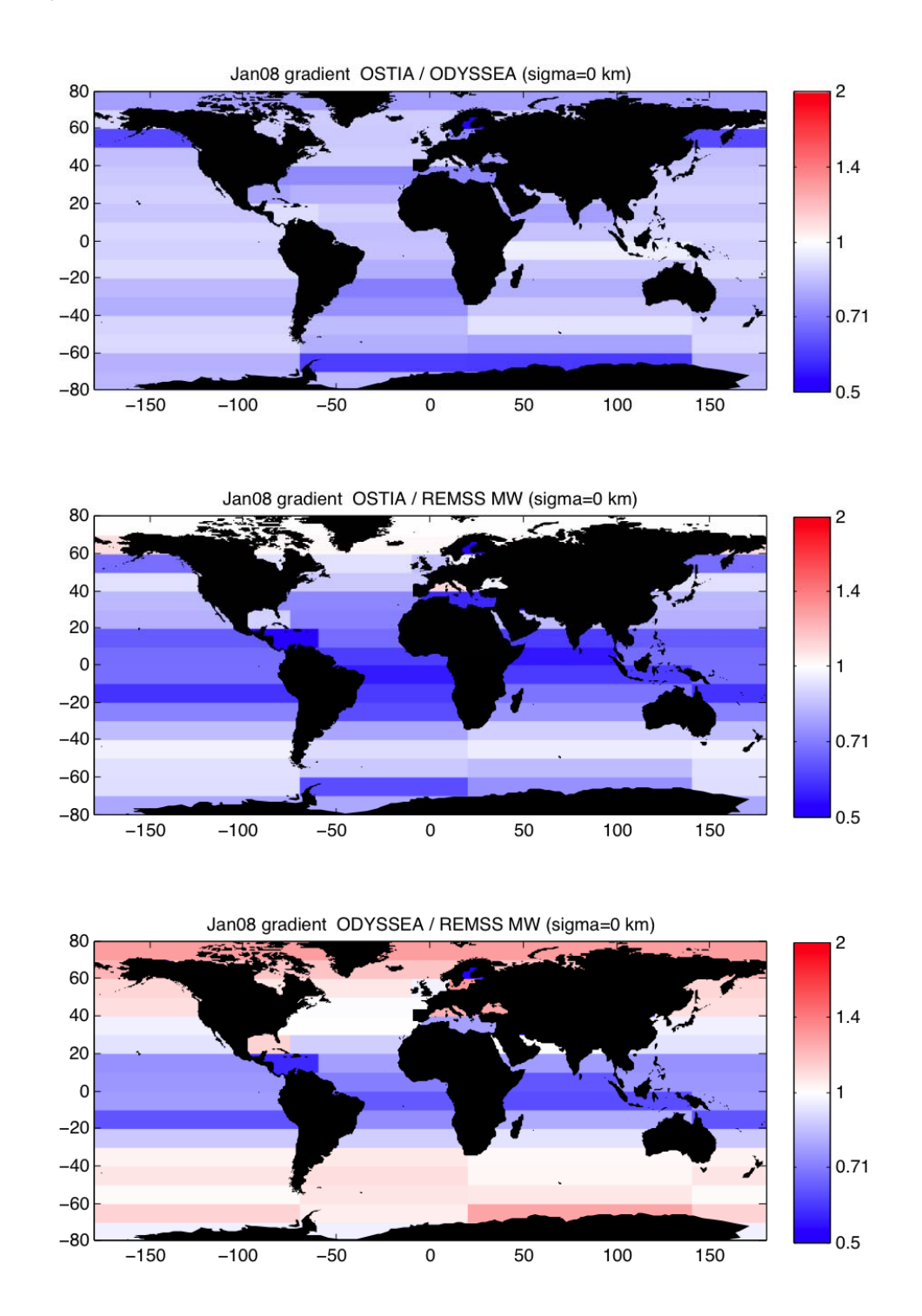
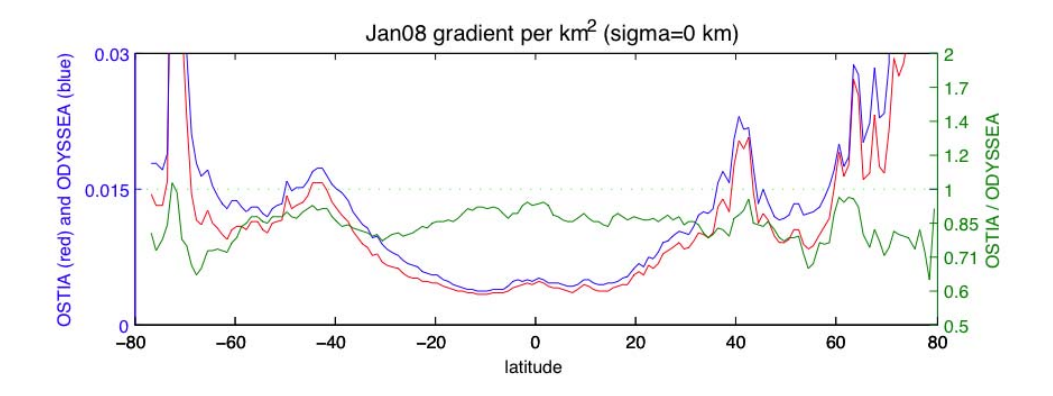
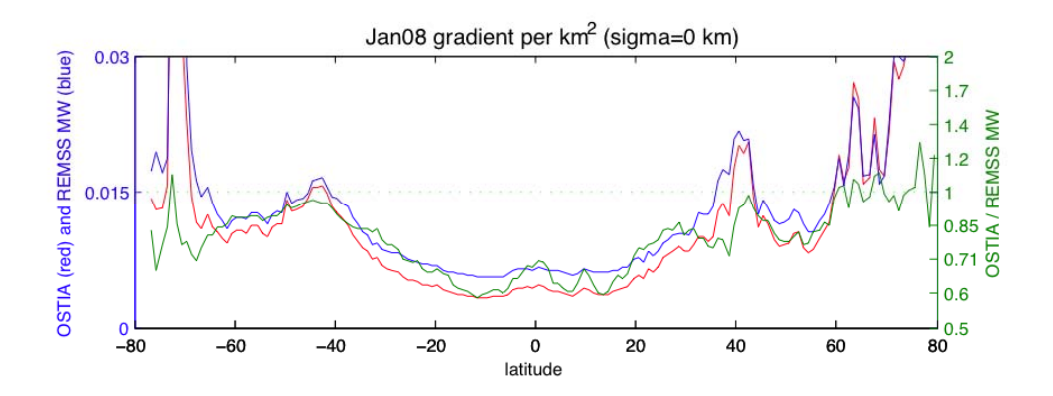


Figure 4-16: Regional ratios of monthly average SST gradient over the month of January 2008 for the OSTIA, ODYSSEA and REMSS MW analysis SST products. Note that the regions are split every 10° latitude in each ocean and that the average gradient is computed by averaging the gradient calculated on each day of the month, with no smoothing involved (σ =0 km).





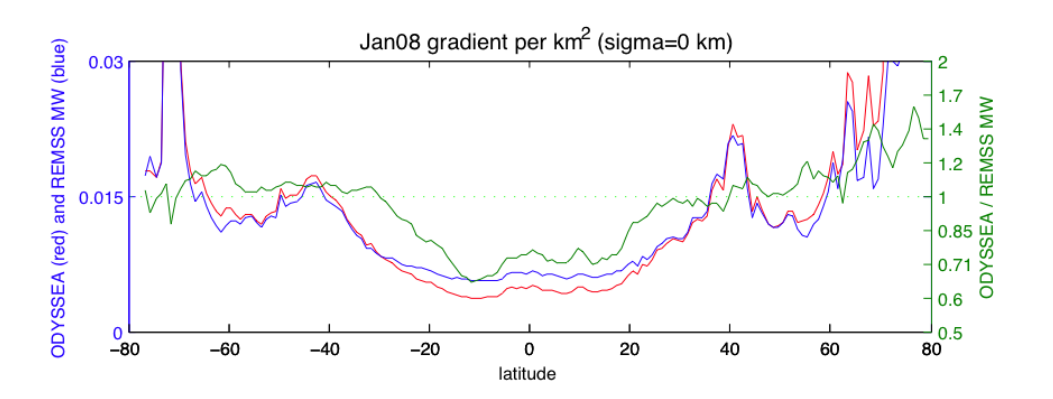
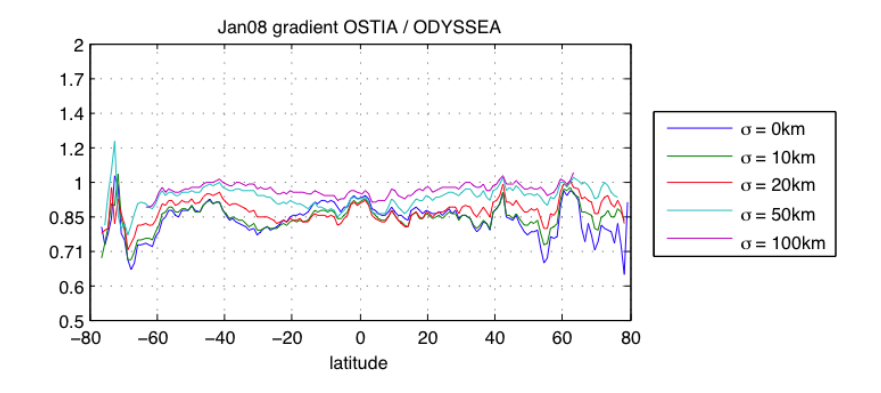
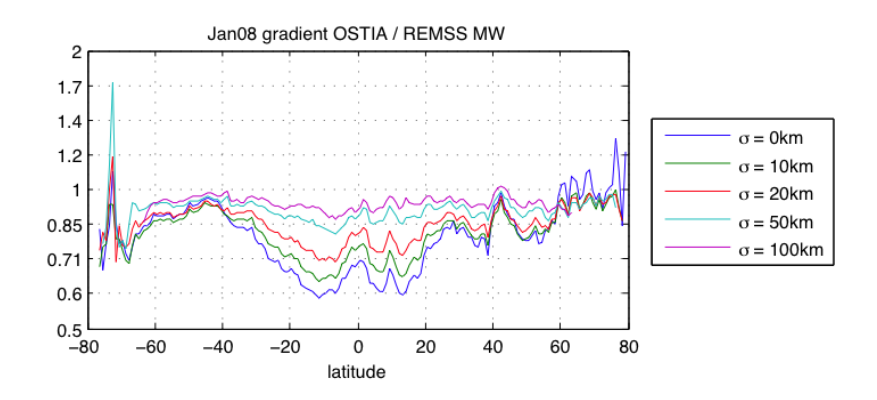


Figure 4-17: Monthly zonal average SST gradient and ratios (green) over the month of January 2008 for the OSTIA, ODYSSEA and REMSS MW analysis SST products. Note that the average gradient is computed by averaging the gradient calculated on each day of the month, with no smoothing involved $(\sigma_s=0 \text{ km})$.





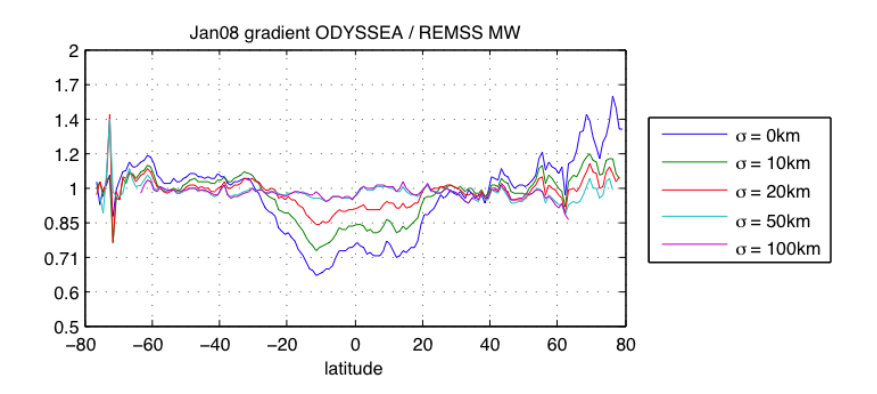


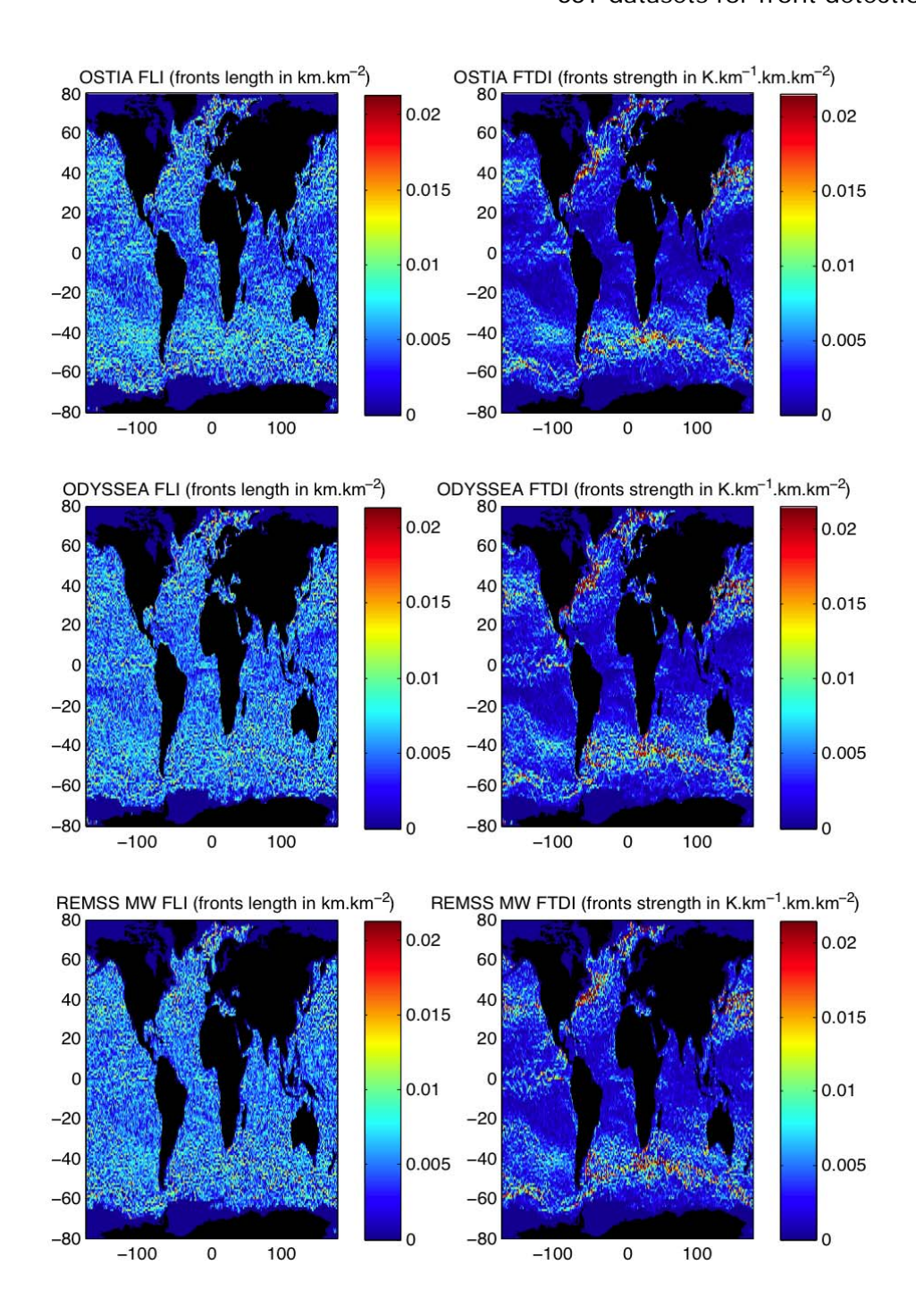
Figure 4-18: Monthly zonal average SST gradient ratios over the month of January 2008 for the OSTIA, ODYSSEA and REMSS MW analysis SST products. Note that the average gradient is computed by averaging the gradient calculated on each day of the month, with varying smoothing involved (σ_s =0 to 100 km).

4.4 Qualitative comparison of detected fronts

The differences in feature resolution and gradient magnitude of the products described in the previous sections result in different fronts being detected. Figure 4-19 shows the frontal indexes detected over 5 days of OSTIA, ODYSSEA and REMSS MW with the Cayula method and a window size of 180 km. The analyses presented in this section are based on the Cayula algorithm despite the recommendation made in section 3.6 to rather use the Canny algorithm. The reason for this is the fact that at the time these analyses were performed, the Cayula algorithm was the baseline for achieving this thesis. It was however the practical implementation and exploitation of the Cayula algorithm which made the author of this thesis aware of some of the issues associated with it. The Canny algorithm was subsequently implemented and explored as a result of this scientific development.

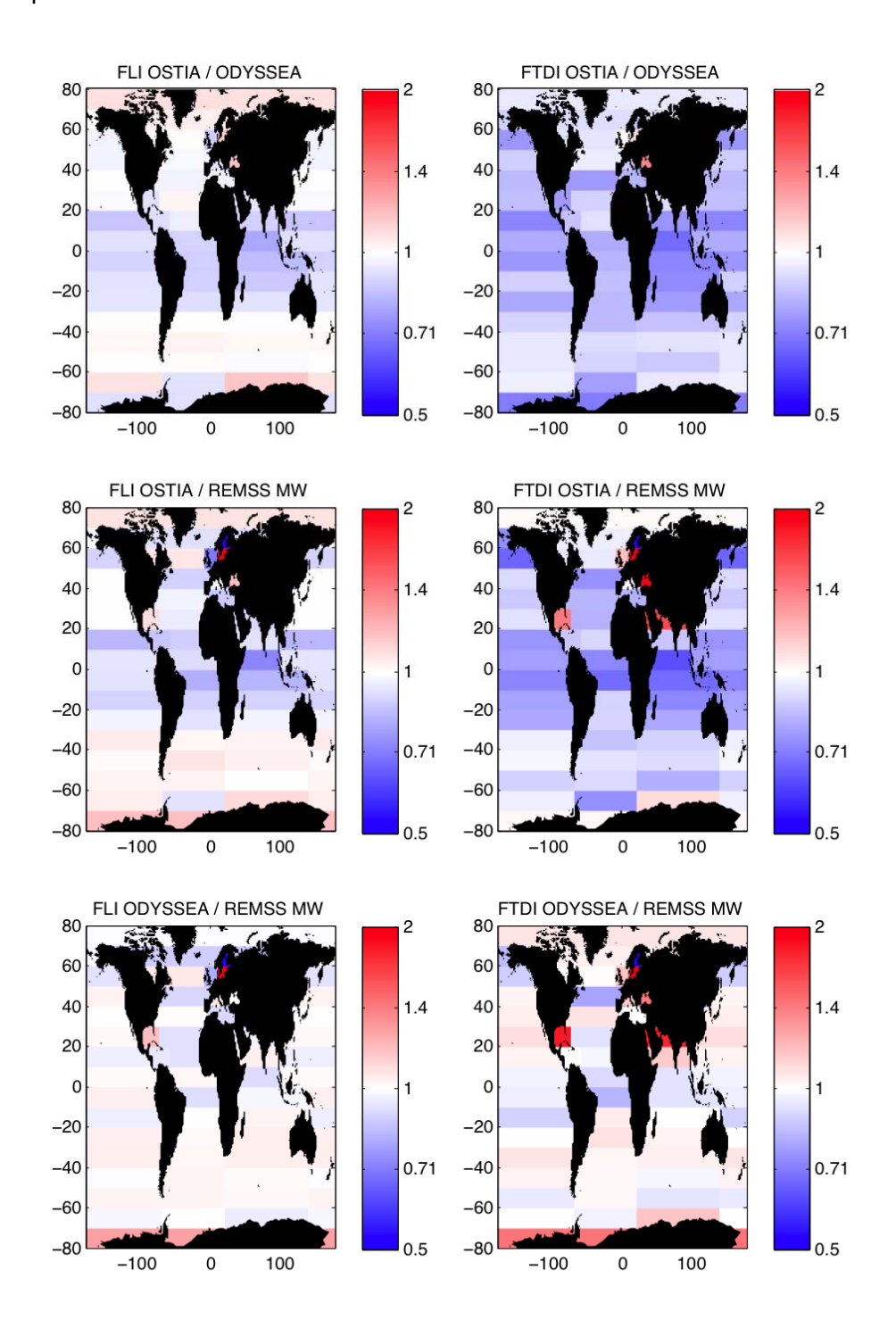
As explained in chapter 3, because the Cayula algorithm is parameterized with $\Delta T_{min} = 0 K$, fronts are detected all over the ocean and the FLI is uniformly distributed. The index of frontal strength FTDI however resolves the mesoscale activity in similar places as the gradient index does on Figure 4-15. The maps of the indices do not allow one to spot obvious differences between the three products. This can be done by calculating the ratio of regional averages of the frontal indexes as presented on Figure 4-20 and Figure 4-21. The frontal length is fairly close on the three products, while ODYSSEA frontal strength is everywhere larger than that of OSTIA. Despite the differences in feature resolution and gradient magnitude of ODYSSEA and REMSS MW, the frontal indexes detected on these two products are very close. This is likely due to the fact that the mentioned differences involve small scales and that the latter do not affect the Cayula algorithm with a window size of 180 km. Figure 4-21 shows that OSTIA FTDI is between 0% and 20% lower than ODYSSEA FTDI, whereas ODYSSEA FTDI lays within 85% and 115% of REMSS MW FTDI. The Frontal Gradient Index, calculated from the gradient magnitude ($\sigma = 0 \ km$) on the fronts, is plotted on Figure 4-22. It is more variable amongst the three products, OSTIA FGI is within 0% and 35% lower than ODYSSEA FGI and ODYSSEA FGI lies within 65% and 140% of REMSS MW FGI. This illustrates that the index based on the gradient magnitude is obviously more sensitive to the small scales differences in the gradient magnitude than the index representing

the difference in temperature on both sides of the front as detected by the Cayula algorithm.



Cayula regular resampling on 01/01/2008 to 05/01/2008

Figure 4-19: Front Length Index (FLI, left) and Front Temperature Difference Index (FTDI, right) of OSTIA, ODYSSEA and REMSS MW between 01/01/2008 and 05/01/2008. Fronts were detected with the Cayula algorithm, with a window size WS=180 km, and no minimum temperature difference: $\Delta T_{min} = 0 \ K$.



Cayula regular resampling on 01/01/2008 to 05/01/2008

Figure 4-20: Front Length Index (FLI, left) and Front Temperature Difference Index (FTDI, right) ratios of OSTIA, ODYSSEA and REMSS MW between 01/01/2008 and 05/01/2008. Fronts were detected with the Cayula algorithm, with a window size WS=180 km, and no minimum temperature difference: $\Delta T_{min} = 0~K$.

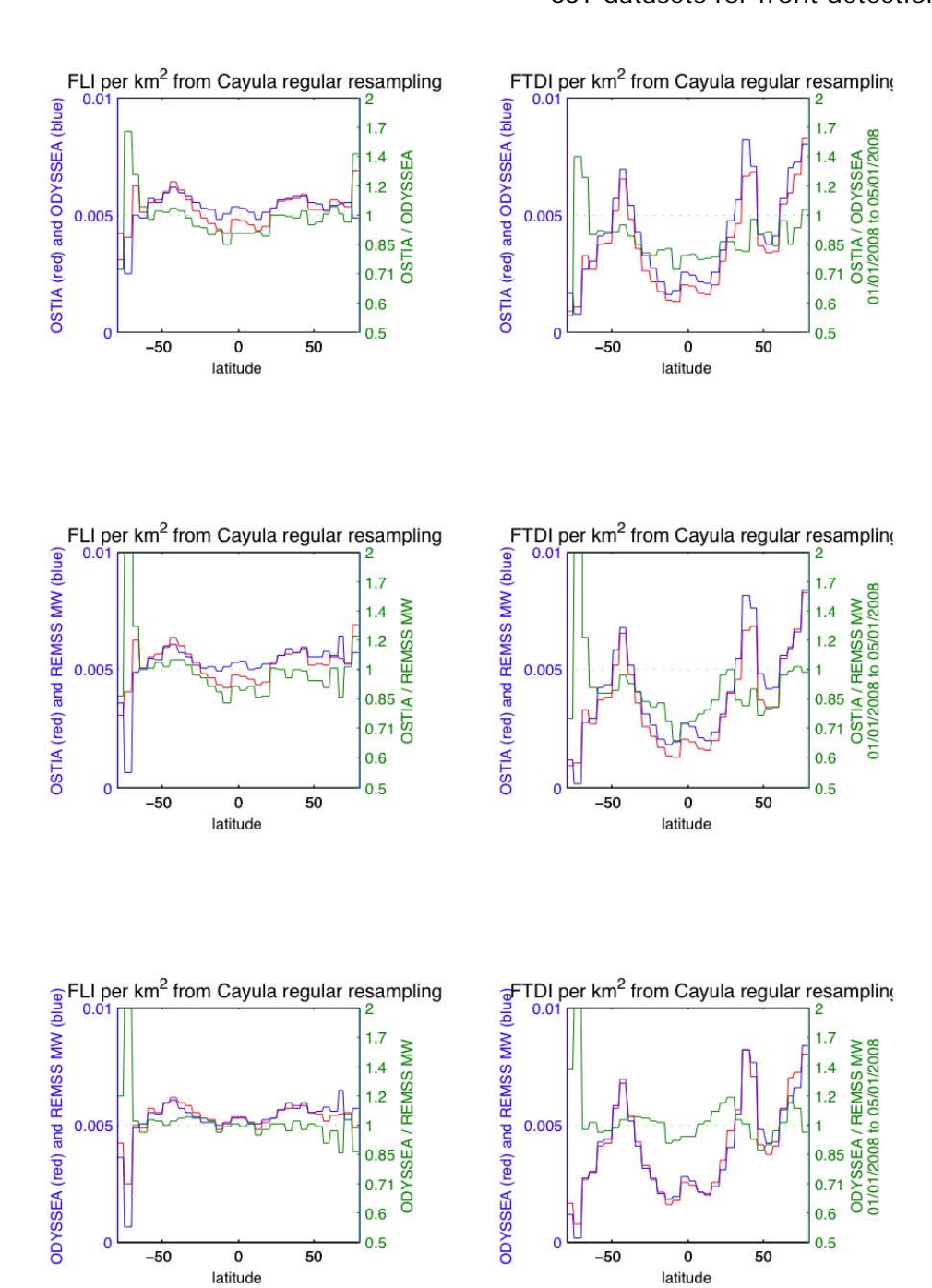


Figure 4-21: Zonally averaged Front Length Index (FLI, left) and Front Temperature Difference Index (FTDI, right) and ratios of OSTIA, ODYSSEA and REMSS MW between 01/01/2008 and 05/01/2008. Fronts were detected with the Cayula algorithm, with a window size WS=180 km, and no minimum temperature difference: $\Delta T_{min} = 0~K$.

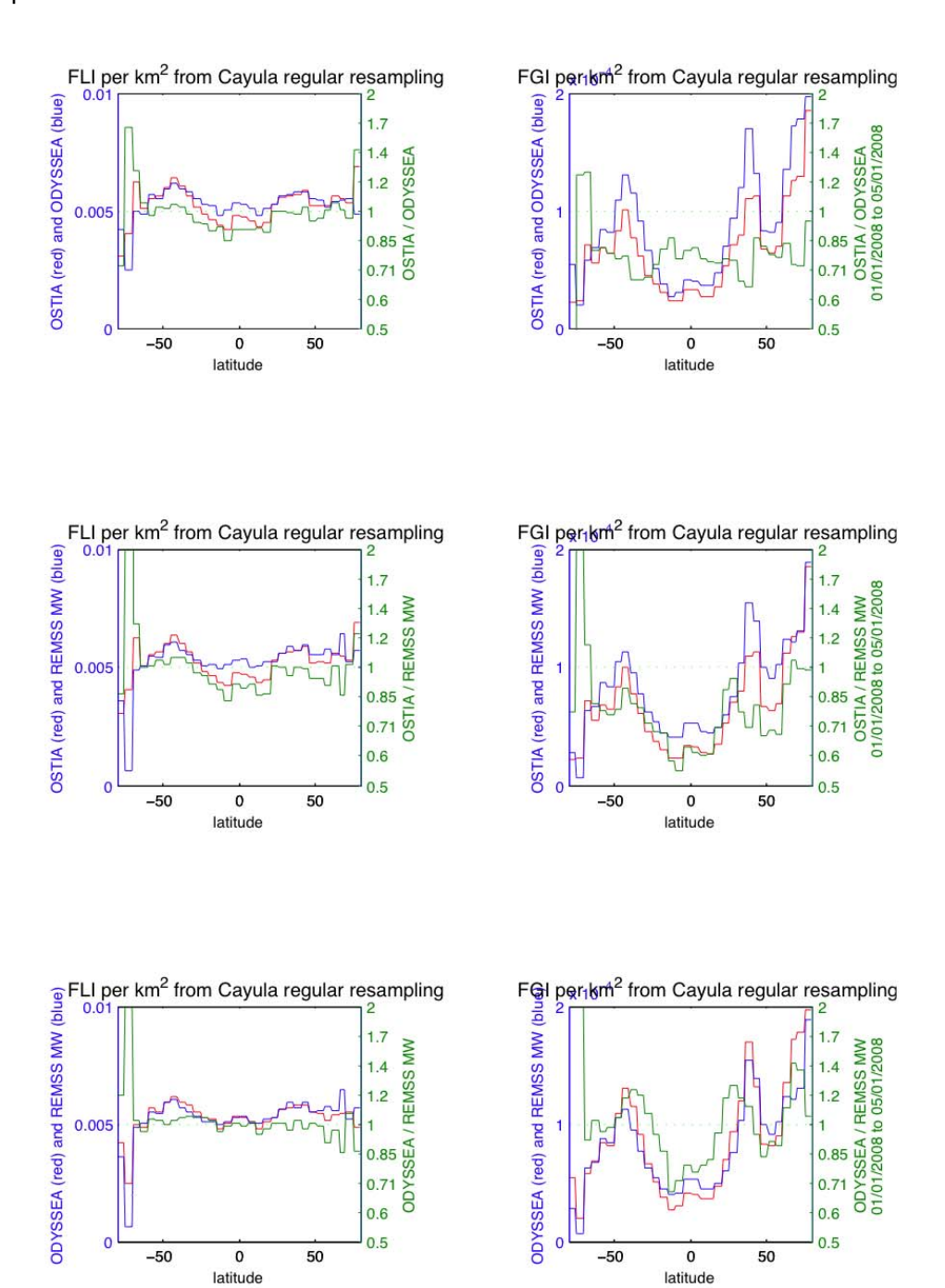


Figure 4-22: Zonally averaged Front Length Index (FLI, left) and Front Gradient Index (FGI, right) and ratios of OSTIA, ODYSSEA and REMSS MW between 01/01/2008 and 05/01/2008. Fronts were detected with the Cayula algorithm, with a window size WS=180 km, and no minimum temperature difference: $\Delta T_{min} = 0 K.$

latitude

latitude

4.5 From temperature gradient to density gradient

Chapter 2 showed that resolving the density gradient in the mixed layer allows one to quantify dynamical properties of the vertical exchanges occurring at density fronts in certain conditions. In this thesis the temperature gradient in the mixed layer is used as a proxy for the density gradient, assuming the salinity constant over the front. This strategy is valid if and only if the temperature change dominates the salinity change in the equation of state which relates the temperature and salinity to the density. Where it is not the case, the density gradient cannot be estimated from the temperature gradient alone. Doing so indeed results in the underestimation of the density gradient in the case of a front warm and fresh on one side and cool and salty on the other or in the extreme case of a salinity front with constant temperature. Conversely, the density gradient is overestimated where the front is warm and salty on one side and cool and fresh on the other, the worst case being the exact cancelation of temperature and salinity gradients effects on density. This phenomenon is called compensation because temperature and salinity compensate in their effect on density. It has been known for some time for certain fronts at scales of a few tens to one hundred kilometres (Roden 1975). Compensation was also measured at horizontal scales as small as 10 km (Ferrari & Rudnick 2000). The correlation between thermohaline gradients is often quantified in terms of the ratio of the relative effect of potential temperature and salinity on density, the density ratio,

$$R = \frac{\alpha \cdot \Delta \theta}{\beta \cdot \Delta S} \tag{4-1}$$

where θ is the temperature, and S is the salinity, and ρ the density, and $\alpha = -\rho^{-1}(\partial \rho/\partial \theta)$ and $\beta = \rho^{-1}(\partial \rho/\partial S)$ are the expansion coefficients of temperature and salinity. Although the density ratio has been used vertically to characterize thermohaline structure from vertical profiles, it is applied on horizontal spatial differences in this thesis. The relative error in the density gradient calculated under the assumption that the salinity is constant is

$$\frac{\Delta \rho_{real}}{\Delta \rho_{estimated}} = \left(1 - \frac{1}{R}\right),\tag{4-2}$$

where $\Delta \rho_{estimated} = -\alpha \cdot \Delta \theta$. Compensated fronts have a density ratio of 1, they are characterized by a temperature gradient but a constant density. In this

configuration a non-real density gradient is detected on SST. A front where the effect of temperature on density is opposed to but twice that of salinity has a density ratio of 2. In this later case the density gradient is overestimated by 100% from SST. Fronts where the effect of temperature on density dominates that of salinity have a density ratio $|R| \gg 1$. The higher |R| is, and the more accurate is the estimation of the density gradient from the temperature gradient alone.

The existence of compensated fronts can be explained in the following way: assume that atmospheric forcing, mesoscale stirring and entrainment of thermocline waters create random distributions of temperature and salinity in the mixed layer. Regions will exist in which the horizontal gradients of temperature and salinity will happen to compensate in their effect of density, whereas in other regions they will create horizontal density gradients. The horizontal density gradients at small scale will slump under the action of gravity and restratify the mixed layer. Any subsequent strong vertical mixing results in a weakening of the horizontal density gradients. The thermohaline gradients that are compensated do not slump and do not experience horizontal dispersion and therefore persist (Ferrari & Rudnick 2000). At larger scales, slumping can occur, as due to baroclinic instability, but density gradients can persist in geostrophic balance. The phenomenon of compensation should thus be most prominent at scales smaller than about 10 km (Rudnick & Martin 2002). The most exhaustive study of the compensation in the world's ocean is presented by Rudnick and Martin (2002). The authors based their investigations on 15 years of towed instrument (SeaSoar) in-situ campaigns in the Pacific, Atlantic and Indian Ocean. They found compensation in all oceans, on 3-4 km horizontal scales, when the mixed layer is deep and significant thermohaline variability exists. The tendency for compensation is stronger as mixed layer depth increases and for mixed layer deeper than 75 m, a density ratio near 1 is typical. Conversely, compensation is not typical in shallow mixed layers, or when thermohaline variability is weak. Regions such as the subtropical gyres where the variability in salinity is low at small and meso-scales do not experience significant compensation. At moderate mixedlayer depths between 25 and 75 m, the density ratio is poorly defined. At the smallest mixed layer depths, temperature dominates density variability (R is large). The authors speculate that horizontal density gradients exist in all

conditions, in the deep winter mixed layer depth or in the shallow summer one, but they are confined to frontal regions while most of the ocean has compensated thermohaline variability.

The consequence of these findings for this thesis is that the estimation of the density gradient from the temperature gradient in the mixed layer is considered reliable for shallow mixed layer depths. One should be confident in the dynamical frontal indexes based on parameterizations that estimate the dynamics as a function of the horizontal density gradient only when the mixed layer depth is shallower than 75 m. This is a fundamental limitation of the usage of SST for vertical circulation parameterization over fronts. It should be stressed however that the need for such parameterization is more stringent over the shallow mixed layer depth regions because when the mixed layer is deep, vertical circulation is dominated by the wind stress induced mixing. In addition, surface temperature can be used as a passive tracer to measure turbulence in compensated and non-compensated situations. The simple frontal indexes are thus a valid way to observe turbulence in all conditions, while the dynamical indexes are restricted to the shallow mixed layer regions. Improvements in the understanding of the density ratio in the deep mixed layer or new systems for high resolution salinity satellite acquisition could overcome this limitation.

4.6 Conclusion on the dataset/method to use

It is not possible to study the small scales and benefit from a high temporal coverage on the same SST dataset. It was therefore necessary to adopt two parallel strategies with regard to the input SST data on which the fronts are searched for. They are summarised in Table 4-3.

The first strategy takes advantage of the spatial and temporal coverage of some of the GHRSST Level-4 product. The selected product is OSTIA and OSTIA reanalysis because they offer the longest time span. The following chapter explores in more details the seasonal variability in the presence of small scales within several Level-4 SST products. In the two following chapters it will be

discussed whether these products should be smoothed before the fronts are detected to avoid artefact variability generated by the cloud coverage.

The fronts are detected with the Canny algorithm because it is more easily linked to the dynamics as explained in chapter 3.

The second strategy focuses on the small scale variability. Since it is not resolved by the Level-4 SST products, the ODYSSEA Level-3 super-collated products are chosen. The pixels that originate from microwave acquisitions are discarded and only infrared ones are kept in order to keep the spatial resolution consistency. No smoothing is applied to preserve all the small scale activity. The Canny algorithm is also selected because of its relevance in the geophysical studies, despite its reduced ability to detect fronts in the vicinity of missing data.

Focus	SST dataset	smoothing filter	method	time span
time and space coverage	OSTIA + OSTIA reanalysis	Various levels of smoothing +none	Canny	1985-today
small scale variability	ODYSSEA Level-3 infrared only	none	Canny	October 2007- December 2009

Table 4-3: summary of the two stages of frontal exploration.

5. Chapter 5: Frontal Indices

5.1 Introduction

This chapter deals with the practical implementation of the principles and results presented in the first three chapters. The description of the dynamics of the mixed-layer associated with surface density fronts (chapter 2) is combined with the discussion on the frontal detection algorithms (chapter 3) and the exploration of multi-sensor SST datasets (chapter 4) to produce a novel set of frontal indices which attempt to capture physical parameters of the mixed-layer. The objective of this chapter is to demonstrate that the physics presented in the first chapter can be applied in practice on satellite images of surface temperature. A methodology is presented to compute maps and time series of physically meaningful frontal indexes. This methodology relies mostly on three parameters: the level of smoothing applied on the SST image before the fronts are searched, the minimum strength of the fronts that shall be retained and composited in the indexes, and in some cases the assumed width of the fronts. These input parameters are chosen based on the literature and practical deductions. The sensitivity of the results to these parameters is discussed when no objective choice was possible. Some of the indexes provide objective results that can be compared to the literature; others need to be calibrated through the optimal choice of parameter values to return results comparable to independent estimates in the literature of the physical parameter. In both cases, the construction of the indexes allows the robust assessment of the outcomes of the first three chapters as well as some assumptions made in some physical oceanography publications.

The common characteristics of the calculated frontal indexes are presented first. The computational aspects are then exposed. The conversion of the SST to surface density is described, including a discussion on how to minimize the error due to frontal compensation of salinity and temperature. In the remaining subsections of the chapter several indexes are presented and discussed, in order of increasing complexity. Each of them is applied to a specific scientific case and is explored from both a qualitative and quantitative perspective.

5.1.1 General aspects of the frontal indexes

The frontal indexes presented in this thesis are quantitative values of a frontal property that are calculated per surface area and per time span. They are stored on three-dimensional maps with latitude, longitude and time as dimensions. The maps are all consistent in both space and time so that their values for various places and dates can be combined or compared. In order to explore their spatial and temporal variability while minimizing the disk space necessary to store them, they are always created in two versions simultaneously:

- a) The High Spatial Resolution (HSR): this version provides a high spatial resolution of 0.1° but a low temporal resolution of 1 month.
- b) The High Temporal Resolution (HTR): this version provides a low spatial resolution of 1° but a high temporal resolution of 1 day.

It would be very memory consuming to store the frontal indexes at both a high spatial resolution and temporal resolution. Hence, even though the indexes are initially calculated daily over the original SST resolution (typically 0.1°), they are integrated in space in the HTR index file and in time in the HSR one. This allows one to drastically optimize the storage space required as the fronts are calculated on regional to global space scales and annual to decadal time scales. The HSR index allows the display of monthly composite maps of the frontal indexes. On the other hand the HTR index permits the plotting of the spatially averaged frontal indexes over a user-defined region against time. Every time an index is calculated, it is stored in monthly HSR files and a single HTR file.

Each frontal index is stored in a Matlab object file which contains:

a) Metadata associated with the frontal index: the name, description of the run, the type (HSR or HTR), the spatial and temporal resolution, the creation date, last update date, a modification log and the complete configuration parameters used as input to the run that has created the index.

- b) Auxiliary data: the latitude, longitude and time associated to the index three-dimensional grid, the days that were processed, the name of the input SST files ingested and the surface area (in km²) of ocean in each pixel.
- c) Available SST surface: reported for each pixel (in km²). This is equal to the ocean surface in the case of the interpolated Level-4 products but is reduced on the Level-2 and Level-3 products when less or no data are available over some regions, generally due to cloud coverage or satellite repeat cycle. This information is recorded over the same spatial and temporal resolution as the frontal indexes as this allows spatial averages per unit of surface to be calculated.
- d) The frontal indexes themselves: the frontal index object stores two indexes, a Frontal Length Index (FLI) and an index that is specific to the run. The FLI keeps track of the total length of the fronts (in km) while the second index is generally linked to the strength of these fronts as the next sections will explain. Each of these two indexes is accompanied by metadata that is composed of a name, a description and units.

The frontal object was designed in the frame of this thesis to support the processes of generating and exploring the frontal information. The metadata and auxiliary data associated to the object allow the user to keep track of the processing performed to create the object, they avoid manipulation errors and allow the parallel processing described below. The Matlab frontal object also includes a set of functions that allow the display of the index in space or time. The plotting functions make use of the metadata to calculate in a statistically meaningful way the temporal or spatial averages for display. The metadata is also automatically displayed on the plots and the units are converted when needed. While the rationale behind this strategy is to offer simplicity to non-expert users of the front detection routines, it has proven to be very valuable

also to the author of this thesis given the high number of runs that were needed.

5.1.2 Computational aspects

The calculation of the frontal index results is achieved with Matlab routines. The generic approach to compute the frontal indexes on one day over a defined region is the following:

- a) Ingestion of SST data from the selected day over the defined region. When needed, SSH data and climatologies of MLD (mixed layer depth) and SSS (sea surface salinity) are also ingested.
- b) If needed the SST is converted to surface density.
- c) If requested, the SST or density field is resampled and/or filtered.
- d) Fronts are detected with the Cayula or Canny methods.
- e) Vector fronts are transferred to frontal indexes.
- f) Results are stored in the frontal indexes Matlab object described in 5.1.1.

The design of the Matlab routines was driven by the characteristics of the processing involved and the needs related to their usage. To calculate a frontal index, one requires:

- The processing of a large number of input files.
- The setting of a large number of parameters.
- A large number of operations to be computed by the routines.

These requirements have driven the design of the processing methodology in different ways. This is described in the following sub-sub-sections.

5.1.2.1 Approach to handle a large number of files

In order to explore the temporal variability of frontal indexes, one needs to calculate them for a time series which should be as long as possible. A global input SST file is needed for each day on which the frontal index is calculated. The approach that was followed is to maximize the time span of the frontal indexes by downloading the complete data sets of SST products presented in Table 4-1. This resulted in above 20000 high-resolution SST files and 6000 altimetry images. This database takes 190 Gb when the files are compressed. The compression factor being close to 10 on average, the approach is to keep only the compressed files. The routines are developed such that they are able to locate the required compressed file and un-compress it before the data are ingested. The un-compression being much faster than the compression, the files are not compressed back after being used. Instead, the compressed file is never removed and the un-compressed file is simply deleted after reading.

5.1.2.2 Approach to handle a large number of parameters

The methodology presented in this thesis to calculate frontal indexes is based on a large number of parameters. Also many runs were needed to obtain the results, each of these runs being defined by a precise set of parameters. In order to keep the set of routines user-friendly and to avoid manipulation errors, the whole software was coded with configuration control. This means that all the parameters were identified, classified and gathered in configuration files. The user simply has to create, or copy and modify, the set of configuration files before starting a processing run. These parameter files are loaded by the routines and parsed through each function that requires runspecific parameterization. The consistency within the parameters is checked to avoid processing errors, and the configuration parameters are stored together with the frontal index results to allow the user to keep track of the settings applied. The set of parameters that the user is invited to define is summarized in Table 5-1.

Table 5-1: Set of parameters for the detection of fronts and the calculation of frontal indexes with the routines developed in the context of this thesis.

generic parameters	mode	e.g. "FrontalIndex" for frontal index calculation		
	run_name	reference of the run		
	run_description	description of the run		
	parallel processing	parallel	1 for parallel processing, 0 otherwise	
		reset_variables	to continue a run started before or to start a new one	
	parameters	loadFilesDuringAllocatedTime	to ensure each parallel process is loading the files at a different time	
		pauseDuringWorkHours	to pause the processing during the day not to overload a shared workstation	
	time management	stopProcessingAt	to stop the run at a defined time even if the run is not finished	
		restartMatlabEvery	to restart Matlab regularly and avoid memory leakage	
	id	user name		
Dataset parameters	name	name of the SST dataset to detect fronts on (e.g. "OSTIA", "ODYSSEA")		
	returnOnlyInfraRedFromL3	to discard microwave measurements from Level-3 products		
	continueOSTIA_RANwithOSTIA	to build a long time series with OSTIA_RAN and OSTIA		
	regionName	full name of the region		
	lats	latitude bounds of the selected region		
Region parameters	lons	longitude bounds of the selected region		
	HighTemporalResolution	temporal resolution of HTR		
	HighSpatialResolution	spatial resolution of HSR		
	startDate	first day of the time series to process		
Time parameters	endDate	last day of the time series to process		
	dateIncrement	increment of the time series to process		
	name	method name ("Cayula" or "Canny")		
	detectsFrontsOn	"temperature" or "density"		
		initialResampling	to resample the image	
	resampling	interpMethod	interpolation technique	
	filtering	filterImage	to filter the image before fronts are detected	
Front		filter	"mean" or "gaussian"	
Front detection Method parameters		filterSize	size of the filter in km	
		fastFilter	to apply a faster approximation filter	
		highPassFilter	to remove low spatial frequencies	
	minimumFrontLength	minimum length in km of the fronts to be retained		
	divideGrid	if needed, resolution of the division grid to process the original image in bits		
	Cayula method	regularResampling	to resample the image on a sinusoidal	
		regularResamplingPixelSize	width of the pixels of the sinusoidal	
	minimumFrontLength divideGrid	filterImage filter filterSize fastFilter highPassFilter minimum length in km of the if needed, resolution of the dimage in bits regularResampling	to filter the image before fronts a detected "mean" or "gaussian" size of the filter in km to apply a faster approximation to remove low spatial frequencie fronts to be retained ivision grid to process the original to resample the image on a sinusequal-area grid	

		windowSize	size in pixels of the Cayula window decomposition
		minimumTempDiff	minimum temperature difference in K within the Cayula window
		outputFronts	value to keep as frontal strength: "temp_diff" or "gradient"
	Canny method	thresholds	T1 and T2 thresholds of the Canny method
Frontal Index	name	name of the frontal index to calculate based on the detected fronts (e.g. "FGI" or "Spall95_Subduction")	
construction parameters	FrontalWidth	frontal width assumed in the calculation of some frontal indexes	

5.1.2.3 Approach to handle a very large processing load

Detecting fronts on many high-resolution SST images requires a large number of operations. It was necessary to optimize the processing to keep the run computation time realistic. An important action towards achieving this was to implement the algorithms with matrix operations rather than iterative loops which are very much slower. Whenever possible, compiled in-built Matlab functions were exploited to speed-up the processing. Image processing Matlab library provided efficient functions that had to be used in a specific way to retain the geophysical meaning of the processing. The GSW library that was used for the sea water equation of state was optimized so that it could be applied on large two-dimensional data sets. One part of the frontal detection algorithms could not be implemented with matrix operations. This consists of the front-following step that links potential frontal pixels into front vectors. This is an iterative process with a non-linear memory usage which can be optimized by processing the SST images chunk by chunk. The SST image is divided into typically 10° chunks and the frontal index is calculated per chunk. The prior spatial filtering step is also computationally heavy due to the geographical projection of the data. As explained in chapter 3, to keep a filter width that is fixed in km, one should adapt its size in pixels depending on the latitude as the conversion from longitude increment to km is not constant. As a consequence, one needs a different filter shape for each line of latitude in the SST image. This is not implementable with the Image Processing Matlab functions so it was decided to apply a fixed filter shape per chunk which allowed the use of the fast in-built Matlab functions. This approximation was investigated and showed to generate a negligible level of error in the filtering.

In order to further speed-up the processing, parallel processing functionalities were introduced in the developed routines. This allows launching the

computation of a run on several processors of the same workstation and on several workstations simultaneously. The advantage is to multiply the processing power available and divide the processing time by the number of processors running. Obviously, the parallel processing capability brings additional complexity to the implementation of the algorithms. The jobs of the processors running simultaneously need to be orchestrated so that the workload is efficiently distributed across the processing resources. The processors communicate with each-other with the help of common files that allow keeping track of the processing progress and ensuring two processors are not doing the same thing twice. The parallelization is achieved at the level of the choice of the SST image. This means that each processor takes the responsibility to process a particular product that corresponds to a day on which the run is asked to detect fronts. The resulting frontal index files are common to the mobilized processors and each processor is saving its results on them. Care is taken so that several instances of Matlab distributed on different processors do not read or write these common files simultaneously since this would result in file corruption. The configuration parameters are compared to the ones attached to the frontal index files to avoid human manipulation errors and guarantee consistency of the results within one file.

Despite the various optimization strategies implemented in the routines, getting the frontal index results requires very long processing runs. With 4 processors running in parallel some runs may take up to a week to complete. Hence, the software had to be designed in a way that it offers autonomy and robustness. The capability to automatically quit and restart Matlab and continue the processing every hour was added in order to contain the Matlabtypical memory leakages that slow the processing after a few hours of continuous computations. The powerful workstations that these routines run on are shared with other users and are regularly serviced by the IT support. Consequently, the processing run should be robust to regular breaks in order to free the machine to another user or allow a reboot of the workstation after an update. This process becomes very time-consuming for the user of the routines if the latter are not robust and autonomous enough. This is the reason why they were implemented such that they may be stopped or killed at any point and restarted at a later stage by a simple and unique command. The restarted routines are able to continue the processing where it was stopped

without any major user intervention. This strategy also demonstrated its utility during the development stages as it allows easy recovery from crashes. The thorough logging across the processing is part of this strategy as it allows the user to keep track of the processing progress.

Figure 5-1 presents the architecture of the routines and the data flow between the Matlab functions. The function *computeFrontalIndexParallel.m* is in charge of the orchestration, the parallel distribution of the work and the saving of the results. It interacts with the processing status files which are run-specific but shared between processors, and the results data bank. For each day from which the processor is required to detect fronts, it calls computeFrontalIndexOneDay.m which returns the frontal indexes over the defined region on the day that is parsed through. The latter function is in charge of the data ingestion and the SST grid division into chunks. For each chunk it calls computeEdges.m which returns the frontal index over the parsed chunk of data. The latter filters and resamples the SST data and converts it to sea surface density if required. It also computes the gradient and applies the front detection algorithm that is parameterized in the configuration files (Canny or Cayula). It then calls computeFrontalIndexFromEdges.m which inputs detected frontal vectors and returns the frontal index over the chunk as defined in the configuration files.

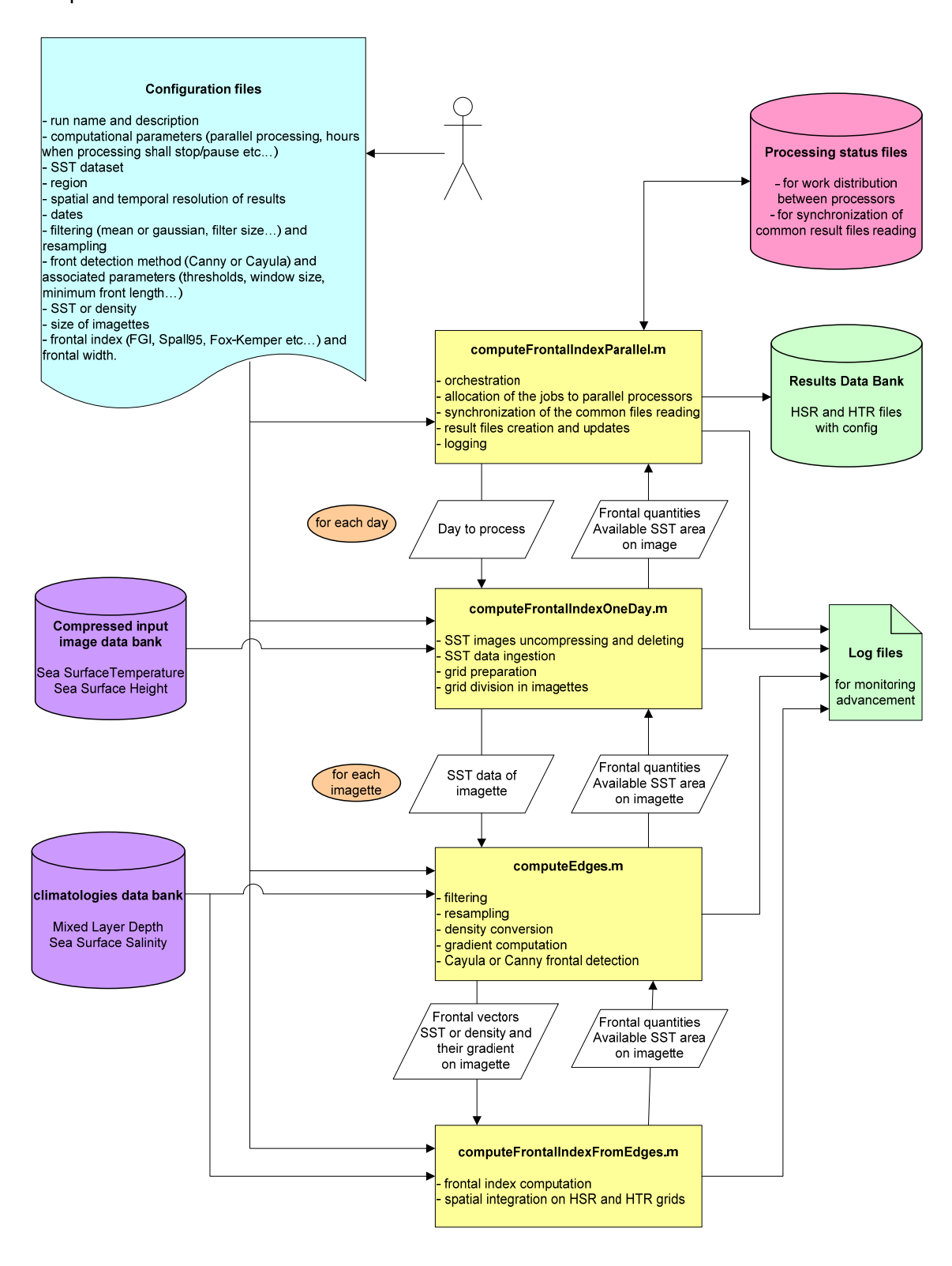


Figure 5-1: General architecture of the frontal detection routines developed in the context of the thesis

5.1.3 Density gradient calculation

As explained in chapters 2 and 4, the density gradient is calculated from the SST images before the fronts are detected, in a geophysically meaningful way. To do so, after an initial resampling and filtering of the SST image, the SST gradient is calculated. The SST gradient is translated into a density gradient, assuming a constant salinity across the front with the formula:

$$\frac{\partial \rho}{\partial x} = \alpha \cdot \rho_0 \cdot \frac{\partial \theta}{\partial x} \tag{5-1}$$

Where θ is the temperature, ρ is the density, ρ_0 is the reference density, and $\alpha = -\rho^{-1}(\partial \rho/\partial \theta)$ is the expansion coefficient of temperature.

 α is dependent both on temperature and salinity. It is calculated with the function gsw_alpha.m of the Gibbs-SeaWater (GSW) Oceanographic Toolbox (http://www.teos-10.org/software.htm). This function uses the computationally-efficient 48-term expression for density in terms of salinity, conservative temperature and pressure (McDougall et al. 2010). In order not to create artificial jumps in the surface density gradient, a monthly salinity climatology is ingested and smoothed to the resolution of the SST. This climatology is the monthly 1° World Ocean Atlas (WOA) 2009 (Antonov et al. 2006).

Equation (5-1) assumes that the salinity is constant across the front. Section 4.5 showed that this assumption is not always valid, and the salinity variations may complicate the relation between temperature and density. The principal risk is to overestimate the density gradient when the front is compensated. The compensation is less likely to occur when the mixed-layer depth (MLD) is shallower than 75m. Therefore the temperature-based mixed-layer depth climatology of de Boyer Montegut et al. (2004) is used to identify the times and locations where the typical mixed-layer depth is deeper than 75m within the three dimensional frontal index data sets. One solution could be to discard any frontal measurements performed over the regions where the MLD is deeper than 75 m at the time of the measurement. Then the time series of frontal quantities would be built by averaging in space the pixels of shallow MLD on each day. This solution was not retained because it would have introduced seasonal biases caused by the seasonal patterns of the MLD.

Instead it was chosen to combine pixels of all MLD in the spatial averaging but to flag the times when the frontal quantity is based on more than 50% of pixels with a deep MLD. The flagged times are displayed in red in the frontal index time series and identify the periods when the confidence in the frontal index is lower due to possible compensation. Figure 5-2 illustrates the regions in the North Atlantic that are affected by a deep MLD across the seasons.

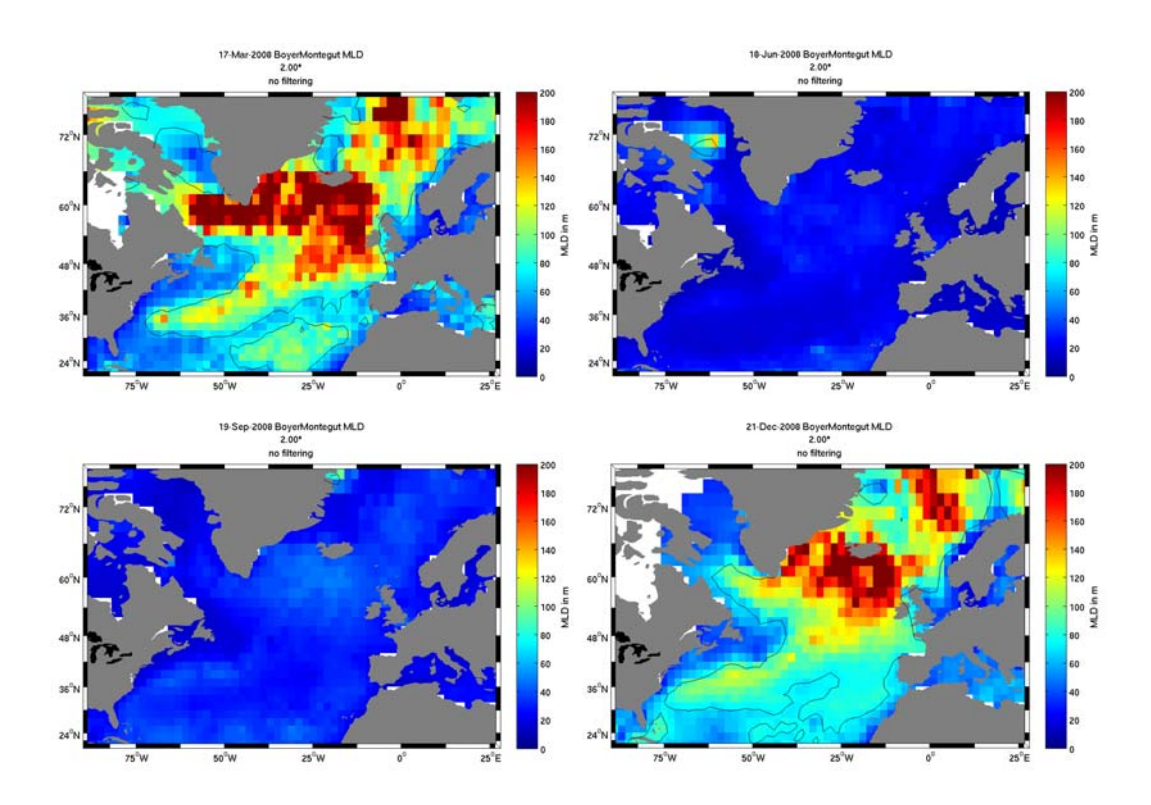


Figure 5-2: De Boyer Montegut et al. (2004) climatology for mixed-layer depth on the North Atlantic for March (top left), June (top right), September (bottom left) and December (bottom right). Depth 75 m is plotted on the black contour.

5.2 Frontal Gradient Index

This section presents the basic Frontal Length Index (FLI) and Frontal Gradient Index (FGI) introduced in Chapter 3. FLI is the total length of the detected fronts in a defined region and over a defined span of time:

$$FLI = \sum_{\substack{days \ in \\ time \ span}} \int_{\substack{fronts \\ in \ region}} dx$$
 (5-2)

Where *x* is the direction following the frontal paths. FGI is the integration of the frontal strength along the detected fronts. The frontal strength is measured as the horizontal density gradient magnitude on the front locations.

$$FGI = \sum_{\substack{\text{days in } \\ \text{time span}}} \int_{\substack{\text{fronts } \\ \text{in region}}} |\nabla_{H}\rho| \cdot dx$$
 (5-3)

When the fronts are detected with the Canny method, they are located on the surface density gradient crests, which means that they lie on local maxima of surface density gradient in the gradient direction. In these conditions:

$$FGI = \sum_{\substack{days \ in \\ time \ span}} \int_{\substack{fronts \\ in \ region}} \left| \frac{\partial \rho}{\partial y} \right| \cdot dx$$
 (5-4)

$$FGI = \left| \frac{\partial \rho}{\partial y} \right| \cdot FLI \tag{5-5}$$

Where y is the direction orthogonal to the front orientation; and $\overline{\left|\frac{\partial \rho}{\partial y}\right|}$ is the average gradient magnitude on the detected fronts.

These indices are a first order indicator of stirring and mixing processes. When the fronts are detected with the Canny algorithm, which is the case in this chapter, the FLI indicates the length of the elongated crests that lie on a gradient whose magnitude is greater than a selected threshold. It should be noted that the FLI carries some information about the strength of the fronts because it is a measure of how many fronts there are that are stronger than the threshold. The FGI is complementary to the FLI because it is also dependent on the average strength of the fronts above the threshold. Equation (5-5) is true for each spatial and temporal pixel of the frontal index separately, FGI and FLI are not proportional for any time and location because the

distribution of the gradient magnitude on the detected fronts is not constant in space and time.

It should be recalled that although these frontal indexes represent averages or integrations of frontal parameters over a defined region and time span, they are calculated on single high-resolution two-dimensional surface density snapshots. Quantitative values of frontal index are calculated per day in a way that is consistent in time so that these values can be compared at different times. However the indexes are processed on each day from the density map of the selected date, with no consideration of the density at the day before or after. This approach is different than that of Miller (2009), who suggested a frontal index that combines the location, strength and persistence of the fronts detected over several days into a single map. This index is efficient to produce a synoptic view of the dynamics over a few days without blurring the changing patterns as occurs when time averaging cloud-affected sequences of SST images. Miller's (2009) frontal index provides qualitative frontal maps that allow intuitive interpretation of mesoscale features. The author of this thesis was not able to develop a reliable methodology to associate fronts detected on one day to those detected on the next, with a quantitative geophysical meaning.

The computation of FLI and FGI relies on two main parameters: the smoothing filter applied on the density scenes before the front detection and the thresholds T₁ and T₂ of the Canny front detection algorithm. Chapter 4 describes how daily variability in the cloud coverage can compromise the temporal and spatial consistency of the spatial scales present in a Level-4 SST product. One way of ensuring this consistency is to apply a low-pass spatial filter on the density field and remove the portion of the spatial spectrum that is dependent on the cloud coverage. This filters out the small scales in which one is not totally confident, either because it is considered as noise, or because it is suspected to carry artefact signals generated by the variability in the availability of infrared SST products. The consequence of the low-pass filter is to modify the spatial spectrum of the density field over which the fronts are detected. This means that the smoothing filter determines which part of the spectrum is explored for fronts. When no filtering is applied or when a small amount of smoothing is involved, the smallest scales of the density field are retained and the fronts are detected on fine features. Conversely, when a

larger amount of smoothing is applied on an image, one can be more confident in the spatial and temporal consistency of the detected fronts but the small scale features are ignored. Therefore the decision on the required amount of smoothing is the result of a trade-off between the confidence in the scale consistency and the ability to resolve small scale frontal features.

The Canny thresholds T_1 and T_2 are set to an equal value:

$$T = T_1 = T_2 {(5-6)}$$

This simplifies the geophysical interpretation of the detected fronts as one can conclude that the fronts are detected on the crests of the density gradient magnitude where the gradient magnitude is greater than T.

Chapter 3 shows that applying a smoothing filter on an image reduces the gradient magnitude on the fronts whose width is of the same order of magnitude or smaller than the smoothing filter size. The decision was taken to apply running mean filters rather than Gaussian ones because the effect of the former on the spectrum is simpler to interpret. The smoothing effect of the running mean filter is equivalent to a spatial sampling at a lower resolution. The gradient reduction depends on the size of the running mean filter and on the width of the fronts. Once a field has been down-sampled or smoothed, the information about the small scales is lost. The width of small fronts is then unknown even though the smoothing filter is known. One can recover the spectrum at the small scales from the larger scale spectrum if the surface density spectrum slope is known. Fox-Kemper et al. (2011) show that if the buoyancy spectral slope is assumed to be locally k⁻², the horizontal buoyancy gradient can be scaled so that it is independent from the resolution of a model grid. The average $\langle |\nabla_H \overline{b^z}|^2 \Delta s / L_f \rangle$, over a scale $L_b \gg \Delta s \gg L_f$ is approximately independent of Δs , where $\nabla_H \overline{b^z}$ is the depth-average of the horizontal buoyancy gradient over the mixed layer. Δs is the model grid-scale dimension in Fox-Kemper et al. (2011). L_f is an estimate of the typical local width of mixed layer fronts. In this thesis we assume that $\nabla_H \overline{b^z} = \nabla_H b$ at the surface. This approximation is developed to account for the small-scales that are not resolved by numerical model resolutions. It was adapted in the context of this thesis to scale the gradient magnitude of datasets with different resolutions in order to allow their inter-comparison. The autocorrelation filter applied in the

optimal interpolation (OI) in the creation of the SST Level-4 products has an effect on small scales similar to the smoothing applied in the front detection process or to a sampling at a coarser resolution. Hence Δs is chosen per SST product as an approximation of the feature resolution, which is the smallest scale resolved within the image. The feature resolution is greater than or equal to the actual product resolution, but it is also dependent on the smoothing involved both in the creation of the product and in the front detection. It should be noted that this scaling is an approximation of the energy at small scales, but only at the scales that are not resolved by a particular product and smoothing. The aim of this study is to push the spatial scales of the SST products to their finest limits; however these limits are different for each product. So this scaling is applied to allow the application of a consistent Canny threshold amongst the products.

The horizontal wavenumber spectrum of near-surface density variance has been shown to scale with k⁻² by a number of studies. Ferrari and Rudnick (2000) used SeaSoar observations to sample the temperature and salinity of the mid-Pacific near-surface ocean over horizontal length scales ranging from 100 m to 100 km. They confirmed this scaling which is consistent with the numerical model with ubiquitous fronts of Capet et al. (2008a). Altimetric velocities also display a near k⁻² rolloff at high wavenumbers despite a strong noise contamination (LeTraon et al., 2008).

If the density variance is assumed to be locally equal to $B(k) = B_o * k^{-2}$, the PSD (power spectral density) of the horizontal density gradient is $B_{gradient}(k) = B_o$. The scaling recovers the energy at scales in $[\Delta s, L_f]$ based on the energy present at scales in $[L_b, \Delta s]$ in a linear function of the scales. It assumes that the PSD of the horizontal density scales to k^{-2} in the missing part of the spectrum ($[\Delta s, L_f]$) but also in the part of the spectrum present in the original image ($[L_b, \Delta s]$). Unfortunately, the level-4 products PSD do not always scale with k^{-2} , as is shown by Reynolds and Chelton (2010), who have calculated an average zonal wavenumber spectrum in several regions. For instance, they showed that the wavenumber dependence of the OSTIA images ranges from k^{-4} to k^{-5} . In such a case the scaling will not bring back all the energy present at scales $[\Delta s, L_f]$ (and not resolved by the product) because the energy at scales $[L_b, \Delta s]$ is

underestimated by OSTIA in the first place. The following analyses in section 5.2 explore the consequences of this spectrum in terms of frontal content.

An important issue is which Canny threshold to retain. The FGI index attempts to capture the fronts associated with vertical exchanges. The thresholds are extracted from the literature and numerical studies that explore these dynamics at fronts. Capet et al. (2008b) define the fronts as the regions satisfying the inequality $|\nabla_H \rho| > 1.2 \times 10^{-4} kg \ m^{-4}$ in their numerical model. Strong frontogenesis conducive of vertical velocities is observed in the model over those regions. However, this density gradient magnitude is observed on none of the Level-4 products, even with no smoothing involved. The scaling described above can be applied to scale the density observed in the Capet et al. (2008b) model to the density calculated from the SST products. The real density gradient would be measured if $\Delta s = L_f$. Hence:

$$|\nabla_{H}\rho_{real}| = |\nabla_{H}\rho_{measured}| \cdot \sqrt{\frac{\Delta s}{L_{f}}}$$
 (5-7)

The equation (5-7) is valid for the measured density gradient both on the numerical model of Capet et al. (2008b) and on the density gradient calculated from the SST. Assuming that L_f is equal on both scenes, this leads to:

$$\left|\nabla_{H}\rho_{meas_SST}\right| = \left|\nabla_{H}\rho_{meas_Capet}\right| \cdot \sqrt{\frac{\Delta s_{Capet}}{\Delta s_{SST}}}$$
 (5-8)

Where $\Delta s_{Capet} = 0.75 \ km$ is the grid-scale of the numerical model. Taking for instance $\Delta s_{SST} = 50 \ km$ as the approximate feature resolution of OSTIA and $|\nabla_H \rho_{meas\ Capet}| > 1.2 \times 10^{-4} kg\ m^{-4}$. One gets

 $|\nabla_H \rho_{meas_SST}| > 1.47 \times 10^{-2} kg \ m^{-3} km^{-1}$ as the Canny threshold. This density gradient magnitude is observed in the California Current region, although the fronts detected are very sparse and do not cover 2.5% of the domain area as occurs in the numerical model of Capet et al. (2008b). Therefore the threshold suggested by Capet et al. (2008b) is not retained.

Spall (1995) used a nonlinear isopycnal primitive equation model to demonstrate how baroclinic instability and the resulting frontogenesis force

the subduction of parcels below and across the fronts. The initial configuration of the front is a variation of $0.3 \ kg \ m^{-3}$ across $16 \ km$, which corresponds to:.

$$|\nabla_H \rho_{Spall}| = 1.875 \times 10^{-5} kg \ m^{-4} = 1.875 \times 10^{-2} kg \ m^{-3} \ km^{-1}$$
 (5-9)

This threshold is retained in this thesis for the calculation of FLI and FGI, it is scaled for each SST dataset following Equation (5-7). The following subsections present the FLI and FGI averaged over the North-Atlantic and plotted against time, while varying the following parameters:

- The SST dataset.
- d is the size of the running mean filter applied to the density image before the fronts are detected.
- L_f is an estimate of the typical local width of mixed layer fronts.
- Δs is an estimate of the feature resolution of a SST product after the smoothing stage which depends on the spatial sampling (resolution), the size of the autocorrelation filter applied in the optimal interpolation stage for Level-4 products and the smoothing applied on the image before the fronts are detected.

The Canny threshold is set to

$$T = \left| \nabla_H \rho_{Spall} \right| \cdot \sqrt{\frac{L_f}{\Delta s}}$$
 (5-10)

The Figure 5-3 displays the area that defines the North Atlantic region, and Figure 5-4 shows the percentage of it that has a mixed layer depth shallower than 75 m against time, as calculated from the Boyer-Montegut MLD climatology.

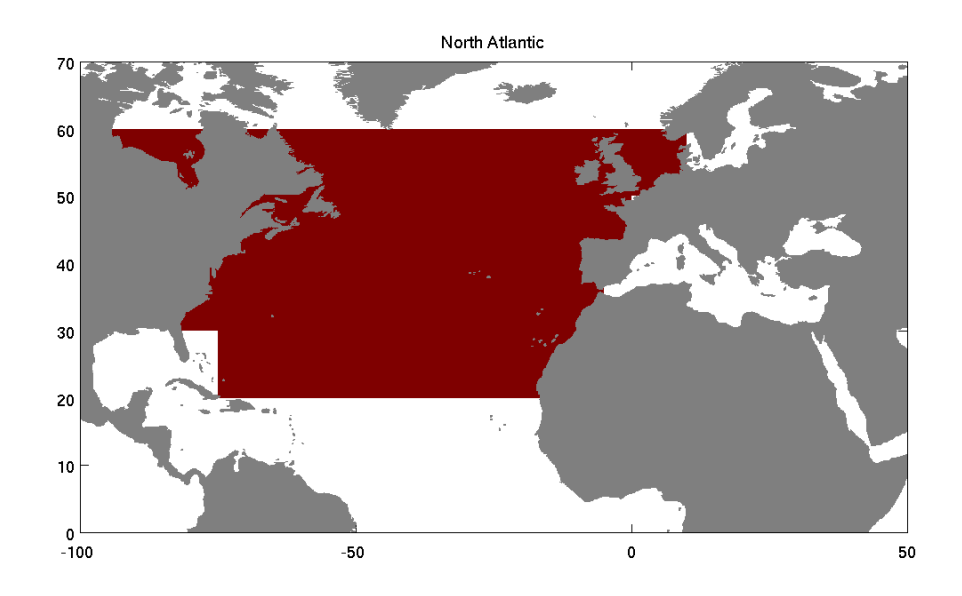


Figure 5-3: North Atlantic region.

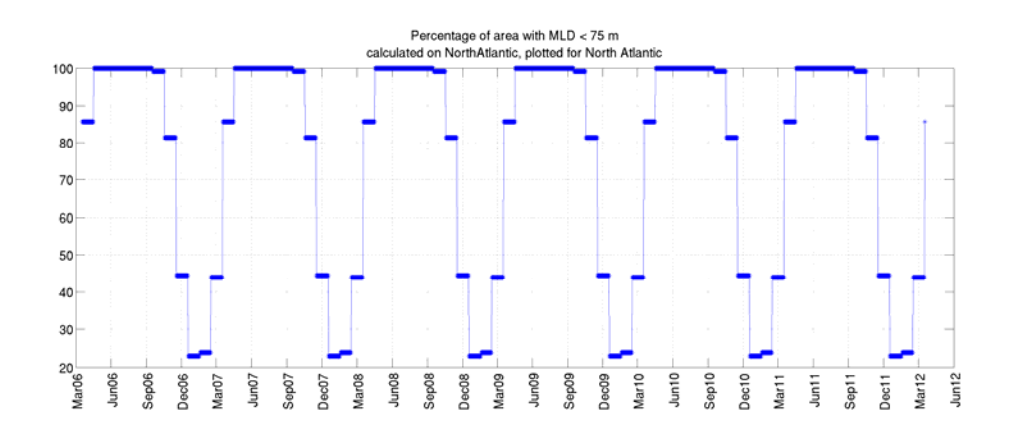


Figure 5-4: Percentage of the area of the North Atlantic region that has a mixed layer depth shallower than 75 m.

5.2.1 FLI and FGI from OSTIA

Figure 5-5 and Figure 5-6 show the FLI and FGI over the North Atlantic region, with d=0 km, $L_f=0.5$ km, and $\Delta s=25$ km on OSTIA. This configuration does not smooth the OSTIA SST images, converts them to surface density gradient and detects fronts with the Canny method and the threshold as defined in Equation (5-10). This methodology ignores the potential artefact small-scale variability in OSTIA which is described in Chapter 4, and applies no low-pass

filter on the SST image to remove it. The scaling function assumes that the feature resolution of the smoothed SST is 25 km, and that the fronts are 0.5 km wide over the region. The profiles of FLI and FGI are very similar and it is even difficult to distinguish them, as was explained previously yet they carry slightly different information about the dynamics. A strong seasonal signal is present in the time series, with minimum of the indexes between March and April and maximum in August. In this time span of 6 years, one can observe inter-annual variability, with a higher annual average in 2006 and higher annual minima in March 2006, March 2007 and March 2010. Periods of deep MLD which are the times when the confidence in the calculated density gradient magnitude is reduced correspond to sharp decreases of the indexes.

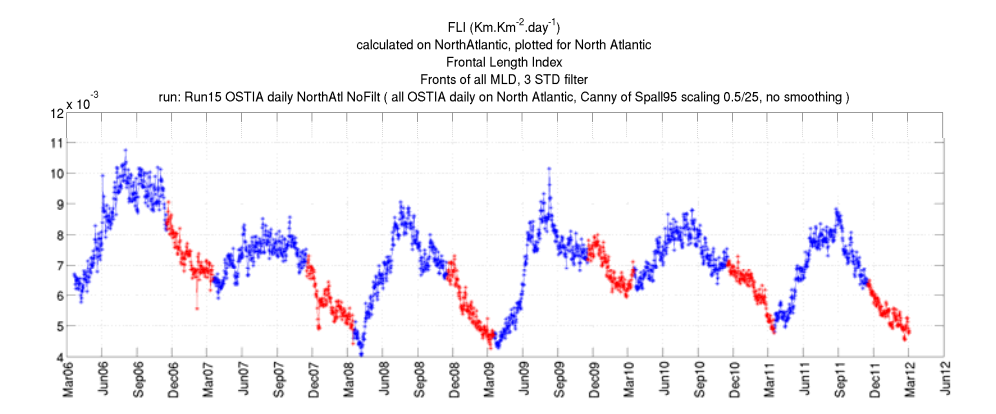


Figure 5-5: Front Length Index (FLI) in $km km^{-2} day^{-1}$ processed on daily OSTIA over the North Atlantic region with d=0 km, $L_f=0.5$ km, and $\Delta s=25$ km. Times when more than 50% of the area MLD is deeper than 75 m are plotted in red.

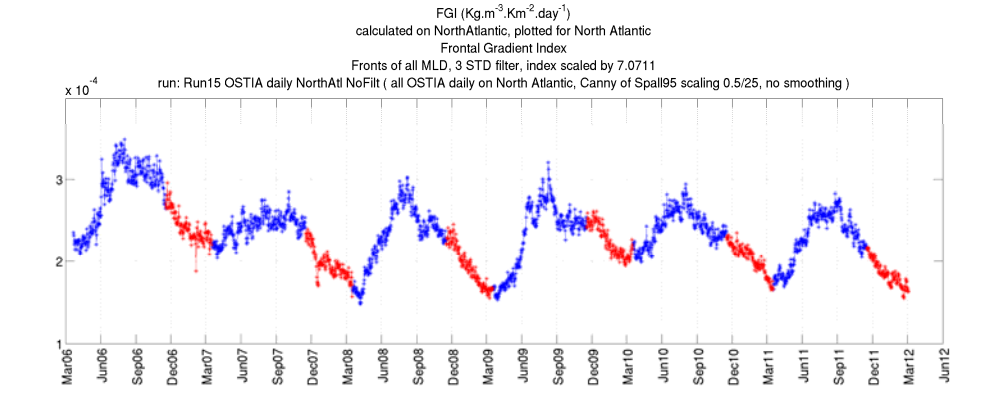


Figure 5-6: Front Gradient Index (FGI) in $kg m^{-3} km^{-2} day^{-1}$ processed on daily OSTIA over the North Atlantic region with d=0 km, $L_f=0.5$ km, and $\Delta s=25$ km. Times when more than 50% of the area MLD is deeper than 75 m are plotted in red.

Figure 5-7 and Figure 5-8 present the same indexes but calculated on a weekly basis. The functions appear less noisy because the daily variability is reduced however the signal is equivalent. This shows that weekly indexes are sufficient when dealing with a time span as large as 6 years to explore the seasonal and inter-annual variability. This result is important in practice because a weekly index is in effect seven times quicker to process than the same on a daily frequency.

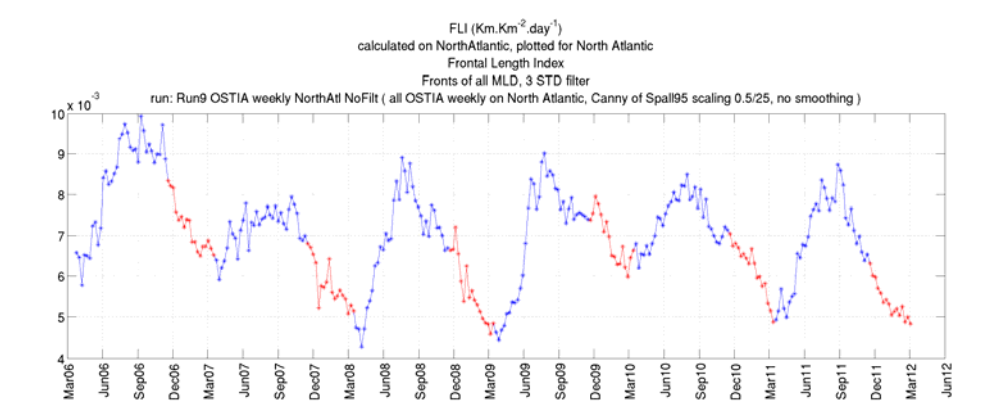


Figure 5-7: Front Length Index (FLI) in $km km^{-2} day^{-1}$ processed on weekly OSTIA over the North Atlantic region with d=0 km, $L_f=0.5$ km, and $\Delta s=25$ km. Times when more than 50% of the area MLD is deeper than 75 m are plotted in red.

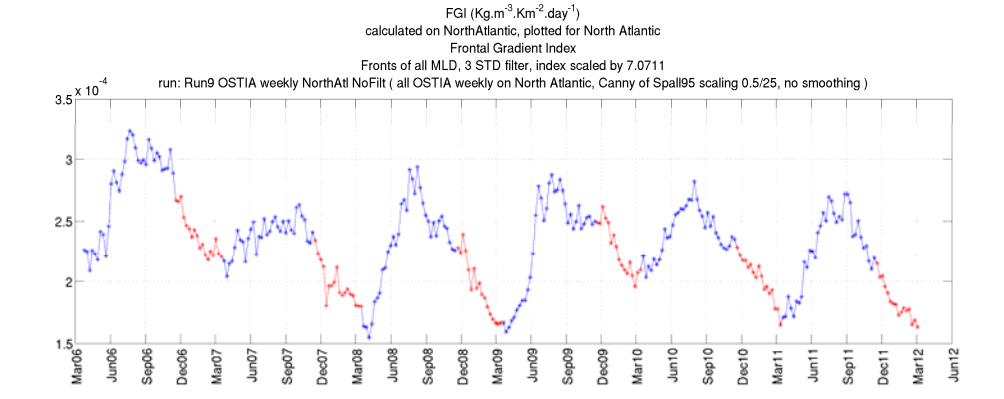


Figure 5-8: Front Gradient Index (FGI) in $kg m^{-3} km^{-2} day^{-1}$ processed on weekly OSTIA over the North Atlantic region with d=0 km, $L_f=0.5 km$, and $\Delta s=25 km$. Times when more than 50% of the area MLD is deeper than 75 m are plotted in red.

Figure 5-9 displays maps of monthly averages of FGI for August 2006 when the index was the highest according to Figure 5-6, August 2007 when the index was at an inter-annual low for a summer time and for April 2008 when FGI was the lowest. Comparing August 2006 and August 2007, it is possible to explain the higher average during the first month by what seems to be a more stretched Gulf Stream on the West and stronger fronts on the western coasts of Europe. The comparison with the maps of April 2008 is striking, much less frontal index is detected around the Gulf Stream which appears much narrower, and barely any front is detected along the East American coastline and on the Western European seas.

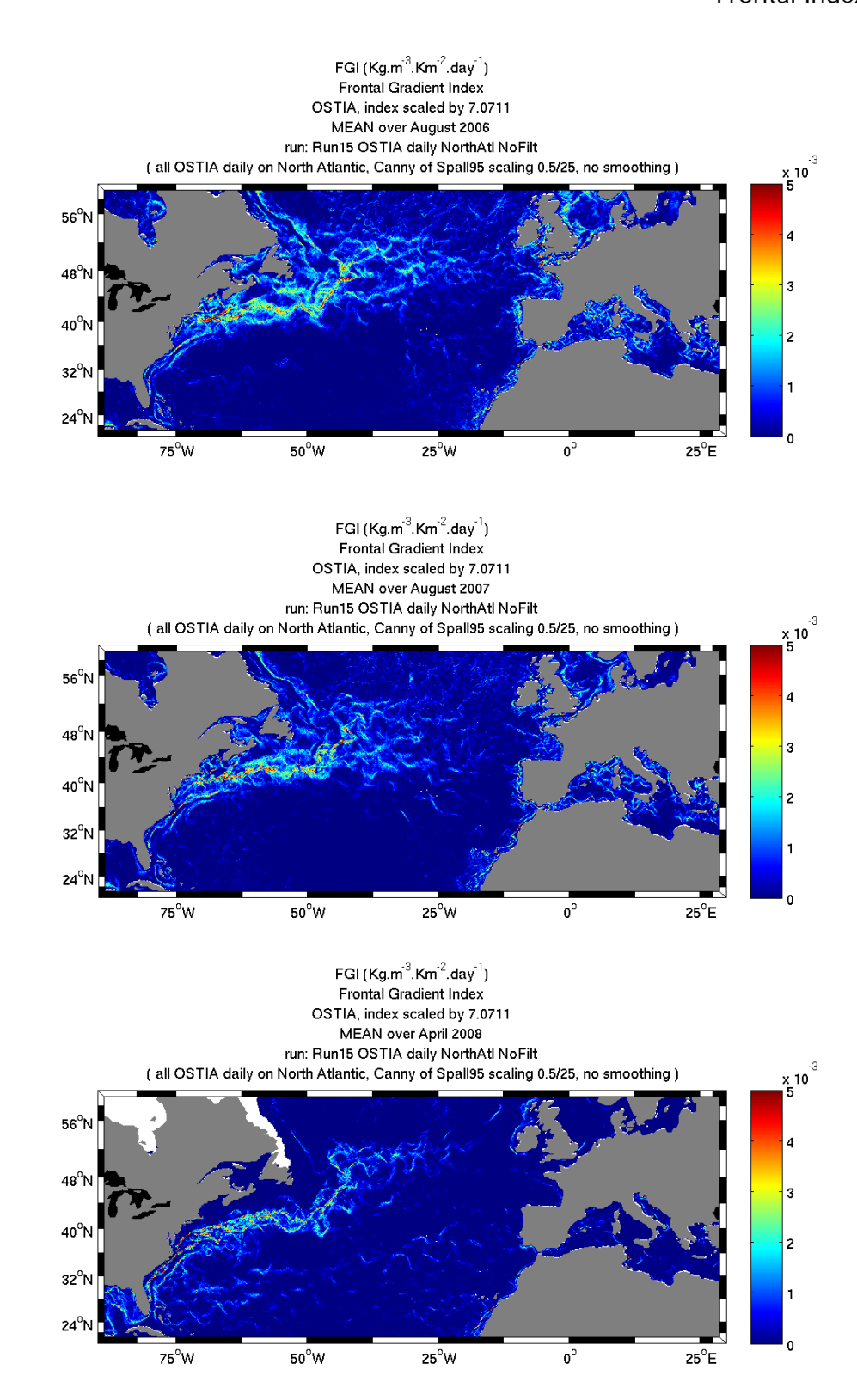


Figure 5-9: Maps of average monthly Front Gradient Index (FGI) in $kg \ m^{-3} \ km^{-2} day^{-1}$ processed on daily OSTIA over the North Atlantic region with $d=0 \ km$, $L_f=0.5 \ km$, and $\Delta s=25 \ km$. Top: August 2006, middle: August 2007, bottom: April 2008.

Figure 5-10 displays the daily percentage of cloud coverage over the North Atlantic. One can notice a seasonal variability in this temporal signal, with a low cloud coverage of about 50 % during the summer and a high of nearly 65 % in the winter. It was explained in Chapter 4 how the temporal variability in clouds affects the feature resolution of Level-4 analysis SST products. This is due to variations in the quantity of infrared measurements available for the construction of the products and to the fact that the OSTIA spatial autocorrelation filter gets coarser when less high-resolution data are available around a particular day. This effect may explain part of the seasonal signal in the frontal indexes which would be an artefact of the construction process of OSTIA products.

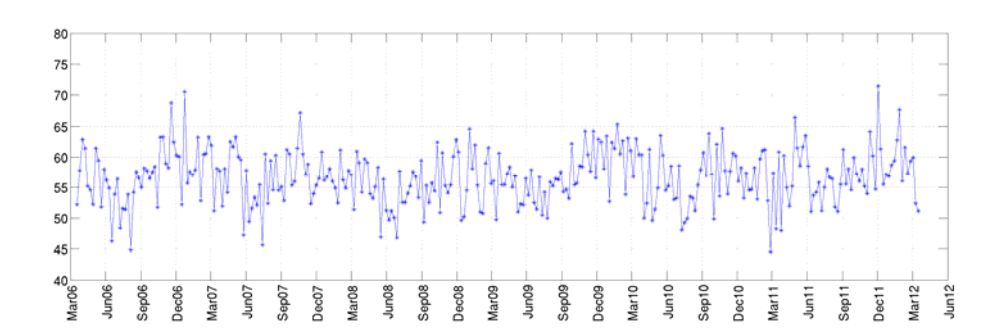


Figure 5-10: NOAA NCEP reanalysis daily percentage of cloud coverage over the North Atlantic.

Figure 5-11 and Figure 5-12 present the FLI and FGI over the North Atlantic region, with d=0 km, $L_f=0.5$ km, and $\Delta s=50$ km on OSTIA. The difference with the previous figures is that the feature resolution Δs is assumed to be twice as large. As a consequence the Canny threshold is reduced to account for a higher estimated smoothing in the production of the dataset. It is not surprising that about twice as many fronts are detected, with a FLI reaching 0.02 km km^{-2} day^{-1} . What is less intuitive is that both FLI and FGI seem to be nearly proportional when considering $\Delta s=25$ km and $\Delta s=50$ km. This tends to show that the variation of the amount of fronts between the two Canny thresholds is linear in OSTIA.

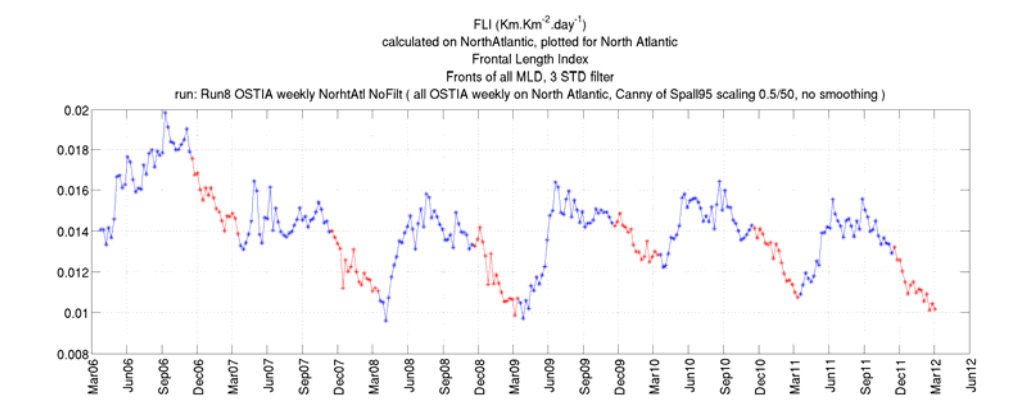


Figure 5-11: Front Length Index (FLI) in $km km^{-2} day^{-1}$ processed on weekly OSTIA over the North Atlantic region with d=0 km, $L_f=0.5$ km, and $\Delta s=50$ km. Times when more than 50% of the area MLD is deeper than 75 m are plotted in red.

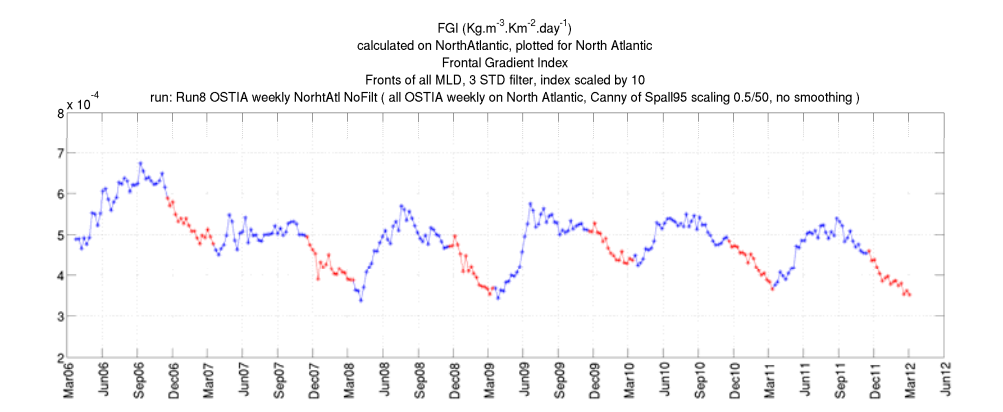


Figure 5-12: Front Gradient Index (FGI) in $kg m^{-3} km^{-2} day^{-1}$ processed on weekly OSTIA over the North Atlantic region with d=0 km, $L_f=0.5 km$, and $\Delta s=50 km$. Times when more than 50% of the area MLD is deeper than 75 m are plotted in red.

Figure 5-13 and Figure 5-14 present the FLI and FGI over the North Atlantic region, with d=25~km, $L_f=0.5~km$, and $\Delta s=25~km$ on OSTIA. This methodology assumes that the artefact small-scale variability which is potentially present in OSTIA, as described in Chapter 4, is removed by the 25 km low-pass smoothing filter. Then the scaling function assumes that the feature resolution of the smoothed SST is 25 km, and that the fronts are 0.5 km wide over the region. Comparing Figure 5-14 with Figure 5-8 which is the

equivalent run without the 25 km running mean filter, one can see that in the smoothed run, there is less inter-annual variability, especially on year 2006 which does not have the highest mean FGI over the North Atlantic. Instead it is 2009 that has the highest mean. However there are still similarities between the two runs. For instance, in both cases, March 2007 and March 2010 have higher annual minima than the other years of the time span. It can be added that the FLI and FGI index are more than twice as small on the smoothed dataset, which is logical as the scaling is equal in both runs. This result clearly shows that there is a non-negligible amount of frontal energy at scales finer than 25 km in the OSTIA products across the seasons.

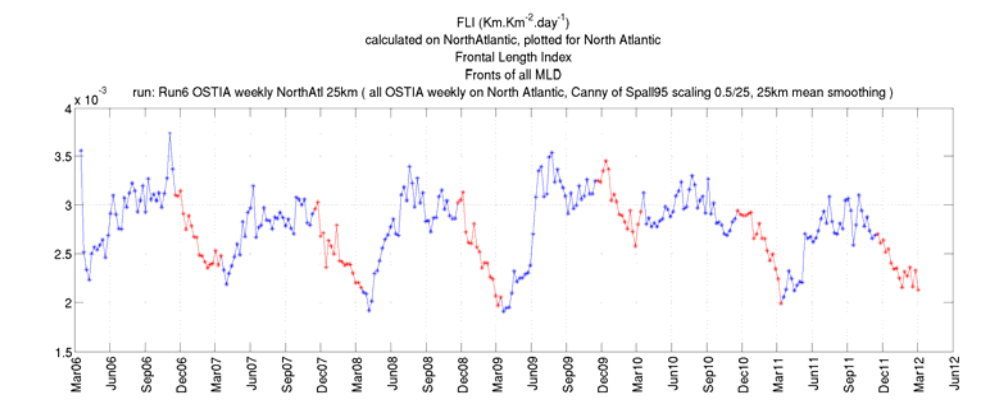


Figure 5-13: Front Length Index (FLI) in $km km^{-2} day^{-1}$ processed on weekly OSTIA over the North Atlantic region with d=25 km, $L_f=0.5 km$, and $\Delta s=25 km$. Times when more than 50% of the area MLD is deeper than 75 m are plotted in red.

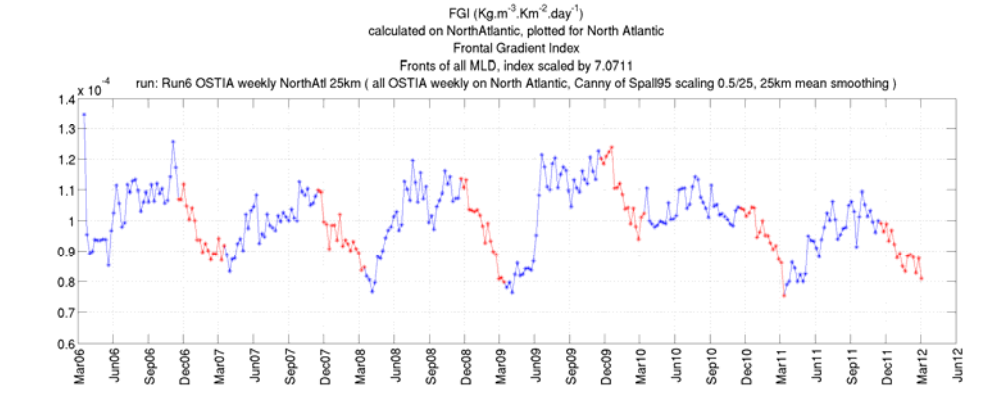


Figure 5-14: Front Gradient Index (FGI) in $kg m^{-3} km^{-2} day^{-1}$ processed on weekly OSTIA over the North Atlantic region with d=25 km, $L_f=0.5 km$, and $\Delta s=25 km$. Times when more than 50% of the area MLD is deeper than 75 m are plotted in red.

Figure 5-15 and Figure 5-16 present the FLI and FGI over the North Atlantic region, with $d = 50 \, km$, $L_f = 0.5 \, km$, and $\Delta s = 50 \, km$ on OSTIA. On this run the OSTIA dataset is smoothed with a low-pass 50 km filter and the gradient is scaled for an assumed 50 km feature resolution. FLI and FGI have a comparable range to those of the run with 25 km smoothing (Figure 5-13 and Figure 5-14). This tends to show that the scaling assumption is valid, and the spatial density spectrum between 50 km and 25 km is close to k⁻². However the seasonal cycle is less pronounced on the 50 km smoothing case due to additional minima in August 2007 and August 2010. One can consider that these frontal indexes do not suffer from artefact seasonal variability due to the cloud coverage thanks to the initial 50 km low-pass filtering of OSTIA images. Indeed this filtering removes the fine features that are present on infrared observations but absent from the microwave ones. As the spatial coverage of microwave sensors is nearly global each day, it is fair to assume that no artefact temporal variability of small scales presence in OSTIA images remains above 50 km.

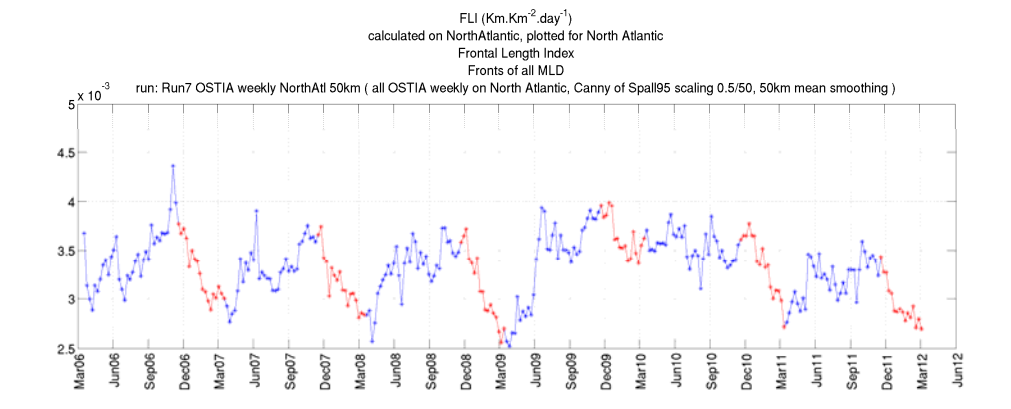


Figure 5-15: Front Length Index (FLI) in $km km^{-2} day^{-1}$ processed on weekly OSTIA over the North Atlantic region with d = 50 km, $L_f = 0.5 km$, and $\Delta s = 50 km$. Times when more than 50% of the area MLD is deeper than 75 m are plotted in red.

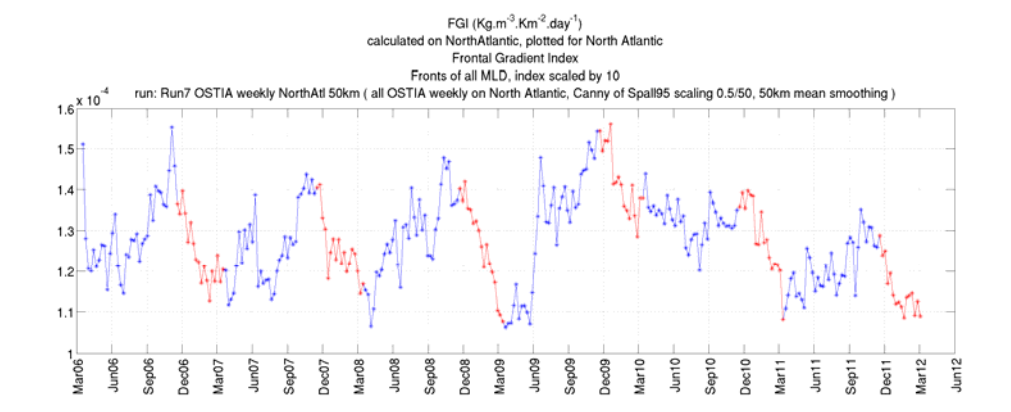


Figure 5-16: Front Gradient Index (FGI) in $kg m^{-3} km^{-2} day^{-1}$ processed on weekly OSTIA over the North Atlantic region with d = 50 km, $L_f = 0.5 km$, and $\Delta s = 50 km$. Times when more than 50% of the area MLD is deeper than 75 m are plotted in red.

Figure 5-17 and Figure 5-18 present the FLI and FGI over the North Atlantic region, with d=25 km, $L_f=1$ km, and $\Delta s=25$ km on OSTIA. The difference with Figure 5-13 and Figure 5-14 is that the front width is assumed to be 1 km rather than 0.5 km. It is logical that half the frontal index is detected because assuming that the fronts are twice as wide implies that the scaling for a 25 km low-pass filter is less intense hence the scaled horizontal density gradient magnitude is lower and fewer fronts are detected on it. It is also worth noting that the FLI and FGI variability is very similar to that of the above-mentioned

run with $L_f=0.5\,km$. Therefore it seems that the frontal width parameter has an effect on the magnitude of the indexes but their variability appears robust to it.

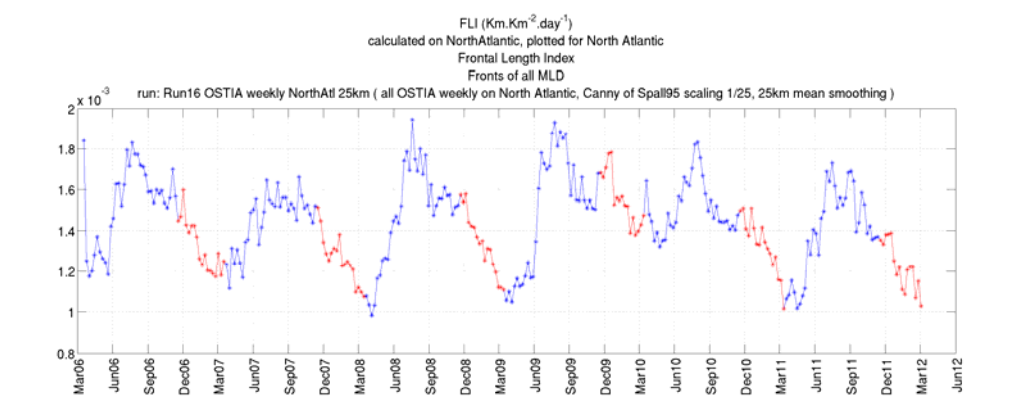


Figure 5-17: Front Length Index (FLI) in $km km^{-2} day^{-1}$ processed on weekly OSTIA over the North Atlantic region with d=25 km, $L_f=1 km$, and $\Delta s=25 km$. Times when more than 50% of the area MLD is deeper than 75 m are plotted in red.

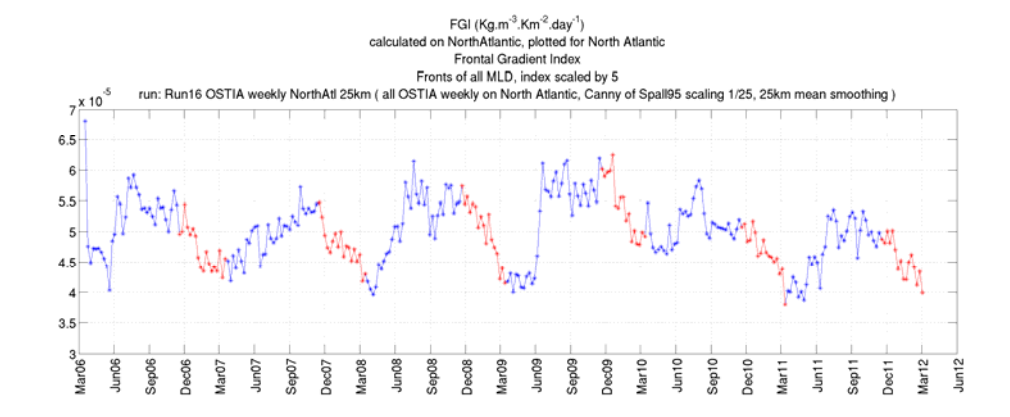


Figure 5-18: Front Gradient Index (FGI) in $kg m^{-3} km^{-2} day^{-1}$ processed on weekly OSTIA over the North Atlantic region with d=25 km, $L_f=1 km$, and $\Delta s=25 km$. Times when more than 50% of the area MLD is deeper than 75 m are plotted in red.

Figure 5-19 and Figure 5-20 present the FLI and FGI over the North Atlantic region, with d=0~km, $L_f=1~km$, and $\Delta s=25~km$ on OSTIA. The difference with the previous run is that no smoothing is applied on the OSTIA images. This run

is to be compared to Figure 5-7 and Figure 5-8, which are based on the same parameters except an assumed frontal width twice as large. It presents a FLI of half the size, which means that half the number of fronts are detected. FGI is smaller by a factor of 2. This example also shows that the indexes variability is very comparable when the fronts are assumed to be 0.5 km or 1 km wide over the region. However the absolute values of FGI depend on the assumed frontal width as it is involved in the density gradient magnitude scaling following Equation (5-7).

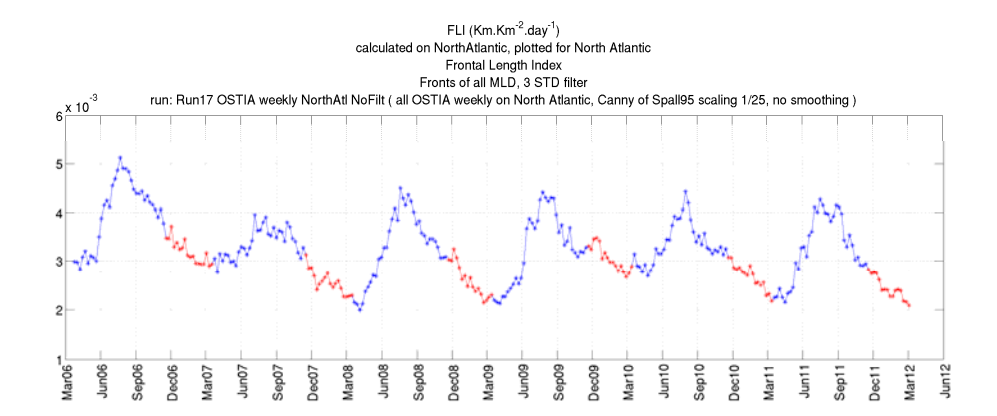


Figure 5-19: Front Length Index (FLI) in $km km^{-2} day^{-1}$ processed on weekly OSTIA over the North Atlantic region with d=0 km, $L_f=1$ km, and $\Delta s=25$ km. Times when more than 50% of the area MLD is deeper than 75 m are plotted in red.

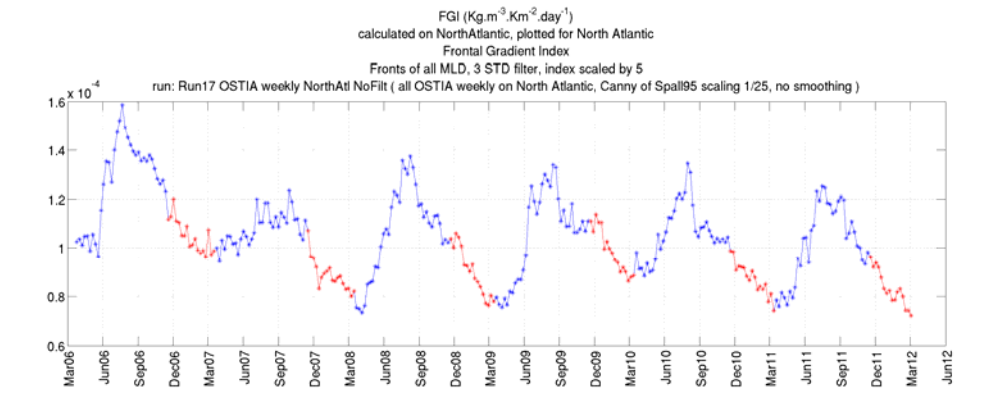


Figure 5-20: Front Gradient Index (FGI) in $kg m^{-3} km^{-2} day^{-1}$ processed on weekly OSTIA over the North Atlantic region with d=0 km, $L_f=1 km$, and $\Delta s=25 km$. Times when more than 50% of the area MLD is deeper than 75 m are plotted in red.

The general pattern of seasonal frontal variability is robust to the parameters of the front detection method. It features a lowest frontal activity around April in the North Atlantic and a highest one around August. It is important to explore this variability and assess to what extent it is the consequence of artefacts of the Level-4 SST production. Chapter 4 showed that Level-4 products may suffer from a time-varying amount of small-scale activity due to a seasonal signal in the cloud coverage. One way of looking at the question is to explore the temporal variability of the SST and the SST gradient magnitude. Figure 5-21 presents the average OSTIA SST over the North Atlantic. It is close to an annual sinusoidal cycle with a low in March and a high in August, similar to the FLI and FGI indexes. Figure 5-22 to Figure 5-25 show the un-scaled OSTIA SST gradient magnitude but on different parts of its spectrum. Figure 5-22 is the un-scaled SST gradient over its complete spectrum, since the SST is not filtered. It exhibits an annual cycle with a low in August and a high in February, almost in anti-phase to the SST average and the FLI and FGI indexes. Figure 5-23 is similar except that the SST was smoothed with a low-pass filter of 50 km prior to the gradient computation. The magnitude of the gradient of the smoothed OSTIA is obviously lower than that of the original OSTIA images. The gradient magnitude is reduced by 12% after the scales smaller than 50 km are removed. According to the scaling (5-7), this would mean that the original OSTIA images have an average feature resolution of 39 km over the North Atlantic. It was shown above that OSTIA images include a non-negligible amount of frontal energy at scales lower than 25 km. This would tend to show that the feature resolution, whose average is 39 km over the region, is varying in space or in time providing the k-2 assumption is correct. Since the basin average of the gradient magnitude of the original OSTIA appears to be proportional to the 50 km smoothed OSTIA with a constant ratio in time, it can be inferred that the feature resolution is close to constant in time but varying in space.

Figure 5-24 shows the un-scaled gradient magnitude calculated on OSTIA images that are filtered by a 50 km high-pass filter. This ensures that the large scale meridional temperature gradient is not taken into account. The seasonal variability is reduced but still present in the small scale part of the gradient magnitude spectrum. The cycle is the same as for the larger scale gradient, in

anti-phase from the FLI and FGI. In Figure 5-25, which is the un-scaled gradient magnitude of 100 km high-pass filtered OSTIA images, one can see that the seasonal variability is increased by the presence of larger spatial scales. The difference between the frontal index and the index of average gradient of high-pass filtered images makes the case for the frontal indexes. Indeed FLI and FGI show something other than simply the gradient of the small scale temperature. Due to the Canny methodology, fronts characterize regions where the gradient is intensified in a local maxima. This analysis demonstrates that the periods when the gradient of the small scales is high are not simultaneous with those when the frontal indexes are high. Chapter 2 showed that it is relevant to quantify the frontal zones where the horizontal buoyancy gradient is enhanced rather than simply averaging the gradient over the region.

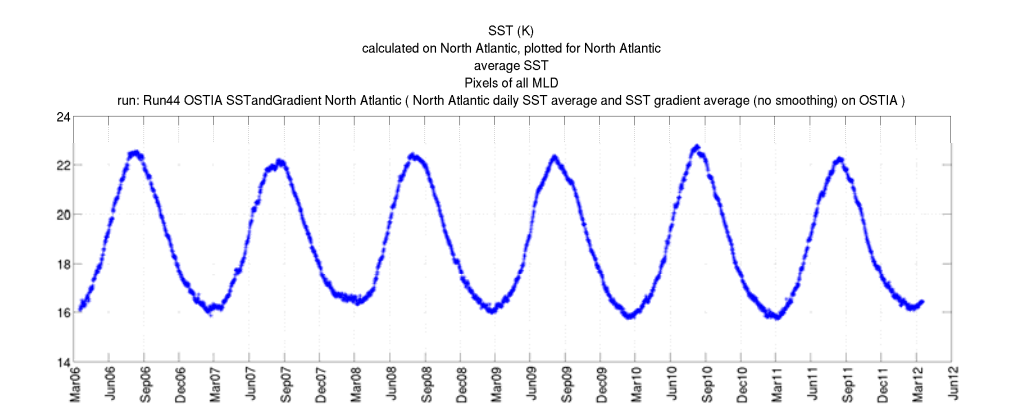


Figure 5-21: Average OSTIA SST over the North Atlantic.

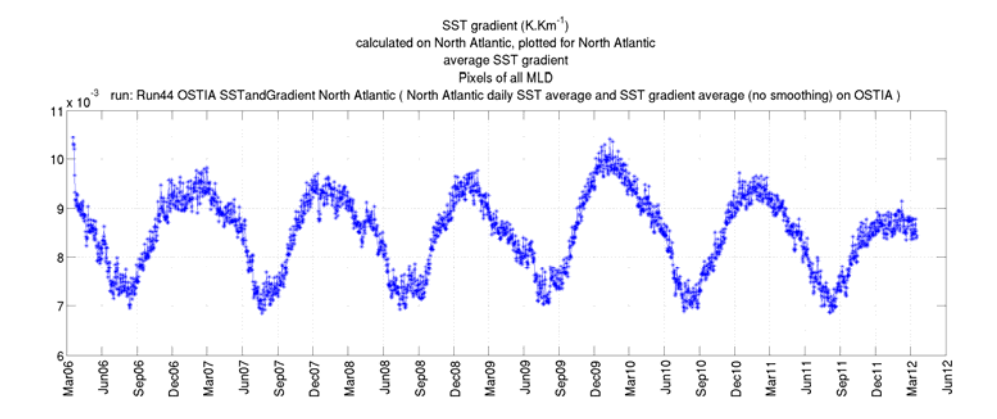


Figure 5-22: Average OSTIA SST un-scaled gradient magnitude over the North Atlantic.

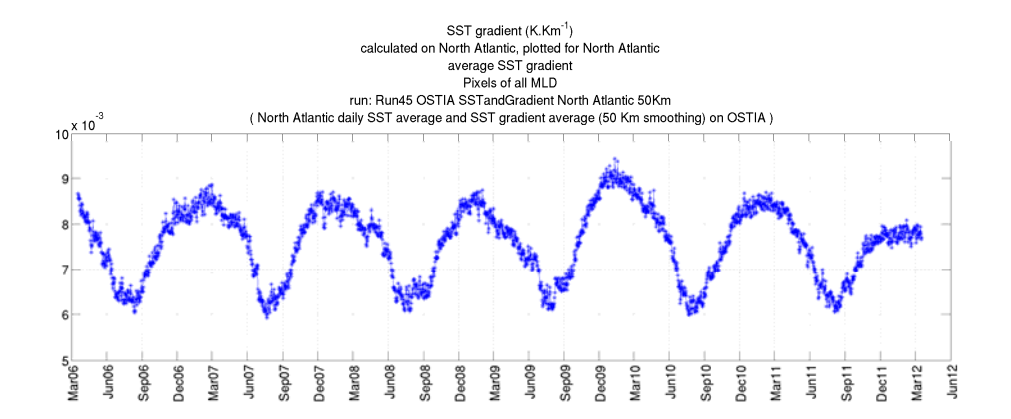


Figure 5-23: Average OSTIA SST un-scaled gradient magnitude over the North Atlantic. The SST images are smoothed by a low-pass 50 km filter before the gradient is calculated.

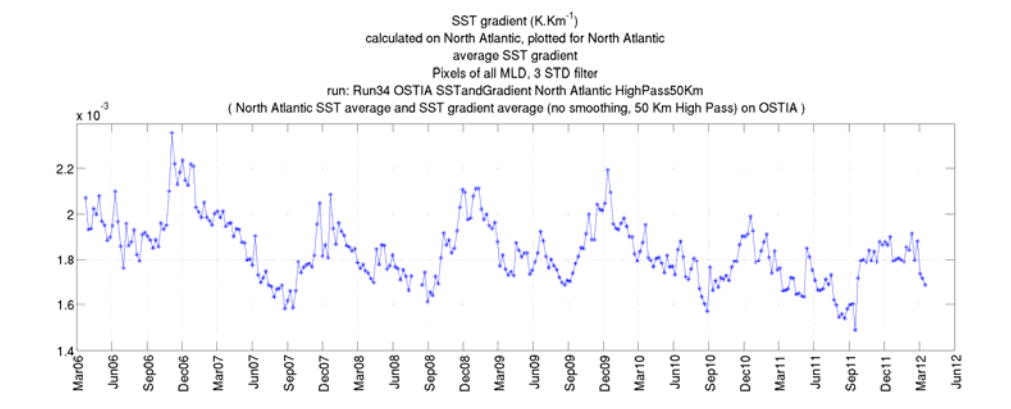


Figure 5-24: Average OSTIA SST un-scaled gradient magnitude over the North Atlantic. The SST images are convoluted by a high-pass 50 km filter before the gradient is calculated.

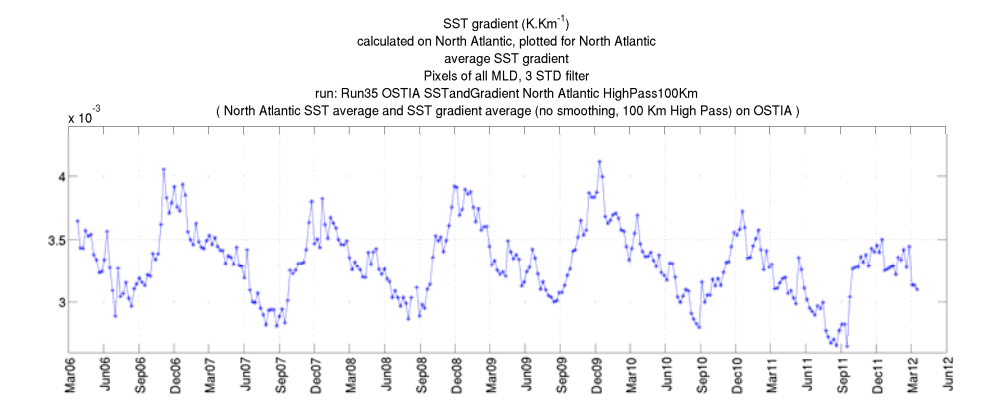


Figure 5-25: Average OSTIA SST un-scaled gradient magnitude over the North Atlantic. The SST images are convoluted by a high-pass 100 km filter before the gradient is calculated.

5.2.2 FLI and FGI from ODYSSEA

Another way to assess the amount of artefact signal introduced by inconsistencies of the Level-4 production into the frontal indexes is to compare the results obtained from various datasets. In this section, the frontal indexes calculated on ODYSSEA (version 2.0) are presented. As described in chapter 4, ODYSSEA products are produced through a different methodology than that of OSTIA. The discrepancy between the frontal indexes calculated from different SST products, that are estimations of the same real but unknown scene, gives

an indication of the contribution of the source Level-4 image error to the frontal error.

Figure 5-26 and Figure 5-27 present the FLI and FGI over the North Atlantic region, with d = 0 km, $L_f = 0.5 \text{ km}$, and $\Delta s = 25 \text{ km}$ on ODYSSEA (version 2.0). They can be directly compared to Figure 5-5 and Figure 5-6 which are the same indexes computed with the same parameters on OSTIA. These runs feature no smoothing prior to the frontal detection, hence the finest features present in the source SST images are retained. It is striking that the ODYSSEA FLI is about 30% lower than the OSTIA FLI, which means that a significant proportion of fronts are detected on OSTIA but not on ODYSSEA. Meanwhile, the annual range of ODYSSEA FGI is very close to that of OSTIA FGI. It can be concluded that less fronts are detected on the raw ODYSSEA images but that the ones that are detected are significantly stronger that the ones on OSTIA, leading to a FGI of the same magnitude. Although the ODYSSEA indexes exhibit a clear seasonal variability, their inter-annual signal is different from that of OSTIA. For example the annual averages of FLI and FGI on OSTIA are significantly higher in 2006. However some common patterns are seen between the results of the two datasets. For instance the annual frontal indexes minima in 2007 and 2010 were higher than those in the other years on both datasets. Besides, ODYSSEA frontal indexes appear to be noisier in time, especially in 2009. This could be due either to a stronger temporal smoothing in the OSTIA production which would smooth out high temporal variability or to a higher error in the ODYSSEA images. It should be added that the ODYSSEA dataset was only available until end of 2010.

The processing of the frontal indexes reveals some variability in the fine scale content of the source dataset that is sometimes unlikely to be natural, such as the sudden drop in FLI and FGI around beginning of October 2010, or sometimes clearly an artefact of the SST product like the multiplication by a factor 10 of the indexes at the end of December 2007 (filtered out on Figure 5-26 and Figure 5-27). The second example is an indication of a sudden massive divergence in the optimal interpolation process at these dates which produced completely unrealistic maps of SST for a few days on ODYSSEA. The first example was investigated by plotting the ODYSSEA gradient magnitude over the month of October 2010 over the North Atlantic. It can be observed on

Figure 5-28 that the fine features evolve from one day to another until October the 10th 2010, at which point the dynamics seem to freeze and gradually smoothen in space until October the 14th when the scene appears unusually smooth. From October the 15th onward the fine features reappear and change from day to day. It can be assumed that the cause of the strong event is that no input Level-2 data were ingested in the ODYSSEA optimal interpolation for 5 days and that the autocorrelation spatial filter consequently became larger as the confidence in the small scale features extracted from previous days was reduced more and more.

Figure 5-29 and Figure 5-30 present the FLI and FGI over the North Atlantic region, with d=50~km, $L_f=0.5~km$, and $\Delta s=50~km$ on ODYSSEA. They can be directly compared to Figure 5-15 and Figure 5-16 which are the same indexes computed with the same parameters on OSTIA. Both FLI and FGI are much larger on ODYSSEA than on OSTIA after the source images are smoothed with a 50 km low pass filter. Similarly to the previous run, ODYSSEA frontal indexes exhibit a larger variability from one day to the next, and artefacts of the ODYSSEA production are seen in the indexes.

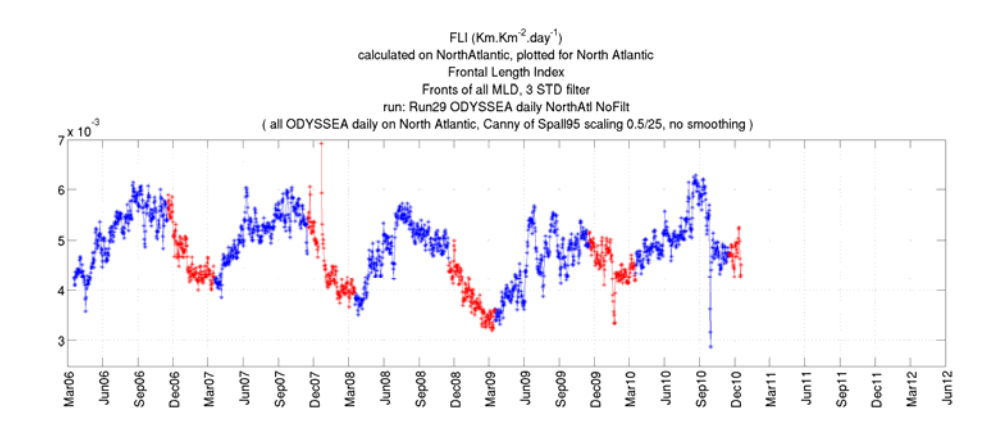


Figure 5-26: Front Length Index (FLI) in $km km^{-2} day^{-1}$ processed on daily ODYSSEA over the North Atlantic region with d = 0 km, $L_f = 0.5 km$, and $\Delta s = 25 km$. Times when more than 50% of the area MLD is deeper than 75 m are plotted in red.

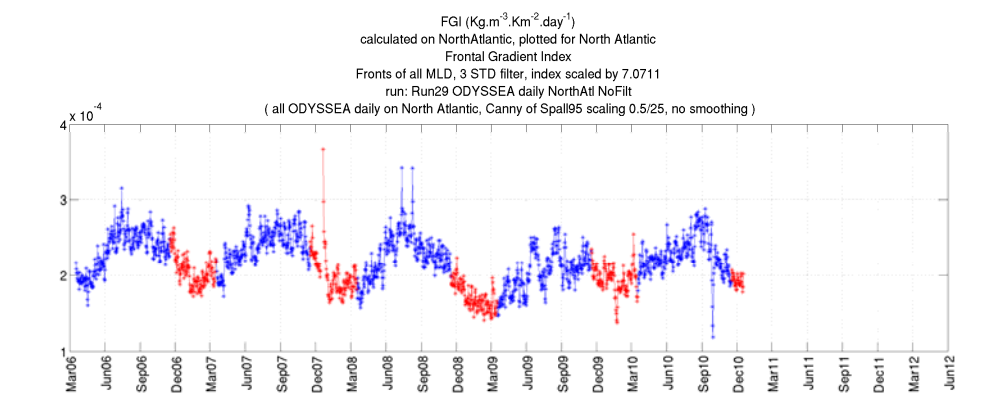


Figure 5-27: Front Gradient Index (FGI) in $kg \ m^{-3} \ km^{-2} day^{-1}$ processed on daily ODYSSEA over the North Atlantic region with $d=0 \ km$, $L_f=0.5 \ km$, and $\Delta s=25 \ km$. Times when more than 50% of the area MLD is deeper than 75 m are plotted in red.

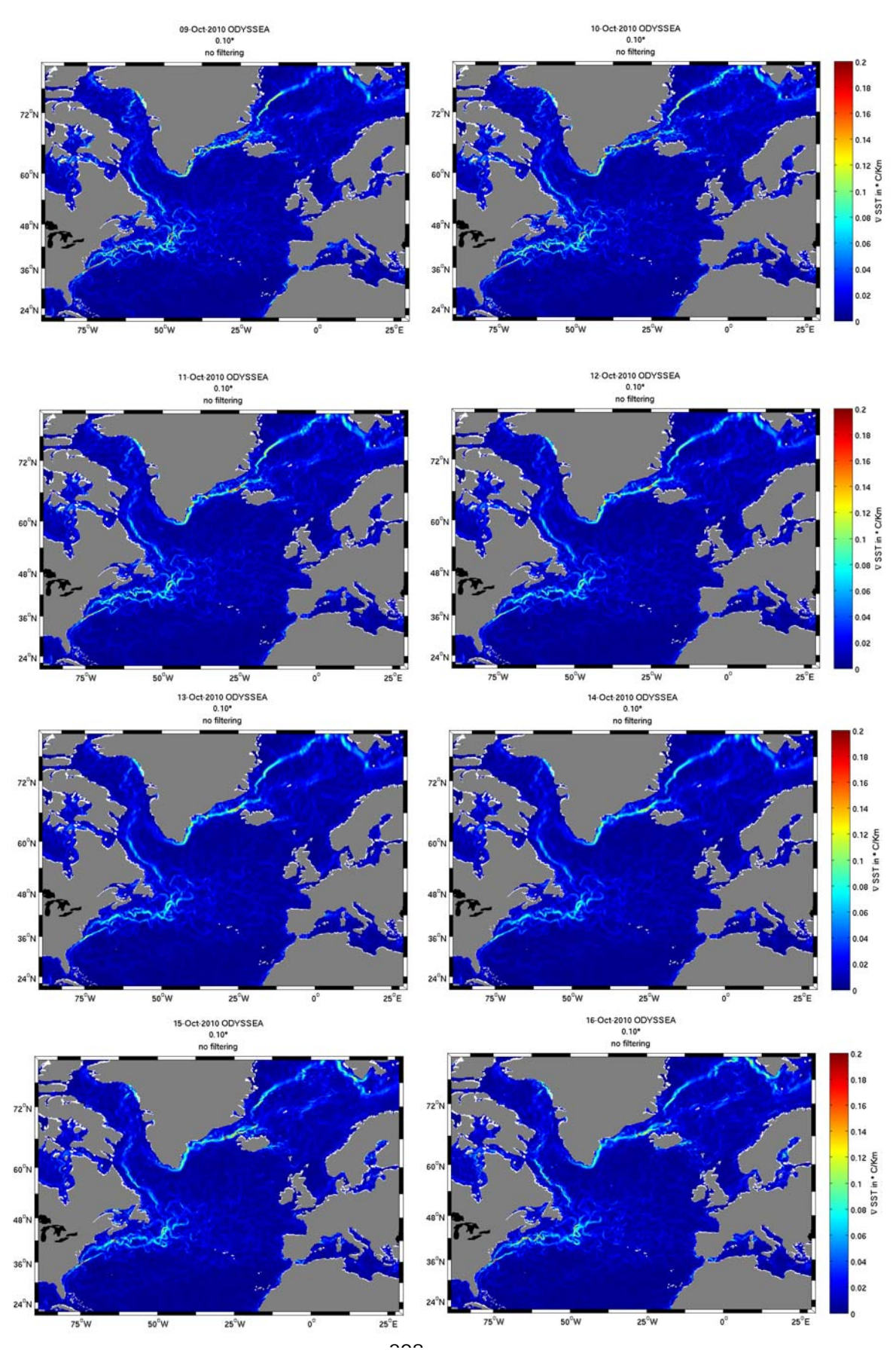


Figure 5-28: Sequence of un-scaled ODYSSEA SST gradient magnitude from 09/10/2010 to 16/10/2010, from left to right and top to bottom

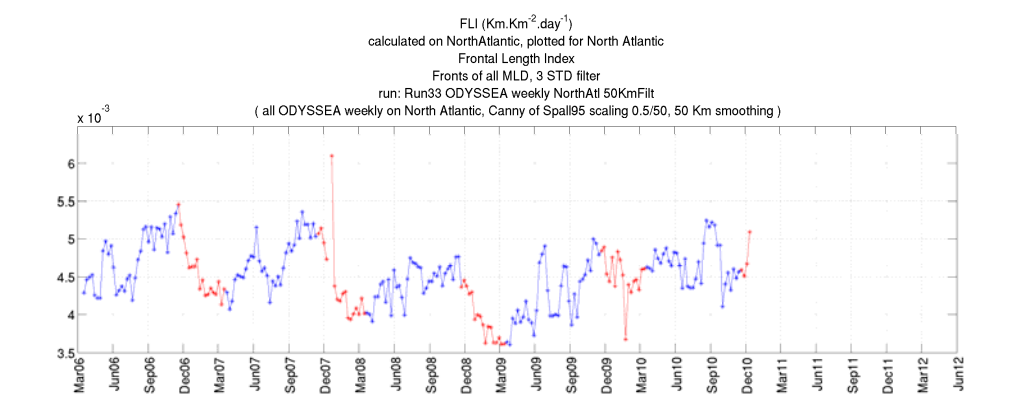


Figure 5-29: Front Length Index (FLI) in $km km^{-2} day^{-1}$ processed on weekly ODYSSEA over the North Atlantic region with d = 50 km, $L_f = 0.5 km$, and $\Delta s = 50 km$. Times when more than 50% of the area MLD is deeper than 75 m are plotted in red.

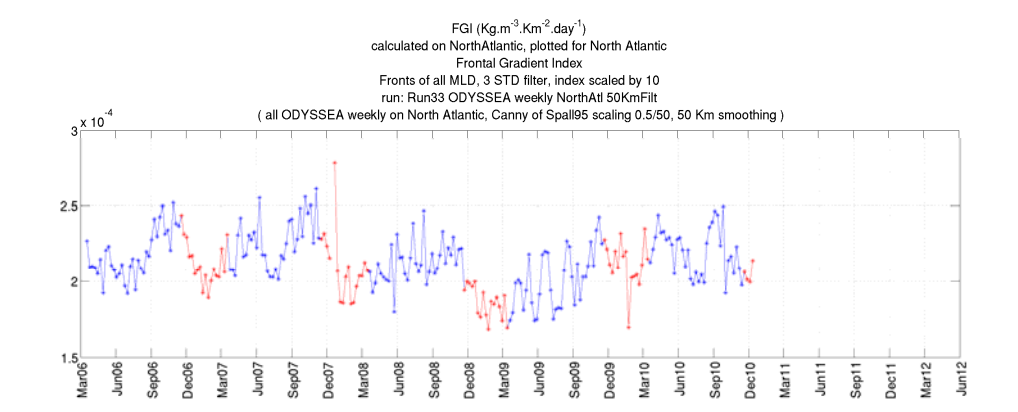


Figure 5-30: Front Gradient Index (FGI) in $kg m^{-3} km^{-2} day^{-1}$ processed on daily ODYSSEA over the North Atlantic region with d=50 km, $L_f=0.5 km$, and $\Delta s=50 km$. Times when more than 50% of the area MLD is deeper than 75 m are plotted in red.

Figure 5-31 shows the un-scaled gradient magnitude of the raw ODYSSEA images averaged over the North-Atlantic. Comparing with Figure 5-22 which presents the equivalent results for the OSTIA product, one can see that the gradient magnitude of the raw ODYSSEA images is about 15% higher than on OSTIA. Another difference worth noting is the inter-annual trend observable in each datasets. While the annual average of OSTIA gradient magnitude is stable between 2007 and 2009, there is a clear negative trend on ODYSSEA. Figure

5-32 shows the un-scaled gradient magnitude of the 50 km low-pass filtered ODYSSEA images averaged over the North-Atlantic. The variations are similar to those seen on Figure 5-31, with less noise and an average reduced by about 15%. The reduction of daily noise is more obvious between Figure 5-31 and Figure 5-32 than between Figure 5-22 and Figure 5-23. This indicated that a lot of noise in the daily ODYSSEA gradient magnitude lays in the scales shorter than 50 km. It should also be stressed that the gradient magnitude with 50 km smoothing is about 15% higher on ODYSSEA than on OSTIA. This means that there is still more dynamics above 50 km on ODYSSEA.

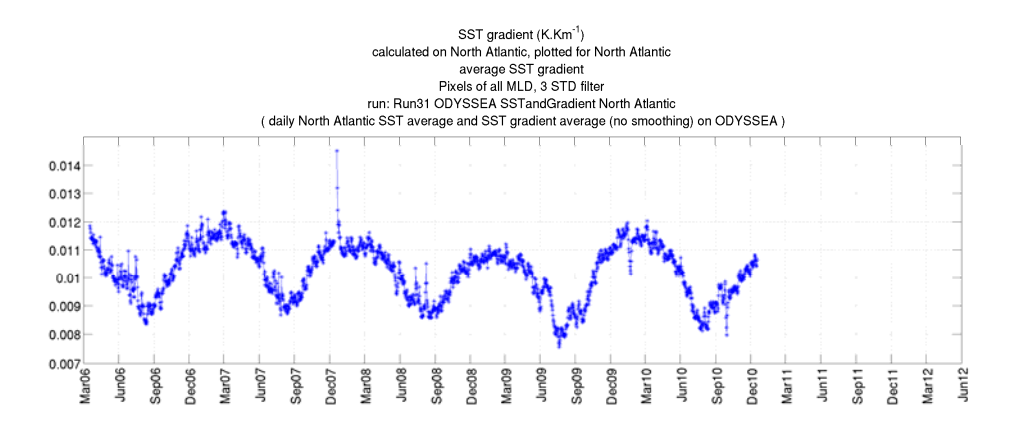


Figure 5-31: Average un-scaled ODYSSEA SST gradient magnitude over the North Atlantic.

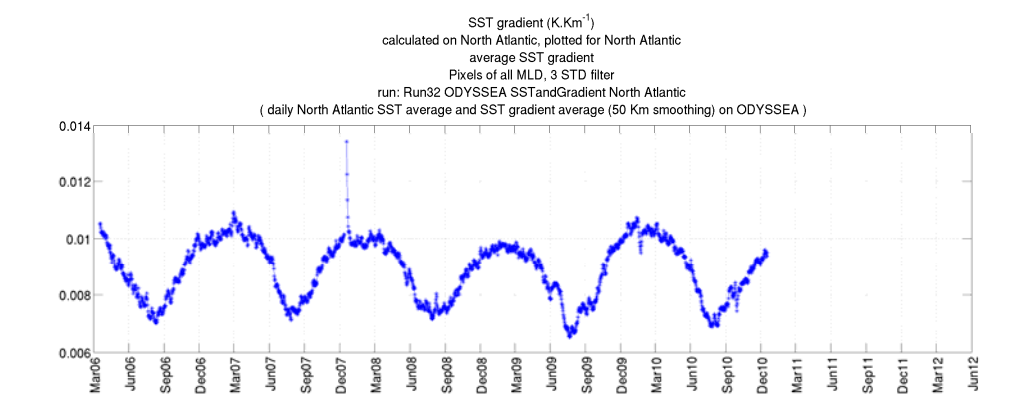


Figure 5-32: Average un-scaled ODYSSEA SST gradient magnitude over the North Atlantic. The SST images are smoothed by a low-pass 50 km filter before the gradient is calculated.

Figure 5-33 and Figure 5-34 illustrate the difference in the scales that are present in OSTIA and ODYSSEA products. It is clear that ODYSSEA images retain much more energy at the small scales and OSTIA gradient magnitude appears to be a smoothed version of ODYSSEA gradient magnitude. There is however more confidence in the spatial consistency of the presence of the small scales in OSTIA images. One can indeed observe moving patterns of smoother areas in sequences of ODYSSEA gradient magnitude maps that are likely to be due to evolving cloud coverage.

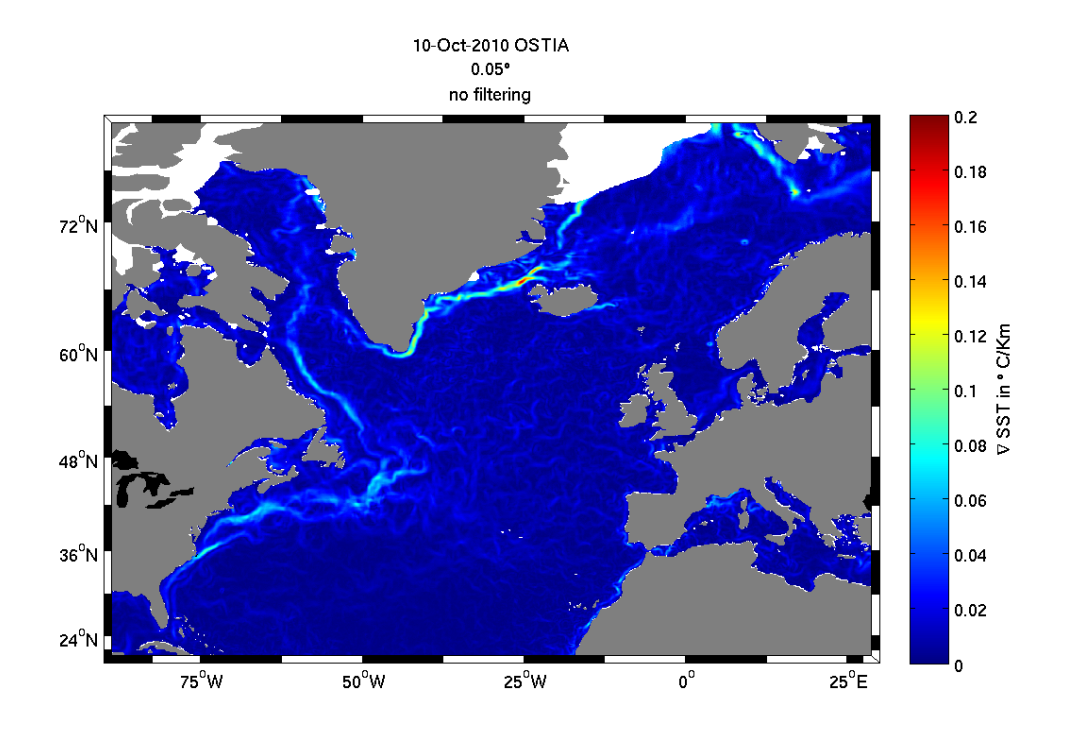


Figure 5-33: Un-scaled OSTIA SST gradient magnitude on 10/10/2010.

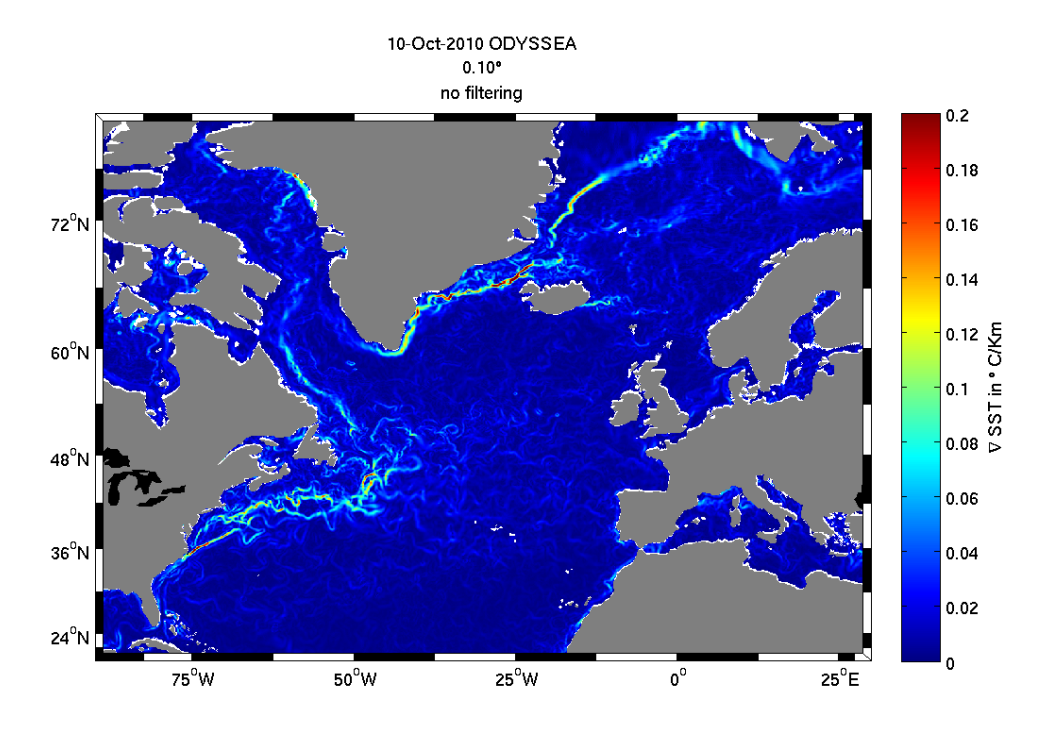


Figure 5-34: Un-scaled ODYSSEA SST gradient magnitude on 10/10/2010.

5.2.3 FLI and FGI from REMSS_MW

Figure 5-35 to Figure 5-38 present the FLI and FGI calculated on the microwave-only product REMSS_MW, with d=0 Km, $L_f=0.5$ Km, $\Delta s=25$ Km and $50 \, Km$. The first thing to note is that there is an obvious seasonal variability in the microwave Level-4 product. Comparing Figure 5-35 and Figure 5-37, one can say that the seasonal variability of the FLI is increased by searching for weaker fronts. As for the other products, the frontal indexes reach their annual minimum around March and their annual maximum around September. Since REMSS does not include any infrared data, the scales present in it are not affected by the cloud coverage. Hence the seasonal variability observed in the frontal indexes can be described as natural. Even though the REMSS MW images are produced from spatially consistent input source images, the microwave acquisitions from various sensors are merged by means of an optimal interpolation (OI) which is prone to errors. A few REMSS MW images have returned unnaturally high frontal indexes (not shown on the figures), and investigations have exposed errors in the outputs of the OI. Indeed, a close look at the gradient magnitude of the REMSS_MW across the periods when errors are suspected show that the feature resolution of the product suddenly gets sharper for a day before going back to normal on the next day. This behaviour is difficult to spot by eye, however the frontal and the gradient indexes are able to act as diagnostic tools to detect it. Comparing Figure 5-35 with Figure 5-7, one can observe that more than twice as many fronts are detected on OSTIA than on REMSS_MW. This can be due either to the fact that OSTIA ingests high resolution infrared SST or to a higher smoothing in the production of REMSS_MW data. Comparing Figure 5-37 with Figure 5-15, one can say that 40% more fronts are detected on REMSS_MW than on OSTIA when the latter is smoothed by a 50 km low pass filter. However, when this smoothing is reduced to 25 km as on Figure 5-13, the frontal indexes are very close between smoothed OSTIA and raw REMSS_MW (Figure 5-35). REMSS_MW products feature a slightly higher gradient index than OSTIA, both when taken raw (Figure 5-39 and Figure 5-22) and when smoothed by a 50 km running mean (Figure 5-40 and Figure 5-23). Note that Figure 5-39 and Figure 5-40 exhibit the errors in the optimal interpolation previously mentioned.

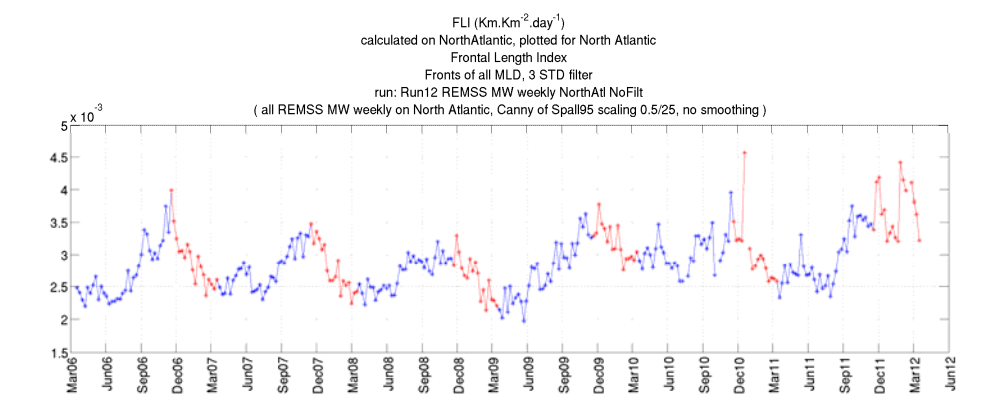


Figure 5-35: Front Length Index (FLI) in $km \ km^{-2} day^{-1}$ processed on weekly REMSS_MW over the North Atlantic region with $d=0 \ km$, $L_f=0.5 \ km$, and $\Delta s=25 \ km$. Times when more than 50% of the area MLD is deeper than 75 m are plotted in red.

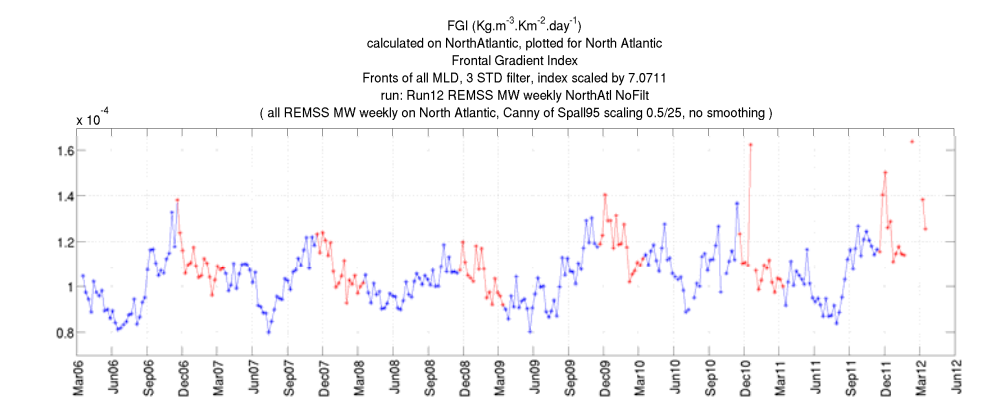


Figure 5-36: Front Gradient Index (FGI) in $kg \ m^{-3} \ km^{-2} day^{-1}$ processed on weekly REMSS_MW over the North Atlantic region with $d=0 \ km$, $L_f=0.5 \ km$, and $\Delta s=25 \ km$. Times when more than 50% of the area MLD is deeper than 75 m are plotted in red.

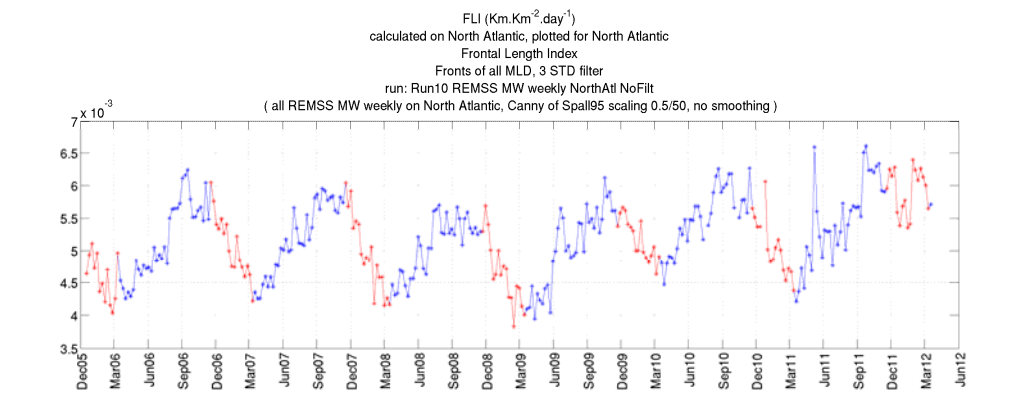


Figure 5-37: Front Length Index (FLI) in $km \ km^{-2} day^{-1}$ processed on weekly REMSS_MW over the North Atlantic region with $d=0 \ km$, $L_f=0.5 \ km$, and $\Delta s=50 \ km$. Times when more than 50% of the area MLD is deeper than 75 m are plotted in red.

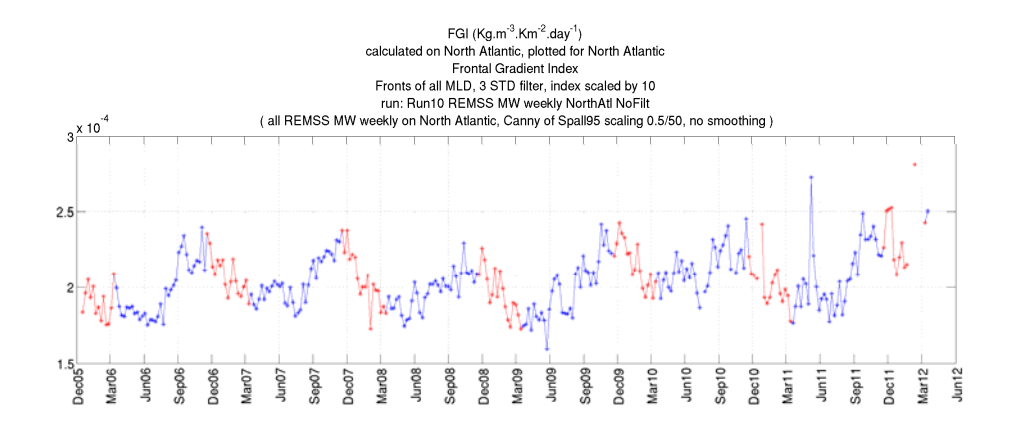


Figure 5-38: Front Gradient Index (FGI) in $kg \ m^{-3} \ km^{-2} day^{-1}$ processed on weekly REMSS_MW over the North Atlantic region with $d=0 \ km$, $L_f=0.5 \ km$, and $\Delta s=50 \ km$. Times when more than 50% of the area MLD is deeper than 75 m are plotted in red.

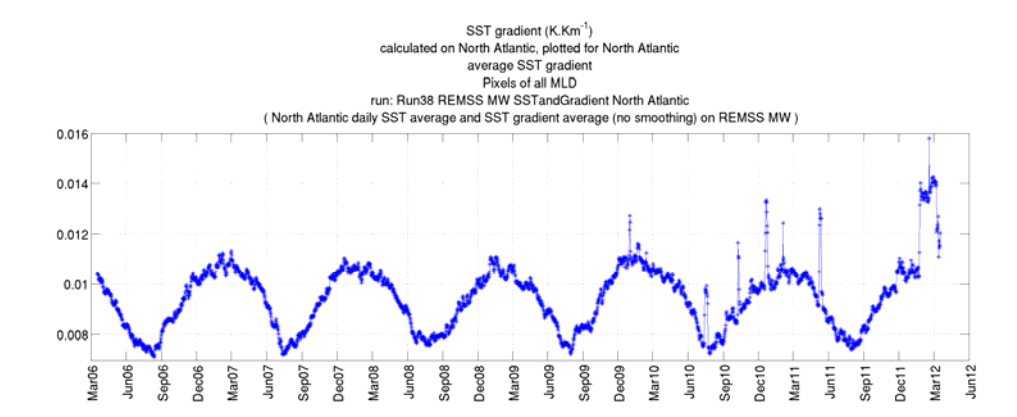


Figure 5-39: Average un-scaled REMSS_MW SST gradient magnitude over the North Atlantic.

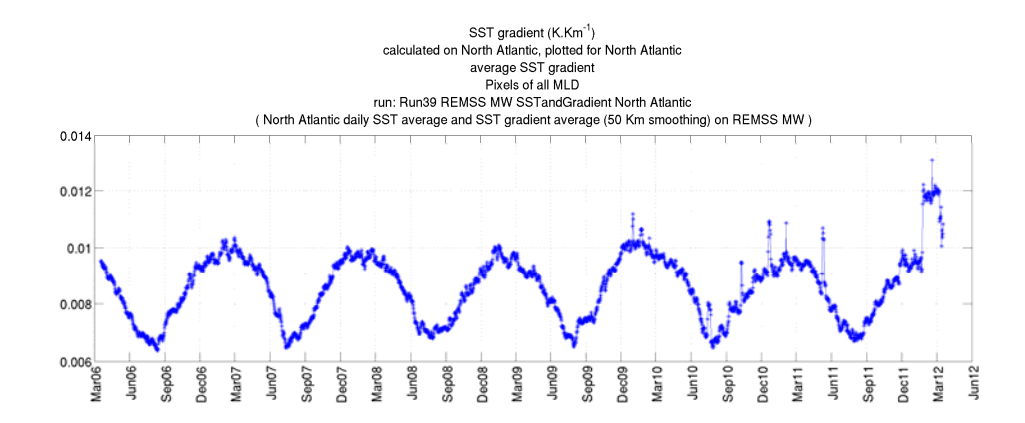


Figure 5-40: Average un-scaled REMSS_MW SST gradient magnitude over the North Atlantic. The SST images are smoothed by a low-pass 50 km filter before the gradient is calculated.

5.2.4 FLI and FGI from IFREMER_L3_IR

Figure 5-41 to Figure 5-46 present the FLI and FGI calculated on the product IFREMER_L3 from which infrared-only pixels are extracted (therefore called IFREMER_L3_IR) with d=0 Km, $L_f=0.5$ Km, $\Delta s=0$ Km, 25 Km and 50 Km. One can note that the seasonal variability observed on the other SST datasets is present on each of these frontal indexes. This seasonal variability is entirely natural since the creation of IFREMER_L3_IR data does not involve any interpolation and the scales present are consistent in time and space. Figure 5-47 and Figure 5-48 present the same indexes as shown on Figure 5-41 and Figure 5-42 but averaged over the NA1 region which is a small area in the

middle of the Sargasso sea (30 ° N<latitude<35 ° N and 45 ° W<longitude<40 ° W). The seasonal variability is present in the time series of the frontal indexes averaged over NA1. This indicates that the seasonal variability observed in the North Atlantic averages is not an artefact of the spatial and temporal patterns in the cloud coverage which may force the averaging over different areas of different frontal densities during different seasons.

The FLI is higher on Figure 5-41 than on Figure 5-5 which is calculated with OSTIA SST. This indicates that the assumption underlying Figure 5-5 is not valid and that the feature resolution of OSTIA is higher than 25 km. The IFREMER_L3_IR feature resolution is only limited by the spatial sampling of 10 km. Conversely, Figure 5-41 shows a comparable FLI range with Figure 5-11 which is the OSTIA FLI over the same region with an assumed feature resolution of 50 km. This shows that the assumption of $\Delta s = 50 \, Km$ for OSTIA is closer to reality. However Figure 5-42 exhibits a FGI that is 35% higher than the FGI shown on Figure 5-12 calculated with the same assumption. This discrepancy can be interpreted as follows: whereas the scaling of the density gradient magnitude allows correcting for the coarser OSTIA feature resolution effect on the amount of detected fronts, it is not sufficient to retrieve the exact gradient magnitude at the crest of the front. One can make the hypothesis that the enhanced slope of the density at the front's centre is underestimated by the k⁻² density assumption. This point supports the case for the use of high resolution non-smoothed SST data.

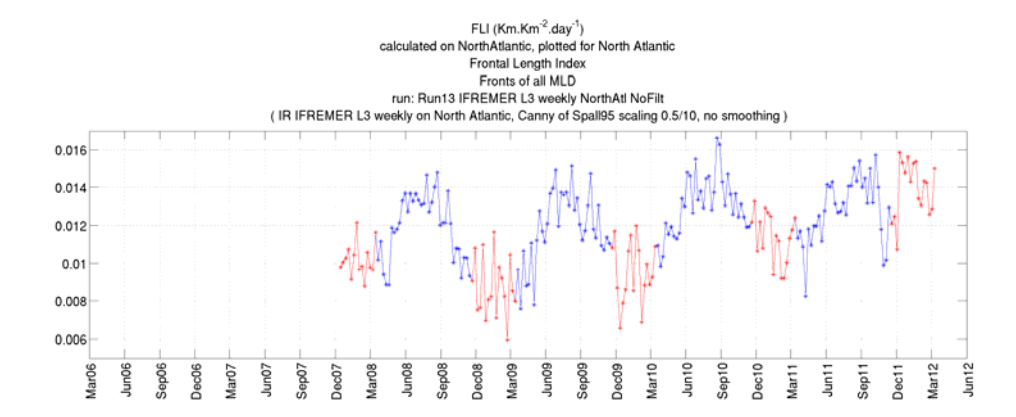


Figure 5-41: Front Length Index (FLI) in $km \ km^{-2} day^{-1}$ processed on weekly IFREMER_L3_IR over the North Atlantic region with $d=0 \ km$, $L_f=0.5 \ km$, and $\Delta s=10 \ km$. Times when more than 50% of the area MLD is deeper than 75 m are plotted in red.

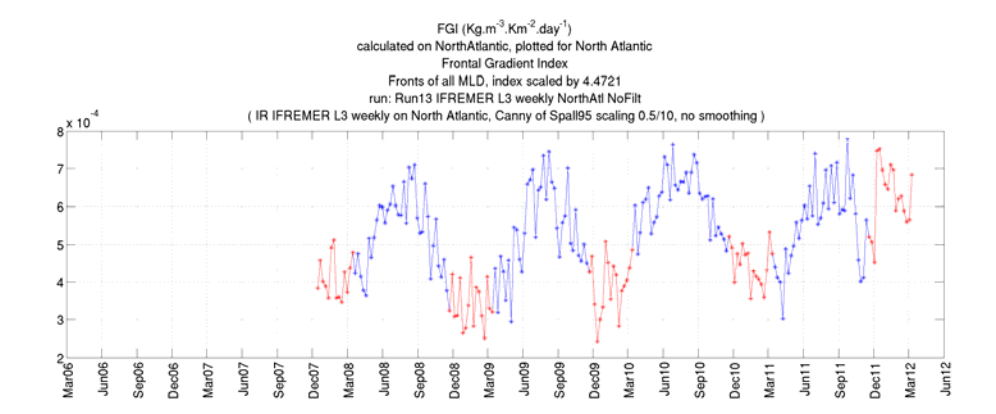


Figure 5-42: Front Gradient Index (FGI) in $kg m^{-3} kday^{-1}$ processed on weekly IFREMER_L3_IR over the North Atlantic region with d=0 km, $L_f=0.5$ km, and $\Delta s=10$ km. Times when more than 50% of the area MLD is deeper than 75 m are plotted in red.

Figure 5-43 and Figure 5-44 present the FLI and FGI calculated after an initial smoothing of the IFREMER_L3_IR data of d=25~km and an assumed feature resolution of $\Delta s=25~km$ for the gradient scaling. They compare very well in range to Figure 5-41 and Figure 5-42, showing that the scaling is performing between 10 km and 25 km. The signal however seems noisier on the smoothed IFREMER_L3_IR data. This can be attributed to the reduction of the amount of SST available after the smoothing close to coastlines or cloud edges.

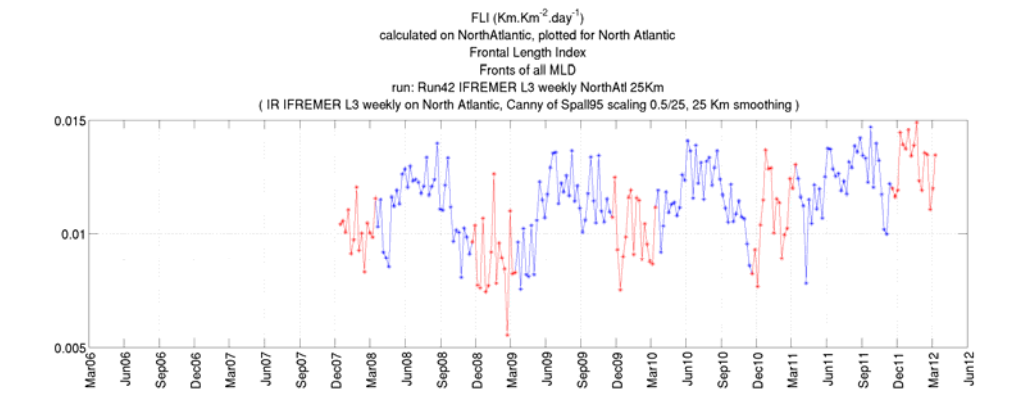


Figure 5-43: Front Length Index (FLI) in $km km^{-2} day^{-1}$ processed on weekly IFREMER_L3_IR over the North Atlantic region with d=25 km, $L_f=0.5 km$, and $\Delta s=25 km$. Times when more than 50% of the area MLD is deeper than 75 m are plotted in red.

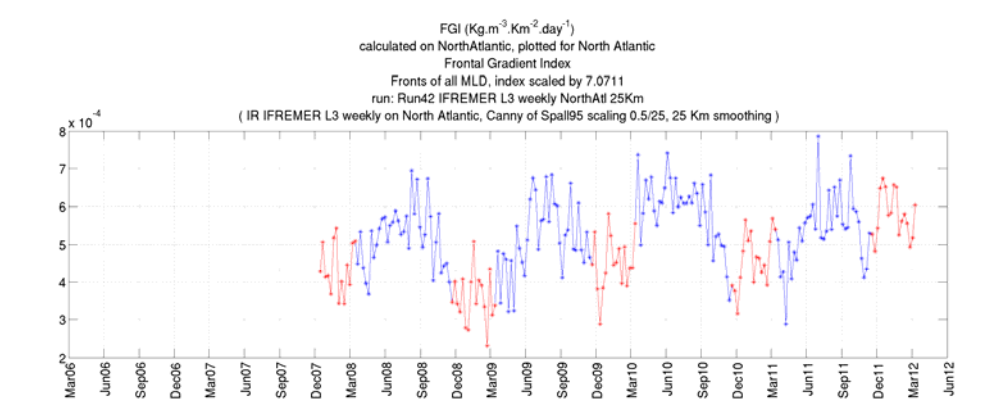


Figure 5-44: Front Gradient Index (FGI) in $kg m^{-3} km^{-2} day^{-1}$ processed on weekly IFREMER_L3_IR over the North Atlantic region with d=25 km, $L_f=0.5 km$, and $\Delta s=25 km$. Times when more than 50% of the area MLD is deeper than 75 m are plotted in red.

Figure 5-45 and Figure 5-46 present the FLI and FGI calculated after an initial smoothing of the IFREMER_L3_IR data of $d=50\,km$ and an assumed feature resolution of $\Delta s=50\,km$ for the gradient scaling. Compared to Figure 5-41 and Figure 5-42 where the density field was not smoothed, both FLI and FGI are 50% lower on the smoothed and scaled field. This clearly demonstrates that the k^{-2} scaling does not bring back all the fronts when the features finer than 50 km are lost. This again stresses the need for high-resolution SST products of at least 25 km for accurate front detection.

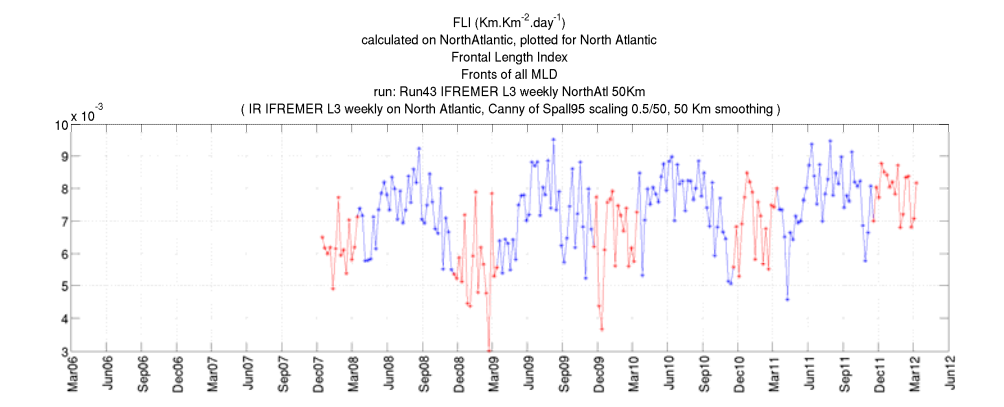


Figure 5-45: Front Length Index (FLI) in $km km^{-2} day^{-1}$ processed on weekly IFREMER_L3_IR over the North Atlantic region with d=50 km, $L_f=0.5 km$, and $\Delta s=50 km$. Times when more than 50% of the area MLD is deeper than 75 m are plotted in red.

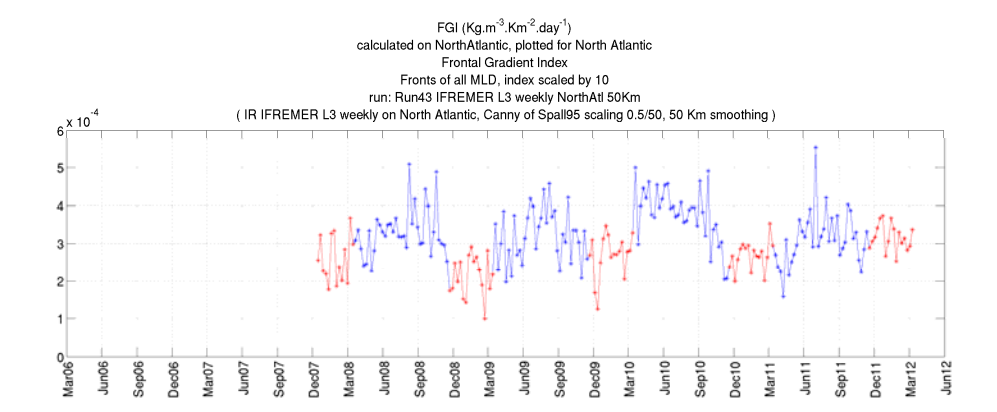


Figure 5-46: Front Gradient Index (FGI) in $kg m^{-3} km^{-2} day^{-1}$ processed on weekly IFREMER_L3_IR over the North Atlantic region with d=50 km, $L_f=0.5 km$, and $\Delta s=50 km$. Times when more than 50% of the area MLD is deeper than 75 m are plotted in red.

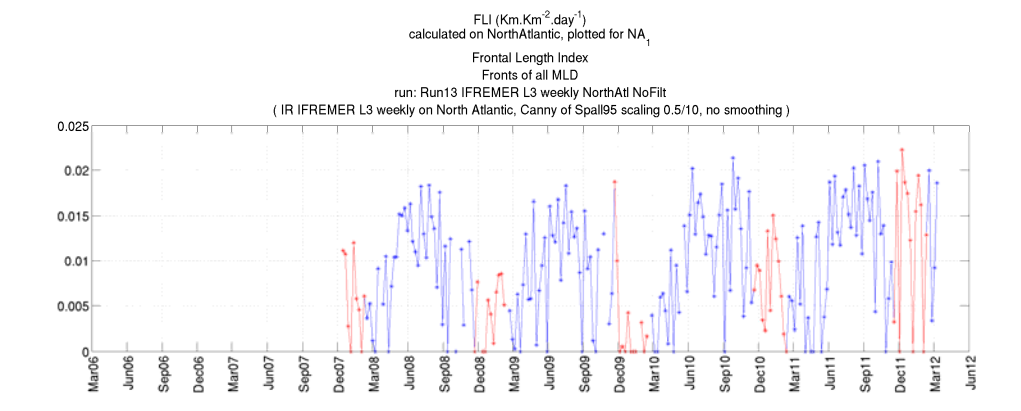


Figure 5-47: Front Length Index (FLI) in $km km^{-2} day^{-1}$ processed on weekly IFREMER_L3_IR over the NA1 region with d=0 km, $L_f=0.5$ km, and $\Delta s=10$ km. Times when more than 50% of the area MLD is deeper than 75 m are plotted in red.

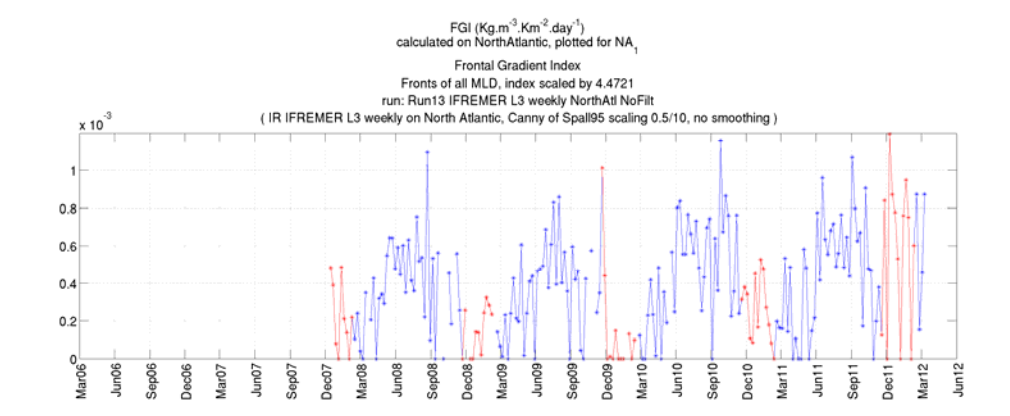


Figure 5-48: Front Gradient Index (FGI) in $kg m^{-3} km^{-2} day^{-1}$ processed on weekly IFREMER_L3_IR over the NA1 region with d=0 km, $L_f=0.5 km$, and $\Delta s=10 km$. Times when more than 50% of the area MLD is deeper than 75 m are plotted in red.

Figure 5-49 and Figure 5-50 present the average North-Atlantic IFREMER_L3_IR gradient magnitude from raw data and 50 km low-pass filtered data. As the feature resolution of the raw IFREMER_L3_IR SST (10 km) and of the filtered IFREMER_L3_IR SST (50 km) are well known, the k⁻² assumption from which the density magnitude gradient scaling is derived can be assessed. Following (5-7), one can derive:

$$|\nabla_{H}\rho_{L3_{raw}}| = |\nabla_{H}\rho_{L3_{50km}}| \cdot \sqrt{\frac{50}{10}} \approx |\nabla_{H}\rho_{L3_{50km}}| \cdot 2.2$$
 (5-11)

Where $\rho_{L3_{raw}}$ is the raw density derived from IFREMER_L3_IR data, whereas $\rho_{L3_{50km}}$ is smoothed with a 50 km low-pass filter. It should be noted that the assumption of a constant salinity across the fronts allows one to replace density with temperature in (5-11). The ratio of the time average of the measured gradient magnitudes shown on Figure 5-49 and Figure 5-50 is equal to:

$$\frac{\overline{\left|\nabla_{H}\rho_{L3_{raw}}\right|}}{\left|\nabla_{H}\rho_{L3_{50km}}\right|} \approx 2.1 \tag{5-12}$$

Therefore the SST observations of IFREMER_L3_IR over the North Atlantic strongly confirm the k^{-2} assumption between the scales of 10 km and 50 km.

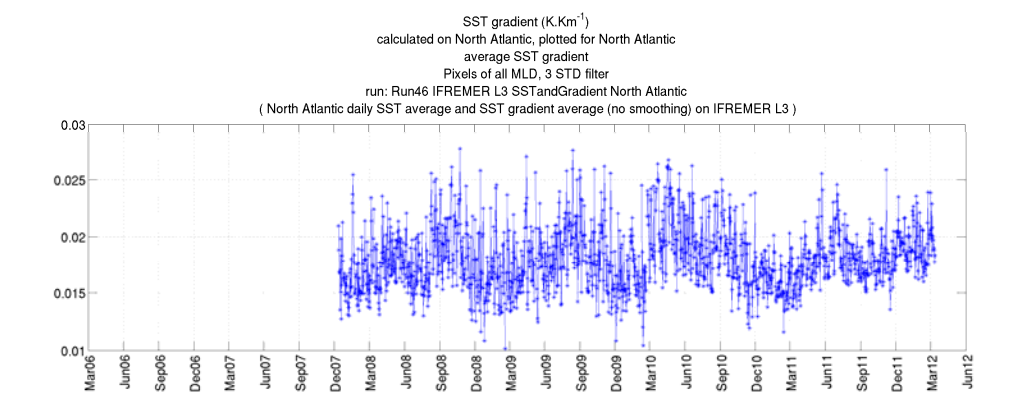


Figure 5-49: Average un-scaled IFREMER_L3_IR SST gradient magnitude over the North Atlantic.

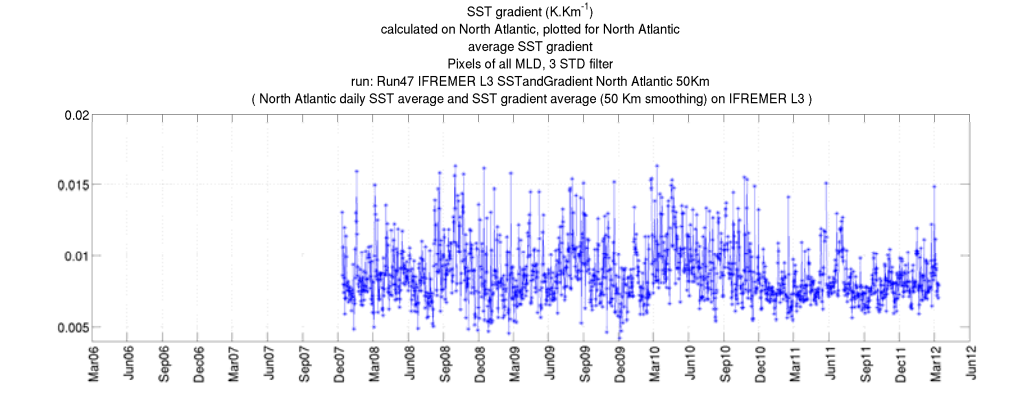


Figure 5-50: Average un-scaled IFREMER_L3_IR SST gradient magnitude over the North Atlantic. The SST images are smoothed by a low-pass 50 km filter before the gradient is calculated.

5.3 Spall (1995) Index Of Subduction

This index is a first order estimation of the subduction at upper ocean fronts driven by internal instabilities. As discussed in section 2.2.2, Spall (1995) estimated the total permanent subduction rate to be 20 m/year, for a region representative of the North Atlantic Subtropical Convergence Zone, using a nonlinear isopycnal primitive equation mode, although local and temporary subduction can be much larger. Here, an evaluation of the Spall index is built on the FLI index in a simple way: wherever a front is detected on a SST image, it is assumed that the phenomenon modelled by Spall (1995) is occurring. The strength of the subduction is constant for all fronts detected above the threshold of Spall (1995) and with the scaling described in section 5.2 to compensate for the low feature resolution of the source images. A simple scaling is applied to estimate the subduction generated by each kilometre of front, it is calculated from the parameters of Spall (1995): 300 km of front in a 300 x 300 km domain leads to an average of 20 m/year permanent subduction rate over the domain 25 days after the front was initialised and left to evolve under the action of baroclinic instability. This leads to a volume of permanently subducted water per kilometre of front of:

$$V_{Spall} = 1.644 \times 10^7 \, m^3 \, day^{-1} km^{-1} \tag{5-13}$$

Equation (5-13) allows a total length of detected fronts (FLI) to be related to a volume and a rate of permanently subducted water at fronts. As the Spall95_Subduction index is calculated proportionally to FLI, it has the same variability. Figure 5-51 shows the permanent subduction calculated on OSTIA with $d = 0 \, km$, $L_f = 0.5 \, km$, $\Delta s = 25 \, km$ over the North Atlantic. This run assumes the fronts to be 0.5 km wide and the raw OSTIA images to have a feature resolution of 25 km. The average permanent rate of subduction at fronts varies between 25 m/year and 60 m/year with annual lows around March/April. This is of the same order of magnitude as estimates of subduction due to large-scale variations in atmospheric forcing, which are typically 50-100 m/year (Spall 1995). Spatial maps of monthly average permanent subduction calculated with this index are shown on Figure 5-52 for two typical maximum months (August 2006 and August 2007) and for a typical minimum month (April 2008). They show a strong spatial variability with an intensive permanent subduction in the Gulf Stream region, the Mediterranean Sea, the North Sea and on Moroccan Coasts around August. Conversely, the permanent subduction at fronts appears extremely low over the Sub-Tropical gyre of the North Atlantic. Around April, there is less subduction on average over the North-Atlantic, especially around the Gulf Stream but also over the Mediterranean Sea. There is however an increased subduction over the Sub Tropical gyre.

Figure 5-53 presents the same subduction index calculated with an assumed frontal width of $L_f=1\,km$. The variability is not changed although the magnitude of the subduction is largely reduced as it varies between 12 m/year and 31 m/year. This run is closer to the 20 m/year subduction estimated by Spall (1995). This illustrates the sensitivity of the permanent subduction rate index to the assumed frontal width.

The results of this parameterization should be interpreted with caution over the shelf seas where the fronts are controlled by rather different dynamics. Moreover these regions are often unstratified.

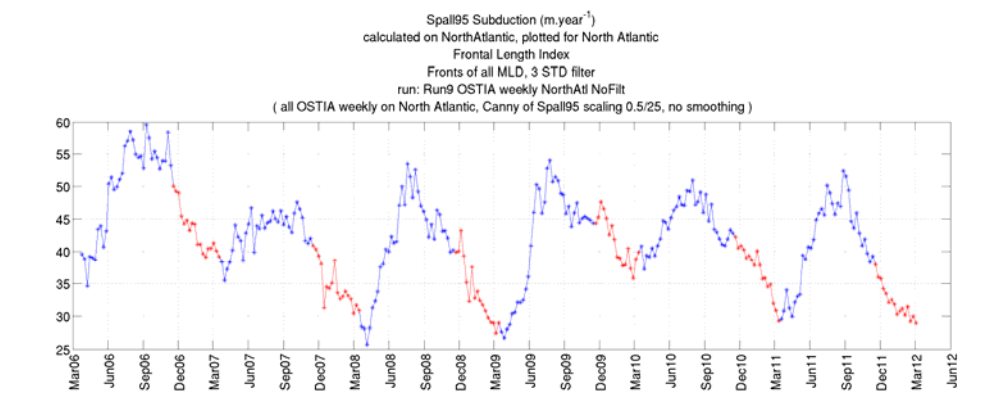


Figure 5-51: Spall (1995) index of permanent subduction (Spall95_Subduction) in $m\ year^{-1}$ processed on weekly OSTIA over the North Atlantic region with $d=0\ km,\ L_f=0.5\ km,\$ and $\Delta s=25\ km.$ Times when more than 50% of the area MLD is deeper than 75 m are plotted in red.

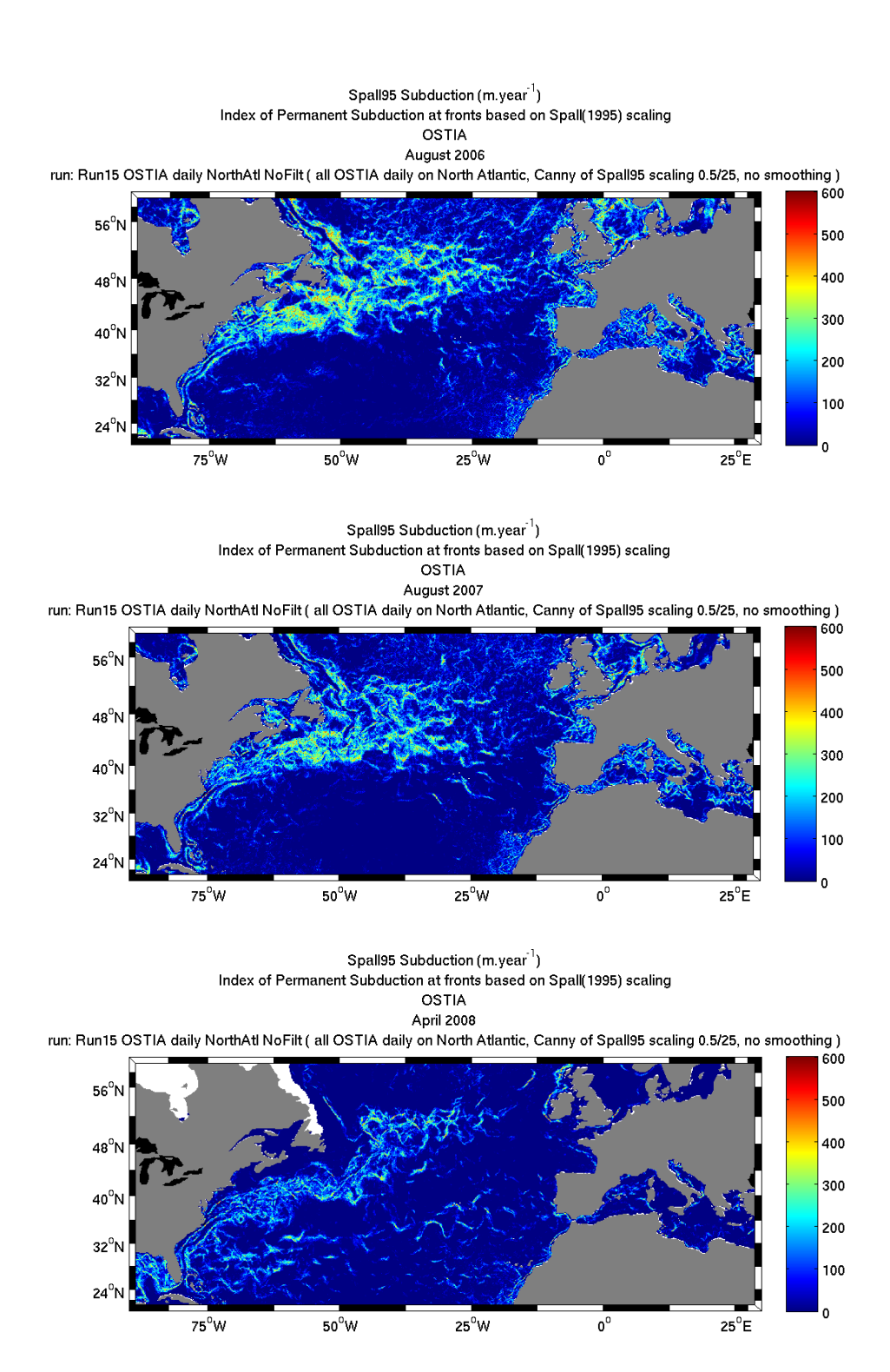


Figure 5-52: Maps of average monthly Spall95_Subduction index in m $year^{-1}$ processed on daily OSTIA over the North Atlantic region with d=0 km, $L_f=0.5$ km, and $\Delta s=25$ km. Top: August 2006, middle: August 2007, bottom: April 2008.

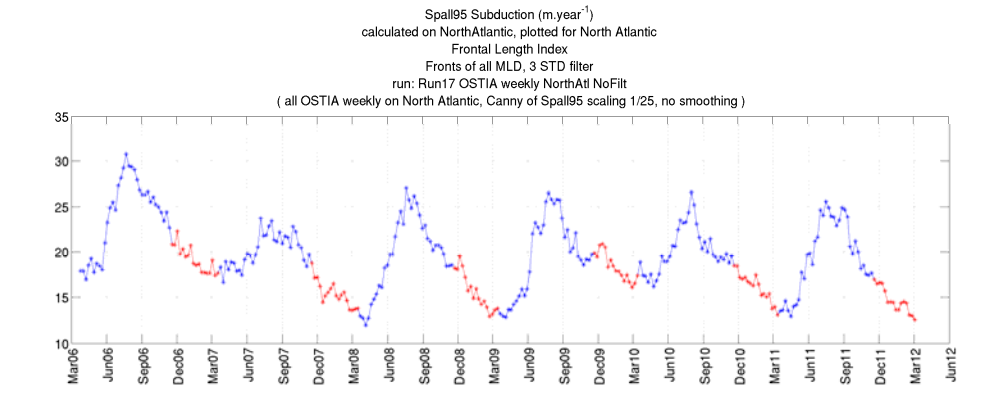


Figure 5-53: Spall (1995) index of permanent subduction (Spall95_Subduction) in $m\ year^{-1}$ processed on weekly OSTIA over the North Atlantic region with $d=0\ km$, $L_f=1\ km$, and $\Delta s=25\ km$. Times when more than 50% of the area MLD is deeper than 75 m are plotted in red.

5.4 Lapeyre and Klein (2006) index of vertical velocity

The Lapeyre_Klein index aims at capturing the vertical velocity generated by frontogenesis when a background straining field stirs a filament as described by Lapeyre and Klein (2006). These filaments are bounded by fronts, which are strengthened whenever the fronts are elongated (see section 2.2.5). The resulting thermal-wind imbalance generates vertical motions that are governed by the Omega equation. The authors calculate a scaling of this equation, based on SQG regime characteristics, they obtain:

$$w(z) = \frac{g\sigma}{N^2} \frac{\Delta \rho}{\rho_0} \frac{z}{D} \exp(z/D)$$
 (5-14)

Where z is the depth, w is the vertical velocity generated by frontogenesis, σ is a scale for the surface large-scale strain field, D is a scale for the vertical decay of density, N^2 is the Brunt-Väisälä frequency:

$$N^2 = -\frac{g}{\rho_0} \partial_z \rho \tag{5-15}$$

 $\Delta \rho$ is the density variation across the fronts that bound the filament. D is the vertical length scale to which the density decays exponentially.

The vertical profile of w(z) is maximum at z = D, where

$$w_{max} = w(D) = \frac{g\sigma}{N^2} \frac{\Delta \rho}{\rho_0} e$$
 (5-16)

The Lapeyre_Klein index developed in the context of this thesis is a measure of the upwelling across the depth *D* at small scale fronts. Fronts are detected with the Canny algorithm and the maximum vertical velocity generated by frontogenesis is evaluated as follows:

• The surface large scale strain field σ is calculated following Johnston et al. (2011):

$$\sigma = \sqrt{\left(\frac{\partial u}{\partial x} - \frac{\partial v}{\partial y}\right)^2 + \left(\frac{\partial v}{\partial x} + \frac{\partial u}{\partial y}\right)^2}$$
 (5-17)

x and y are the horizontal coordinates and u and v are horizontal velocities, which are positive eastward and northward. σ is calculated from gridded altimetry products of absolute geostrophic velocities. The altimeter products were produced by Ssalto/Duacs and distributed by Aviso, with support from Cnes (http://www.aviso.oceanobs.com/duacs/).

- The Brunt-Väisälä frequency is scaled following Lapeyre and Klein (2006) for small scale filaments: N = 62.5 f.
- $\Delta \rho$ is calculated from the density gradient magnitude measured by the Canny algorithm over the crest of the fronts and the assumed front width.

As for the previously mentioned indexes, the Lapeyre_Klein index depends on four parameters: the SST dataset, d the size of the smoothing filter, L_f an estimate of the typical local width of fronts, and Δs an estimate of the feature resolution of the SST product after the smoothing stage.

The parameter L_f influences the index in three independent ways:

• As with the previously mentioned indexes, it is used for the scaling of the density following Equation (5-7).

- It is also used in the calculation of $\Delta \rho$ from the density gradient magnitude measured by the Canny algorithm over the crest of the fronts.
- Finally, it is accounted for in the integration of the vertical velocity calculated on the crests of the fronts into a vertical transport over the surface of the fronts. The underlying assumption is that the upwelling occurs with the same strength across the width of the front and that it is not present further away from the crest than half the width of the fronts on each side.

The sensitivity of the frontal index to L_f is a competition between opposite effects. When it increases, the scaling of the density is reduced. Conversely, when L_f increases $\Delta \rho$ increases which results in a higher vertical velocity w_{max} estimated on the crest of the fronts. In addition, the calculated vertical velocity is integrated over a larger frontal width.

Because the index targets the small scale fronts, it is calculated on IFREMER Level-3 SST products, from which the infrared measurements are extracted. No smoothing being applied in the production of these products, the feature resolution is equal to the images grid resolution $\Delta s = 10 \ km$. Neither is smoothing applied before the fronts are detected: $d = 0 \ km$. The Canny threshold is set to $T = 10^{-3} \ kg \ m^{-3} \ km^{-1}$, which is a very low value allowing the capture of the highest number of fronts, even the weakest ones.

The index is first calculated over the Sargasso Sea, the region in the gyre in the middle of the North Atlantic. The definition of the Sargasso region is presented as a red dotted rectangle in Figure 5-56. It is of interest as it is believed to be a region of low dynamical activity in an oligotrophic balance. As discussed in Chapter 2, it is suspected that the vertical nutrient flux budget could be closed by the vertical exchanges at fronts.

Figure 5-54 presents the Frontal Length Index (FLI) integrated over the Sargasso region defined in Figure 5-56. It is detected on the infrared IFREMER Level 3 products, with no smoothing involved at all (apart from the downsampling of the Level-2 single-sensor SST datasets from about 1 km to 10 km, the final resolution of the Level-3). The seasonal cycle is visible with a lower

FLI during winter and a higher one during summer. The frontogenesis-induced upwelling at fronts as estimated following Lapeyre and Klein (2006) scaling is averaged over the Sargasso Sea region into the Lapeyre_Klein_SSH index shown on Figure 5-55. This index also exhibits a seasonal variability with a higher upwelling during summer. However it also features an inter-annual signal under the form of a higher summer maximum during 2010 than during 2009 or 2008.

The temporal average upwelling rate due to vertical circulation at fronts is 0.15 m/day. This value is comparable in magnitude with the value estimated by Lapeyre and Klein (2006) of about 0.85 m/day. The discrepancy may be a consequence of the difference in dynamical activity between the region numerically simulated by Lapeyre and Klein and the Sargasso region. Indeed the authors base their analysis on a turbulent eddy field which is more energetic than the Sargasso region. Another reason could be a wrong assumption about the fronts width followed by the author of this thesis. Ignoring the sensitivity of the frontal detection process to the parameterized frontal width, which is due to the density scaling, the Lapeyre_Klein_SSH index calculated with two different frontal width would be purely proportional. Indeed,

$$w(L_f = x \, km) = w(L_f = 1 \, km) \cdot x^{3/2}$$
 (5-18)

where $w(L_f=x\,km)$ is the Lapeyre_Klein_SSH index of upwelling calculated while assuming a frontal width $L_f=x\,km$. Hence, while the assumption $L_f=1\,Km$ leads to a temporal average upwelling rate due to vertical circulation at fronts of $\overline{w}(L_f=1\,km)=0.15\,m/day$, assuming $L_f=0.5\,km$ would have led to $\overline{w}(L_f=0.5\,km)=0.05\,m/day$. Conversely, a larger assumed frontal width would lead to a higher estimated frontal upwelling: $\overline{w}(L_f=2\,km)=0.43\,m/day$ and $\overline{w}(L_f=5\,km)=1.68\,m/day$.

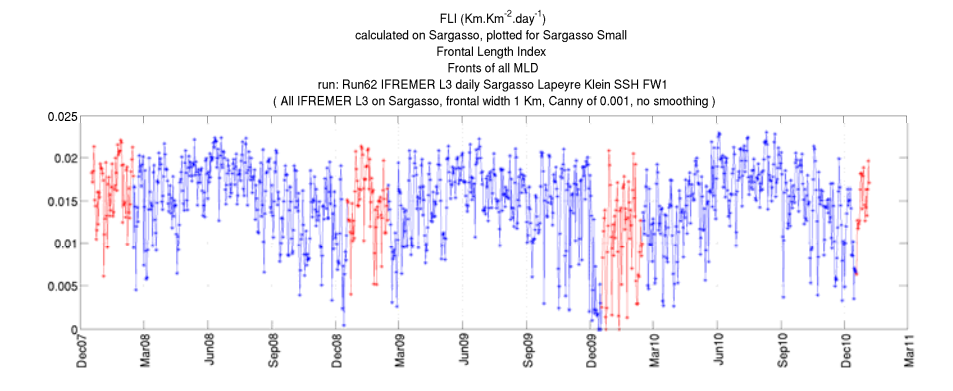


Figure 5-54: Front Length Index (FLI) in $km km^{-2} day^{-1}$ processed on daily IFREMER_L3_IR over the Sargasso Sea region with d=0 km, $L_f=1 km$, $\Delta s=10 km$, and $T=10^{-3} kg m^{-3} km^{-1}$. Times when more than 50% of the area MLD is deeper than 75 m are plotted in red.

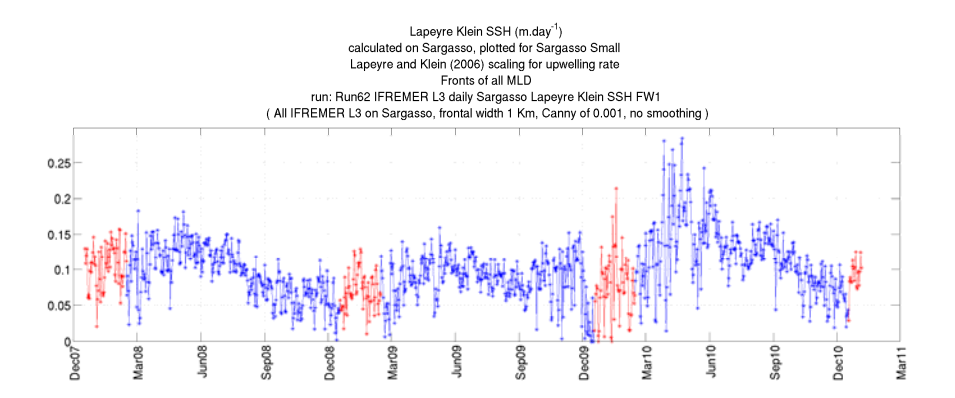


Figure 5-55: Lapeyre_Klein_SSH index of frontogenesis induced upwelling in $m.day^{-1}$ processed on daily IFREMER_L3_IR over the Sargasso Sea region with d=0 km, $L_f=1$ km, $\Delta s=10$ km, and $T=10^{-3}$ kg m^{-3} km^{-1} . Times when more than 50% of the area MLD is deeper than 75 m are plotted in red.

Although the quantitative measure of the small scale frontal upwelling due to large scale strain requires a more precise understanding of the frontal width, the spatial and temporal variability is independent from it and conclusions can be drawn based upon them. The monthly composite of the index over the Sargasso region is mapped on Figure 5-56. It shows that the upwelling occurs mainly over the Gulf Stream region, this is not surprising as it is known to be a dynamic area. However one can observe scattered and very localized frontal areas where the vertical transport is taking place at a lower rate even at places

where not much vertical activity is expected at small scales. This measured activity has a non-negligible effect on the vertical transport once averaged over the Sargasso Sea as shown on Figure 5-55.

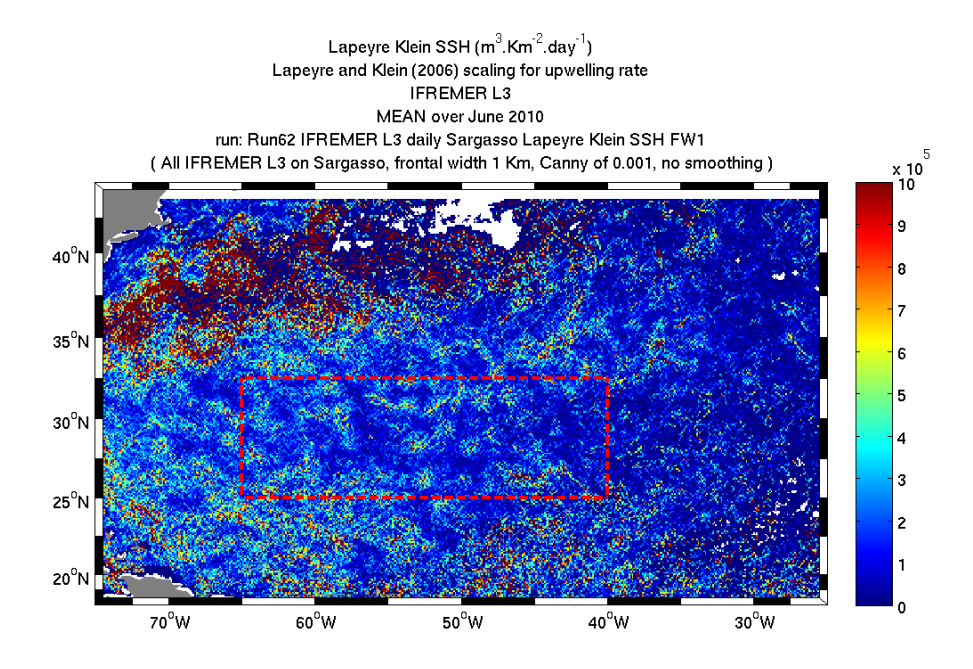


Figure 5-56: Monthly composite of the Lapeyre_Klein_SSH index of frontogenesis induced upwelling in June 2010 processed on daily IFREMER_L3_IR over the Sargasso Sea region (shown by the red dotted line) with $d = 0 \ km$, $L_f = 1 \ km$, $\Delta s = 10 \ km$, and $T = 10^{-3} \ kg \ m^{-3} \ km^{-1}$.

Figure 5-57 and Figure 5-58 present the temporal variability of the FLI and Lapeyre_Klein indexes over the Mediterranean Sea. They are calculated in the same way as over the Sargasso Sea except for the mesoscale strain which is estimated from the Mediterranean MADT AVISO product. Both the FLI and the Lapeyre_Klein indexes exhibit seasonal variability with a low in winter and a high in summer. It is interesting to note that the two indexes show different annual signal and that the Lapeyre_Klein index seasonal variability is more pronounced. The Lapeyre_Klein index over the Mediterranean Sea is about twice as high as that of Lapeyre_Klein_SSH over the Sargasso Sea. It should be added that assuming the mesoscale strain to be constant at $\sigma = 2.5 \cdot 10^{-6} \, s^{-1}$, following the classical value related to small-scale filaments taken by Lapeyre and Klein (2006), leads to the underestimation of the Lapeyre_Klein_SSH by a

factor of two. Finally, there is no clear inter-annual signal in the Lapeyre_Klein index over the Mediterranean Sea over the years when IFREMER Level-3 data are available.

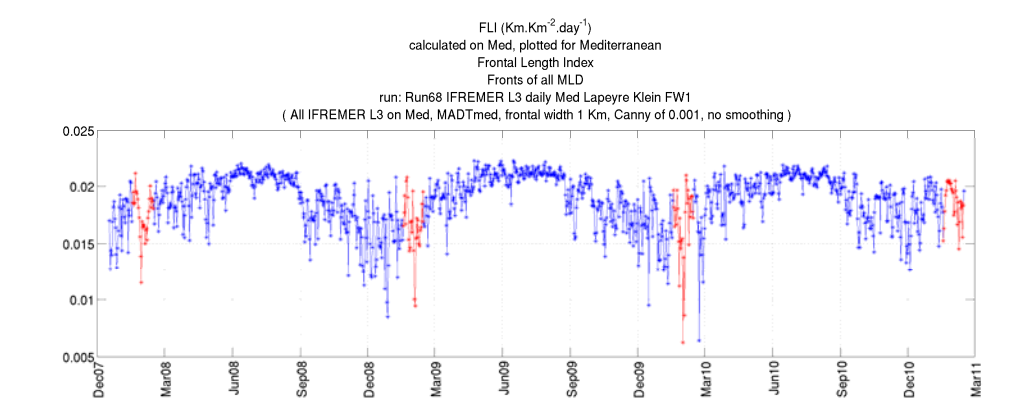


Figure 5-57: Front Length Index (FLI) in $km \, km^{-2} day^{-1}$ processed on daily IFREMER_L3_IR over the Mediterranean Sea region with $d=0 \, km$, $L_f=1 \, km$, $\Delta s=10 \, km$, and $T=10^{-3} \, kg \, m^{-3} \, km^{-1}$. Times when more than 50% of the area MLD is deeper than 75 m are plotted in red.

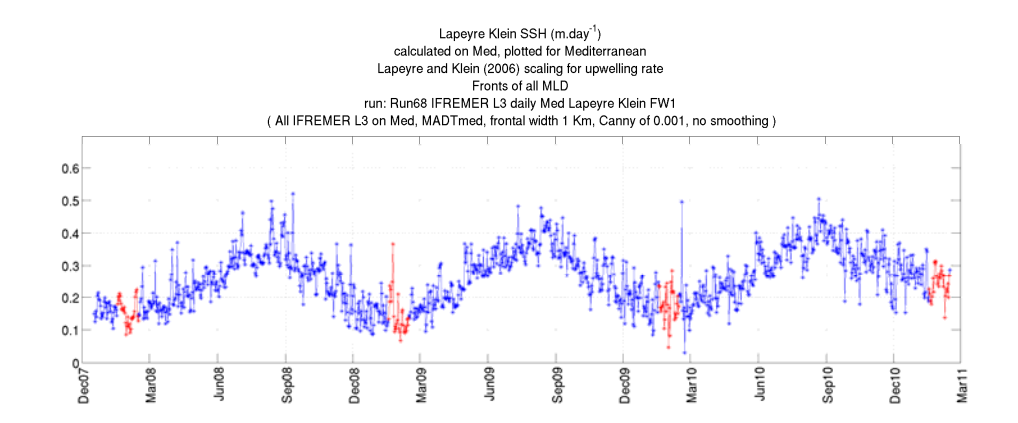


Figure 5-58: Lapeyre_Klein index of frontogenesis induced upwelling in $m.day^{-1}$ processed on daily IFREMER_L3_IR over the Mediterranean Sea region with d=0 km, $L_f=1$ km, $\Delta s=10$ km, and $T=10^{-3}$ kg m^{-3} km^{-1} . Times when more than 50% of the area MLD is deeper than 75 m are plotted in red.

Figure 5-59 presents the average spatial variability of the Lapeyre_Klein index over the Mediterranean Sea during the month of September 2010. As for Figure 5-56, higher upwelling rates are observed in the vicinity of strong fronts

and eddies, although a non-negligible portion of it occurs in less dynamical regions.

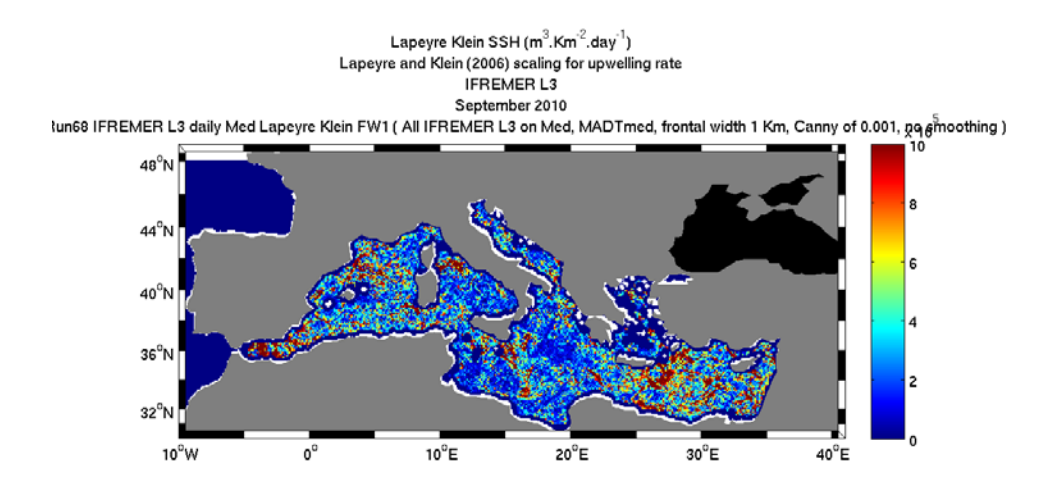


Figure 5-59: Monthly composite of the Lapeyre_Klein index of frontogenesis induced upwelling in September 2010 processed on daily IFREMER_L3_IR over the Mediterranean Sea region with d=0 km, $L_f=1$ km, $\Delta s=10$ km, and $T=10^{-3}$ kg m^{-3} km⁻¹.

5.5 Capet et al. (2008) index of frontogenesis

This section presents the exploration of the frontogenesis driven by the horizontal strain following analytical and numerical results of Capet et al. (2008b) through satellite observations. Section 2.4 introduces the frontogenesis function defined by Capet et al. (2008b):

$$F_S = Q_S \cdot \nabla_H \rho \tag{5-19}$$

Where

$$Q_S = -\left(\frac{\partial u}{\partial x}\frac{\partial \rho}{\partial x} + \frac{\partial v}{\partial x}\frac{\partial \rho}{\partial y}, \frac{\partial u}{\partial y}\frac{\partial \rho}{\partial x} + \frac{\partial v}{\partial y}\frac{\partial \rho}{\partial y}\right)$$
(5-20)

x and y are the horizontal coordinates and u and v are horizontal velocities, which are positive eastward and northward.

 F_S is a measure of the rate of increase of the horizontal density gradient arising from the straining by the horizontal velocity field. Hoskins (1982) states:

$$\frac{D|\nabla_H \rho|^2}{Dt} = F \tag{5-21}$$

Where F is the addition of the straining by the horizontal density field (F_S), the straining deformation by vertical velocity, the vertical mixing and the horizontal diffusion.

A frontal index is constructed that is a quantitative measure of F_S over the detected fronts. The author of this thesis is not aware of any direct analytical link between this function and the rate of vertical velocity at fronts. However Capet et al. (2008b) show a very strong correlation between F_S and vertical circulation at small scale. F_S is then considered as a valuable indicator of vertical exchanges at fronts driven by frontogenesis.

As done in the previous section, the horizontal surface velocity field is approximated to its mesoscale geostrophic component. It is taken from satellite AVISO altimetry measurements. As opposed to the Lapeyre_Klein_SSH index presented in the previous section, the Capet_Fs index accounts for the relative orientations of the surface fronts and the surrounding mesoscale field.

Figure 5-60 displays a fairly cloud-free Level-3 SST map of the California upwelling that Capet et al. (2008b) attempted to model. This image features small scale frontal instabilities along the upwelling which are comparable to the ones present on Capet et al. model output shown on Figure 2-7. The model output benefits from a finer spatial resolution (0.75 km) than the Level-3 SST image (0.1°). The horizontal surface density gradient magnitude is shown on Figure 5-61. It can be compared to the model output on Figure 2-8.a. Note that the density on Figure 5-61 is scaled following (5-7) and an assumed front width of 0.5 km. Scaling the model output density gradient to account for its resolution in the same way would require the multiplication of the model output density gradient by 1.22. The scaled maximum density gradient observed on the model is

$$|\nabla_h \rho|_{max \, model} = 12.2 \times 10^{-5} \, kg. \, m^{-4}$$
 (5-22)

Whereas the scaled maximum observed on the Level-3 SST image (after a few high pixels are discarded) is

$$|\nabla_h \rho|_{max.SST} = 15 \times 10^{-5} \, kg.m^{-4}$$
 (5-23)

Section 5.2 shows that the OSTIA SST products do not allow one to measure the high density gradient magnitude that Capet et al. (2008b) model is claiming to occur over the California Current system, even after the scaling to account for their reduced feature resolution is applied. Conversely, Equations (5-22) and (5-23) demonstrate that the IFREMER Level-3 SST products feature such high density gradient magnitude once they are scaled.

Figure 5-62 displays F_S calculated from the SST shown on Figure 5-60 and the AVISO altimetry product. Comparing to Figure 2-8.c, the spatial distribution of F_S appears similar from the model and as calculated from satellite observations. It generally follows the patterns of high density gradient with an added effect originating from the position of the fronts within the straining field. Most of the strong frontal regions on Figure 5-62 feature a frontogenesis function F_S above $3 \times 10^{-14} \, kg^2 m^{-8} s^{-1}$. The model output features most fronts above $6 \times 10^{-14} \, kg^2 m^{-8} s^{-1}$, which is twice as high. This discrepency is most probably due to the low resolution of the altimetry data compared to the model horizontal velocities and to the fact that the ageostrophic circulation effect on local strain is ignored in the calculations leading to Figure 5-62.

The Capet_Fs index is based on the frontogenesis function F_S as defined above but integrated only on the front crests. It is therefore a measure of the amount of fronts and the frontogenetic forcing of the mesoscale straining field on them. This is illustrated on Figure 5-65 which represents the map of Capet_Fs on one day. The time series of the geographically-averaged Capet_Fs index is shown on Figure 5-67 while the FLI based on the same parameters is shown on Figure 5-66. These two indices are calculated with d=25 km, $L_f=0.5$ km, and $\Delta s=25$ km on OSTIA. It is worth noting that the MLD is constantly shallower than 75 m in the California Current region.

The seasonal variability is obvious in these two signals, whereas the cloud coverage shown on Figure 5-64 does not feature any clear seasonal variability. This indicates that the seasonal variability observed in OSTIA fronts over this region is not an artefact of the data introduced by the seasonal variability of

the cloud coverage. As for the Lapeyre_Klein_SSH index, it should be stressed that, although the FLI and Capet_Fs feature a common seasonal variability, they are not proportional and a signal is clearly added within Capet_Fs by the frontogenesis function. Comparing the two indexes around March 2007, one can notice a difference in the indexes shapes. On March 2007 both indexes reach an annual minimum, but the Capet_Fs index remains low much longer than the FLI. One can conclude that not only the FLI is low at that period but also the frontogenesis function. A low frontogenesis function can be caused either by a low density gradient magnitude, which also results in a lower FLI, or a low Q_S , or a low projection of Q_S on the density gradient. The fact that the Capet_Fs index remains low longer than FLI indicates that the straining of the mesoscale field is reduced around March. Figure 5-68 illustrate the difference between the simple FLI and the Capet_Fs index embedding the configuration of the flow with regard to the fronts. In August 2009 fronts are detected nearly evenly over the California Current region, however the frontogenesis appears to occur with more strength close to the coastline at 40°N. Other areas are populated with many fronts but do not seem to host strong frontogenesis action of the mesoscale flow as resolved by the altimetry products.

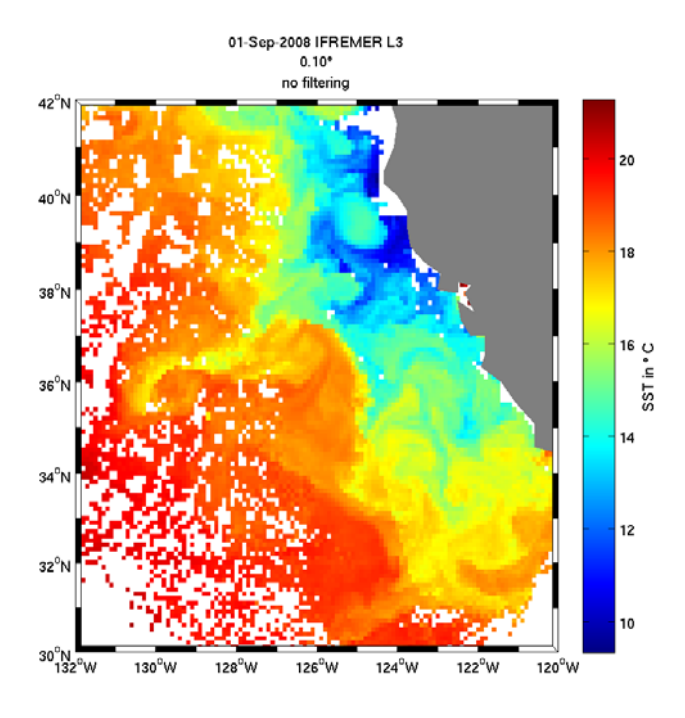


Figure 5-60: IFREMER Level-3 SST image of the California Current upwelling on 01/09/2008.

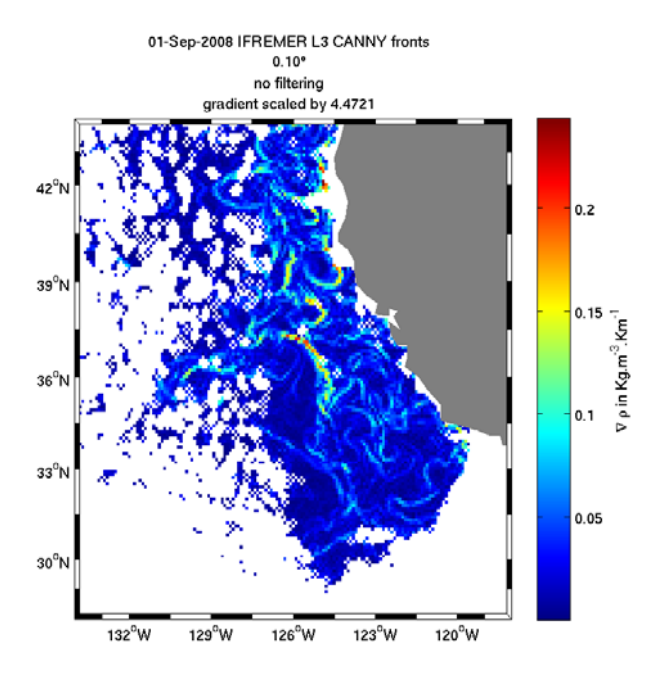


Figure 5-61: Density gradient magnitude on 01/09/2008 calculated from the SST shown on Figure 5-60.

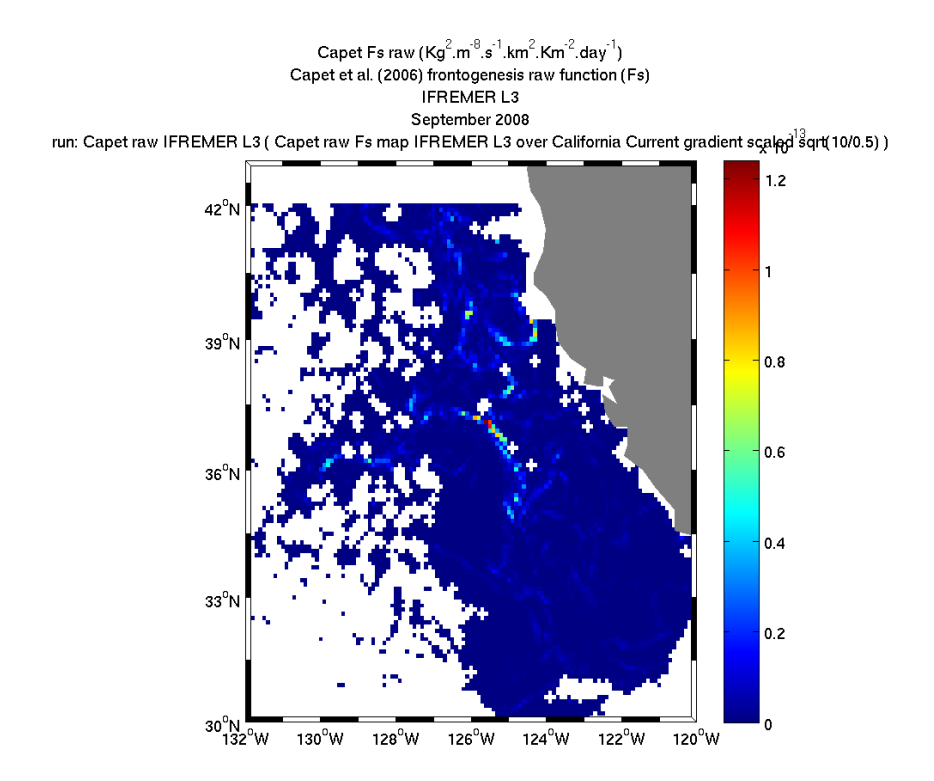


Figure 5-62: Frontogenesis function F_S in $kg^2m^{-8}s^{-1}$ calculated from the density gradient magnitude shown on Figure 5-61 and altimetry data on 01/09/2008.

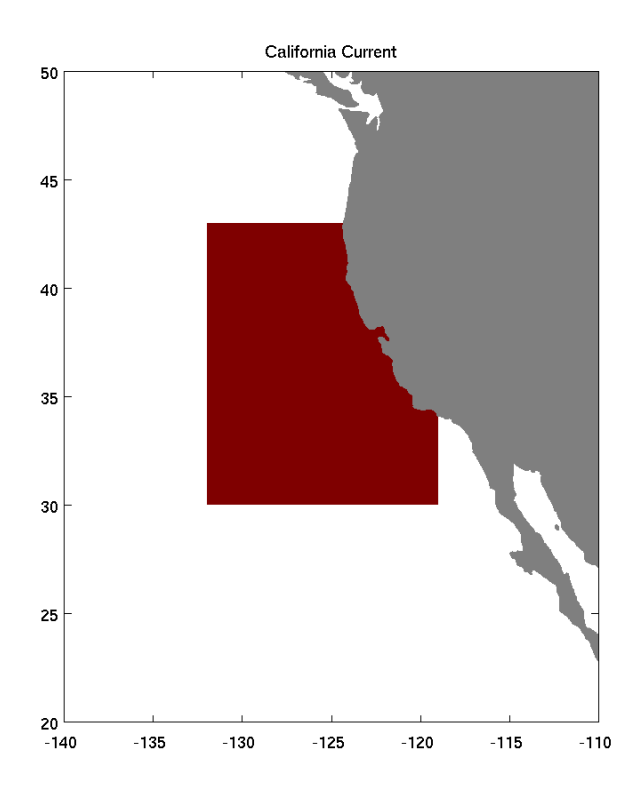


Figure 5-63: California Current region over which the frontal indexes are calculated on Figure 5-66 and Figure 5-67.

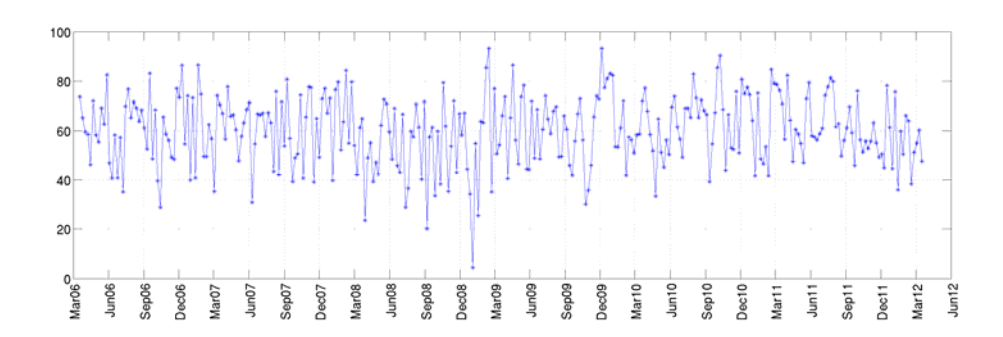


Figure 5-64: Percentage of cloud coverage over the California Current region from NOAA.

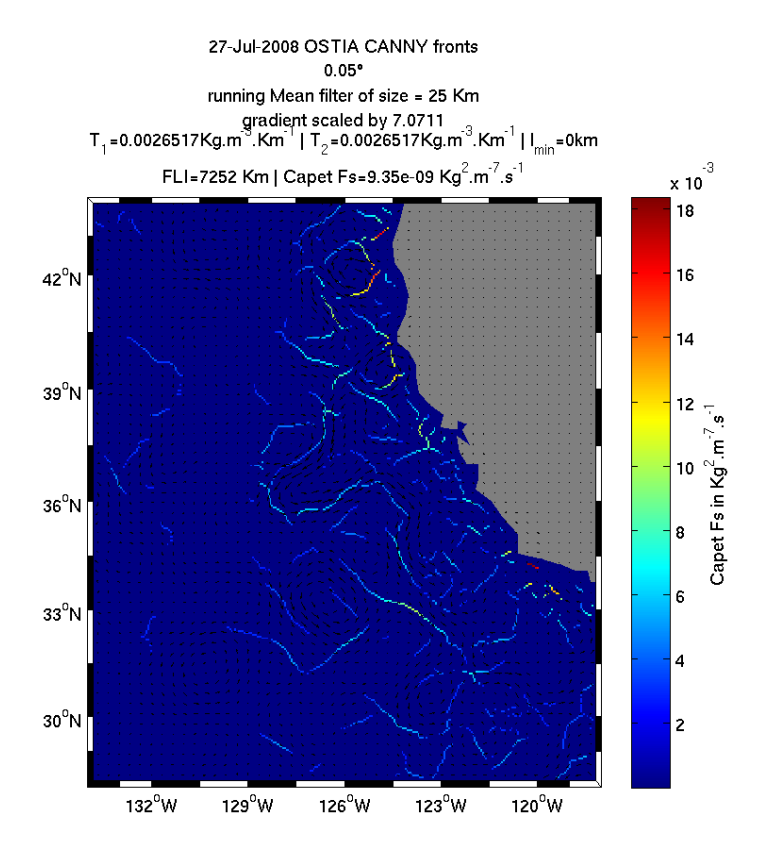


Figure 5-65: Frontogenesis funtion F_S in $kg^2m^{-8}s^{-1}$ calculated on OSTIA of 27/07/2008 in the California Current Region, plotted on the fronts detected with d=25~km, $L_f=0.5~km$, and $\Delta s=25~km$. Black arrows are the altimetry AVISO MADT horizontal velocities on the same day, used in the calculation of F_S .

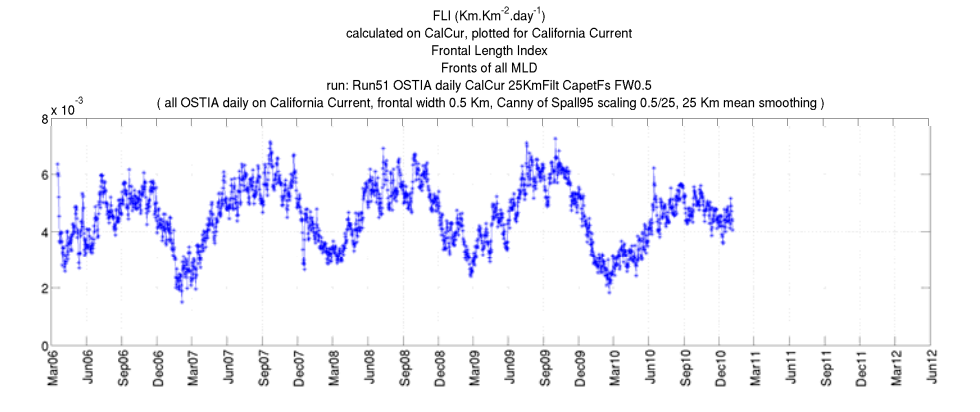


Figure 5-66: Front Length Index (FLI) in $km km^{-2} day^{-1}$ processed on daily OSTIA over the California Current region with d=25 km, $L_f=0.5 km$, and $\Delta s=25 km$. The MLD is constantly shallower than 75 m.

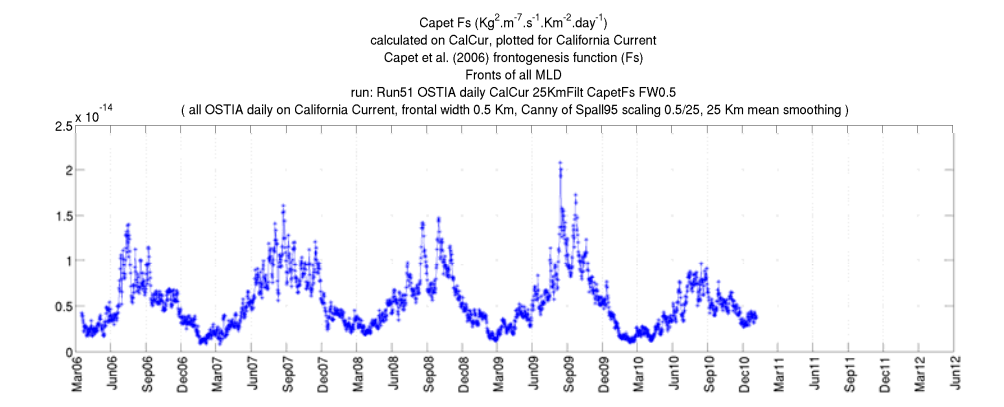


Figure 5-67: Capet_Fs index of frontogenesis in $kg^2m^{-7}s^{-1}km^{-2}day^{-1}$ calculated on daily OSTIA SST images over the California Current region with d=25~km, $L_f=0.5~km$, and $\Delta s=25~km$. The MLD is constantly shallower than 75 m.

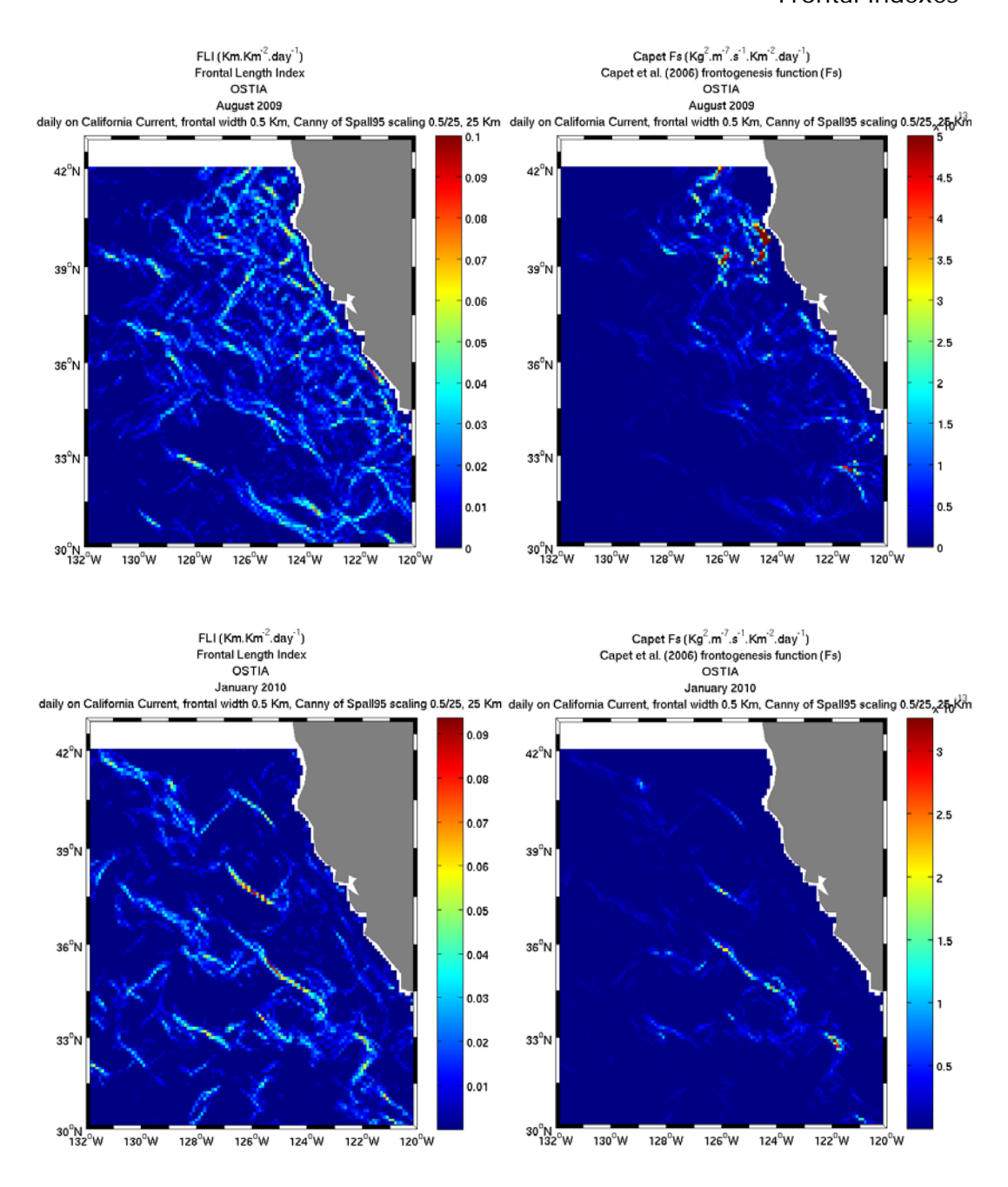


Figure 5-68: Monthly-averaged FLI and Capet_Fs index calculated on OSTIA with d=25~km, $L_f=0.5~km$, and $\Delta s=25~km$, shown on August 2009 and January 2010.

5.6 Fox-Kemper and Ferrari (2008) index of restratification at fronts

This section presents the Fox_Kemper frontal index that attempts to capture the restratification by mixed layer eddies (MLE) that develop from baroclinic instabilities of ocean fronts. MLE effects on stratification are described in section 2.3. This frontal index is based on the parameterization of the MLE restratification suggested by Fox-Kemper and Ferrari (2008) (hereafter referred to as F-KF). The equivalent vertical heat flux due to MLE restratification is estimated as a function of the horizontal buoyancy gradient, the mixed layer depth and the inertial period:

$$c_p \rho \overline{\overline{w'T'}} = \frac{c_p \rho}{g \alpha} \frac{C_e \left| \nabla \overline{\overline{b}}^z \right|^2 H^2}{|f|}$$
 (5-24)

Where c_p is the water specific heat, α is the thermal expansion coefficient, $C_e=0.06$ is the stirring efficiency coefficient estimated by F-KF, H is the mixed layer depth. $\nabla \bar{b}^z$ is the horizontal buoyancy gradient averaged vertically over the mixed layer. The buoyancy is defined by $b=-g\rho/\rho_0$. The double overline indicates horizontal averaging onto the grid of the coarse numerical model this parameterization is developed for, and primes denote submesoscale perturbations from the coarsened averages.

MLE fluxes are a rearrangement of buoyancy and not a source, but F-KF convert the flux to heat flux units in order to allow ready comparison of the MLE restratifying fluxes to air-sea heat fluxes.

This parameterization is intended to improve coarse resolution OGCM that do not resolve the submesoscale by having them account for the restratification produced by horizontal buoyancy gradients which occurs at small scales. However F-KF estimate the climate implications of this parameterization by applying the restratification scaling to satellite observations. They estimate the mixed layer depth from the de Boyer Montegut et al. (2004) climatology and use a constant $\alpha_T = 2 \cdot 10^{-4} K^{-1}$. They claim that estimating the horizontal buoyancy gradient from SST satellite data leads to unrealistically high values of vertical fluxes that would quickly restratify the mixed layer worldwide. Their interpretation is that the SST overestimates the buoyancy gradient because of

temperature-salinity compensation at the surface. Alternatively, they estimate the horizontal buoyancy gradients from satellite altimetry. They calculate the vertical fluxes to be comparable to monthly mean air-sea fluxes in large areas of the ocean which suggests that restratification by mixed layer eddies is a leading order process in the upper ocean.

The index implemented in the context of this thesis relies on preliminary frontal detection on the surface density fields derived from SST images. The parameterization is applied only at the fronts and across their width. This strategy allows minimizing the bias created by the compensation, as does the flagging of the estimations relying on a majority of pixels with a mixed layer depth deeper than 75 m. As for the Lapeyre_Klein frontal index, the Fox_Kemper index relies on the assumed frontal width L_f . This parameter affects the calculation of the index in the scaling of the density gradient magnitude to account for the limited feature resolution of the SST images. Independently, it is also used in the calculation of the surface over which the estimated flux is integrated (along the detected front length and across the assumed front width) for the calculation of spatial averages. The mixed layer depth is again extracted from the de Boyer Montegut et al. (2004) climatology. The thermal expansion coefficient is not taken to be constant as assumed by F-KF but is estimated from the SST and the WOA climatology for SSS with the GSW toolbox. The estimation of the horizontal buoyancy gradient from the SST rather than from satellite altimetry obviously permits the observation of much finer spatial and temporal scales (O(10 km) and O(1 day) versus O(100 km) and (30 days)).

The time series of the geographically-averaged Fox_Kemper index is shown on Figure 5-70 while the FLI based on the same parameters is shown on Figure 5-69. These two indices are calculated with $d=0\ km$, $L_f=0.5\ km$, and $\Delta s=10\ km$ on IFREMER_L3_IR over the North-Atlantic region. The FLI index features a seasonal variability described above with a low in winter and a high in summer. Conversely, the Fox_Kemper index features an opposite seasonal variability. This is due to the strong influence of the mixed layer depth in this index. The mixed layer depth contributes to the Fox_Kemper signal with more strength than the quantity of detected fronts. The former is extracted from a monthly climatology which explains small discontinuities in the Fox_Kemper

temporal signal. The variability of Fox_Kemper within one month hence is entirely due to the variability of detected fronts and their strength. This shows that the frontal signal is not negligible in the Fox Kemper index.

The North-Atlantic average of MLE-induced restratifying flux varies from 1 W.m⁻² in the summer to 15 W.m⁻² in the winter when the MLD is large. It should be recalled that the winter values are associated with a lower confidence since the phenomenon of compensation is more likely to introduce a bias.

Figure 5-71 presents the spatial distribution over the world ocean of the monthly average of MLE-induced restratifying flux in February 2010 and August 2010. It compares fairly well with the heat flux calculated by F-KF from altimetry shown on Figure 5-72. In February, the F-KF heat flux is slightly higher on the Gulf Stream West of 30°W and nearly zero elsewhere. The flux shown on Figure 5-71 is lower however more spread around over the ocean, with non-negligible values south of the Gulf Stream and north of the Antarctic Circumpolar Current in the South Atlantic. The restratifying flux is also twice as high as calculated by F-KF on the Mediterranean Sea. Similarly to F-KF results, a high restratifying flux is observed in regions which are crucial for communication between the atmosphere and ocean such as deep water formation regions. F-KF compared the restratifying flux to the Grist and Josey (2003) air-sea heat flux dataset and found that the flux they calculated is most of the time comparable to the air-sea heat flux. During active convection events in times of extreme heat fluxes, MLE fluxes are overwhelmed by air-sea fluxes, although they are comparable to the monthly mean fluxes and will restratify after cooling events (F-KF).

The Fox_Kemper index was also calculated with an assumed front width of $L_f=1\ km$. Far fewer fronts were detected although the surface over which the flux is integrated is increased and the resulting restratifying flux is very close in absolute value to the one shown on Figure 5-70. This shows that this index has a low sensitivity to L_f .

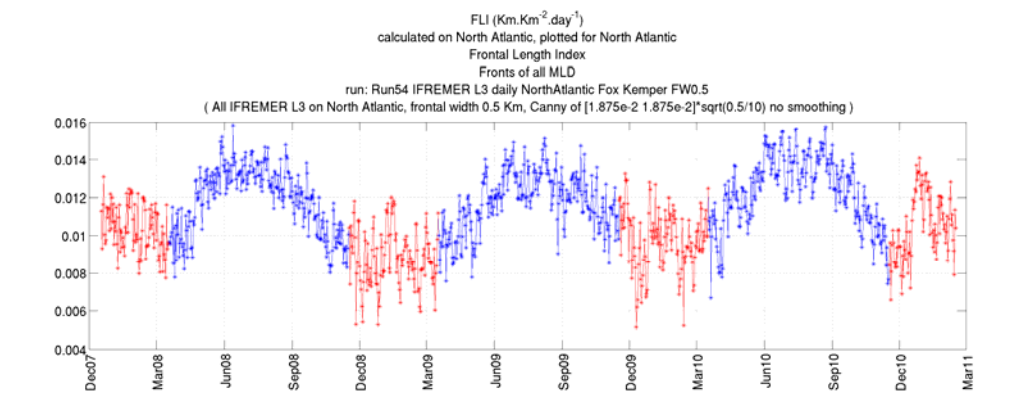


Figure 5-69: Front Length Index (FLI) in $km km^{-2} day^{-1}$ processed on daily IFREMER_L3_IR over the North Atlantic region with d=0 km, $L_f=0.5 km$, and $\Delta s=10 km$. Times when more than 50% of the area MLD is deeper than 75 m are plotted in red.

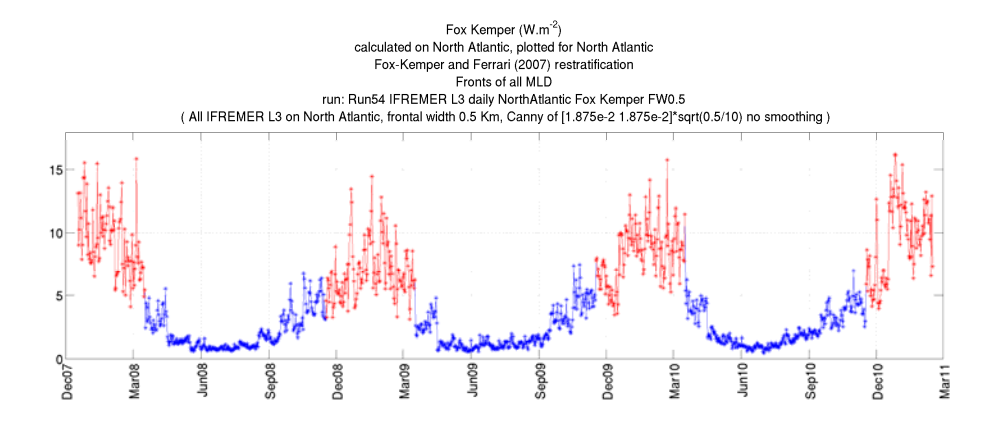


Figure 5-70: Fox_kemper index of restratification at fronts in $W.m^{-2}$ processed on daily IFREMER_L3_IR over the North Atlantic region with d=0~km, $L_f=0.5~km$, and $\Delta s=10~km$. Times when more than 50% of the area MLD is deeper than 75 m are plotted in red.

Fox Kemper (W.m⁻²) Fox-Kemper and Ferrari (2007) restratification IFREMER L3 February 2010 run: Run73 IFREMER L3 daily global Fox Kemper FW0.5 (All IFREMER L3 global on Feb 2010, frontal width 0.5 Km, Canny of [1.875e-2 1.875e-2]*sqrt(0.5/10) no smoothing) 100 60°N 80 70 30⁰N 60 **0**° 50 40 30°S 30 20 60°S 10 180°W 120°W 60°W 60°E 120°E 180°W

Fox Kemper (W.m⁻²) Fox-Kemper and Ferrari (2007) restratification IFREMER L3 August 2010 run: Run74 IFREMER L3 daily global Fox Kemper FW0.5 (All IFREMER L3 global in Aug 2010, frontal width 0.5 Km, Canny of [1.875e-2 1.875e-2]*sqrt(0.5/10) no smoothing) 100 90 60°N 80 70 30°N 60 00 50 40 30°S 30 20 60°S 10

Figure 5-71: Monthly average of Fox_kemper index of restratification at fronts in $W.m^{-2}$ processed on daily IFREMER_L3_IR with d=0~km, $L_f=0.5~km$, and $\Delta s=10~km$. February 2010 (top) and August 2010 (bottom).

60°E

120°E

180°W

120°W

 $60^{\circ}W$

180°W

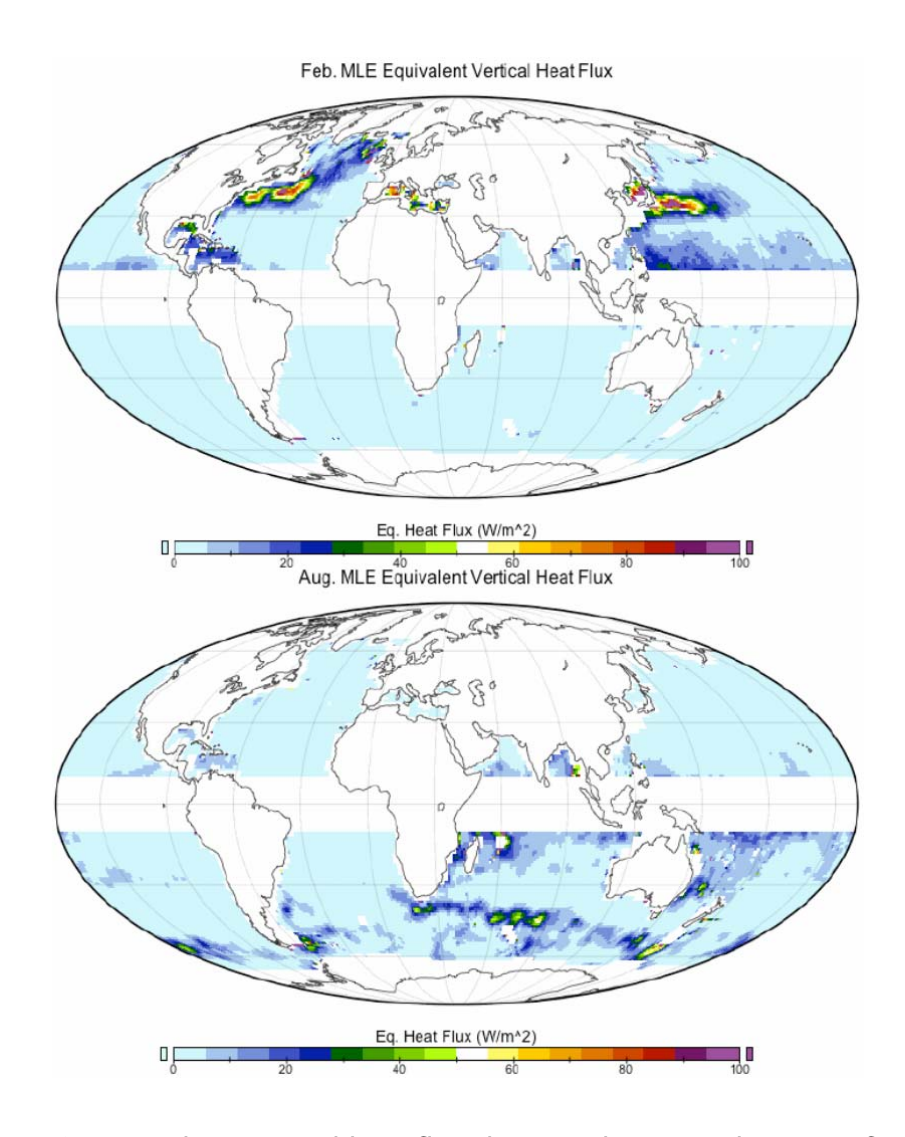


Figure 5-72: Equivalent vertical heat flux due to submesoscale restratification of the mixed layer as estimated by Fox-Kemper and Ferrari (2008). February (top) and August (bottom).

5.7 Conclusion

This chapter has built on the combination of results from the first three chapters. Dynamical studies presented in chapter 2 which allow surface horizontal density gradients to be related to vertical exchanges were used in synergy with the critical understanding of frontal detection methods and of analysis SST products presented in chapter 3 and 4 respectively. A methodology for the processing of frontal indexes was developed (see section 5.1.2) that allows a large number of adjustable parameters to be handled. The combinations of these can potentially specify a very large amount of operations. This methodology relies on a Matlab-based software that was developed by the author of this thesis in order to produce the results discussed in the rest of the chapter. This software is a very important achievement of the study as it was proved capable of dealing with the complexity involved in the frontal detection within high resolution SST data and over long time series. It also demonstrated the necessary flexibility to adapt to many different input data and frontal calculations. Finally its robustness permitted massive data crunching exercises that led to the diversity of results presented in this chapter and the next.

The approach used for scaling of the horizontal gradient based on the k² assumption to account for the resolution and the feature resolution of the input dataset was investigated and shown to be performing well between 10 and 50 km (see section 5.2.1). This scaling performs well at estimating the effect of smoothing on spatial averages of the temperature gradient but does not precisely reconstruct the SST gradient at the front crests. The highest resolution SST data are therefore still needed for optimized frontal exploration. The errors associated with this scaling are two-fold: first the SST images may not have a wavenumber spectrum scaled to k² (in particular when the product is very smooth like OSTIA), and second because the k² is good at approximating the gradient average over a large region but not as accurate for reconstructing the gradient at the front crest where the Canny algorithm assesses the frontal strength.

A strategy was implemented in section 5.1.3 to minimize the errors introduced by temperature-salinity compensation at fronts, by flagging results associated to a mixed-layer depth larger than 75 m. This approach is an attempt to make

the most of currently available results by others on temperature/salinity compensation in the mixed layer, although these results are not fully conclusive. Therefore the flagging of potential compensation in this thesis should be interpreted with care. A great deal of additional confidence would be attached to the results of this thesis if a better understanding were reached on the phenomenon of compensation. A methodology to calculate density gradient from temperature gradient with a climatology of surface salinity was also described, assuming a constant salinity across the fronts (i.e. no compensation).

The frontal detection methodology as presented (see section 5.2) relies strongly on three parameters: the estimated finer spatial scale present in the ingested SST images, the minimum strength of the fronts that are retained and composited in the indexes, and in some cases the assumed width of the fronts. It was considered important to select the most appropriate values for these parameters for each study cases as they have a combined effect on the amount of detected fronts and on their estimated strength. The threshold on the minimum strength of fronts to retain is important as it is understood that the combined effect of weak fronts can be a significant contributor in some geophysical budgets. Little was found in the dynamical studies on the minimum strength at which a front has an impact on regional budgets. A threshold suggested by Capet el a. (2008b) was discarded as it was not observed in the Level-4 SST images. The choice was made to retain a threshold based on the results presented by Spall (1995) as it appeared to return an appropriate quantity of fronts when used in combination with the SST gradient scaling. The frontal width was taken as 0.5 km but the variability of the results was conserved when assuming a frontal width of 1 km.

Future theoretical or analytical studies could largely improve the selection of these parameters and therefore provide more confidence in the absolute frontal indexes. In-situ measurements of temperature and salinity by ferry-boxes on research ships or opportunity ships have the potential to provide surface density profiles with a spatial resolution sufficiently fine to explore the frontal width spatial and temporal variability. Satellite SST images could be used in synergy to account for the angle between the ship track and the considered fronts. Infrared Sea Surface Temperature Autonomous Radiometer (ISAR) acquisitions on ships of opportunity also provide this potential for sea

surface temperature (Donlon et al. 2008). The drawback of such measurements is their low spatial and temporal coverage limited to the ship tracks and position at any given time. High-resolution satellite Level-2 SST data such as AATSR could be used in a complementary approach which would take advantage of their global coverage (despite cloud hindering) for fronts of width larger than 1 km.

The estimation of the amount of small scales present in the SST images is an important factor in the quantitative frontal results. The resolved scales are well understood for Level-2 and Level-3 products, but it was explained that they are not easily estimated on Level-4 SST products. Absolute care must be taken when detecting fronts on Level-4 SST products as this detection relies on small scale variations. Yet the scales resolved by a particular Level-4 SST product may vary in space and time as a result of available SST data and the complex behaviour of the Optimal Interpolation. For the time being, very little information is provided to the users of such products regarding the smoothing involved in its production. It is a strong recommendation concluding this thesis that more visibility on this aspect should be provided to the users by the Level-4 SST producers. This information is however not straightforward to obtain, even for the engineers and scientists in charge of the Level-4 SST production. This is why a large effort and an important outcome of this thesis is the in-depth analysis of the scales present in the various Level-4 SST products by means of their frontal content. This analysis was required to gain confidence in the geophysical results of this thesis but will also be an independent assessment of great interest to the Level-4 SST producers.

The basic frontal indexes of frontal length (FLI) and strength (FGI) were introduced in section 5.2 and were shown to be useful indicators in the study of the scales and artefacts present within the Level-4 analysis SST products. It was shown that OSTIA data have an average feature resolution of about 40 km over the North Atlantic with a significant portion below 25 km. The analyses showed that this feature resolution varies in space but most probably not in time. The frontal indexes could also be used for inter-comparisons between the various available Level-4 SST products. The difference between OSTIA and ODYSSEA is interesting as fewer fronts are detected on ODYSSEA but those that are detected are stronger than OSTIA. ODYSSEA was shown to retain more energy at small scales although it appears to be more inconsistent in time with

regard to the presence of these small scales. REMSS_MW contains a similar quantity of fronts as OSTIA after the latter is filtered by a 25 km low-pass filter. ODYSSEA and REMSS are generally noisier than OSTIA. Several instances of production artefacts were detected by means of the frontal indexes, some of these artefacts being not easily spottable by eye. The inter-annual variability of the FGI is different when detected on these various Level-4 products. This stresses the importance of eliminating the biases introduced by the spatial and temporal variability of the feature resolution. For inter-annual frontal exploration, the Level-3 datasets are the most relevant as they have a constant feature resolution. Since the Level-3 datasets are not available on periods longer than a few years, the following chapter is constructed on frontal results obtained from the OSTIA reanalysis product. OSTIA optimal interpolation offers the best spatial and temporal consistency of the feature resolution of the Level-4 products.

A seasonal signal with a high frontal index during the summer and a low one during winter was observed on every product over the North Atlantic. It was demonstrated to be mostly a natural signal through frontal exploration on unsmoothed Level-3 SST data. This aspect is explored in more detail in the next chapter.

Several quantitative indexes of dynamics occurring at fronts were constructed from the processing of SST images but also in synergy with altimetry data and climatologies of salinity and mixed layer depth, making use of the published state of the art of the dynamics occurring at fronts. The Spall_95 index presented in 5.3 relies on simple scalings of the subduction at fronts based on Spall (1995). This index does not deliver much more than the FLI index, apart from attempting to carry quantitative estimates of subduction at fronts. A limited confidence is associated to it as it relies strongly on the assumption on the frontal width. It should be regarded as a qualitative scientific index in the open ocean. In common with the other indexes presented, the author of this thesis does not believe it to be valid on shelf-sea waters.

The Lapeyre_Klein index, discussed in 5.4, is more advanced, being based on a scaling of the Omega equation. It relies on the actual strength of the fronts and on the mesoscale strain calculated from altimetry data. This index also depends on the assumed frontal width although it was shown that the index

spatial and temporal variability is independent from it. Still, even if the precise value is not known, results show that a non-negligible and seasonally variable vertical transport at small scales due to large scale strain interaction with fronts is occurring over the Sargasso Sea. Twice as much vertical transport at fronts is estimated over the Mediterranean. This index is judged to be a useful scientific indicator of vertical transport at fronts that could be made more accurate in absolute if a better understanding of the frontal width was obtained.

The Capet_Fs index developed and exposed in 5.5 attempts to capture the frontogenesis function discussed by Capet et al. (2008b). This index also makes use of the altimetry but, contrary to the Lapeyre_Klein index, it accounts for the relative orientation of the fronts with the mesoscale strain. It is also dependent on the assumed frontal width and does not provide an estimation of vertical transport. It is however a valuable scientific indicator of where frontogenesis is occurring and it provides an important independent assessment of several aspects of the numerical model used by Capet et al. (2008b) against observations.

Finally the Fox_Kemper index was presented in 5.6; it attempts to capture the restratification at fronts by Mixed Layer Eddies based on a parameterization suggested by Fox-Kemper and Ferrari (2008). This index provides a useful global distribution of restratification fluxes that compare well with the estimates made by Fox-Kemper and Ferrari (2008) based on altimetry measurements. As for the previously mentioned indexes, it relies on the assumed frontal width. It is however not very sensitive to frontal width because it is affected by this parameter in several ways that partly compensate each other. Its limitation is mainly that its high values are associated with a lower level of confidence since they mostly occur when the mixed layer is deep and compensation is more likely to introduce a bias.

These novel indexes, based on frontal detection on SST data, show a very promising potential for retrieving dynamical information on the mixed layer. Since they are a first attempt to do so, they require more analyses to produce quantitative values that can be relied on. Such analyses would involve the accurate selection of input parameters such as the frontal width but also the understanding of the conditions in which these indexes are valid.

Nevertheless, the FLI and FGI indexes are in themselves a good first order measure of stirring and mixing processes and they are based on fewer assumptions. It is thus worth exploring their qualitative variability across the globe's oceans and across several decades as is done in the next chapter.

6. Chapter 6: Climatic variability of frontal activity

This chapter presents the exploration of climatic signals in the frontal activity measured on the ocean surface. It builds on the analytical processes developed in Chapters 3, 4 and 5 to produce massive three-dimensional datasets of space-time distribution of ocean thermal fronts. The main difference compared with the analyses presented in chapter 5 is that the frontal indexes discussed in this chapter are calculated globally on long time series of satellite-derived Level-4 SST products. In particular, fronts are detected on the daily global OSTIA reanalysis (OSTIA_RAN) dataset which covers a time span of 22 years (1985 to 2007). OSTIA_RAN is, like OSTIA, a daily analysis of the global SST produced by the UK Met-Office on a 1/20 degree grid. The OSTIA_RAN blends satellite data provided by the Pathfinder AVHRR project and reprocessed (A)ATSR together with in-situ observations from the ICOADS dataset (Donlon et al. 2012, Stark et al. 2007).

Chapter 5 demonstrated that a genuine seasonal signal is present within the frontal gradient index (FGI) over the North-Atlantic. This chapter sets out to identify how fronts vary with space and time from an inter-annual perspective. To achieve this goal, the fronts were calculated globally from OSTIA_RAN products every 7 days from 1985 to 2007. The methodology applied was described in chapter 5. The frontal index examined is the FGI as it is a simple expression of the frontal dynamics which relies on fewer hypotheses than the more elaborate indexes presented in chapter 5. The calculation of climate-scale variability of these complex frontal indexes requires a careful examination of the hypotheses involved in the index construction and is out of the scope of this PhD thesis.

This chapter will provide a brief tour of different views that emphasize various aspects of the spatial and temporal frontal index variability present within the very large three-dimensional dataset which results from the frontal index calculation stage. Along the way it is also intended to identify the scientific potential of visualizing the behaviour of fronts. It should be stressed however

that the scope of this chapter is limited to providing a critique of this scientific potential rather than to develop any particular scientific application in detail.

Climate scientists are trying to observe and predict changes in sub-mesoscale and mesoscale processes. This chapter is aimed at demonstrating the power of the innovative tools developed in the context of this thesis for finding subtle change in the small scale processes that are correlated to frontal activity. It is an invitation for oceanographers to exploit the local weather of the frontal indexes in synergy with other data in the frame of regional studies. The frontal index data-cube (two spatial dimensions and one temporal dimension as introduced in 4.1.1) calculated for this chapter has the potential to provide new insights on how the ocean actually works.

6.1 Wavenumber spectrum of OSTIA_RAN

As discussed in section 5.2, the surface density wavenumber spectrum is assumed to locally scale to k⁻² in order to estimate the SST gradient energy unresolved by the SST product of feature resolution Δs. It was also pointed out that Reynolds and Chelton (2010) have shown a wider range of spectral slopes present in OSTIA level-4 SST products. Since the OSTIA_RAN product is used in the rest of this chapter to illustrate climate variability of frontal activity it seemed important to test whether the k⁻² assumption is fair for this dataset. Following the methodology of Reynolds and Chelton (2010), the wavenumber spectrum was computed from daily OSTIA_RAN SST in January 2007 along each latitude of grid points within a domain in the Tropical Pacific. These individual spectra were then ensemble averaged over the latitudes and the 31 days of the month. Figure 6-1 shows a SST wavenumber spectrum which scales remarkably well to the k⁻² slope over the scales present in the images. This provides some confidence to the scaling of the SST gradient performed in the following sections that use OSTIA_RAN.

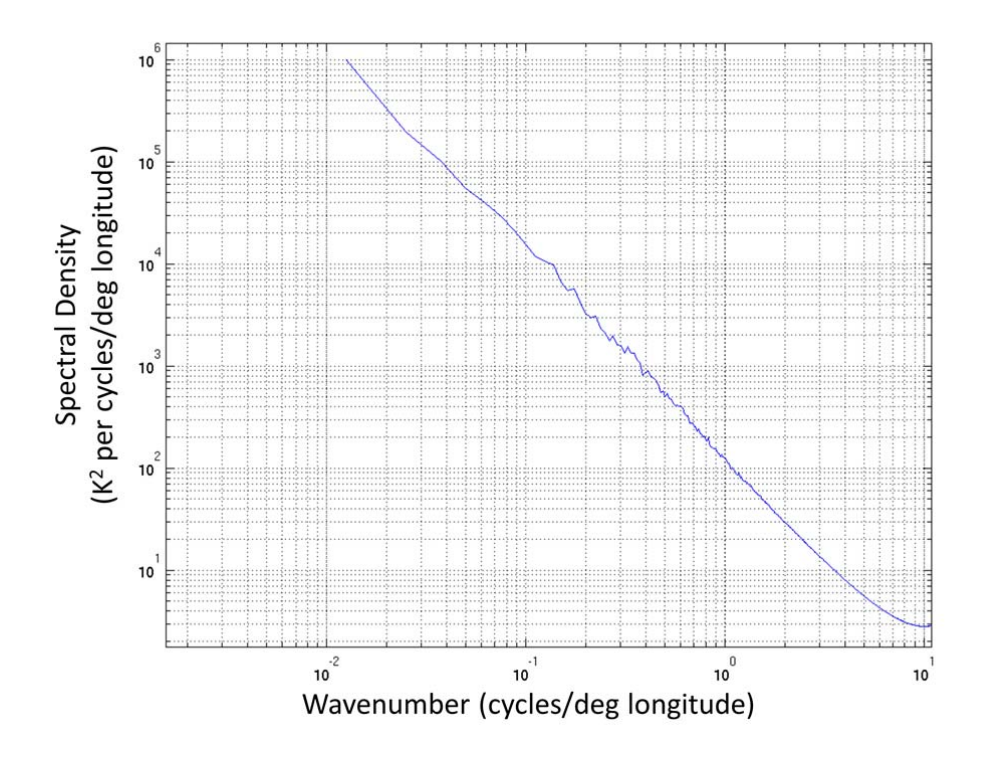


Figure 6-1: OSTIA_RAN zonal wavenumber spectrum for January 2007 over the Tropical Pacific (10°S-10°N, 180°W-100°W).

6.2 Global spatial distribution of the FGI

Figure 6-2 presents the global map of the temporally averaged FGI calculated on OSTIA_RAN with $d=0\ km$, $L_f=0.5\ km$, and $\Delta s=25\ km$. The relationship between these parameters and the Canny algorithm thresholds are described in section 4.2. This configuration applies no smoothing on the SST images prior to the front detection, the thresholds are calculated following Spall's (1995) derived values of horizontal density gradient magnitude. The horizontal density magnitude is scaled assuming a constant frontal width of 0.5 km and a 25 km feature resolution of the SST dataset. This figure shows the long term average over the period 1985-2005, however it should be stressed that the fronts were detected on daily global SST images of 0.05 degree resolution, sub-sampled at a weekly frequency. It displays a strong FGI temporal average over the main western boundary currents, the Gulf Stream and the Kuroshio, as well as over the Antarctic Circumpolar Current, the Agulhas retroflection and the Malvinas/Falklands retroflection. In addition strong FGI average is

found over some coastal waters where upwelling is occurring such as the Benguela, California, Morocco and Chile. It is also observed around Australian coastlines and on the Eastern side of New-Zealand, over the shelf sea waters of the North Sea, Red Sea and Persian Gulf. A fine line of strong FGI starts from the Chile upwelling and extends towards the West following the Equator. In addition, one can notice that the open ocean is divided into regions of very low FGI and others of medium FGI. Medium FGI is found extending from high FGI regions whereas very low FGI regions are found in mid-latitudes far from the coasts and the main currents and South of the ACC. It is not clear whether the low FGI South of the ACC is genuine or whether it is an artefact of the OSTIA_RAN dataset. This could be a consequence of poor data coverage where there is a high cloud coverage reducing the availability of reliable high-resolution (IR) data input to OSTIA_RAN. It is therefore interesting to note a circular patch of medium FGI in the North-West Indian Ocean whose diameter is approximately 20 degrees.

The FGI temporal standard deviation over the same period is shown on Figure 6-3. The spatial distribution of the FGI temporal standard deviation is very close to that of the FGI temporal mean. The only exception is situated over the Arctic ocean where the average FGI is rather low but the standard deviation is higher than that of areas of similar mean FGI.

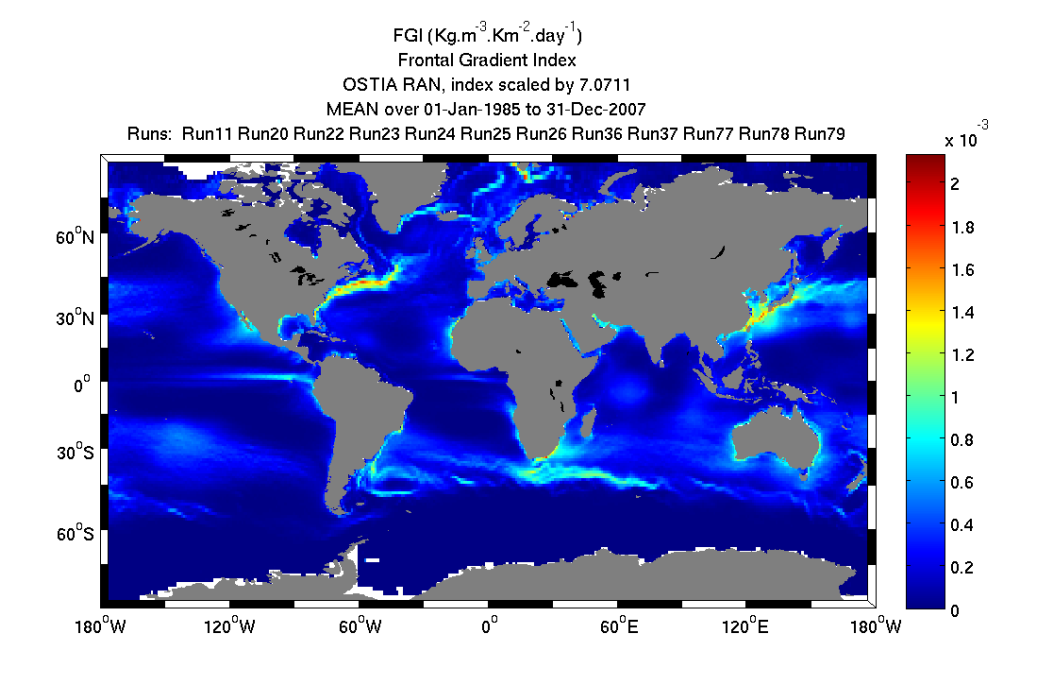


Figure 6-2: Long term (1985 to 2007) mean Front Gradient Index (FGI) in $kg m^{-3} km^{-2} day^{-1}$ processed on weekly OSTIA_RAN with d = 0 km, $L_f = 0.5 km$, and $\Delta s = 25 km$.

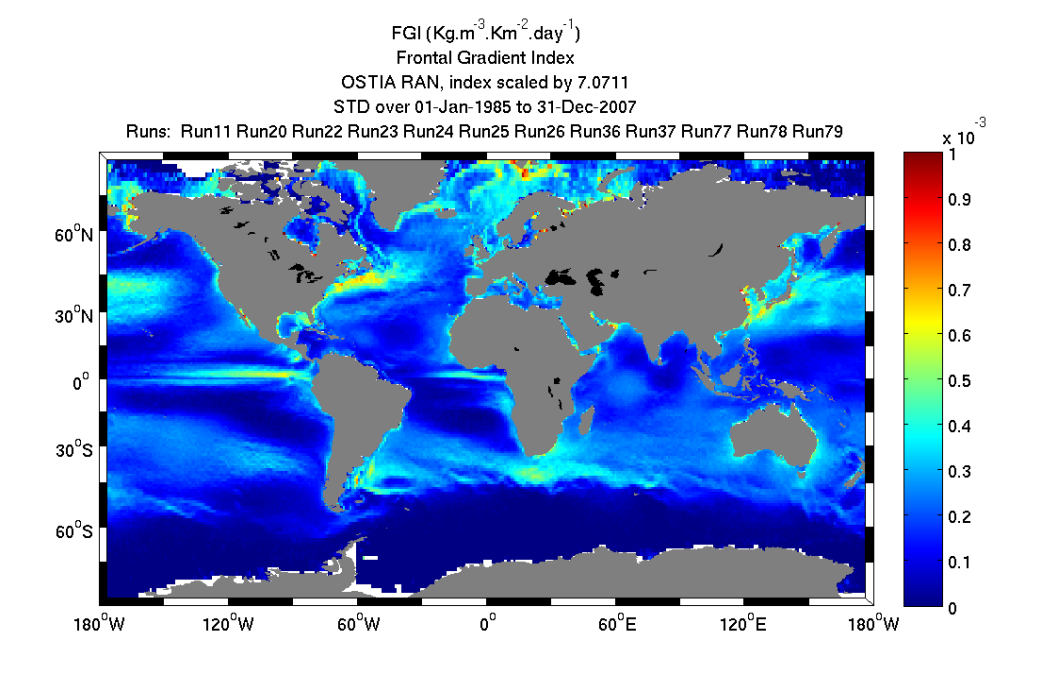


Figure 6-3: Long term (1985 to 2007) standard deviation Front Gradient Index (FGI) in $kg \ m^{-3} \ km^{-2} day^{-1}$ processed on weekly OSTIA_RAN with $d=0 \ km$, $L_f=0.5 \ km$, and $\Delta s=25 \ km$.

6.3 Temporal distribution of the FGI

Figure 6-4 presents the temporal variation of the FGI spatially averaged over the North-Atlantic. The North-Atlantic region is shown in section 4.2. On Figure 6-4, the FGI calculated on OSTIA_RAN is plotted with stars, from 1985 to end of 2007. The FGI calculated on OSTIA images in January 2008 is plotted with circles. The OSTIA_RAN version is CF-1.0 and OSTIA's is v01-fv02. One can first observe the same dominant seasonal signal as discussed in chapter 5 with a low around March and a high around July or August. One can also notice an inter-annual signal of up to 10 years period. It is worthwhile to mention that no obvious discontinuity can be seen at the end of 1991 when ATSR images from ERS-1 became available and start to be combined with the AVHRR ones. Finally, there seems to be a discontinuity between the OSTIA_RAN FGI and the OSTIA FGI at the transition between the two datasets at the end of 2007. This point is explored in more detail below.

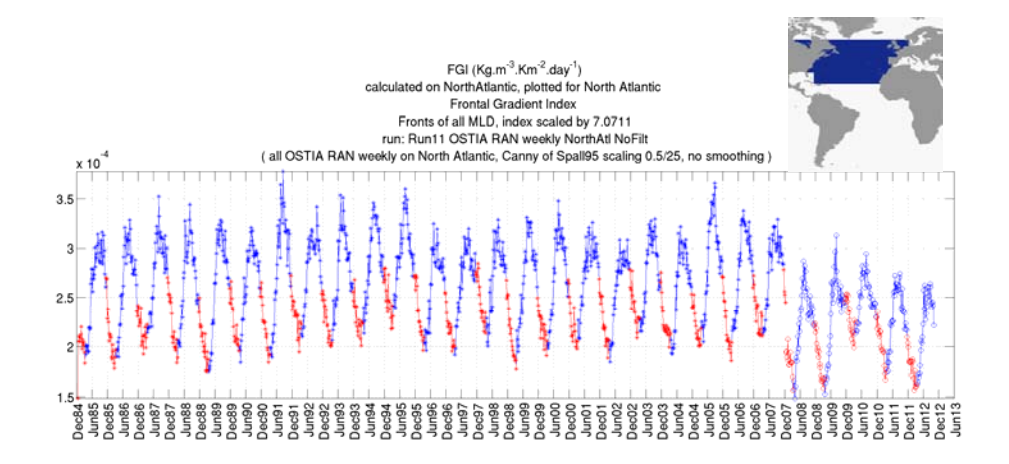


Figure 6-4: Front Gradient Index (FGI) in $kg m^{-3} km^{-2} day^{-1}$ processed on weekly OSTIA_RAN (stars) and OSTIA (circles) over the North Atlantic region with d=0 km, $L_f=0.5 km$, and $\Delta s=25 km$. Times when more than 50% of the area MLD is deeper than 75 m are plotted in red.

Figure 6-5 displays the FGI from OSTIA_RAN and OSTIA over the Northern part of the Tropical Atlantic (latitudes from 0°N to 20°N). Figure 6-6 shows the same index over a small portion latitudinal band around the Equator over the Atlantic Ocean (latitudes 10°S to 10°N). These two figures exhibit a dominant seasonal signal with a lower inter-annual signal. It should be noted that over

these regions the MLD is never deeper than 75 meters over more than 50% of the selected area. The amplitude of the seasonal variability is reduced in comparison to the FGI over the whole North-Atlantic shown on Figure 6-4. The regular inter-annual behaviour is almost entirely replaced by a more irregular time variability on Figure 6-7 which displays the FGI over the Southern part of the Tropical Atlantic Ocean (latitudes from 20°S to 0°N). Instead an interannual harmonic of about 5 to 6 years seems to dominate. A much less noisy seasonal variability is observed over the South Atlantic FGI, as shown on Figure 6-8. The latter displays both an inter-annual signal in the annual average of FGI and in the annual range of FGI (difference between maximum and minimum turning points of FGI each year). One may suspect a discontinuity between the years 1991 and 1992 at a point in time when ATSR measurements started to be incorporated in the daily OSTIA_RAN analysis. No discontinuity is however obvious at the transition between OSTIA_RAN FGI and OSTIA FGI over the South-Atlantic. The FGI over the Mediterranean Sea is shown on Figure 6-9. The seasonal signal is very strong over this region, whereas no clear harmonic is perceivable within the inter-annual variability. It is worth mentioning the rare jump in annual maximum of Mediterranean FGI between the years 2002 and 2003. It is not clear whether there is a discontinuity between OSTIA_RAN and OSTIA over the region.

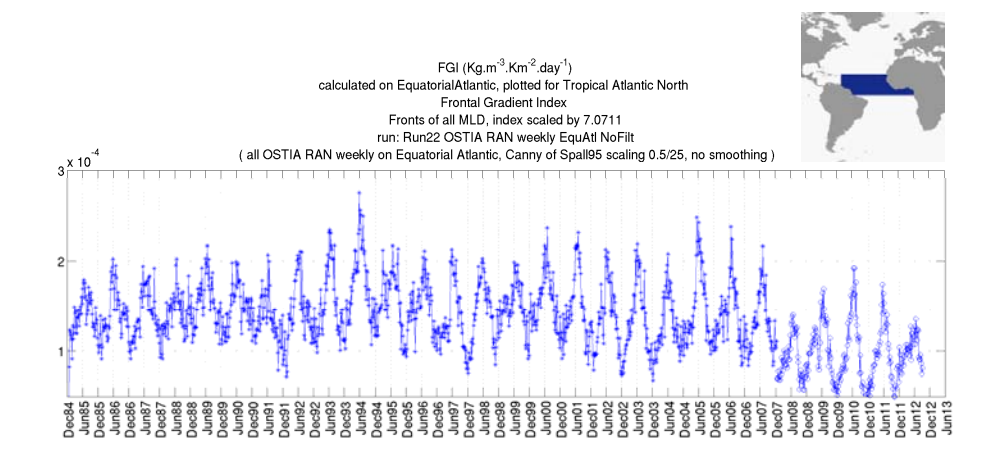


Figure 6-5: Front Gradient Index (FGI) in $kg m^{-3} km^{-2} day^{-1}$ processed on weekly OSTIA_RAN and OSTIA over the Tropical Atlantic North region with d=0 km, $L_f=0.5 km$, and $\Delta s=25 km$. Times when more than 50% of the area MLD is deeper than 75 m are plotted in red.

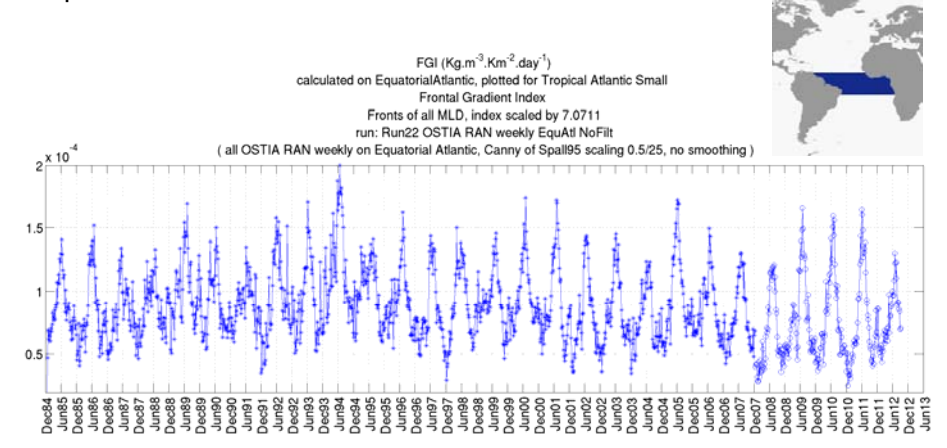


Figure 6-6: Front Gradient Index (FGI) in $kg m^{-3} km^{-2} day^{-1}$ processed on weekly OSTIA_RAN and OSTIA over the Equatorial Atlantic region with d = 0 km, $L_f = 0.5 km$, and $\Delta s = 25 km$. Times when more than 50% of the area MLD is deeper than 75 m are plotted in red.

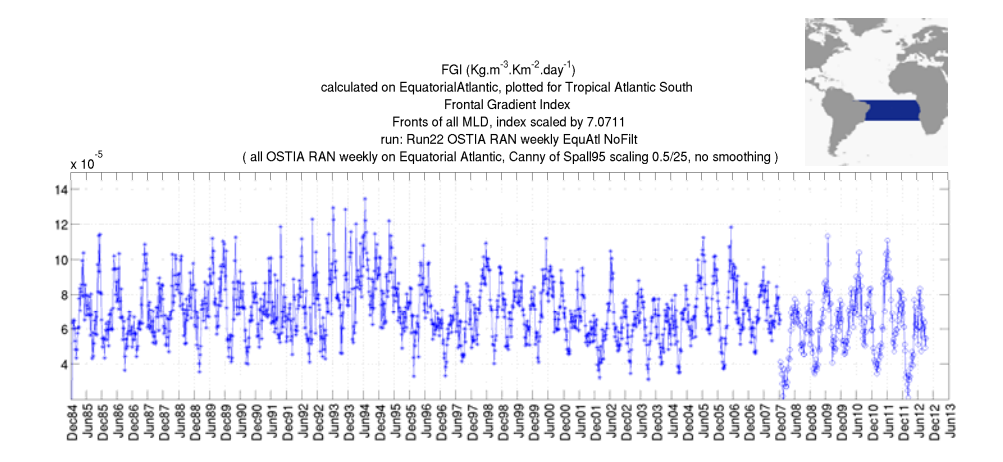


Figure 6-7: Front Gradient Index (FGI) in $kg m^{-3} km^{-2} day^{-1}$ processed on weekly OSTIA_RAN and OSTIA over the Tropical Atlantic South region with d=0 km, $L_f=0.5 km$, and $\Delta s=25 km$. Times when more than 50% of the area MLD is deeper than 75 m are plotted in red.

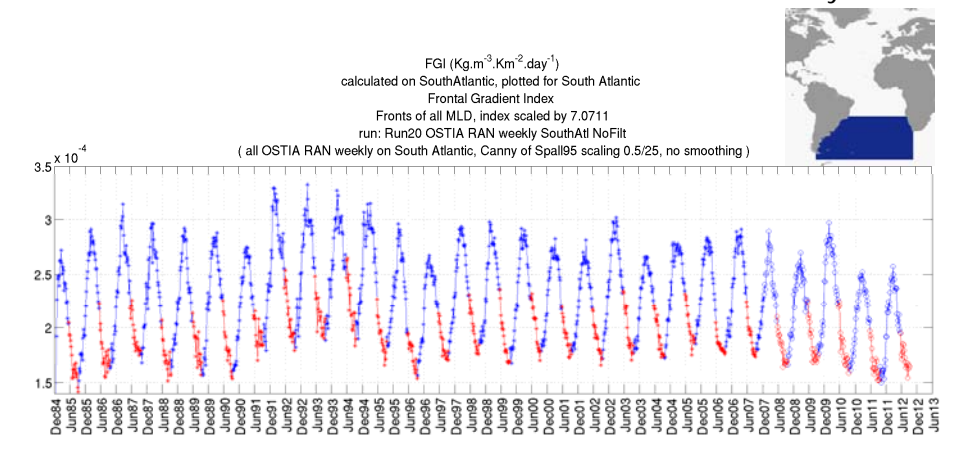


Figure 6-8: Front Gradient Index (FGI) in $kg m^{-3} km^{-2} day^{-1}$ processed on weekly OSTIA_RAN and OSTIA over the South Atlantic region with d=0 km, $L_f=0.5 km$, and $\Delta s=25 km$. Times when more than 50% of the area MLD is deeper than 75 m are plotted in red.

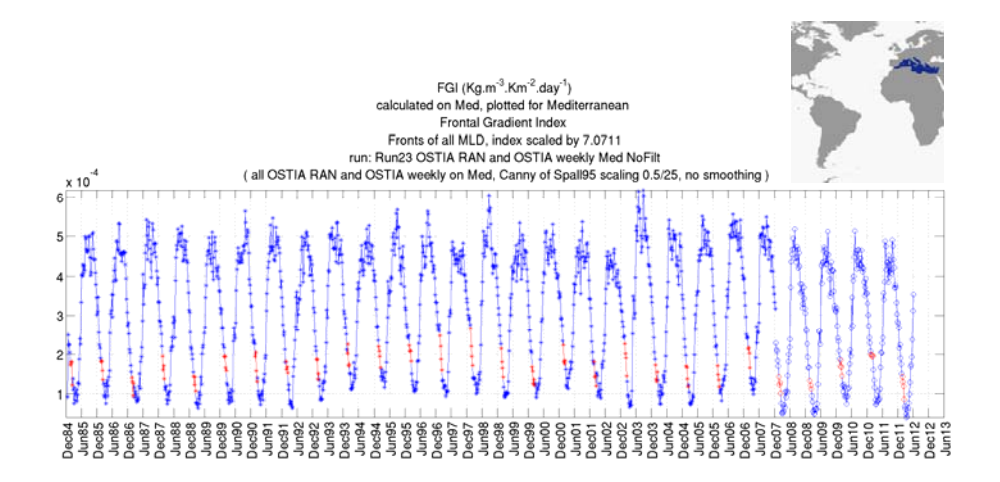


Figure 6-9: Front Gradient Index (FGI) in $kg m^{-3} km^{-2} day^{-1}$ processed on weekly OSTIA_RAN and OSTIA over the Mediterranean Sea with d=0 km, $L_f=0.5 km$, and $\Delta s=25 km$. Times when more than 50% of the area MLD is deeper than 75 m are plotted in red.

6.4 Comparison of the OSTIA_RAN FGI with the OSTIA FGI

Some of the previous figures shown in this chapter hinted at a discrepancy in the detected fronts between OSTIA_RAN and OSTIA. The discontinuity is more obvious in Figure 6-10 which shows the FGI over the North-Atlantic processed on SST images that are smoothed with a spatial 25 km running mean $(d=25~km,\,L_f=0.5~km,\,$ and $\Delta s=25~km)$. It is also the case after a 50 km

smoothing filter is applied, as shown on Figure 6-11. Figure 6-12 presents the difference between the annual averages of FGI calculated on OSTIA_RAN and OSTIA, both from the year 2007 and after a 25 km smoothing. Note that OSTIA data are available on the year 2007 although it is not shown on Figure 6-4 to Figure 6-11. The FGI calculated on the OSTIA dataset is consistently and significantly lower than that of the OSTIA_RAN. Like the OSTIA dataset, the OSTIA_RAN dataset was produced by the Met-Office, it is however more recent and its Optimal Interpolation algorithm produces sharper images. This may explain the discrepancy between the FGI indexes of both datasets. The fact that this discrepancy remains after a spatial smoothing of 25 km or 50 km tends to show that the spectra of the data sets are not equivalent at these scales. It is difficult to explain why this discrepancy is enhanced after the spatial smoothing. The cause of this phenomenon is probably a combination of the Optimal Interpolation differences between the two data sets and the inherent behaviour of the front detection algorithm. Figure 6-13 and Figure 6-14 show the monthly averaged HSR FGI (High Spatial Resolution as described in 4.1.1) for the month of January 2007 as calculated from OSTIA_RAN and OSTIA respectively. These two figures present estimations of the frontal activity based on SST Level-4 images of two distinct data sets which attempt to capture the same reality. It is striking how the weak fronts are detected on OSTIA_RAN but not on OSTIA, whereas the strong fronts are present on both data sets. OSTIA is constructed with input SST images from more satellites than OSTIA RAN. For instance OSTIA includes SEVIRI and AMSR-E measurements while OSTIA_RAN relies on (A)ATSR and AVHRR only. This could lead to the presence of finer scales in OSTIA whereas the two figures show the opposite. One can conclude from this that the optimal interpolation scheme of OSTIA RAN resolves finer scales than the (older) one of OSTIA.

The consequence of the described discrepancy in the presence of small scales within OSTIA_RAN and OSTIA is that these two data sets cannot be combined to obtain a longer and continuous SST dataset for the climatic exploration of fronts. As seen on Figure 6-4, the FGI is inconsistent across both datasets and this generates a temporal signal in the FGI time series which is a pure artefact of the difference in optimal interpolation. In the rest of this chapter, OSTIA_RAN and OSTIA will not be combined and the statistics will be based on

OSTIA_RAN fronts only, detected in the 23 years long period between 1985 and 2007.

In this chapter, the OSTIA_RAN SST images are not filtered prior to frontal detection. This allows one to make use of the finest scales present in the products. As all the Level-2 images that feed the OSTIA_RAN estimation process are infrared images, the inconsistencies in the feature resolution can only originate from the spatially non-uniform autocorrelation length scale or the effect of the cloud coverage variability. The spatial variability of the autocorrelation length scale is not considered a major hindrance as it changes very smoothly in space and does not vary in time. The variability of the feature resolution as a consequence of the cloud coverage changes is more of a concern. Yet there exists no spatial cut-off frequency able to remove such bias from the SST. It was therefore decided not to filter OSTIA RAN images.

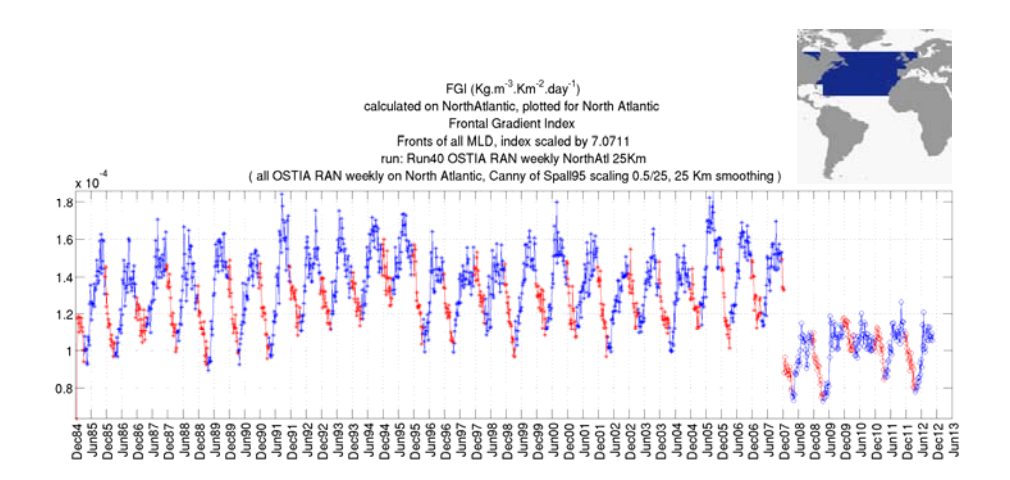


Figure 6-10: Front Gradient Index (FGI) in $kg m^{-3} km^{-2} day^{-1}$ processed on weekly OSTIA_RAN (stars) and OSTIA (circles) over the North Atlantic region with d = 25 km, $L_f = 0.5 km$, and $\Delta s = 25 km$. Times when more than 50% of the area MLD is deeper than 75 m are plotted in red.

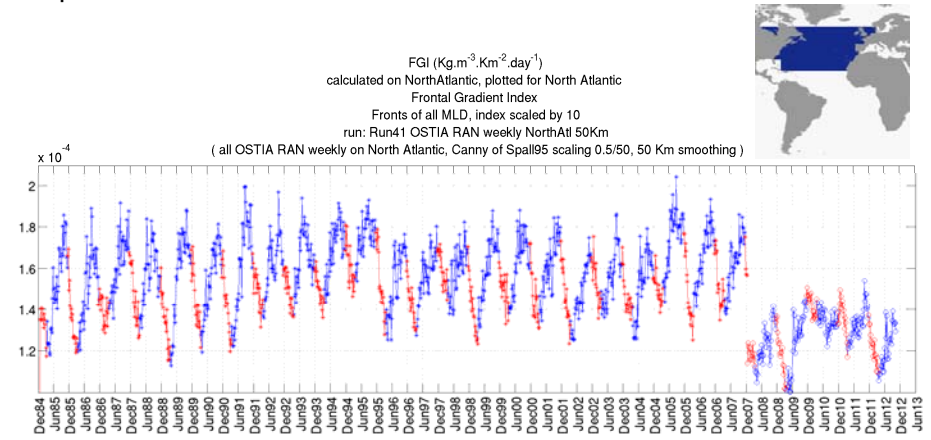


Figure 6-11: Front Gradient Index (FGI) in $kg \ m^{-3} \ km^{-2} day^{-1}$ processed on weekly OSTIA_RAN (stars) and OSTIA (circles) over the North Atlantic region with $d=50 \ km$, $L_f=0.5 \ km$, and $\Delta s=25 \ km$. Times when more than 50% of the area MLD is deeper than 75 m are plotted in red.

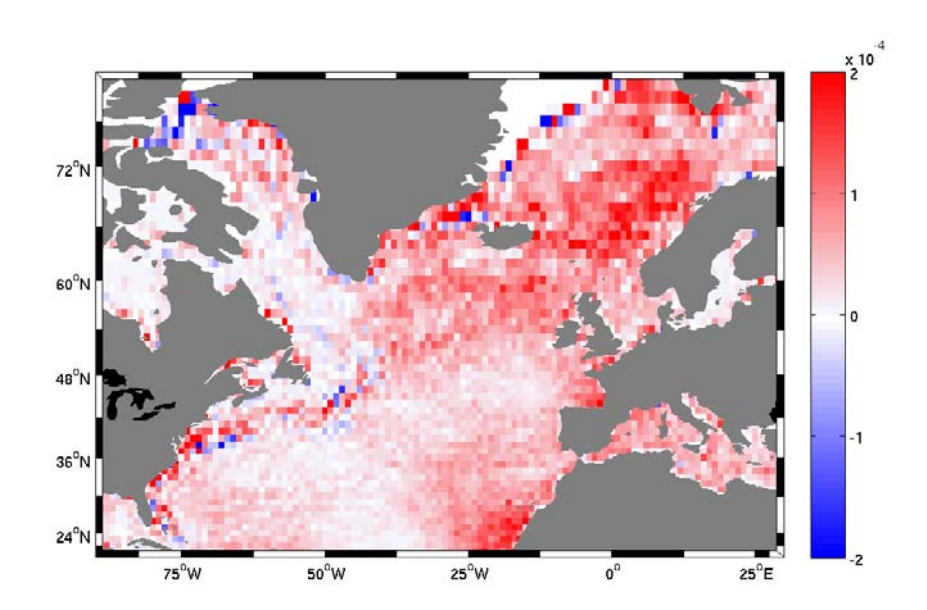


Figure 6-12: 2007 annual mean Front Gradient Index (FGI) difference between OSTIA_RAN and OSTIA in $m^{-3} km^{-2} day^{-1}$, both calculated with d=25 km, $L_f=0.5 km$, and $\Delta s=25 km$.

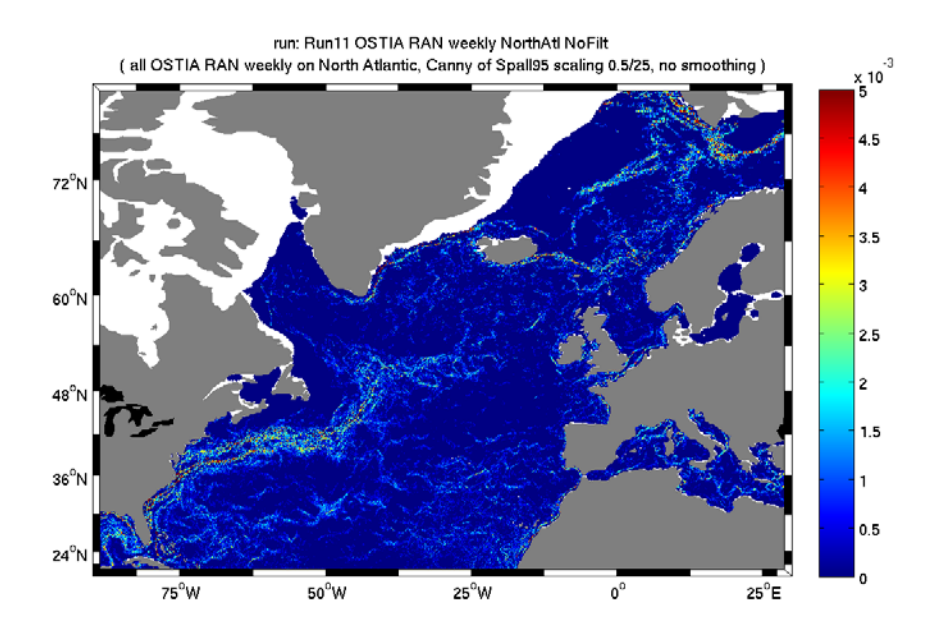


Figure 6-13: High Spatial Resolution monthly mean of Front Gradient Index (FGI) in $kg m^{-3} km^{-2} day^{-1}$ processed on weekly OSTIA_RAN with d = 0 km, $L_f = 0.5 km$, and $\Delta s = 25 km$ on January 2007.

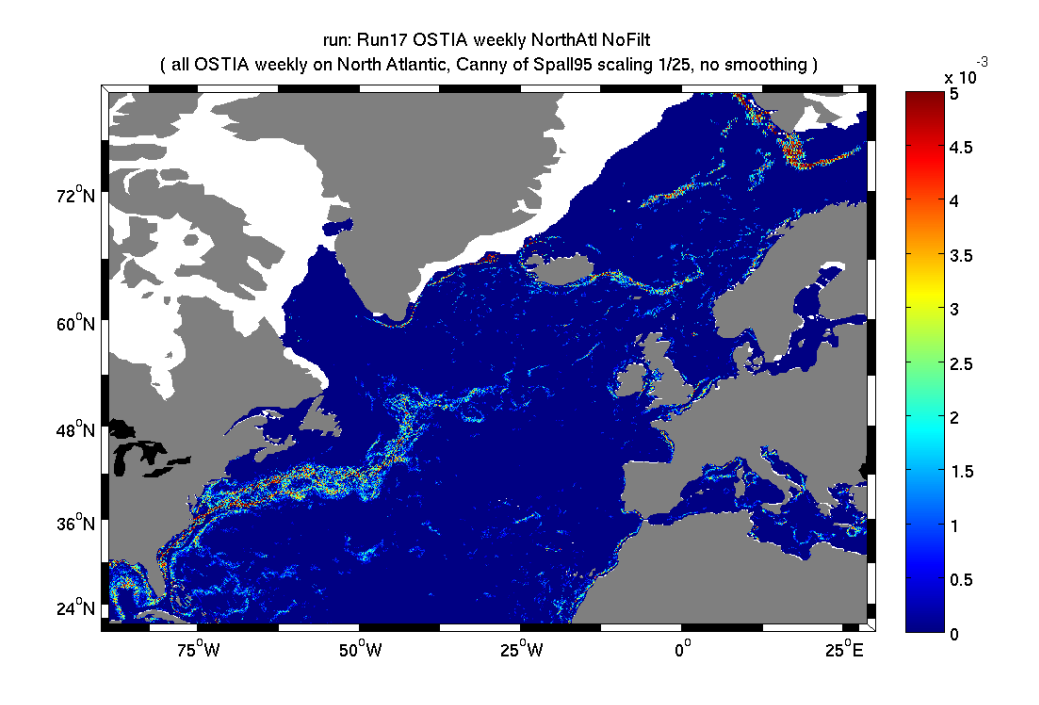


Figure 6-14: High Spatial Resolution monthly mean of Front Gradient Index (FGI) in $kg m^{-3} km^{-2} day^{-1}$ processed on weekly OSTIA with d = 0 km, $L_f = 0.5 km$, and $\Delta s = 25 km$ on January 2007.

6.5 Climatological variability of the FGI

The typical seasonal pattern can be explored by calculating the FGI climatological average seasonal cycle from the datacube of FGI as a function of space and time. Figure 6-15 shows the seasonal cycle of FGI over several latitudinal bands in the North Atlantic. Between 40°N and 60°N the seasonal FGI cycle is very clear with a maximum in August and a minimum in March. Figure 6-16 and Figure 6-17 display the FGI seasonal cycle for latitudinal stripes over the Tropical and South Atlantic. The typical seasonal FGI can be fairly different in regions close to each other. For instance, one can see from Figure 6-16 that the seasonal cycle between 0°N and 5°N reaches a maximum in July and a minimum in February. Meanwhile, the FGI averaged between 5°N and 10°N is highest in March and lowest in November. Figure 6-17 shows that the FGI features a seasonal variability South of 30°S, with a maximum in February/March and a minimum around September/October.

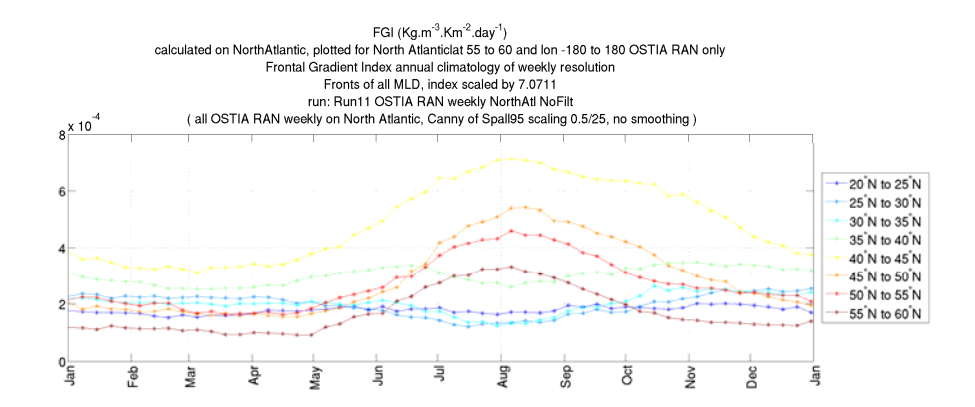


Figure 6-15: Climatology of Front Gradient Index (FGI) in $kg \ m^{-3} \ km^{-2} day^{-1}$ processed on weekly OSTIA_RAN over the North Atlantic region with $d=0 \ km$, $L_f=0.5 \ km$, and $\Delta s=25 \ km$, for several latitude bands.

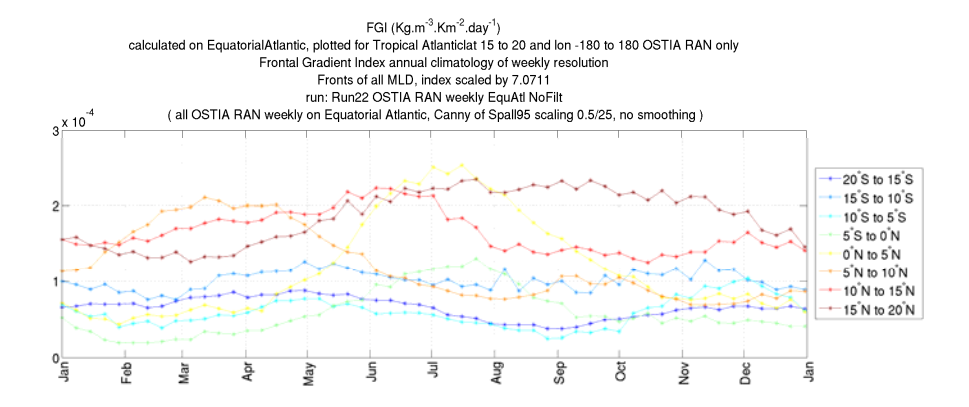


Figure 6-16: Climatology of Front Gradient Index (FGI) in $kg m^{-3} km^{-2} day^{-1}$ processed on weekly OSTIA_RAN over the Tropical Atlantic region with d = 0 km, $L_f = 0.5 km$, and $\Delta s = 25 km$, for several latitude bands.

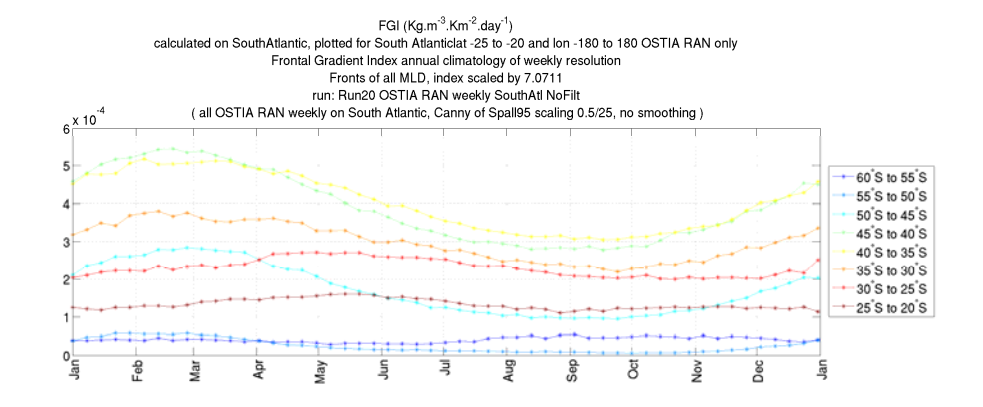


Figure 6-17: Climatology of Front Gradient Index (FGI) in $kg \ m^{-3} \ km^{-2} day^{-1}$ processed on weekly OSTIA_RAN over the South Atlantic region with $d=0 \ km$, $L_f=0.5 \ km$, and $\Delta s=25 \ km$, for several latitude bands.

These climatological averages of the seasonal cycle not only provide a temporal cycle but also quantitative information on the FGI, such as the typical peak-to-peak fluctuation in a year. The previous figures present the seasonal cycle averaged over a region and based on the 23 years of OSTIA_RAN, but it can be calculated in the same way for each pixel on the world's oceans from the datacube. For each pixel the peak to peak of the climatologically averaged seasonal cycle is calculated and the result is plotted on Figure 6-18. The timings of the minimum and maximum of the seasonal cycle for each pixel are also calculated and shown on Figure 6-19 and Figure 6-20.

This peak to peak fluctuation of the annual cycle over each location looks very similar to, although a bit noisier than, the temporal FGI standard deviation on each pixel (Figure 6-3). This map shows the areas where the variability of FGI within one year is large in absolute value. This fluctuation is correlated to the absolute FGI long term mean shown on Figure 6-2.

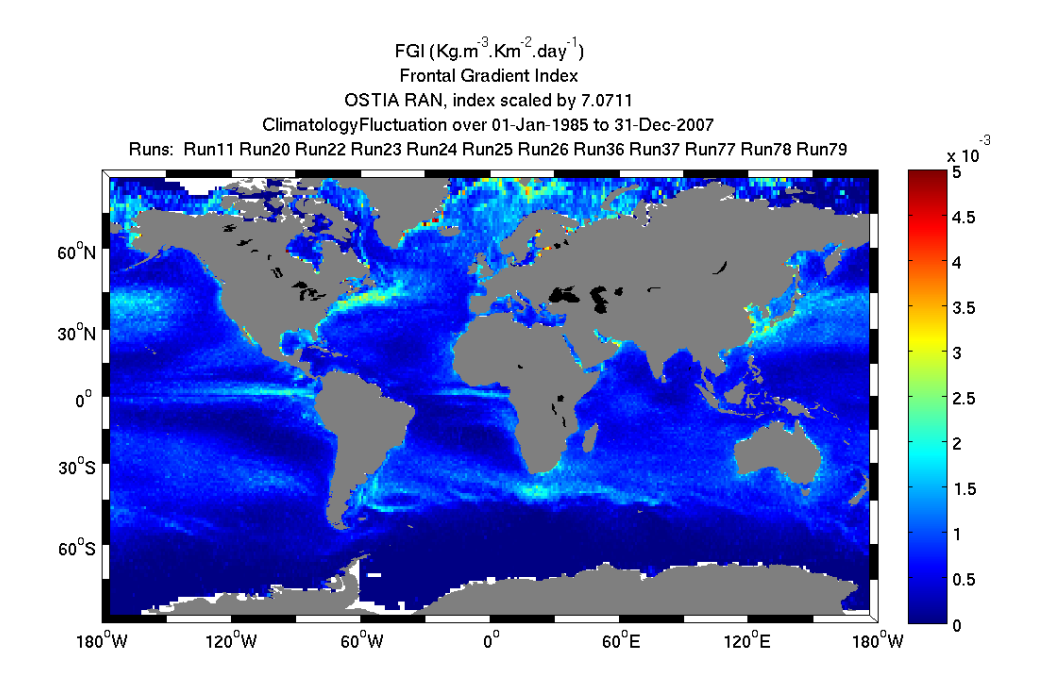


Figure 6-18: Peak to peak of seasonal cycle of Front Gradient Index (FGI) in $kg m^{-3} km^{-2} day^{-1}$ processed on weekly OSTIA_RAN with d = 0 km, $L_f = 0.5 Km$, and $\Delta s = 25 km$ (1985 to 2007).

The temporal phase of the typical seasonal FGI cycle presented in Figure 6-15 to Figure 6-17 is obtained by averaging large portions of the ocean basins. The spatial averaging hides details of regional and local variability of the climatological behaviour. One way to avoid this limitation is to plot on a map the timing of typical FGI minimum (maximum) as a function of the location as done on Figure 6-19 (Figure 6-20). These two figures offer a novel view on how the ocean frontal activity typically changes within the year. The first thing to remark is the general pattern over both hemispheres where the FGI is maximum over the summer and minimum around early spring. This general pattern is consistent with the large geographical averages of Figure 6-15 to

Figure 6-17. However, the surprising aspect is the spatial variability which creates numerous yet coherent regions of independent phasing of the FGI cycle. Figure 6-19 and Figure 6-20 allow one to segregate the oceans into regions of temporally coherent frontal activity. It is not the scope of this study to identify the physical mechanisms involved in the generation of the variability of the frontal activity described in this chapter. The author of this thesis however expresses the hope that oceanographers will study these phenomena and advance their understanding. This work contributes to unveiling some aspects of the frontal phenomenology, it is now up to other scientists to explain what creates these spatially consistent ocean regions!

One may wonder whether the frontal activity seasonal pattern is correlated to that of the mixed layer depth (MLD). Indeed a geographically limited mixing event may generate a strong front only if the mixed layer is strongly stratified. It seems natural to suggest that the FGI and the mixed layer depth (taken positive) are anti-correlated. This is explored in Figure 6-21 which maps the correlation between the FGI and the monthly MLD extracted from the Boyer Montegut et al. (2004) climatology. These two quantities are anti-correlated at mid and high-latitudes, with values lower than -0.3 higher than 40 °N and around 40 °S. However between 40 °S and 40 °N the correlation is closer to zero with even small positive values in some regions. The MLD is therefore able to explain a part of the frontal index seasonality only over mid and high latitudes.

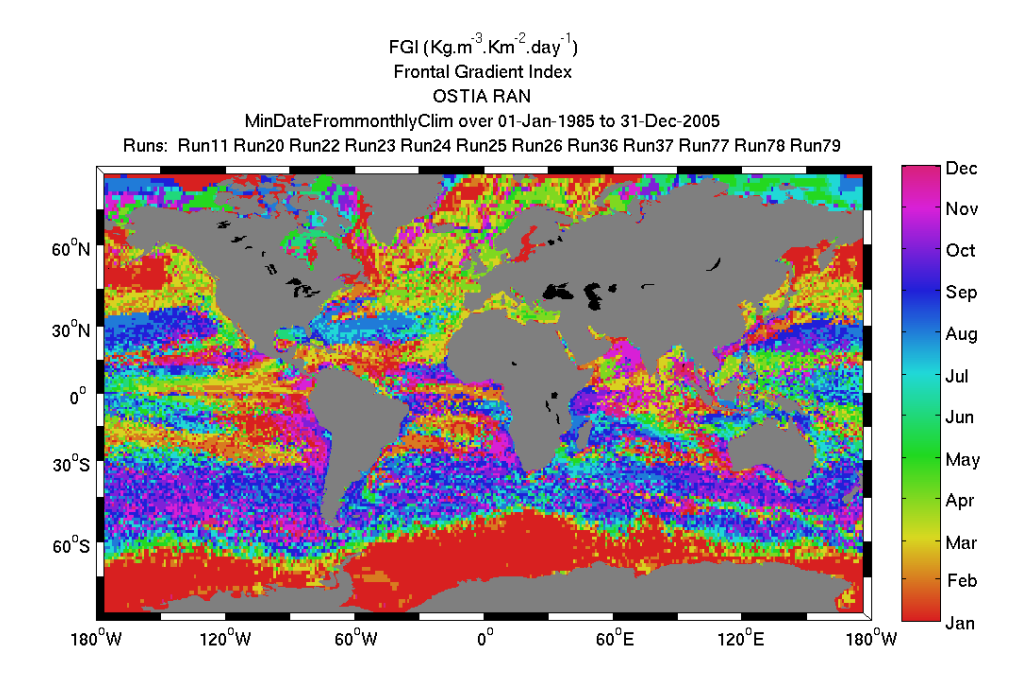


Figure 6-19: Date of minimum climatology of Front Gradient Index (FGI) processed on weekly OSTIA_RAN with d=0 km, $L_f=0.5$ km, and $\Delta s=25$ km.

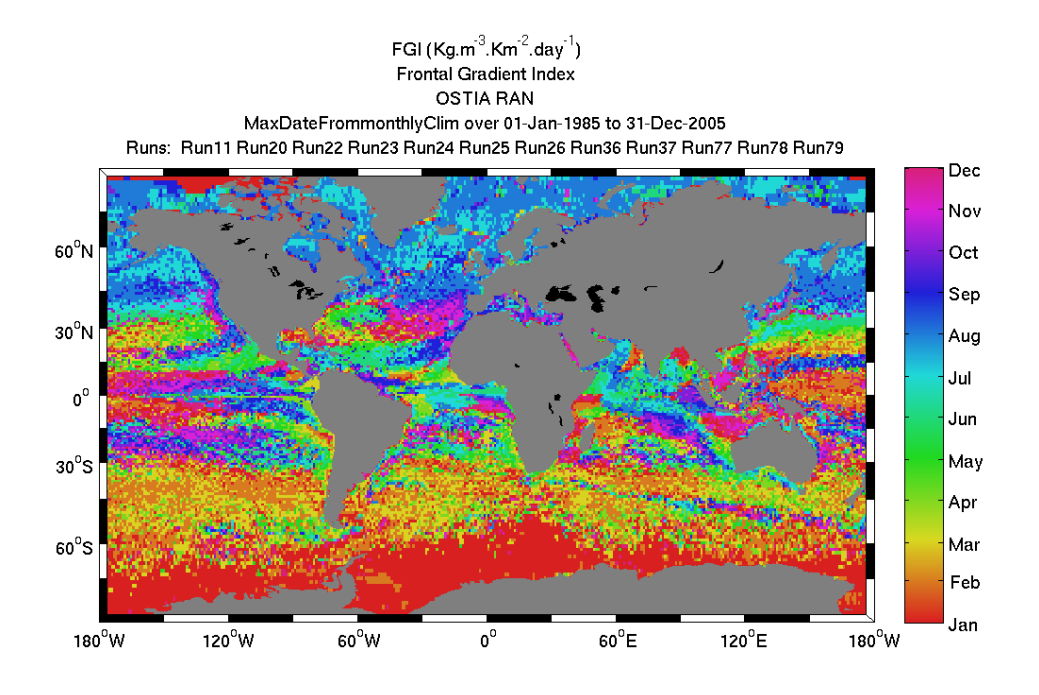


Figure 6-20: Date of maximum climatology of Front Gradient Index (FGI) processed on weekly OSTIA_RAN with d=0 km, $L_f=0.5$ km, and $\Delta s=25$ km.

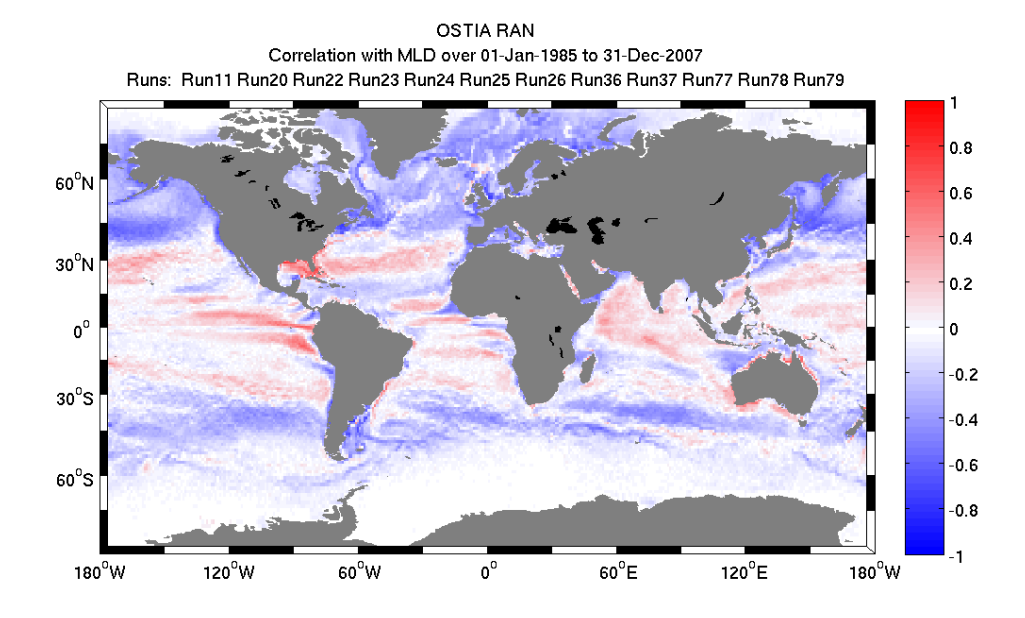


Figure 6-21: Correlation between Front Gradient Index (FGI) processed on weekly OSTIA_RAN with d=0 km, $L_f=0.5$ km, and $\Delta s=25$ km and monthly Boyer Montegut et al. (2004) Mixed Layer Depth (resampled on a 1 day resolution by nearest-neighbour).

6.6 High spatial resolution signal exploration

As was explained in 4.1.1, the frontal index computation routines store the resulting frontal quantities in two complementary datasets. The first one is the High Temporal Resolution (HTR) and the second is the High Spatial Resolution (HSR). The results presented above (except Figure 6-13 and Figure 6-14) are based on the HTR which features a daily temporal resolution but a low 1° spatial resolution. In contrast, the HSR features a low temporal resolution of one month but a high spatial resolution of 0.1°. It should be added that while the 23 years of OSTIA_RAN were searched for fronts on a global scale to produce the results shown in this chapter and stored on the HSR and HTR, it remains possible to generate a spatially limited frontal index datacube with both a fine temporal and spatial resolution. The latter can only be done on a limited area due to memory constraints. To achieve this result, the region of interest should be identified on the HTR or HSR in the first place.

This section aims to illustrate the power of the HSR dataset for resolving small spatial changes of the frontal activity over time. Figure 6-23 shows the Hovmöller plot of the FGI on a meridional transect against time. The transect

location is shown on Figure 6-22, it is a line at longitude 150°E between latitudes 20°N and 50°N. For each month between 1985 and 2007, the HSR FGI is extracted over this transect and longitudinally averaged in a 5° window. The Hovmöller plot hints at a 13 years period North-South oscillation of the southern edge of the Kuroshio Current which lays on average along 35°N at 150°E. This inter-annual oscillation appears very clearly on the Hovmöller plot and its amplitude is nearly 3° (333 km). The position of the northern edge of the Kuroshio also appears to be oscillating on a decadal time scale but it is seen less clearly as it is blurred by the presence of a strong seasonal signal.

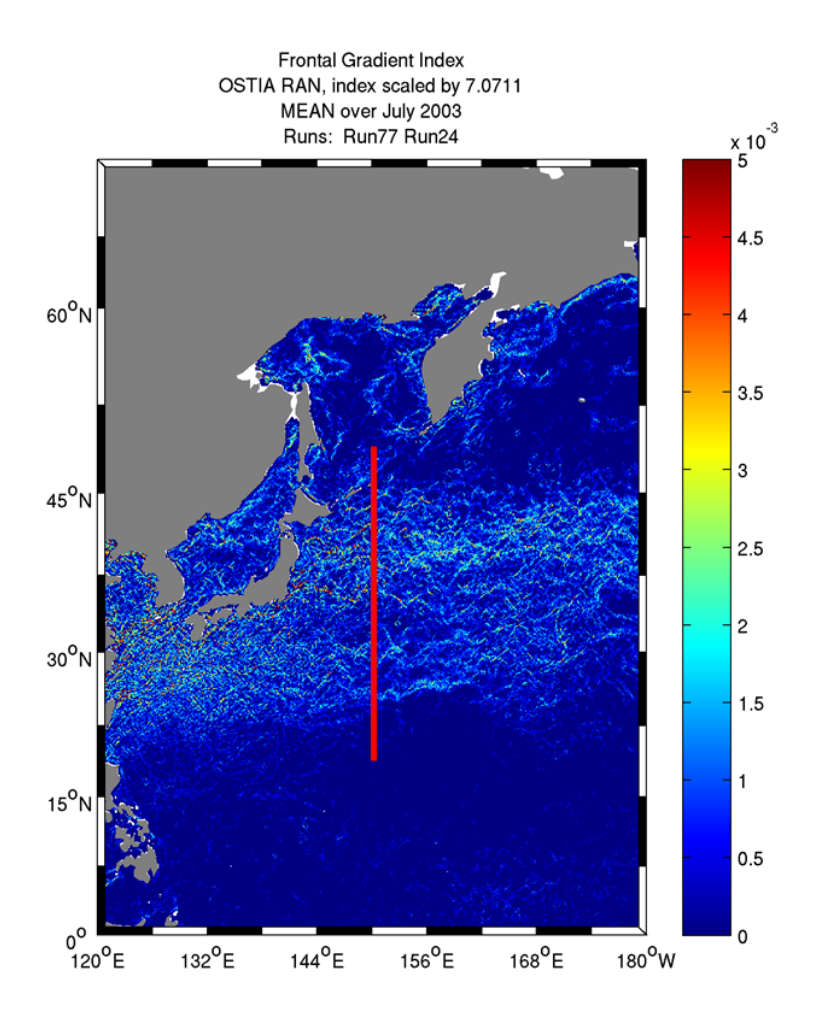


Figure 6-22: July 2003 monthly average Front Gradient Index (FGI) processed on weekly OSTIA_RAN with $d = 0 \ km$, $L_f = 0.5 \ km$, and $\Delta s = 25 \ km$.

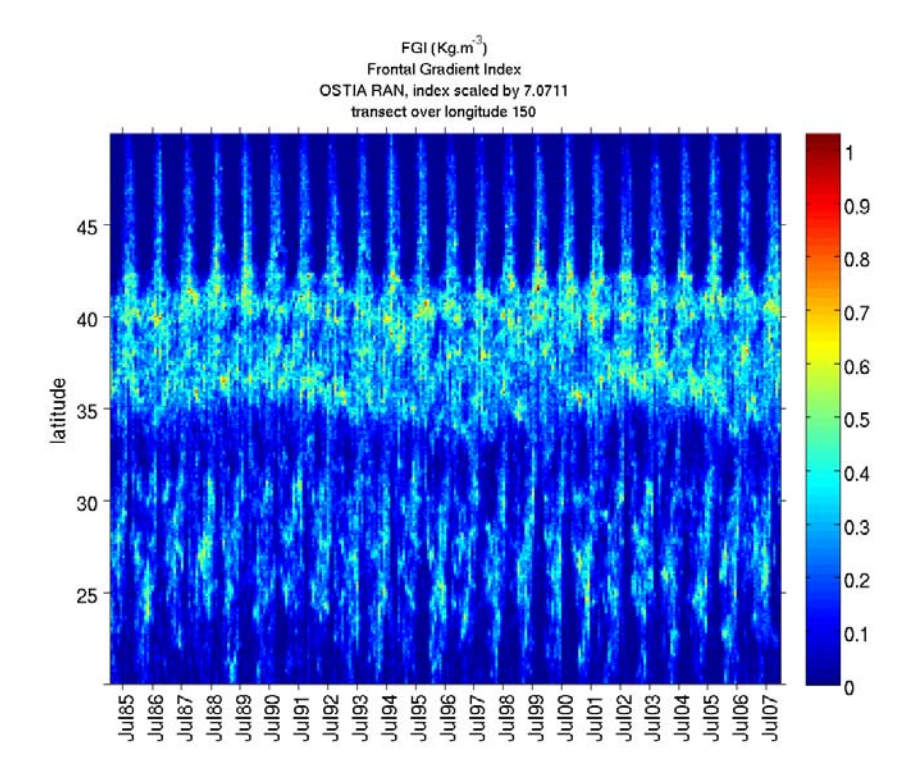


Figure 6-23: Hovmöller plot of the Front Gradient Index (FGI) processed on weekly OSTIA_RAN with d=0 km, $L_f=0.5$ km, and $\Delta s=25$ km, at longitude 150° E $\pm 2.5^{\circ}$ and latitude between 20° N and 50° N (as shown on Figure 6-22).

6.7 Quantitative trends of the FGI

The spatial representations of the signals present in the FGI datacube are typically presented as averages of a particular aspect over time. Therefore they mask inter-annual variability of the index. Conversely, the temporal distributions of the FGI shown in previous sections of this chapter are averaged over a whole ocean basin and hide details of regional and local variability of the FGI. Figure 6-24 shows the trend of the FGI over the 23 years of OSTIA_RAN for each pixel of the HTR grid. It is calculated, for each pixel, as the slope of the linear least-squares fit of the temporal evolution of the FGI over the pixel. This figure unveils an aspect of the inter-annual temporal distribution at the local spatial scale. It reveals coherent regions of the oceans which evolve in time with the same absolute magnitude. The general pattern of this map is a positive trend at mid to high latitudes and a negative trend over some consistent regions of the Equatorial and Tropical latitudes. In addition, the FGI is increasing in the East Pacific cold tongue, in the

Mediterranean Sea and along the Morocco upwelling. Adjacent stripes of positive and negative trends are observed over the Gulf Stream or the ACC. These are probably due to lateral shifts of the strong fronts associated to these currents over the explored time period.

Figure 6-25 shows the relative inter-annual trend expressed as a percentage of the local FGI per year. It can be analysed with an eye on Figure 6-2 which shows the long term FGI mean. The general pattern is similar on the absolute and relative trend maps, except some regions such as the Gulf Stream where the absolute trend is high whereas the relative trend is low because the FGI is high. Some regions such as the Tropical South Atlantic exhibit a very high relative annual trend from a very low mean index.

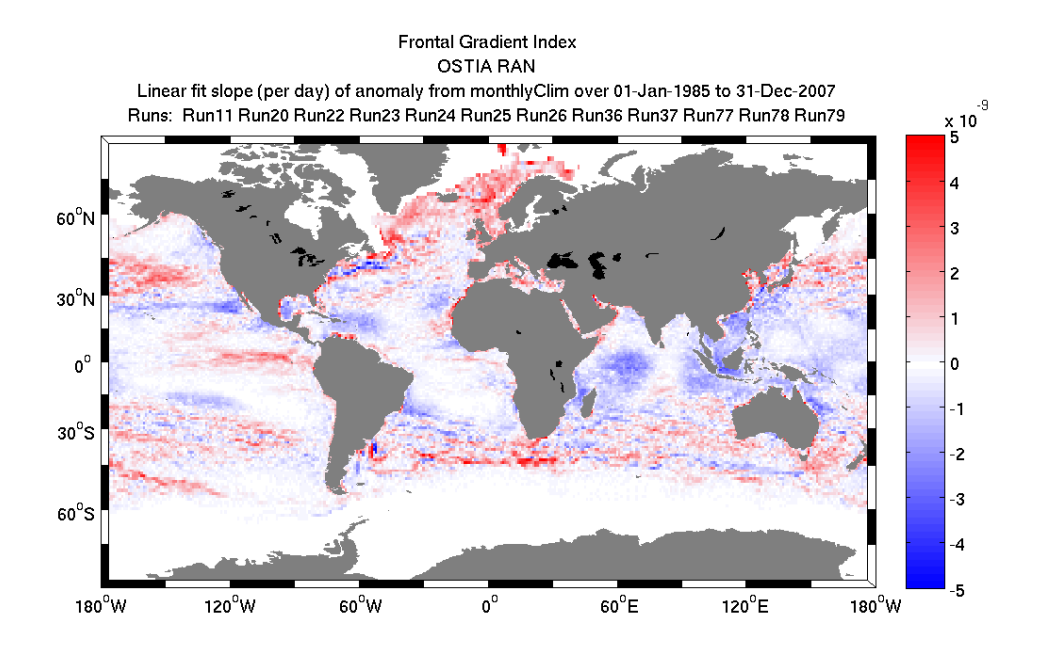


Figure 6-24: Daily trend of Front Gradient Index (FGI) in $kg\ m^{-3}\ km^{-2}day^{-2}$ processed on weekly OSTIA_RAN with $d=0\ km$, $L_f=0.5\ km$, and $\Delta s=25\ km$ calculated over the years 1985 to 2007.

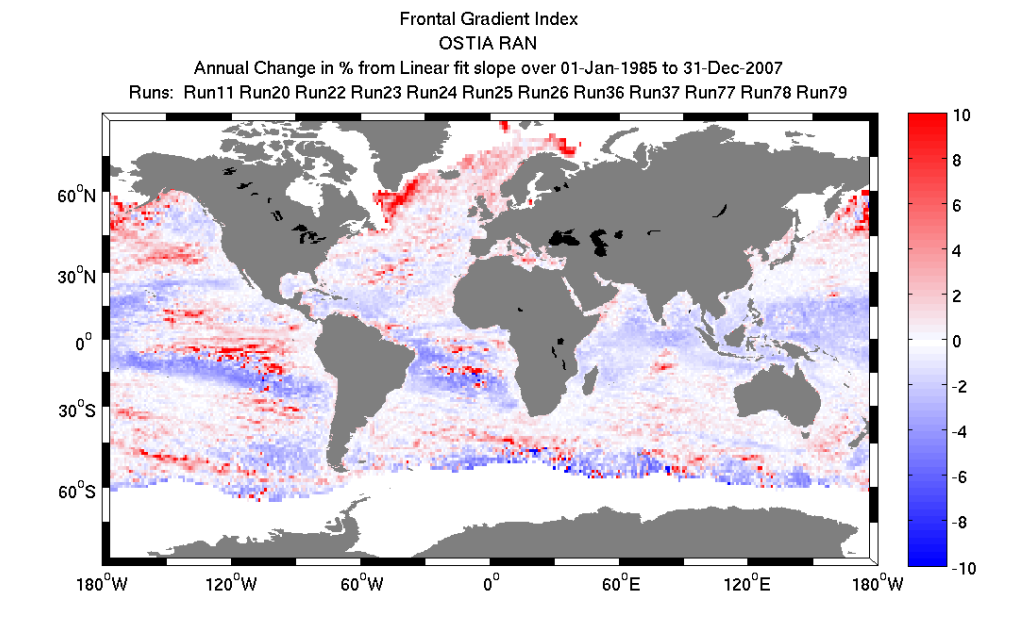


Figure 6-25: Normalized trend of Front Gradient Index (FGI) in % $year^{-1}$ processed on weekly OSTIA_RAN with d=0 km, $L_f=0.5$ km, and $\Delta s=25$ km calculated over the years 1985 to 2007.

These maps divide the global oceans into regions of consistent long term trend. Tools were developed to allow the exploration of inter-annual statistics over precise areas as a function of the spatial segmentation identified within any spatial statistical display such as Figure 6-24 and Figure 6-25. These tools allow the user to easily travel through the FGI datacube by the click of the mouse. A background map needs first to be selected, for instance the absolute long term trend shown on Figure 6-24. The user then defines boxes by drawing them with the mouse (Figure 6-26) and the routines plot inter-annual statistics as in Figure 6-27 to Figure 6-30. The automatic process involves the selection of the pixels that lie inside the box and the filtering of the time series of the mean area FGI by a monthly running filter. Then the annual mean, the annual minimum and annual maximum FGI are plotted on the top panel against time. The dates of annual minimum and maximum of the filtered data are also shown on the middle and bottom panel respectively. These figures reveal the low frequency temporal evolution of the FGI mean but also of the annual fluctuation between the annual minimum and the annual maximum. The top panel contains more information than a simple value of trend, it discloses the variability from one year to another, cycles of frequency lower

than a year⁻¹. For instance the FGI of the area 2 offshore Mauritania (Figure 6-27) increased by 0.5 kg.m⁻³.km⁻².day⁻¹ over the 23 years period with a sharp rise around 1991 and a fairly stationary annual mean during the other years before and after. Conversely, area 4 (Figure 6-28) shows an average decrease of 1.5 kg.m⁻³.km⁻².day⁻¹ from 1994 to 2007. The area 5 (Figure 6-29) reveals a strong inter-annual variability of the mean FGI with fast variations from one year to the next. The annual fluctuation between the annual minimum and maximum is also varying quickly, for example it is 0.3 kg.m⁻³.km⁻².day⁻¹ in 2002 and 0.7 kg.m⁻³.km⁻².day⁻¹ in 2004.

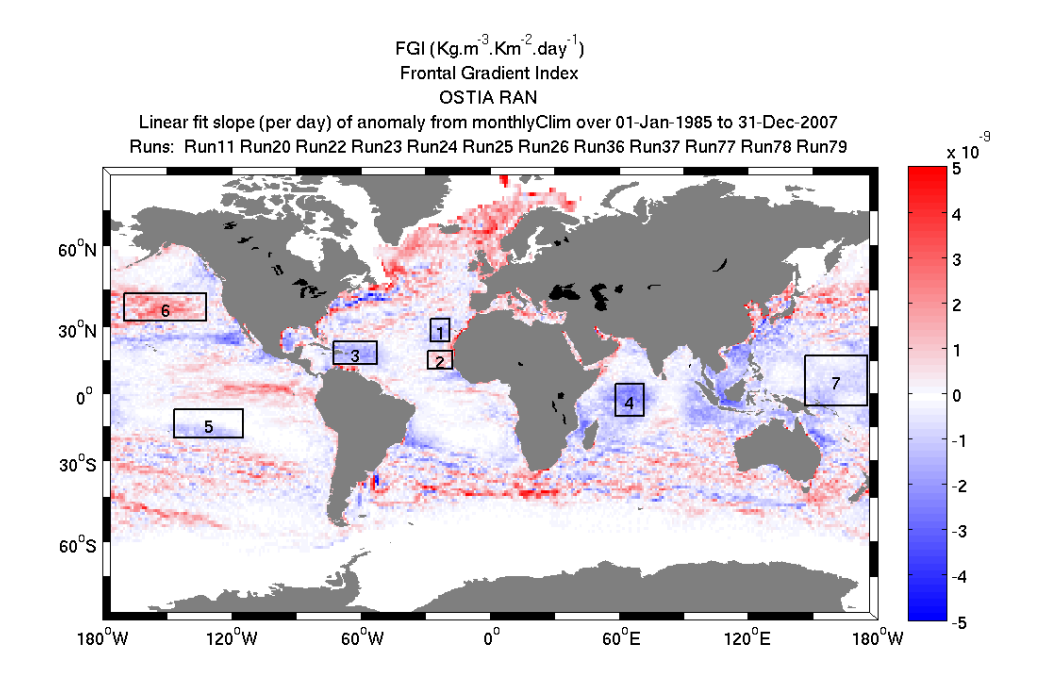


Figure 6-26: Daily trend of Front Gradient Index (FGI) in $kg\ m^{-3}\ km^{-2}day^{-2}$ processed on weekly OSTIA_RAN with $d=0\ km$, $L_f=0.5\ km$, and $\Delta s=25\ km$ calculated over the years 1985 to 2007. Areas whose inter-annual statistics are shown below are delimited by the boxes.

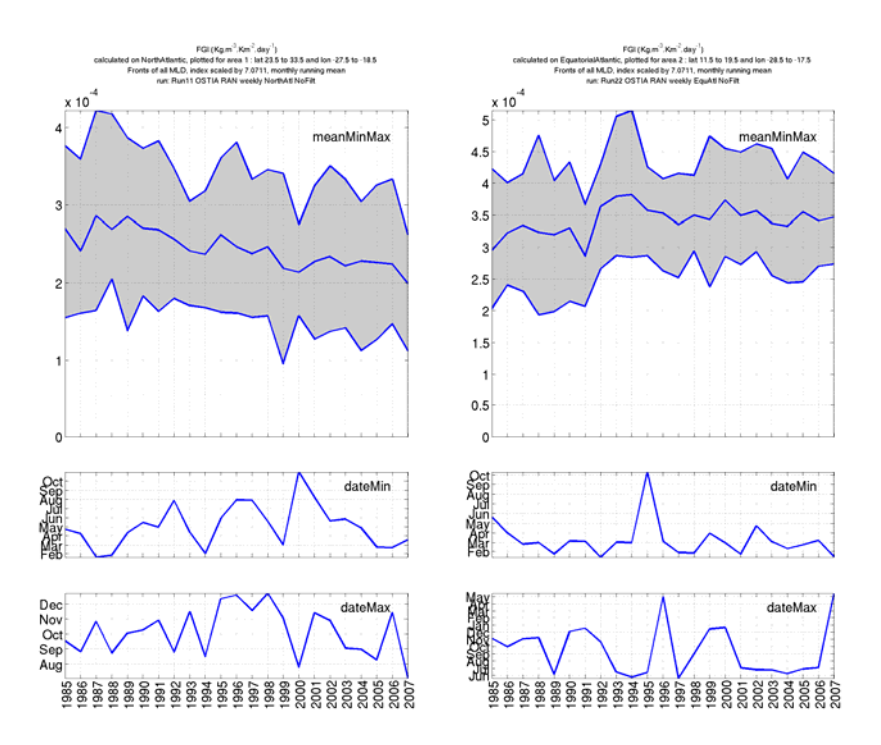


Figure 6-27: Annual mean, annual minimum and annual maximum of FGI (top), date of annual minimum of FGI (middle) and date of annual maximum OF FGI (bottom). The FGI is extracted from the box 1 (left) and box 2 (right) shown on Figure 6-26, it is filtered by a monthly running filter.

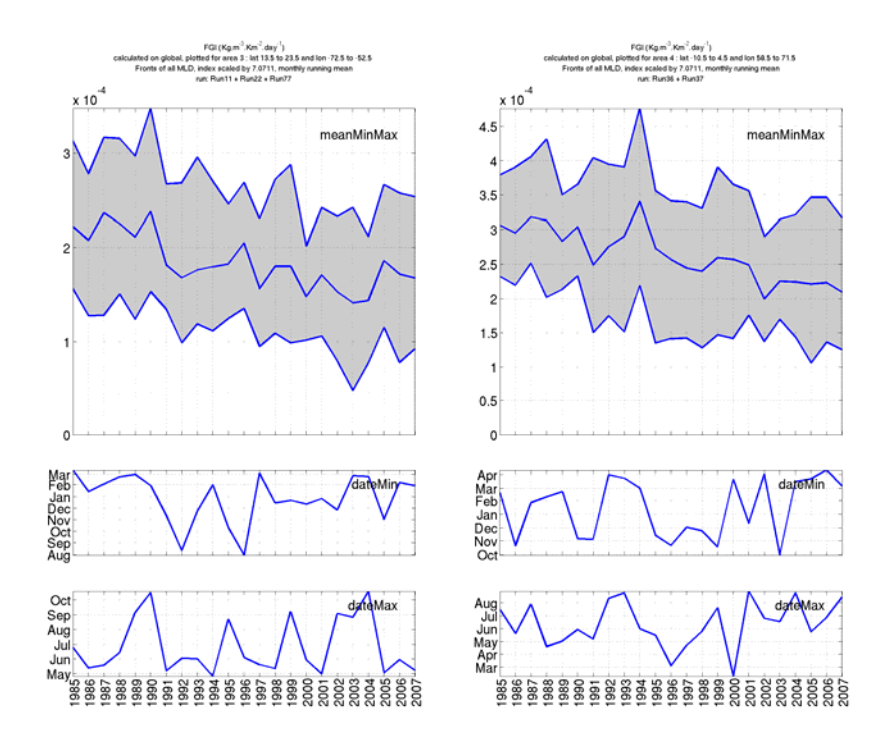


Figure 6-28: As for Figure 6-27 but for box 3 (left) and box 4 (right) on Figure 6-26

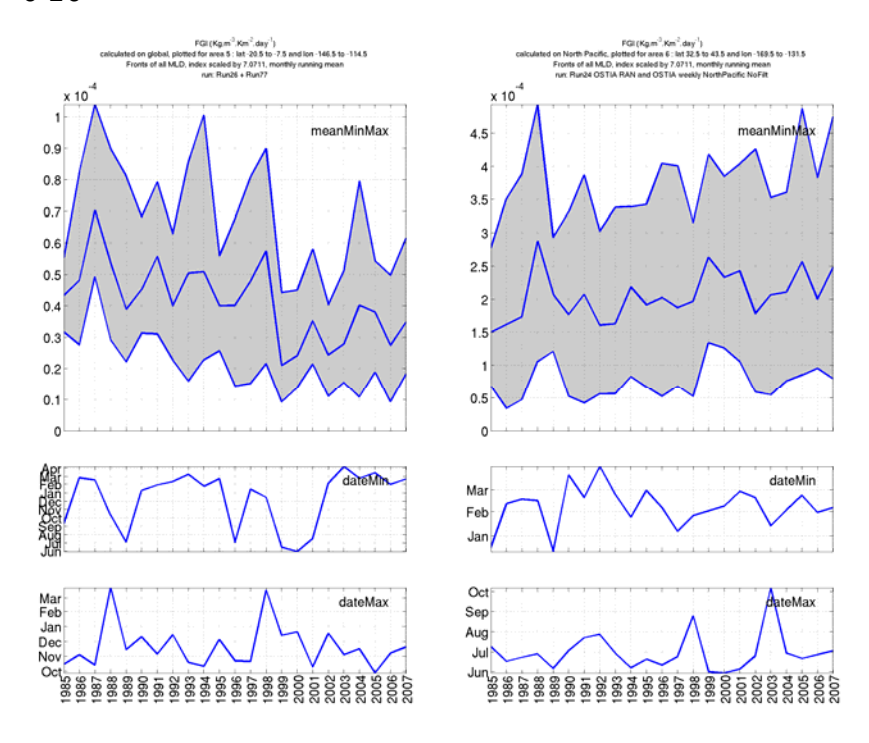


Figure 6-29: As for Figure 6-27 but for box 5 (left) and box 6 (right) on Figure 6-26

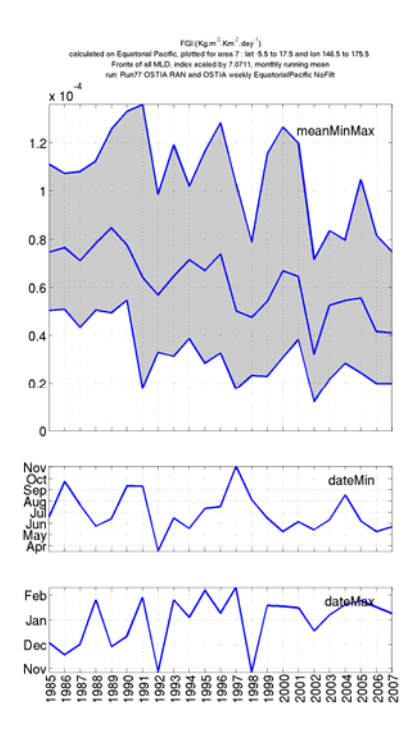


Figure 6-30: As for Figure 6-27 but for box 7 on Figure 6-26

Figure 6-31 shows the time series of the FGI averaged over the whole global oceans. The higher global FGI was observed in June 1994. The long term trend on a global scale is negligible (less than -0.03% per year). The global FLI (not shown) decreases on average by -0.16% per year. Figure 6-32 presents the time series of the averaged FGI for latitudes between 45 °S and 45 °N. There is a small negative trend over this part of the world's oceans of -0.12% per year and -0.25% for the FLI (not shown). The fact that the FLI decreases faster than the FGI means that, even though fewer fronts are detected on average from 1985 to 2007, the ones which are detected are slightly stronger. This result is in disagreement with that of Cornillon and Obenour (2012) which reported an increase of their frontal index of 0.47% per year with the day SST and 0.59% per year with the night data. Their frontal index is a frontal probability, therefore it is close to the FLI. Their fronts were detected on the AATSR reprocessing for climate (ARC) with the Cayula front detection method. It was shown in chapter 3 (section 3.5.3.1) that the Cayula method is sensitive to noise and detects fewer fronts where the noise is higher. Since the noise level of the ARC data is decreasing over the period chosen by the authors (1991-2010), it could be suggested that the long term increase of the frontal

probability measured by Cornillon and Obenour (2012) is an artefact of the frontal detection method and of the SST input dataset.

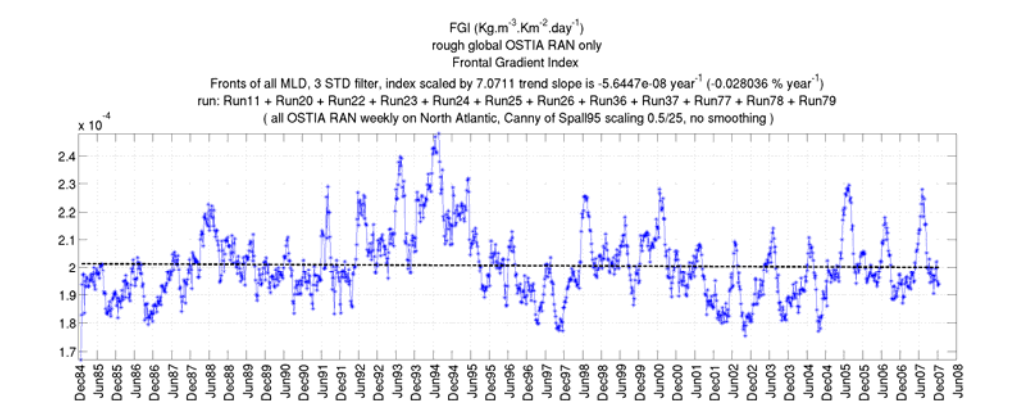


Figure 6-31: Front Gradient Index (FGI) in $kg m^{-3} km^{-2} day^{-1}$ processed on weekly OSTIA_RAN and OSTIA over the whole oceans with d=0 km, $L_f=0.5 km$, and $\Delta s=25 km$. Times when more than 50% of the area MLD is deeper than 75 m are plotted in red. The long term linear fit is plotted as a dashed line.

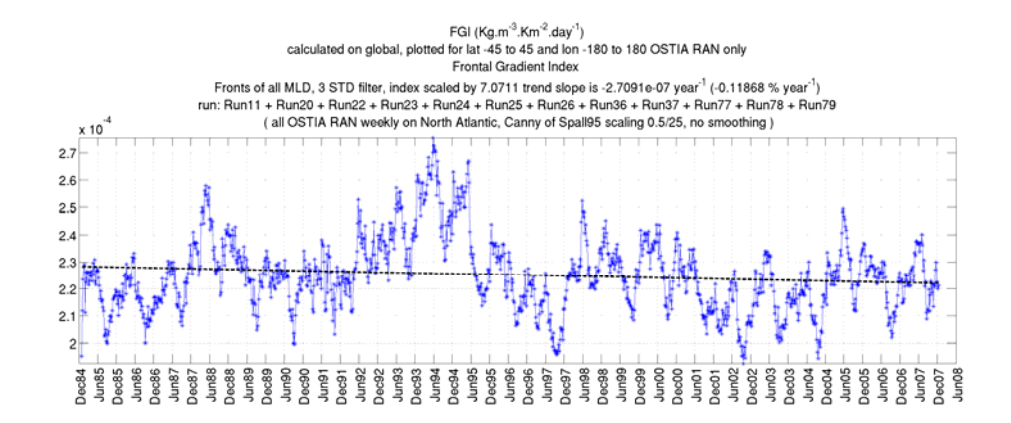


Figure 6-32: Front Gradient Index (FGI) in $kg m^{-3} km^{-2} day^{-1}$ processed on weekly OSTIA_RAN and OSTIA for latitudes between 45 °S and 45 °N with d=0 km, $L_f=0.5 km$, and $\Delta s=25 km$. Times when more than 50% of the area MLD is deeper than 75 m are plotted in red. The long term linear fit is plotted as a dashed line.

6.8 Correlations with climatic indexes

The FGI datacube spatial and temporal variability was extracted and presented in a variety of ways in the previous sections. It is striking how much the frontal activity can change from one year to another over the same region. It is not clear today what physical changes in the ocean and atmosphere can cause these variations in the frontal activity. This section explores whether the temporal variability of the FGI is correlated to some of the regional climate indexes. Correlation of these quantities would be a hint of a potential causality between what is captured in the climate index and the frontal activity.

The climate index of interest considered in this section is the El Niño-Southern Oscillation (ENSO). It is captured in the NINO 3.4 Index generated by NOAA's National Center for Environmental Prediction. NINO 3.4 is the 5-months running means of SST anomaly in the region 5 °N-5 °S, 120 °W-170 °W and normalized by its standard deviation over the period from 1950 to 1979. Trenberth (1997) suggests that an El Niño can be said to occur if NINO 3.4 exceeds 0.4 °C for 6 months or more. As seen on Figure 6-33, there was an El Niño in 1991-1992 and a very strong one in 1997-1998. In contrast, it is assumed that La Niña occurs when ENSO 3.4 is less than -0.4 °C.

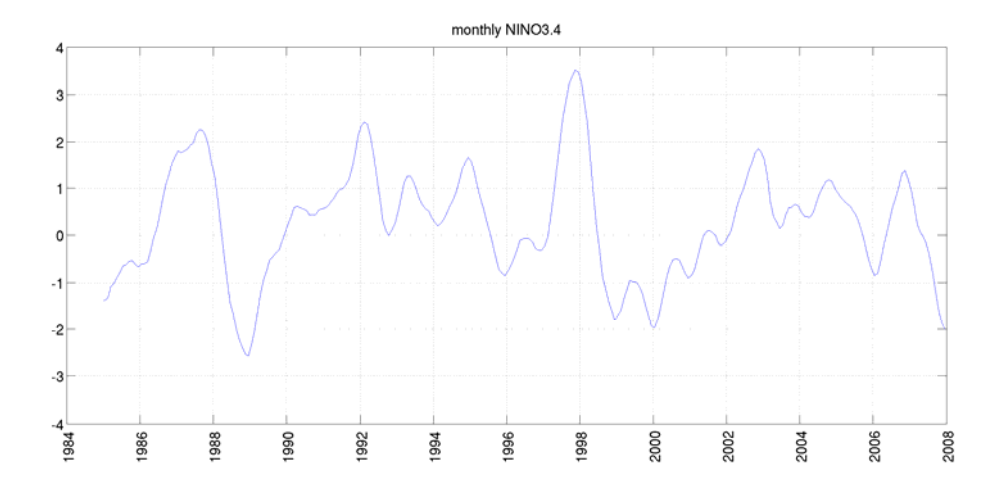


Figure 6-33: NINO 3.4 index (in °C) as downloaded from (http://www.esrl.noaa.gov/psd/gcos wgsp/Timeseries/Data/nino34.long.data)

For each pixel of the Pacific Ocean, the monthly climatology of FGI was calculated over the period 1985-2007. It was then subtracted from the daily temporal FGI signal to obtain the anomaly FGI. This anomaly time series was then correlated to the NINO 3.4 index with a lag between the two time series ranging from -90 days to +90 days. The maximum correlation for each pixel is shown on Figure 6-34 while the lag that is associated with the maximum correlation is shown on Figure 6-35. One can first notice the large patch of negative correlation over 10°S-10°N and East of 180°W, which includes the NINO 3.4 region. This patch correlation is achieved with a negative lag of 60-80 days, meaning that an increase (decrease) of FGI is in advance of a decrease (increase) of NINO 3.4. Below are two smaller regions of significant correlation, the first one is centred on 20°S/150°W, and the other one on 40°S/110°S. The former is associated to a consistent positive correlation with NINO 3.4 whereas the latter is associated to a negative one. They are however both best correlated to NINO 3.4 with a positive lag of about 80 days, which means that the NINO 3.4 index is in advance to the FGI over these regions. Therefore, these figures tend to show that an El Niño (La Niña) event is preceded 60-80 days earlier by a decrease (increase) of the FGI in the Equatorial patch. About 80 days after an El Niño (La Niña) event, the FGI increases (decreases) in the middle patch and decreases (increases) in the Southern patch.

This lagged correlation is confirmed by Figure 6-36 and Figure 6-37 which show the FGI HSR monthly index for respectively 3 months around the El Niño event in December 1997 and 3 months around the La Niña event in December 1998. Each figure also shows for comparison the corresponding months in 1993-1994 when no particular ENSO event was occurring. These two figures show a low FGI in the Equatorial patch 2 months before the El Niño of December 1997. Conversely the FGI is higher than normal over the Equatorial patch 2 months before the La Niña of December 1998. The lagged correlation in the middle patch and the Southern one are likely to be explained by the shift of a proportion of the fronts from the Southern patch to the middle one about 3 months after an El Niño event. The opposite displacement of the frontal activity occurs 3 months after a La Niña event.

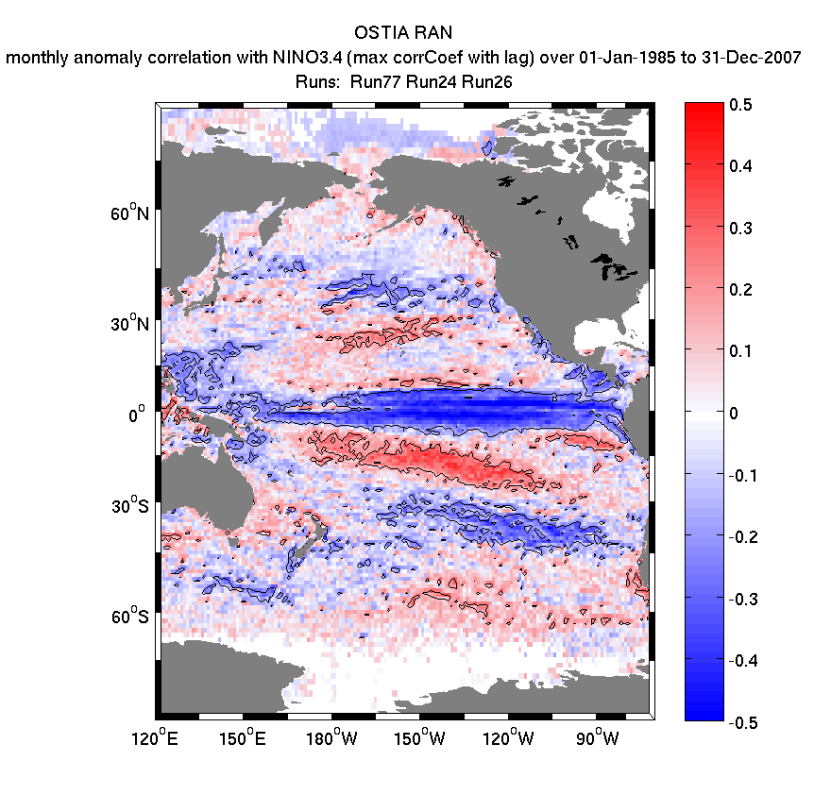


Figure 6-34: Lagged correlation of the monthly anomaly of Front Gradient Index (FGI) with NINO 3.4 in the period 1985 to 2007. The FGI is processed on weekly OSTIA_RAN with d=0 km, $L_f=0.5$ km, and $\Delta s=25$ km. The maximum lag allowed is \pm 90 days. The contour corresponds to an absolute value of the correlation of 0.2.

120°E

150°E

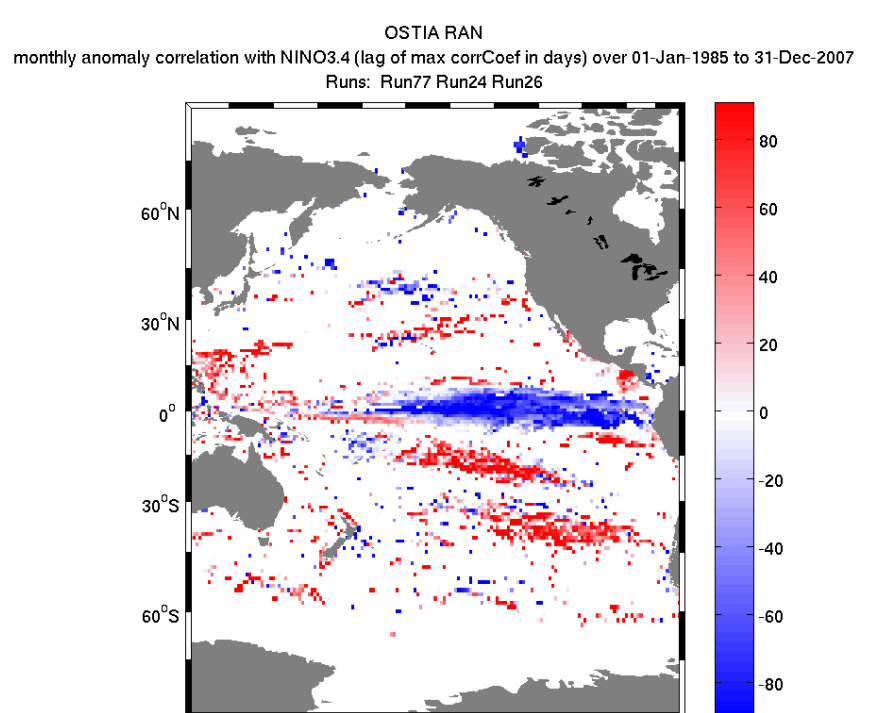


Figure 6-35: Lag (in days) corresponding to the maximum correlation of the monthly anomaly of Front Gradient Index (FGI) with NINO 3.4 in the period 1985 to 2007. The FGI is processed on weekly OSTIA_RAN with d=0 km, $L_f=0.5$ km, and $\Delta s=25$ km. The maximum lag allowed is \pm 90 days. The lag is shown only where the absolute value of the correlation is higher than 0.2. The lag is positive (negative) where NINO 3.4 is in advance (late) with regard to the FGI.

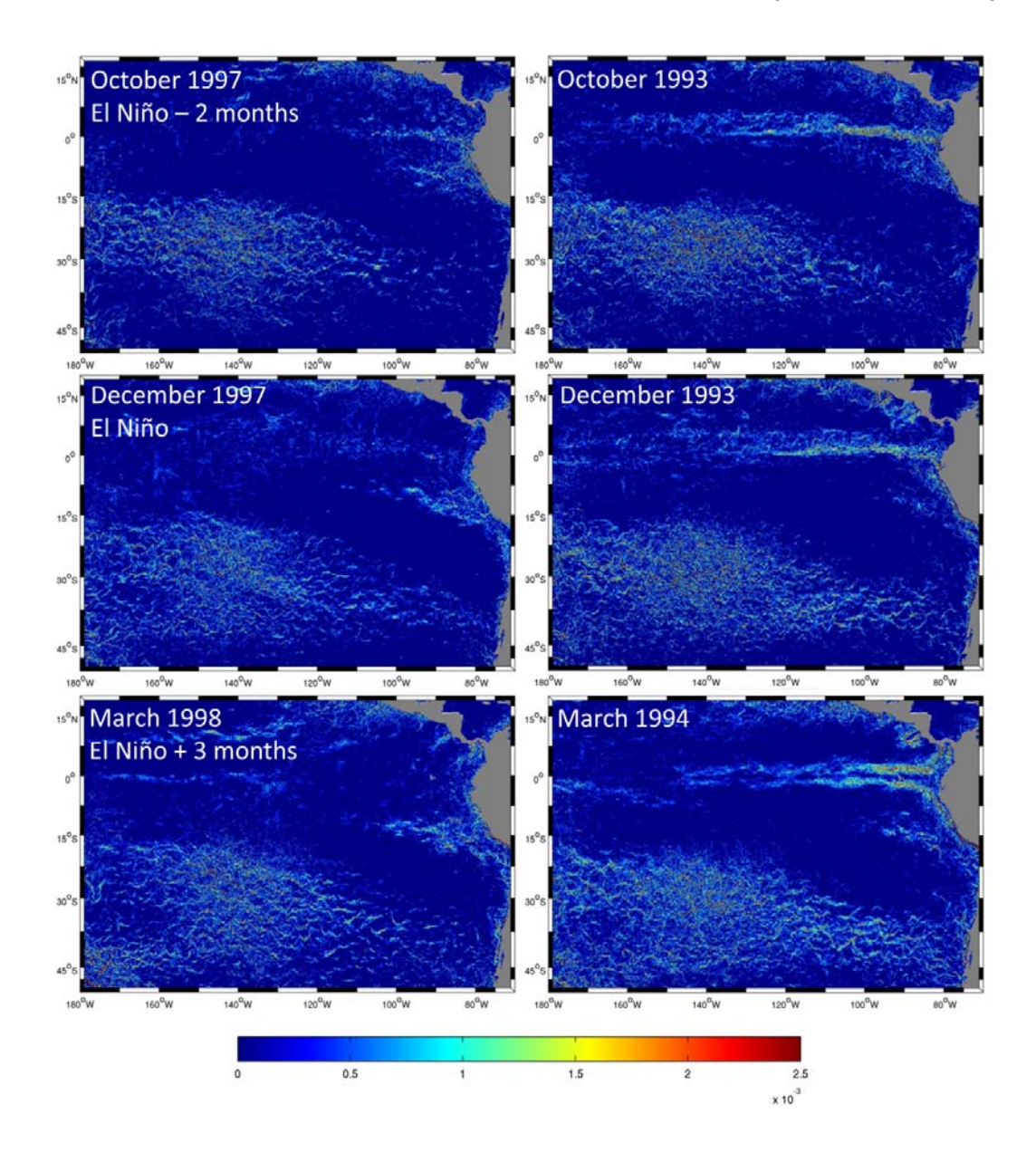


Figure 6-36: Monthly averages of High Spatial Resolution monthly mean of Front Gradient Index (FGI) in $kg \ m^{-3} \ km^{-2} day^{-1}$ processed on weekly OSTIA_RAN with $d=0 \ km$, $L_f=0.5 \ km$, and $\Delta s=25 \ km$. The left column shows three months around the El Niño event of end of 1997. The right column shows the corresponding months 4 years earlier when no El Niño event was occurring.

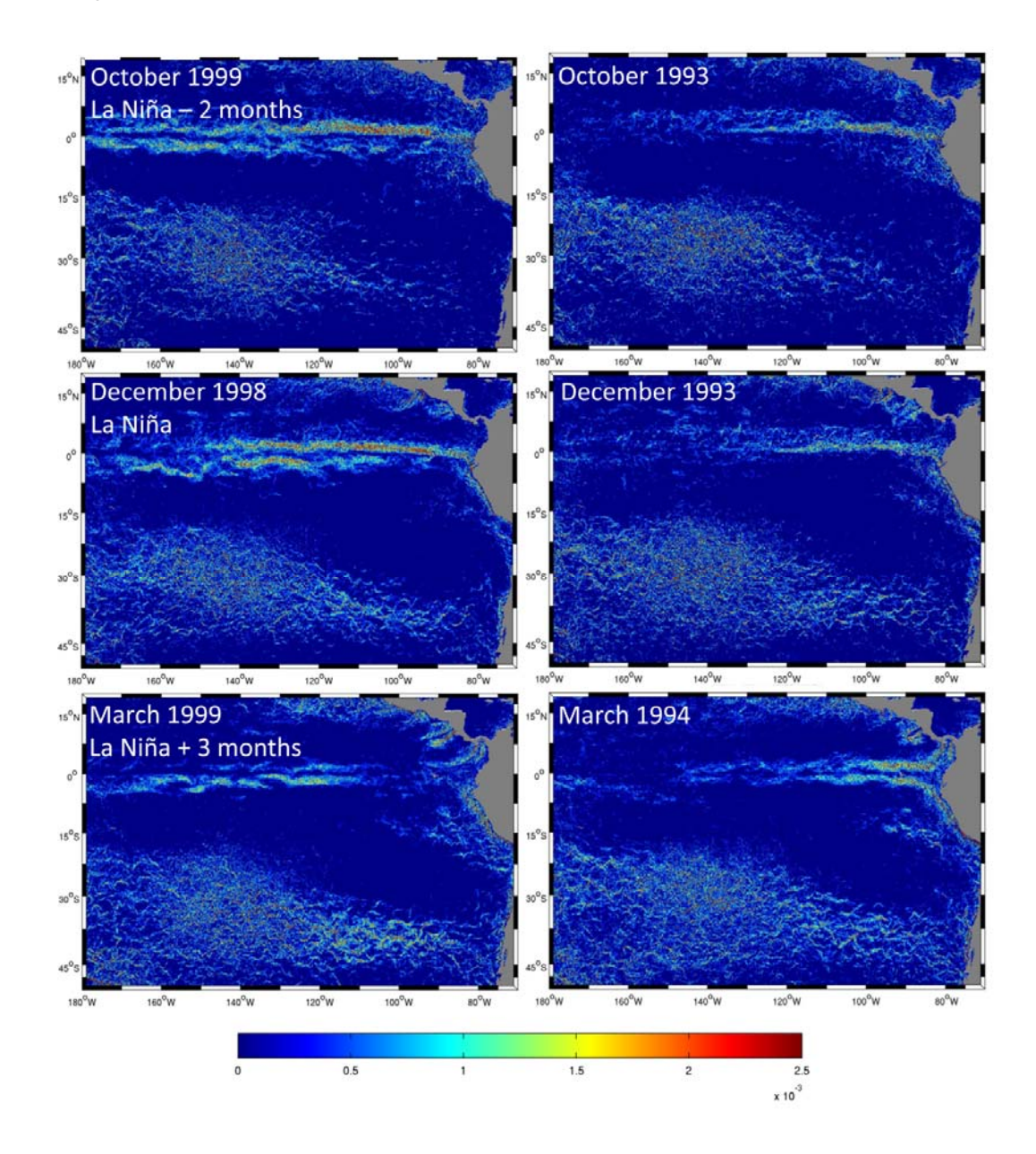


Figure 6-37: Monthly averages of High Spatial Resolution monthly mean of Front Gradient Index (FGI) in $kg \ m^{-3} \ km^{-2} day^{-1}$ processed on weekly OSTIA_RAN with $d=0 \ km$, $L_f=0.5 \ km$, and $\Delta s=25 \ km$. The left column shows three months around the La Niña event of end of 1998. The right column shows the corresponding months 5 years earlier when no La Niña event was occurring.

Following the same methodology as that described in 5.6, the inter-annual statistics of four regions shown in Figure 6-38 are shown on Figure 6-39. The first region lays over the Eastern part of the cold tongue. The El Niño event of 1997 is clearly visible in the annual average drop of 65% of the FGI over the same year. In 1997, the annual maximum of the monthly filtered FGI was reached in January while it occurs on average in July for the other years. The FGI annual average also dropped in 1987 during another El Niño event and peaked in 1988 during a La Niña. Note that the date of maximum of the FGI in 1987 is average, while it drops to May in 1988. In the 1998 La Nina, this date is close to average. The second area is the central part of the cold tongue, its FGI is lower than on the Eastern part. Its annual statistics present the same response to the ENSO events as described for the first region. For instance, during the El Niño of 1997 the FGI is 3 times lower than average, whereas in the 1998 La Nina it raises to 3 times the average. Over the Western part of the cold tongue, captured by the third region, the average FGI is lower. It does however follow the same pattern by dropping during the El Niño events and peaking during La Nina. The fourth region lies over a region of very low FGI below the central part of the cold tongue. The El Niño signal is clearly picked up in the region annual FGI statistics as the annual FGI average sharply increases in the La Nina years of 1988 and 1998. The El Niño events are not seen as the index is very low in the first place. The ENSO can therefore be said to strongly affect the FGI over these regions, mostly with sharp drops (increases) when an El Niño (La Niña) occurs. No clear pattern can be observed for what concerns the timing of the annual maximum and minimum when there is an FNSO event.

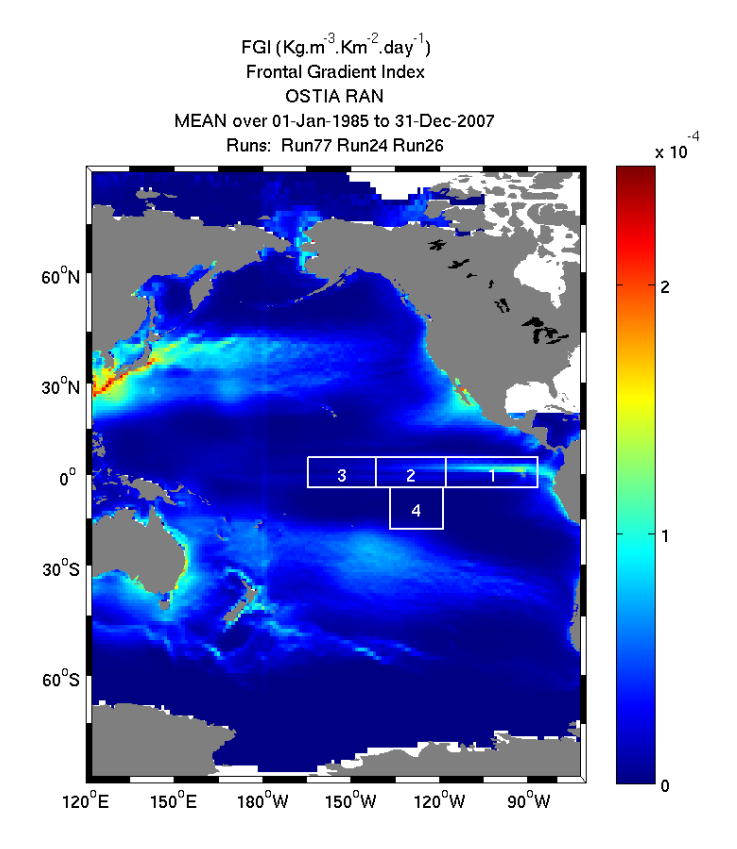


Figure 6-38: Long term (1985 to 2007) mean Front Gradient Index (FGI) in $kg \ m^{-3} \ km^{-2} day^{-1}$ processed on weekly OSTIA_RAN with $d=0 \ km$, $L_f=0.5 \ km$, and $\Delta s=25 \ km$.

Climatic variability of frontal activity

Figure 6-39: Annual mean, annual minimum and annual maximum of FGI (top), date of annual minimum of FGI (middle) and date of annual maximum of FGI (bottom). The FGI is extracted from the boxes 1 to 4 shown on Figure 6-38, it is filtered by a monthly running filter.

6.9 Conclusion

This chapter demonstrates the potential of the front detection routines described in chapter 5 as they are able to detect fronts with a consistently high accuracy, at high resolution, on the global scale and at a climatic time scale. In addition an elaborate set of routines was developed to allow the exploration of the three-dimensional (latitude, longitude and time) dataset of detected Frontal Gradient Index (FGI). These routines build on the object oriented programming of the FGI files. They offer the means to easily plot and save figures of time series or maps with a very wide range of statistics applied. This chapter's figures were all plotted with these automatic tools, some of them are even obtained by the click of the mouse. These statistical analysis routines are an achievement in themselves because they may be used to analyse any other type of three dimensional dataset.

In this chapter, the typical seasonal pattern of the frontal activity at the surface of the oceans was described with an unprecedented accuracy. The seasonal signals were extracted and projected in a variety of ways to deliver a precise view on how this seasonality varies from one place to another.

Changes in time of the local frontal activity were also studied by means of local trend calculations. It was shown that the frontal activity changes in different ways across the globe. The global or regional trends that were calculated previously and by others lack the kind of details that were revealed by this study. Moreover the positive trend that was calculated by Cornillon and Obenour (2012) between 45 S and 45 N was not confirmed by this study. In contrast a small negative temporal trend over this region was found instead. This was suggested to be due to the fact that the Cornillon and Obenour (2012) methodology is based on the Cayula frontal detection algorithm. The latter is more sensitive to noise than the methodology used in this thesis, which is based on the Canny algorithm. Since the noise of the SST product has been continuously improved since 1985, this could explain why Cornillon and Obenour (2012) observe a positive trend. This stresses the importance of a frontal index calculation methodology that is robust to noise or other potential bias sources. The capacity of the frontal index calculation routines to deliver both a high temporal resolution (HTR) and a high spatial resolution (HSR) dataset was also proven useful. The HSR was explored and, by means of a

projection into a Hovmöller plot, it reveals the North-South oscillation of a part of the Kuroshio with an amplitude of 270 km and a period of about 13 years.

The calculated frontal index was shown to be linked over the Equatorial and South Pacific to the NINO 3.4 climate index of the ENSO. Interesting lagged correlations and changes in the typical frontal pattern before and after El Niño or La Niña events were exposed. This is an important result as this allows the frontal activity to be linked to a well-studied climate phenomenon. Evolutions of the frontal activity in some regions have the potential to be predicted based on the prediction of the climate index they are correlated to. It should be stressed that caution must be exercised while analysing the correlations between the fronts and such a major climate index since the ENSO is strongly linked to the atmosphere dynamics. Biases may be introduced by the cloud coverage and this was shown in chapter 4 to have a potential effect on the resolved frontal content of the Level-4 SST products. This stresses the importance of adding a measure of the smoothing involved as a quality indicator to the Level-4 SST datasets. Such a measure could be introduced in the frontal calculation and would improve the confidence in this kind of result.

It should be recalled that this chapter has aimed simply to illustrate potential rather than attempt a systematic analysis of patterns and trends in the spatial and temporal variability of the FGI; the datacube explored in this chapter has many more secrets to reveal. It has demonstrated that the methods to extract information from global 20-year FGI dataset are developed and ready for a more penetrating exploitation by the physical oceanography community. More precise frontal extraction in a defined region, through a more elaborate frontal index such as those presented in chapter 5, based on a higher resolution Level-2/3/4 SST dataset and at a higher temporal sampling rate, can be performed in a user-friendly way using the methods and routines shown in this thesis. The intended scope of the thesis has been achieved, its author hopes to have convinced physical oceanographers that their topical and regional studies could benefit from applying this work!

In the future it would be interesting to also correlate the frontal indexes with observations of Eddy Kinetic Energy (EKE) and stratification. A deeper insight in the correlations between the fronts and these parameters would help predict the likely evolution of frontal activity because EKE and stratification are

Chapter 6

themselves resolved or predicted by the current GCMs. In the case of stratification, the correlation could be based on monthly datasets of stratification index from Argo floats. Besides, gridded satellite altimeter products such as AVISO (Le Traon et al. 1998) can be used to produce global maps of EKE (Fu et al. 2010). The main issues with the altimetry products are their temporal and spatial resolution and the noise contamination. Due to the orbital constraints of the altimeters which produce repeat times of days to weeks, these products do not resolve the small spatial and temporal scales (Arbic et al. 2013). The signal to noise ratio in altimetric data is a strong function of the wavenumber, apparently falling sharply at scales shorter than about 200 km (Ferrari and Wunsch 2010 and Stammer 1997), which also prevents the exploration of small scale signals. This is to say that the frontal variability described in this thesis could not be obtained from altimetry which do not observe the same quantities nor resolve the same scales as the SST satellite missions. Nevertheless, the interactions between the small scale surface fronts and the larger scale EKE field are far from being understood and the suggested correlation has the potential to shed some light on it, as discussed in 2.5.

7. Chapter 7: Conclusion

7.1 Overview of the achievements in a multi-faceted research landscape

The general objectives stated in section 1.1.6 have broadly been met. Even though, in some cases, no definitive absolute answer could be provided, significant results were achieved and the scientific understanding was improved with regard to many aspects of front detection and interpretation. The rationale behind this work was to obtain more oceanographic information from the SST satellite measurements by looking at their mesoscale and submesoscale variability. This objective drove the research activities from the beginning to the end of the PhD. The choice was made to focus on surface fronts because they are linked to intense dynamical activity and can be observed on SST images.

More information on the dynamics of the mixed layer was extracted from the SST data by means of two parallel strategies. On one side the characterization of the spatial and temporal variability of fronts was pushed to a new limit by a rigorous analysis of the algorithmic techniques to detect them on SST images and a thorough investigation on the ability of multi-sensor SST products to resolve these fronts. On the other side a very systematic exploration was carried out of the parameterizations presented by physicists that relate dynamics to the surface density gradient. This work permitted the tuning of frontal detection algorithms such that they identify fronts that are likely to have an impact in the dynamics of the mixed layer. But most importantly, it allowed constructing frontal indexes that attempt to quantify physical phenomena occurring at fronts. The adaptation of dynamical studies to what can be observed from space is a significant step towards bridging between recent physical oceanography results and new improvements in SST remote sensing. These two disciplines have the potential to be used in synergy and to provide unprecedented information on the dynamics of the mixed layer.

This effort to reach oceanographic dynamical parameters from the detected surface fronts and additional parameters such as altimetry observations and climatologies of salinity and MLD is a novel approach and constitutes a

significant scientific achievement of this thesis. Software tools were developed to support this conceptual approach. A very large effort given to the design and implementation of these tools resulted in routines that follow high software engineering standards. They were made user-friendly, highly optimized, robust and versatile in order to allow numerous data crunching exercises on very different SST data sets while following filtering and frontal detection strategies adapted to the dynamical parameters of interest. These software tools were instrumental in the application of the conceptual results to the exploration of frontal dynamics signals globally and over spans of SST data up to 27 years long. All the figures presented in chapter 5 and chapter 6 that display the results of the frontal detection runs were also produced by dedicated visualisation tools which are part of the developed software. Using these tools it was possible to carry out an independent assessment and intercomparison of the scales resolved by the new multi-sensor GHRSST Level-4 products. Interesting oceanographic results were produced by the adaptation of theoretical physical understanding to the frontal observations on SST images. These results are discussed and the potential of such methodologies have been demonstrated. In most cases the quantities are not yet fully reliable but their variations in space and time reveal new aspects of how the ocean actually works. So the objective of providing solid dynamical indicators with an absolute accuracy could not be fully met in the context of this PhD. However this work brings the oceanography community significantly closer to the objective because the methodology developed and presented is robust. Indeed, its processing and input data were systematically characterized and their limitations were thoroughly described. This work is in good part methodological; it was conceived and achieved as such.

Being very user-friendly is another achievement of this thesis, the analyses presented allow other scientists to build on this work. Others can even re-use the software tools because their versatility and robustness permit their straightforward adaptation to future breakthroughs on the dynamical side. This work comes at a good time because fronts are gaining fresh interest and important improvements are being achieved in the understanding of the physical phenomena occurring in their vicinity. At the same time rapid progress is being made in the development, production and distribution of multi-sensor SST products that offer the resolution and coverage required for

such studies. The need for new indicators of the ocean dynamics constructed from satellite observations for monitoring the ocean is widely recognized; this work is a step in this direction.

7.2 Summary of scientific achievements

7.2.1 Objective 1: define a methodology for the detection of fronts on SST images

The first objective was to understand how best to detect temperature fronts on SST images. This question was divided into two questions: what is the best way to detect fronts on a SST image (Q1 of 1.1.6) and what SST dataset is most suitable for this application (Q2 of 1.1.6). While answering both questions, care was taken to characterize the performances of the algorithms and dataset such that physical conclusions can be drawn from the results they return.

The study on the front detection algorithms presented in chapter 3 was the first piece of work carried out for this thesis. A review of the different algorithms to extract fronts on two-dimensional images was achieved and two particular algorithms were identified for their relevance with regard to the foreseen applications: the Cayula method (also called SIED for Single Image Edge Detection) and the Canny method. The Cayula algorithm was implemented in Matlab based on its published description which required a consequent effort of conceptualization, implementation and optimization to allow its use on very large images. The Canny algorithm was implemented based on a compiled Matlab library but required a significant adaptation from an image processing to a geophysical perspective. The process of implementing these algorithms into working routines delivered sufficient expertise and insight to be able to identify their strengths and weaknesses as well as the assumptions and parameters they rely on.

Although the Cayula method for detecting fronts has been widely used by oceanographers, it seems to have never been thoroughly characterized. In the context of this study, since the ultimate goal was to recover physical parameters from the detected fronts, it was not conceivable to leave part of

the processing acting as a black box. Therefore a systematic characterization of the response of the Cayula algorithm to synthetic scenes of fronts of varying intensity, width and noise was performed (3.5.2). This investigation is a novel piece of work that unveils the behaviour of the Cayula algorithm. The same analysis was carried out with the Canny algorithm which proved to be more predictable and consistent in relation to the frontal characteristics, sinuosity and orientation (3.5.3). The latter algorithm proved to be better at detecting fronts of various scales and intensities that are by nature embedded in a complex turbulent flow. It also does not rely on any arbitrary parameter as opposed to the Cayula method and seems to be more easily linkable to dynamical interpretations. This investigation concluded that the Canny algorithm is the most suitable for the exploration of fronts on Level-3 and Level-4 SST products. An in-depth quantitative description of the effect of different smoothing filters to the noise and the small fronts was provided that allows one to perform the trade-off between the reduction of noise and the suppression of the genuine small-scale fronts before the Canny algorithm is executed (3.5.1).

The second important body of work carried out during this PhD project was to quantify the ability of the SST products to resolve the small scale features that are targeted by the front detection algorithms (Q2 of 1.1.6). A detailed review on the Level-2, Level-3 and Level-4 SST was presented in section 4.1. The selection of the input SST dataset and the spatial filtering that is applied to the images prior to the frontal detection are an important part of the methodology. They must both be very carefully decided in order to return frontal results that are scientifically accurate and consistent, and which are able to capture the scales of interest. The choice was made to use new Level-3 and Level-4 multisensor SST products because of their advantages in terms of spatial and temporal coverage. These multi-sensor products have recently achieved a quality leap in the context of the GHRSST program: this concerted international effort has made them more accurate and temporally and spatially finer by improving the statistical methods that produce them and by basing them on a wider selection of input sources. Nevertheless, these products suffer from limitations in the context of the exploration of small scale variability. This study being the first to attempt to achieve the systematic characterization of mesoscale and submesoscale phenomena using these multi-sensor products, it was essential to first characterize the ability of these data sets to resolve the fronts at different scales. The strategy to achieve this characterization was twofold: it tackled the question on one hand in a theoretical context and on the other hand through an experimental approach. On the theoretical side, a significant effort was put into understanding the production process of the Level-4 data and in particular the optimal interpolation. This led to the description of the theoretical situations in which the scales resolved by a particular product (also called "feature resolution") may be limited or even inconsistent in time or in space as presented in section 4.2. The question of the feature resolution of the products is very complex since it depends on assumptions made on the actual scales present in reality across the oceans, on the cloud coverage, on the availability of infrared and microwave satellite observations and on the detailed design of the state estimation filter that lays at the heart of the production of these data sets. Due to the complexity of the optimal interpolation process, it is not yet clear, even to the engineers and scientists that are in charge of this production, what level of smoothing or interpolation is introduced by the optimal interpolation as a function of date and location. This is why the practical exploration of the feature resolution in the various Level-4 products was not only fundamental for this thesis but also equally of great interest to these engineers and scientists. It was a very delicate task to separate the genuine scale of variability of the ocean from the variability introduced by the observation and processing chain of the images that attempt to capture it. This analysis was fundamental because of the dual objectives of this PhD, namely the validation of the input images in parallel with the extraction of natural signals from them. This challenge was tackled in depth by the careful exploration and inter-comparisons of the different products in terms of gradient (4.3), frontal content (4.4) and spatial autocorrelations (4.2.3). This was performed in various filtering conditions and in comparison with results extracted from Level-3 images which are consistent in scales. This process, which was exposed in chapter 4 and chapter 5, brought us closer to establishing a measure of confidence in the use of Level-4 OSTIA SST for genuine frontal exploration.

7.2.2 Objective 2: the derivation of information about oceanographic dynamical parameters

The second objective of this thesis was to work towards the recovery of dynamical parameters of the mixed layer from the observation of temperature fronts at its surface (Q3 of 1.1.6). This particular objective was very ambitious because it involves the use in synergy of the disciplines of both fluid dynamics and remote sensing. As explained in section 1.2.3, previous efforts to link these two disciplines are limited to very specific case studies. This study attempted to be systematic and to offer a methodology that is automatic and objective and which can be used globally. It relies on the thorough review of analytical and numerical studies that provide an understanding of the dynamics occurring in the vicinity of surface density fronts as presented in chapter 2. This resulted in an advanced description of the current knowledge of the frontogenesis, but also of the scientific context that surrounds these studies, the challenges that they face and the main directions in which physical oceanographers are trying to shed light on the small scale frontal dynamics. Based on the understanding of fronts that was acquired by the author carrying out this review, some of the results and parameterizations, such as the Omega equation (5.4), were adapted to be applied to the detection of fronts on SST images. This way, several frontal indexes were defined which provide an estimate of a dynamical parameter of the mixed layer such as vertical velocity (5.4) or restratification (5.6) by Mixed Layer Eddies at fronts. These dynamical indexes were calculated making the most of independent observational data such as altimetry products and climatologies of surface salinity and MLD. Because these indexes also rely on assumptions such as the local frontal width, which is taken constant in this thesis, their exact quantitative estimates cannot be fully trusted. Nevertheless, their variations can be relied on and they shed some interesting light on the vertical exchanges at the small scale in the mixed layer. Moreover, these indexes proved to be valuable independent tools to critically assess purely theoretical results (5.5). Finally, the potential of these dynamical frontal indexes for resolving accurate quantitative dynamical parameters in the future was demonstrated, provided some of the assumptions they rely on are refined. This study is, in this regard, somewhat preliminary and more of a precursor; it has built some foundations through its scientific achievements but more work is required to construct a methodology

able to recover accurate small scale dynamical parameters of the mixed layer from SST images. Such additional analyses do not fall in the scope of this PhD thesis, they are however outlined in section 7.4.

7.2.3 Objective 3: the characterization of the spatial and temporal variability of the frontal activity

The characterization of the spatial and temporal variability of the frontal activity was another objective of this thesis (Q4 of 1.1.6). It was achieved by calculating the basic Frontal Gradient Index (FGI) on several SST products as shown in section 5.2 and chapter 6. A strong seasonal signal was observed on all the products with a high frontal index during the summer and a low one in the winter over the North Atlantic (5.2 and 6.5). The spatial variability was also described and showed large frontal contents over the main western boundary currents and some coastal areas (6.2). The oceans were shown to be divided into regions of low FGI over the mid-latitudes far from the shores and the main currents and regions of medium FGI extending surprisingly far from the regions of high FGI. An enormous run was carried out to measure the FGI on the OSTIA_RAN dataset globally and every 7 days over a time span of 23 years. Section 6.5 showed how the frontal index resulting from this run allows one to characterize the typical annual behaviour of the fronts over each ocean pixel. The phenomenology of the FGI was described by means of global plots of the dates of annual maximum and minimum of the typical FGI over each pixel. The typical annual fluctuation, the temporal mean and standard deviation were also presented. The physical mechanisms that generate the seasonal variability of the fronts were discussed (6.5). Frontogenesis is linked to the turbulence of the surface mixed layer, it can be triggered also by atmospheric effects such as heterogeneous wind mixing or sun heating. It was shown that the FGI is to some extent anti-correlated to the MLD taken positive from mid to high latitudes but it is not the case over most of the other areas. The frontogenesis is controlled by the complex combined effect of these dynamics, but this study does not conclude on the exact origin of the front seasonal variability it revealed.

Changes in time of the typical frontal activity were also explored over the 23 years of available global frontal index. It was exposed that the FGI varies slowly over decadal time scales in different ways over different areas (6.7).

Frontal activity temporal trends observed by others were not confirmed, and both positive and negative trends were revealed by this study. Temporal FGI signals over some regions of the Equatorial Pacific showed to be sensitive or even correlated to the El Niño Southern Oscillation index (6.8). Small meridional displacements of the Kuroshio Current were also revealed by the FGI calculated at a fine spatial resolution (6.6). These analyses demonstrate the potential of this methodology for revealing signals in the ocean surface dynamics by extracting fronts from a series of global high resolution images and applying statistical methods to project the large three dimensional frontal dataset into figures that can be plotted and that carry a scientific meaning. This methodology also allows to point towards many ocean areas that show a spatially consistent behaviour which should trigger the curiosity of physicists and the author of this thesis encourages them to explain the frontal variability exposed.

7.3 Technical achievements

The software tools that were developed during this PhD were not in themselves a scientific objective, they however were a necessary means to accomplish those and thus constitute a great achievement of the thesis. This made the PhD work heavily computational as developing the routines and running them accounted for a large part of the research effort. The entire coding was carried out in Matlab.

7.3.1 Implementation of the front detection algorithms

The first layer of the software that was developed is the scientific routines. The Cayula front detection method was implemented based on its theoretical description that was published in Cayula and Cornillon (1992). This algorithm is fairly complex and its practical implementation raised numerous issues. Being extremely incremental, it required a very large amount of memory and operations in its raw form. As the objective was to run this algorithm on a large number of huge SST images, it needed to be optimized. This was achieved by means of strategies that limited both the number of operations and the required memory. Some of these strategies were based on a divide-

and-conquer approach which divides the input SST matrix into imagettes and reconstructs the fronts that lie over several of them. The algorithm was significantly optimized but the consequence was a sharp increase of the algorithm detailed design complexity. The Canny algorithm was also implemented and optimized as much as possible, and so were the spatial filtering functions.

7.3.2 Implementation of the geo-physical routines

A second layer of routines was added to make the frontal detection, image filtering applicable to geo-physical interpretations and to store the results into meaningful frontal indexes. This layer comprises the calculation of the basic and more advanced frontal indexes from the detected fronts, all the techniques related to the different geographical projections, the geo-physical statistics involved in the calculation of the frontal indexes and in the production of figures.

7.3.3 Implementation of a software engineering layer

Finally a layer of pure software engineering was added on top of the others that deals with the input parameters, the configuration control, the parallelization of the processing across several processors, the access to satellite products and climatologies and the monitoring and logging of the progress and the errors. This last layer was necessary to provide the userfriendliness, the robustness, the optimization and the flexibility which were absolutely instrumental in the achievement of the scientific results. It permitted the completion of nearly one hundred runs, each of which was configured by means of a long and unique list of parameters and involved heavy data crunching that required up to several weeks of processing time on one or more workstations. Since the workstations were shared amongst a group of scientists, strategies were developed and implemented to optimize the required disk space, memory and processor time and to allow the automatic stopping and resuming of calculations. A big effort was also invested in the plotting capabilities of these tools which make the most of object oriented programming and metadata attached to the frontal indexes in order to offer a very straightforward and flexible way to explore the results. The figures are directly produced at a near publication standard which greatly eased the exploration of frontal signals exposed in chapter 5 and chapter 6. While developing these complex yet user-friendly tools, the author also had in mind their potential use by other scientists. Not only were these tools of great support to the conceptual approach developed in this work, but being encapsulated in a finished product fully tested and validated during the author's experimentations, they become potentially reusable by others and therefore even more useful scientifically. It is worth adding that the advanced plotting library that has been developed could be easily reused by anyone wishing to explore the variability of a spatial and temporal geo-physical quantity.

7.4 Where the study can be taken further

This section presents the directions to be followed in order to get more accurate results or to obtain additional ones from the presented methodology.

7.4.1 Improving the Level-4 products feature resolution knowledge

The main way to improve the confidence in the calculated frontal indexes is to select more accurately the parameters that have a significant effect in the detected fronts and in the calculation of the frontal indexes. The first parameter that could be improved is the assumed feature resolution of a SST image. When dealing with Level-4 SST products, this scale was estimated based on analyses of the present scales on a number of images. However the feature resolution is controlled by the state estimation algorithms that produce the SST field from Level-2 single-sensor images. It should be feasible for the Level-4 GHRSST data providers to calculate and record the amount of spatial smoothing introduced by their algorithms. It is a recommendation of the author of this thesis that a matrix of the feature resolution, for instance in kilometres, is attached to the SST as auxiliary data in the GHRSST Level-4 products. The routines developed and presented in this thesis could be easily adapted to cope with a spatially varying feature resolution. Such information would help extracting more accurate frontal indexes but would also improve the interpretation of such results because it would be known with precision where small scales are resolved or not by the input data set. When the feature

resolution is known with precision, the effect of the smoothing on the small scale fronts can be cancelled provided the spatial spectrum slope is known. The k^{-2} assumption was used in this thesis, it is confirmed to be valid by Autret (unpublished work) at the submesoscale and it was shown in this thesis to be valid between 10 and 50 km. Therefore it would be a significant improvement to use the precise value of smoothing in the frontal detection. However this would not allow measuring local departures from the average spectrum slope. This means that datasets with the finest feature resolution should be favoured. Level-3 SST products were shown to be the ultimate input data for front detection because they do not involve any kind of smoothing other than the sampling they are based on. Their feature resolution is perfectly known, and constantly equal to its minimum achievable: the spatial resolution of the image. The advantage of Level-3 products over Level-2 ones is their spatial and temporal coverage. Ideally, the frontal detection routines should be run on Level-3 time series of SST images. Unfortunately, the Level-3 SST products available to the science community are fairly limited, and this thesis is a strong call for the production and distribution of much more of them. It shall be stressed that the presented methodology and routines are perfectly adapted to the Level-3 images, even though they present different characteristics than the Level-4 ones, mostly involving missing data. In order to obtain a constant feature resolution on Level-3 images, the microwave measurements should be discarded. Therefore the Level-3 data used as input to detect fronts do not resolve cloudy regions at all. Care must be taken that this does not introduce biases in the resulting frontal indexes.

In order to quantify in absolute terms how accurately various Level-4 datasets resolve the fronts of all scales, one may identify a number of cloud-free Level-2 scenes to be used as control points. The comparison of the fronts detected on the Level-2 images with those detected on the considered Level-4 images could provide an estimate of the "frontal accuracy" of the Level-4 products. This method may introduce a bias as it would only consider cloud-free configurations. One way to overcome this bias is to generate Level-4 images from a sub-set of the input Level-2 images that are meant to be ingested in the OI process. The fronts from the Level-2 images which are not used in the generation of the Level-4 SST scenes can be used for comparison with the Level-4 fronts. This would be equivalent to comparing the fronts from a cloudy

region of a Level-4 image (where no IR data was available on a particular day) to the real front distribution over this region on this day. This approach is complex and would require the cooperation of the institutions in charge of the production of the Level-4 products.

7.4.2 Improving the knowledge of the frontal width

The other parameter that could be improved is the frontal width as it was shown that its uncertainty limits the ability of the dynamical frontal indexes to return values that can be quantitatively relied on. Two directions are suggested by the author: one could be to simply measure the frontal width directly on the SST image before using it in the calculation of the frontal index. This strategy is limited by the resolution of the SST image, for instance GHRSST Level-3 images provided at the global scale are projected on a grid of about 5 km resolution. The alternative direction is to estimate the frontal width by means of external knowledge, this could be by theoretical physical oceanography, with numerical models or dedicated in-situ measurements. Very high resolution Level-2 satellite SST could also be used to carry out such estimations.

7.4.3 Improving the understanding of the density compensation

This work would also greatly benefit from breakthroughs in the understanding of the phenomenon of compensation in the mixed layer. As the surface density gradient is estimated from the SST gradient assuming a constant salinity across the front, potential compensation of temperature and salinity across the fronts is ignored. The implemented strategy was to flag the cases where the MLD is deeper than 75 m because it is so far understood that compensation is more likely to occur in these conditions. Understanding the scales and conditions at which the compensation occurs, how often this happens and to which extent, is instrumental for the development of methodologies that allow recovering physical parameters from satellite SST observations with confidence. The exploitation of satellite Sea Surface Salinity (SSS) measurements is a potential solution, it is however strongly limited by the resolution of the recovered SSS so far (about 50 km spatial resolution for SMOS).

7.4.4 Developing the dynamical parameterizations and refining the assumptions

The dynamical parameterizations may be improved by a better understanding of the physics associated to fronts. The physicists are making outstanding progress in this domain, and more precise insights are likely to be published in the near future. It is the hope of the author that the physicists will continue to work toward the construction of reliable parameterizations of the mixed layer dynamics based on the surface density gradient and other quantities that can also be measured. Additional analyses to identify the conditions under which these parameterizations are valid or not would also build up the confidence in the dynamical frontal indexes. It should be added that parameterizations that are known to be accurate in limited areas and/or periods still have the potential to answer very important questions when combined with satellite observations. Section 2.2.4 presented a review of the studies based on the eSQG assumption which estimate the complete stream-function in the upperlayer of the ocean from a unique snapshot of the surface density anomaly. This method has the potential to be combined with satellite observations to recover surface currents as shown by Isern-Fontanet et al. (2006). This direction was not explored in this thesis because it is computationally very different from the implemented methods which rely on the detected fronts. This does not mean that the eSQG formulations do not present any interest, and the author recommends them to be analysed in view of their adaptation on systematic and global algorithms. Finally, it is worth adding that the future high resolution altimetry measurements will open a great potential for the use in synergy of high resolution SST and SSH in the context of frontal dynamics exploration.

7.4.5 Using the tools for regional studies

Finally, much more can be done with the tools as they were developed and presented. They can be taken to regional studies with customized data, parameters and indexes as a function of the local conditions and understanding. The extracted index can then be correlated with other local observational data such as ocean colour, wind or any in-situ measurement of relevance to gain knowledge on the relationship between the frontal activity and other phenomena. The question of the links between the fronts and the

Chapter 7

wind may be tackled by means of remote sensing data, even while taking into account the relative orientation of the wind and the fronts as is done by Capet et al. (2008b). As discussed in section 7.2, it would be very interesting to explore the causes of the seasonal and inter-annual variability of the frontal activity described in chapter 5 and chapter 6. In addition, when more confidence will be associated to the dynamic frontal indexes thanks to additional analyses, it will be worth to study them in a climatic perspective as done in chapter 6 with the FGI.

List of References

Aguirre, M., Baillion, Y., Berruti, B. & Drinkwater, M. (2009), Operational oceanography and the Sentinel-3 system, *in* 'Space technologies for the benefit of human society and Earth', Springer, pp. 75–98.

http://link.springer.com/chapter/10.1007/978-1-4020-9573-3_4

Allen, J., Smeed, D., Nurser, A., Zhang, J. & Rixen, M. (2001), 'Diagnosis of vertical velocities with the QG omega equation: an examination of the errors due to sampling strategy', *Deep Sea Research Part I: Oceanographic Research Papers* **48**(2), 315–346.

http://www.sciencedirect.com/science/article/pii/S0967063700000352

Aminou, D. (2002), 'MSG's SEVIRI instrument', *ESA Bulletin*(0376-4265) (111), 15–17.

Antonov, J., Seidov, D., Boyer, T., Locarnini, R., Mishonov, A., Garcia, H., Baranova, O., Zweng, M. & Johnson, D. (2006), 'World Ocean Atlas 2009, vol. 2: salinity', *NOAA Atlas NESDIS* **69**, 184.

Arbic, B. K., Polzin, K. L., Scott, R. B., Richman, J. G., & Shriver, J. F. (2013). 'On Eddy Viscosity, Energy Cascades, and the Horizontal Resolution of Gridded Satellite Altimeter Products'. *Journal of Physical Oceanography*, **43**(2).

Autret, E. & Piollé, J. (2007), 'Deliverable d2. 2.10 implementation of a global SST analysis WP 02 task 2.2'.

Belkin, I. (2002), 'New challenge: ocean fronts', *Journal of Marine Systems* **37**, 1–2.

Belkin, I. & Cornillon, P. C. (2003), 'SST fronts of the pacific coastal and marginal seas', *Pacific Oceanography* 1(2), 90–113.

Belkin, I. & Cornillon, P. C. (2004), 'Surface thermal fronts of the Okhotsk Sea', *Pacific Oceanography* **2**(1-2), 6–19.

Belkin, I. & Cornillon, P. C. (2005), 'Bering sea thermal fronts from Pathfinder data: Seasonal and interannual variability', *Pacific Oceanography* **3**(1), 6–20.

Belkin, I. M. & Gordon, A. L. (1996), 'Southern ocean fronts from the Greenwich meridian to Tasmania', *Journal of Geophysical Research* **101**(C2), 3675–3696. http://www.agu.org/pubs/crossref/1996/95JC02750.shtml

Bell, M., Hines, A. & Martin, M. (2003), *Variational assimilation evolving individual observations and their error estimates*, Ocean Applications, Meteorological Office.

Bell, M. J., Forbes, R. M. & Hines, A. (2000), 'Assessment of the FOAM global data assimilation system for real-time operational ocean forecasting', *Journal of Marine Systems* **25**(1), 1–22.

http://www.sciencedirect.com/science/article/pii/S0924796300000051

Bergeron, T. (1928), 'Uber die dreidimensional verknupfende wetteranalyse I.', *Geofys Publ.* **5**, 1–111.

Bindoff, N. L., Willebrand, J., Artale, V., Cazenave, A., Gregory, J. M., Gulev, S., Hanawa, K., Le Quere, C., Levitus, S., Nojiri, Y. et al. (2007), 'Observations: oceanic climate change and sea level. In: Climate Change 2007: The Physical Science Basis. Contribution of Working Group I to the Fourth Assessment Report of the Intergovernmental Panel on Climate Change [Solomon, S., D. Qin, M. Manning, Z. Chen, M. Marquis, K.B. Averyt, M. Tignor and H.L. Miller (eds.)]', *Cambridge University Press, Cambridge, United Kingdom and New York, NY, USA.* . http://nora.nerc.ac.uk/id/eprint/15400

Blumen, W. (1978), 'Uniform potential vorticity flow: Part I. theory of wave interactions and two-dimensional turbulence', *Journal of the Atmospheric Sciences* **35**(5), 774–783. http://journals.ametsoc.org/doi/abs/10.1175/1520-0469(1978)035%3C0774%3AUPVFPI%3E2.0.CO%3B2

Boccaletti, G., Ferrari, R. & Fox-Kemper, B. (2007), 'Mixed layer instabilities and restratification', *Journal of Physical Oceanography* **37**(9), 2228–2250. http://journals.ametsoc.org/doi/pdf/10.1175/JPO3101.1

Bontempi, P. S. & Yoder, J. A. (2004), 'Spatial variability in SEAWIFS imagery of the South Atlantic Bight as evidenced by gradients (fronts) in chlorophyll a and water-leaving radiance', *Deep Sea Research Part II: Topical Studies in Oceanography* **51**(10), 1019–1032.

http://www.sciencedirect.com/science/article/pii/S0967064504000980

Burls, N. & Reason, C. (2006), 'Sea surface temperature fronts in the midlatitude South Atlantic revealed by using microwave satellite data', *Journal of Geophysical Research* 111.

Canny, J. (1986), 'A computational approach to edge-detection', *IEEE Transactions On Pattern Analysis and Machine Intelligence* **8**, 679–698.

Capet, X., McWilliams, J., Molemaker, M. & Shchepetkin, A. (2008*a*), 'Mesoscale to submesoscale transition in the California Current system. part I: Flow structure, eddy flux, and observational tests', *Journal of Physical Oceanography* **38**(1), 29–43.

http://journals.ametsoc.org/doi/pdf/10.1175/2007JPO3671.1

Capet, X., McWilliams, J., Molemaker, M. & Shchepetkin, A. (2008*b*), 'Mesoscale to submesoscale transition in the California Current system. part II: Frontal processes', *Journal of Physical Oceanography* **38**(1), 44–64. http://journals.ametsoc.org/doi/abs/10.1175/2007JPO3672.1

Capet, X., McWilliams, J., Molemaker, M. & Shchepetkin, A. (2008*c*), 'Mesoscale to submesoscale transition in the California Current system. part III: Energy balance and flux', *Journal of Physical Oceanography* **38**(10), 2256–2269. http://journals.ametsoc.org/doi/abs/10.1175/2008JPO3810.1

Castelao, R. M. (2006), 'Sea surface temperature fronts in the California Current system from geostationary satellite observations', *Journal of Geophysical Research* 111.

Cayula, J.-F. & Cornillon, P. C. (1992), 'Edge detection algorithm for SST images', *Journal of Atmospheric and Oceanic Technology* **9**, 67–80.

Cayula, J.-F. & Cornillon, P. C. (1995), 'Multi-image edge detection for SST images', *Journal of Atmospheric and Oceanic Technology* **12**, 821–829.

Cayula, J. F., & Cornillon, P. (1996). 'Cloud detection from a sequence of SST images'. *Remote Sensing of Environment*, **55**(1), 80-88.

Chapron, B., Bingham, A., Collard, F., Donlon, C., Johannessen, J. A., Piolle, J.-F. & Reul, N. (2010), Ocean remote sensing data integration-examples and outlook, *in* 'OceanObs' 09: Sustained Ocean Observations and Information for Society (Vol. 1), Venice, Italy, 21-25 September 2009'.

Bibliography

http://archimer.ifremer.fr/doc/00029/14046/?utm_source=twitterfeed&utm_medium=twitter

Charney, J. G. (1948), 'On the scale of atmospheric motions', *Geosphys. publ. Oslo* **17(2)**, 1–17.

Chelton, D. B. & Wentz, F. J. (2005), 'Global microwave satellite observations of sea surface temperature for numerical weather prediction and climate research'.

http://scholarsarchive.library.oregonstate.edu/xmlui/handle/1957/27957

Cornillon, P. & Watts, R. (1987), 'Satellite thermal infrared and inverted echo sounder determinations of the Gulf Stream northern edge', *Journal of Atmospheric and Oceanic Technology* **4**(4), 712–723. http://journals.ametsoc.org/doi/abs/10.1175/1520-0426(1987)004%3C0712:STIAIE%3E2.0.CO%3B2

Cornillon, P. & Obenour, K. (2012), 'Thirty Years of Global SST Fronts and Gradients: A Sad Story', *GHRSST XIII workshop*, presentation.

de Boyer Montegut, C., Madec, G., Fischer, A. S., Lazar, A. & Iudicone, D. (2004), 'Mixed layer depth over the global ocean: An examination of profile data and a profile-based climatology', *Journal of Geophysical Research: Oceans* (1978–2012) **109**(C12).

http://onlinelibrary.wiley.com/doi/10.1029/2004JC002378/full

Donlon, C. J., Martin, M., Stark, J., Roberts-Jones, J., Fiedler, E. & Wimmer, W. (2012), 'The operational sea surface temperature and sea ice analysis (OSTIA) system', *Remote Sensing of Environment* **116**, 140–158. http://www.sciencedirect.com/science/article/pii/S0034425711002197

Donlon, C. J., Minnett, P. J., Gentemann, C., Nightingale, T. J., Barton, I. J., Ward, B. & Murray, M. J. (2002), 'Toward improved validation of satellite sea surface skin temperature measurements for climate research', *American Meteorologica Society* **15**.

Donlon, C., Rayner, N., Robinson, I., Poulter, D., Casey, K., Vazquez-Cuervo, J., Armstrong, E., Bingham, A., Arino, O., Gentemann, C. et al. (2007), 'The global ocean data assimilation experiment high-resolution sea surface temperature

pilot project', *Bulletin of the American Meteorological Society* **88**(8), 1197–1213. http://journals.ametsoc.org/doi/abs/10.1175/BAMS-88-8-1197

Eliassen, A. (1948), 'The quasi-static equations of motion', *Geofys* 17(3).

Ferrari, R. & Rudnick, D. L. (2000), 'Thermohaline variability in the upper ocean', *Journal of Geophysical Research: Oceans (1978–2012)* **105**(C7), 16857–16883. http://onlinelibrary.wiley.com/doi/10.1029/2000JC900057/full

Ferrari, R. & Wunsch, C. (2009), 'Ocean circulation kinetic energy: Reservoirs, sources, and sinks', *Annual Review of Fluid Mechanics* **41**, 253–282. http://www.annualreviews.org/doi/pdf/10.1146/annurev.fluid.40.111406.10 2139

Ferrari, R. & Wunsch, C. (2010), 'The distribution of eddy kinetic and potential energies in the global ocean', *Tellus A* **62**(2), 92–108.

Flament, P., Armi, L. & Washburn, L. (1985), 'The evolving structure of an upwelling filament', *Journal of Geophysical Research: Oceans (1978–2012)* **90**(C6), 11765–11778.

http://onlinelibrary.wiley.com/doi/10.1029/JC090iC06p11765/full

Fox-Kemper, B., Danabasoglu, G., Ferrari, R., Griffies, S., Hallberg, R., Holland, M., Maltrud, M., Peacock, S. & Samuels, B. (2011), 'Parameterization of mixed layer eddies. III: Implementation and impact in global ocean climate simulations', *Ocean Modelling* **39**(1), 61–78.

http://www.sciencedirect.com/science/article/pii/S1463500310001290

Fox-Kemper, B., & Ferrari, R. (2008). 'Parameterization of mixed layer eddies. Part II: Prognosis and impact'. *Journal of Physical Oceanography*, **38**(6).

Fox-Kemper, B., Ferrari, R. & Hallberg, R. (2008), 'Parameterization of mixed layer eddies. part I: Theory and diagnosis', *Journal of Physical Oceanography* **38**(6), 1145–1165.

http://journals.ametsoc.org/doi/abs/10.1175/2007JPO3792.1

Fu, L. L., Chelton, D. B., Le Traon, P. Y., & Morrow, R. (2010). 'Eddy dynamics from satellite altimetry'. *Oceanography*, **23**(4), 14-25.

Bibliography

Gentemann, C. L., Donlon, C. J., Stuart-Menteth, A. & Wentz, F. J. (2003), 'Diurnal signals in satellite sea surface temperature measurements', Geophysical Research Letters **30**(3), 1140.

http://www.agu.org/pubs/crossref/2003/2002GL016291.shtml

Glover, D., Doney, S., Nelson, N. & Wallis, A. (2008), 'Submesoscale anisotropy (fronts, eddies, and filaments) as observed near Bermuda with ocean color data'. paper presented at: 2008 ocean sciences meeting, *in* 'Proceedings of the 2008 Ocean Sciences Meeting', pp. 02–07.

Goodwin, G., K. K. B. . W. W. (2000), NOAA KLMusers guide (September 2000 revision), Technical report, NOAA.

http://www2.ncdc.noaa.gov/docs/podug/index.htm

Hakim, G. J., Snyder, C. & Muraki, D. J. (2002), 'A new surface model for cyclone-anticyclone asymmetry', *Journal of the atmospheric sciences* **59**(16), 2405–2420. http://journals.ametsoc.org/doi/abs/10.1175/1520-0469(2002)059%3C2405:ANSMFC%3E2.0.CO%3B2

Holyer, R. J. & Peckinpaugh, S. H. (1989), 'Edge detection applied to satellite imagery of the oceans', *IEEE Transactions on Geoscience and Remote Sensing* **27**(1), 46–56.

Hopkins, J., Challenor, P. G. & Shaw, A. G. P. (2010), 'A new statistical modeling approach to ocean front detection from SST satellite images', *Journal of Atmospheric and Oceanic Technology*.

Hoskins, B. (1982), 'The mathematical theory of frontogenesis', *Annual review of fluid mechanics* **14**(1), 131–151.

http://www.annualreviews.org/doi/abs/10.1146/annurev.fl.14.010182.00102

Hoskins, B., Draghici, I. & Davies, H. (1978), 'A new look at the ω-equation', *Quarterly Journal of the Royal Meteorological Society* **104**(439), 31–38. http://onlinelibrary.wiley.com/doi/10.1002/qj.49710443903/abstract

Hoskins, B. J. & Bretherton, F. P. (1972), 'Atmospheric frontogenesis models: Mathematical formulation and solution', *Journal of the Atmospheric Sciences*

29(1), 11–37. http://journals.ametsoc.org/doi/abs/10.1175/1520-0469(1972)029%3C0011%3AAFMMFA%3E2.0.CO%3B2

Hoskins, B. J. & Draghici, I. (1977), 'The forcing of ageostrophic motion according to the semi-geostrophic equations and in an isentropic coordinate model.', *Journal of Atmospheric Sciences* **34**, 1859–1867. http://adsabs.harvard.edu/abs/1977JAtS...34.1859H

Isaaks, E. H. & Srivastava, R. M. (1989), *Applied geostatistics*, Oxford University Press.

Isern-Fontanet, J., Chapron, B., Lapeyre, G. & Klein, P. (2006), 'Potential use of microwave sea surface temperatures for the estimation of ocean currents', *Geophysical Research Letters* **33**.

Isern-Fontanet, J., Lapeyre, G., Klein, P., Chapron, B. & Hecht, M. W. (2008), 'Three-dimensional reconstruction of oceanic mesoscale currents from surface information', *Journal of Geophysical Research* 113.

Johnston, T., Rudnick, D. L. & Pallàs-Sanz, E. (2011), 'Elevated mixing at a front', *Journal of Geophysical Research: Oceans (1978–2012)* **116**(C11). http://onlinelibrary.wiley.com/doi/10.1029/2011JC007192/full

Karl, T. R., Hassol, S. J., Miller, C. D. & Murray, W. L. (2006), 'Temperature trends in the lower atmosphere. steps for understanding and reconciling differences'.

Kawai, Y., Kawamura, H., Takahashi, S., Hosoda, K., Murakami, H., Kachi, M. & Guan, L. (2006), 'Satellite-based high-resolution global optimum interpolation sea surface temperature data', *Journal of Geophysical Research: Oceans (1978–2012)* 111(C6).

http://onlinelibrary.wiley.com/doi/10.1029/2005JC003313/full

Klein, P., Hua, B. L., Lapeyre, G., Capet, X., Le Gentil, S. & Sasaki, H. (2008), 'Upper ocean turbulence from high-resolution 3D simulations', *Journal of Physical Oceanography* **38**(8), 1748–1763.

http://journals.ametsoc.org/doi/pdf/10.1175/2007JPO3773.1

Klein, P., Isern-Fontanet, J., Lapeyre, G., Roullet, G., Danioux, E., Chapron, B., Le Gentil, S. & Sasaki, H. (2009), 'Diagnosis of vertical velocities in the upper

Bibliography

ocean from high resolution sea surface height', *Geophysical Research Letters* **36**(12), L12603.

http://www.agu.org/pubs/crossref/2009/2009GL038359.shtml

Klein, P. & Lapeyre, G. (2009), 'The oceanic vertical pump induced by mesoscale and submesoscale turbulence', *Annual Review of Marine Science*. 1, 351–375.

Lacasce, J. & Mahadevan, A. (2006), 'Estimating subsurface horizontal and vertical velocities from sea-surface temperature', *Journal of Marine Research* **64**.

Lapeyre, G. & Klein, P. (2006*a*), 'Dynamics of the upper oceanic layers in terms of surface quasigeostrophy theory', *Journal of Physical Oceanography* **36**.

Lapeyre, G. & Klein, P. (2006*b*), 'Impact of the small-scale elongated filaments on the oceanic vertical pump', *Journal of Marine Research* **64**.

Lapeyre, G., Klein, P. & Hua, B. L. (2006), 'Oceanic restratification forced by surface frontogenesis', *Journal of physical oceanography* **36**(8), 1577–1590. http://journals.ametsoc.org/doi/abs/10.1175/JPO2923.1

Le Borgne, P., Marsouin, A., Orain, F. & Roquet, H. (2012), 'Operational sea surface temperature bias adjustment using AATSR data', *Remote Sensing of Environment* **116**, 93–106.

http://www.sciencedirect.com/science/article/pii/S003442571100215X

Legal, C., Klein, P. & Treguier, A.-M. (2007), 'Diagnosis of the vertical motions in a mesoscale stirring region', *Journal of Physical Oceanography* **37**.

Lehahn, Y., d'Ovidio, F., Lévy, M. & Heifetz, E. (2007), 'Stirring of the northeast Atlantic spring bloom: A Lagrangian analysis based on multisatellite data', *Journal of Geophysical Research: Oceans (1978–2012)* **112**(C8). http://onlinelibrary.wiley.com/doi/10.1029/2006JC003927/full

Le Traon, P. Y., Nadal, F., & Ducet, N. (1998). 'An improved mapping method of multisatellite altimeter data'. *Journal of Atmospheric & Oceanic Technology*, 15(2).

Lévy, M., Klein, P. & Treguier, A.-M. (2001), 'Impact of sub-mesoscale physics on production and subduction of phytoplankton in an oligotrophic regime', *Journal of Marine Research* **59**, 535–565.

Mahadevan, A. & Tandon, A. (2006), 'An analysis of mechanisms for submesoscale vertical motion at ocean fronts', *Ocean Modelling* **14**, 241–256.

Mahadevan, A., Tandon, A. & Ferrari, R. (2010), 'Rapid changes in mixed layer stratification driven by submesoscale instabilities and winds', *Journal of Geophysical Research* **115**(C3), C03017.

http://www.agu.org/pubs/crossref/2010/2008JC005203.shtml

Mann, K. H. & Lazier, J. R. (2006), *Dynamics of Marine Ecosystems: Biological-Physical Interactions in the Oceans*, Blackwell Publishing.

Martin, A. P. & Richards, K. J. (2001), 'Mechanisms for vertical nutrient transport within a north Atlantic mesoscale eddy', *Deep Sea Research Part II: Topical Studies in Oceanography* **48**(4), 757–773.

http://www.sciencedirect.com/science/article/pii/S0967064500000965

McDougall, T., Jackett, D., Barker, P., Roberts-Thomson, C., Feistel, R. & Hallberg, R. (2010), 'A computationally efficient 48-term expression for the density of seawater in terms of conservative temperature, and related properties of seawater. submitted to', *Ocean Science Discussions*.

McGillicuddy, D., Robinson, A., Siegel, D., Jannasch, H., Johnson, R., Dickey, T., McNeil, J., Michaels, A. & Knap, A. (1998), 'Influence of mesoscale eddies on new production in the Sargasso sea', *Nature* **394**(6690), 263–266. http://www.nature.com/nature/journal/v394/n6690/abs/394263a0.html

McGillicuddy Jr, D., Anderson, L., Doney, S. & Maltrud, M. (2003), 'Eddy-driven sources and sinks of nutrients in the upper ocean: Results from a 0.1 resolution model of the North Atlantic', *Global Biogeochemical Cycles* **17**(2), 1035. http://www.agu.org/pubs/crossref/2003/2002GB001987.shtml

Merchant, C. & Harris, A. (1999), 'Toward the elimination of bias in satellite retrievals of sea surface temperature: 2. comparison with in situ measurements', *Journal of Geophysical Research: Oceans (1978–2012)*

104(C10), 23579–23590.

http://onlinelibrary.wiley.com/doi/10.1029/1999JC900106/full

Merchant, C., Harris, A., Murray, M. & Zavody, A. (1999), 'Toward the elimination of bias in satellite retrievals of sea surface temperature: 1. theory, modeling and interalgorithm comparison', *Journal of Geophysical Research: Oceans* (1978–2012) **104**(C10), 23565–23578.

http://onlinelibrary.wiley.com/doi/10.1029/1999JC900105/full

Merchant, C., Le Borgne, P., Marsouin, A. & Roquet, H. (2008), 'Optimal estimation of sea surface temperature from split-window observations', *Remote Sensing of Environment* 112(5), 2469–2484.

http://www.sciencedirect.com/science/article/pii/S0034425707004750

Miller, P. (2004), 'Multi-spectral front maps for automatic detection of ocean colour features from SEAWIFS, *International Journal of Remote Sensing* **25**(7-8), 1437–1442.

http://www.tandfonline.com/doi/abs/10.1080/01431160310001592409

Miller, P. (2009), 'Composite front maps for improved visibility of dynamic seasurface features on cloudy SEAWIFS and AVHRR data', *Journal of Marine Systems* **78**(3), 327–336.

http://www.sciencedirect.com/science/article/pii/S0924796309000694

Müller, P., McWilliams, J. & Molemaker, M. (2005), 'Routes to dissipation in the ocean: The 2D/3D turbulence conundrum', *Marine Turbulence* pp. 397–405.

Munk, W., Armi, L., Fischer, K. & Zachariasen, F. (2000), 'Spirals on the sea', *Proceedings of the Royal Society of London. Series A: Mathematical, Physical and Engineering Sciences* **456**(1997), 1217–1280.

http://rspa.royalsocietypublishing.org/content/456/1997/1217.short

Naveira Gabarato, A. C., Leach, H., Allen, J. T., Pollard, R. T. & Strass, V. H. (2001), 'Mesoscale subduction at the Antarctic polar front driven by baroclinic instability', *Journal of physical oceanography* **31**(8), 2087–2107.

http://journals.ametsoc.org/doi/abs/10.1175/1520-

0485(2001)031%3C2087%3AMSATAP%3E2.0.CO%3B2

Olson, D., Hitchcock, G., Mariano, A., Ashjian, C., Peng, G., Nero, R. & Podesta, G. (1994), 'Life on the edge: marine life and fronts', *Oceanography* **7**(2), 52–60. http://www.tos.org/oceanography/archive/7-2_olson.html

Pachauri, R. K. & Reisinger, A. (2007), 'Climate change 2007: Synthesis report. contribution of working groups I, II and III to the fourth assessment report of the intergovernmental panel on climate change', *Intergovernmental Panel on Climate Change*.

Pinot, J.-M., Tintore, J. & Wang, D.-P. (1996), 'A study of the omega equation for diagnosing vertical motions at ocean fronts', *Journal of marine research* **54**(2), 239–259.

http://www.ingentaconnect.com/content/jmr/jmr/1996/00000054/00000002/art00003

Pollard, R. T. & Regier, L. A. (1992), 'Vorticity and vertical circulation at an ocean front', *Journal of Physical Oceanography* **22**, 609–625.

Reynolds, R. W. & Chelton, D. B. (2010), 'Comparisons of daily sea surface temperature analyses for 2007-08', *Journal of Climate* **23**(13), 3545–3562. http://journals.ametsoc.org/doi/abs/10.1175/2010JCLI3294.1

Reynolds, R. W., Rayner, N. A., Smith, T. M., Stokes, D. C. & Wang, W. (2002), 'An improved in situ and satellite SST analysis for climate', *Journal of climate* **15**(13), 1609–1625. http://journals.ametsoc.org/doi/abs/10.1175/1520-0442(2002)015%3C1609:AIISAS%3E2.0.CO%3B2

Reynolds, R. W. & Smith, T. M. (1994), 'Improved global sea surface temperature analyses using optimum interpolation', *Journal of climate* **7**(6), 929–948. http://journals.ametsoc.org/doi/abs/10.1175/1520-0442(1994)007%3C0929%3AIGSSTA%3E2.0.CO%3B2

Reynolds, R. W., Smith, T. M., Liu, C., Chelton, D. B., Casey, K. S. & Schlax, M. G. (2007), 'Daily high-resolution-blended analyses for sea surface temperature', *Journal of Climate* **20**(22), 5473–5496. http://journals.ametsoc.org/doi/abs/10.1175/2007JCLI1824.1

Robinson, I., Piollé, J.-F., LeBorgne, P., Poulter, D., Donlon, C. & Arino, O. (2012), 'Widening the application of AATSR SST data to operational tasks

through the medspiration service', *Remote Sensing of Environment* **116**, 126–139. http://www.sciencedirect.com/science/article/pii/S0034425711002148

Robinson, I. S. (2010), *Discovering the Ocean from Space: The unique applications of satellite oceanography*, Springer.

Robinson, I. S. & Donlon, C. J. (2003), 'Global measurement of sea surface temperature from space: Some new perspectives', *The Global atmosphere and ocean system* **9**(1-2), 19–37.

http://www.tandfonline.com/doi/abs/10.1080/1023673031000080385

Roden, G. I. (1975), 'On North Pacific temperature, salinity, sound velocity and density fronts and their relation to the wind and energy flux fields', *Journal of Physical Oceanography* **5**, 557–571.

Rudnick, D. L. & Martin, J. P. (2002), 'On the horizontal density ratio in the upper ocean', *Dynamics of Atmospheres and Oceans* **36**, 3–21.

Shaw, A. & Vennell, R. (2001), 'Measurements of an oceanic front using a front-following algorithm for AVHRR SST imagery', *Remote sensing of environment* **75**(1), 47–62.

http://www.sciencedirect.com/science/article/pii/S0034425700001553

Shimada, T., Sakaida, F., Kawamura, H. & Okumurab, T. (2005), 'Application of an edge detection method to satellite images for distinguishing sea surface temperature fronts near the Japanese coast', *Remote Sensing of Environment* **98**, 21–34.

Simpson, J. (1990), 'On the accurate detection and enhancement of oceanic features observed in satellite data', *Remote Sensing of Environment* **33**(1), 17–33. http://www.sciencedirect.com/science/article/pii/003442579090052N

Smith, N. & Koblinsky, C. (2001), 'The ocean observing system for the 21st century, a consensus statement', *Observing the Oceans in the 21st Century* pp. 1–25.

Spall, M. A. (1995), 'Frontogenesis, subduction, and cross-front exchange at upper ocean fronts', *Journal of Geophysical Research: Oceans (1978–2012)* **100**(C2), 2543–2557.

http://onlinelibrary.wiley.com/doi/10.1029/94JC02860/full

Spall, M. A. (1997), 'Baroclinic jets in confluent flow', *Journal of physical oceanography* **27**(6), 1054–1071.

http://journals.ametsoc.org/doi/pdf/10.1175/1520-0485(1997)027%3C1054%3ABJICF%3E2.0.CO%3B2

Stammer, D. (1997). 'Global characteristics of ocean variability estimated from regional TOPEX/POSEIDON altimeter measurements'. *Journal of Physical Oceanography*, **27**(8), 1743-1769

Stark, J. D., Donlon, C. J., Martin, M. J. & McCulloch, M. E. (2007), Ostia: An operational, high resolution, real time, global sea surface temperature analysis system, *in* 'Oceans' 07 IEEE Aberdeen'.

Stegmann, P. & Ullman, D. (2004), 'Variability in chlorophyll and sea surface temperature fronts in the long island sound outflow region from satellite observations', *Journal of Geophysical Research: Oceans (1978–2012)* **109**(C7). http://www.agu.org/journals/jc/jc0407/2003JC001984/

Stone, P. H. (1966), 'On non-geostrophic baroclinic stability', *Journal of the Atmospheric Sciences* **23**(4), 390–400.

http://journals.ametsoc.org/doi/abs/10.1175/1520-0469(1966)023%3C0390:ONGBS%3E2.0.CO%3B2

Strass, V. H. (1994), 'Mesoscale instability and upwelling. II: Testing the diagnostics of vertical motion with a three-dimensional ocean front model', *Journal of physical oceanography* **24**(8), 1759–1767.

http://cat.inist.fr/?aModele=afficheN&cpsidt=4198984

Tandon, A. & Garrett, C. (1995), 'Geostrophic adjustment and restratification of a mixed layer with horizontal gradients above a stratified layer', *Journal of physical oceanography* **25**(10), 2229–2241.

http://cat.inist.fr/?aModele=afficheN&cpsidt=3703014

Thomas, L. & Ferrari, R. (2008), 'Friction, frontogenesis, and the stratification of the surface mixed layer', *Journal of Physical Oceanography* **38**(11), 2501–2518. http://journals.ametsoc.org/doi/abs/10.1175/2008JPO3797.1

Bibliography

Thomas, L. N. & Lee, C. M. (2005), 'Intensification of ocean fronts by downfront winds', *Journal of Physical Oceanography* **35**(6), 1086–1102. http://journals.ametsoc.org/doi/abs/10.1175/JPO2737.1

Thomas, L. N., Tandon, A. & Mahadevan, A. (2008), 'Submesoscale processes and dynamics', *Ocean Modeling in an Eddying Regime, Geophys. Monogr. Ser* **177**, 17–38.

Trenberth, K. E. (1997), 'The definition of El Nino', *Bulletin of the American Meteorological Society* **78**(12), 2771–2777.

http://journals.ametsoc.org/doi/abs/10.1175/1520-0477(1997)078%3C2771:TDOENO%3E2.0.CO;2

Turiel, A., Solé, J., Nieves, V., Ballabrera-Poy, J. & Garcá-Ladona, E. (2008), 'Tracking oceanic currents by singularity analysis of microwave sea surface temperature images', *Remote Sensing of Environment* **112**(5), 2246–2260. http://www.sciencedirect.com/science/article/pii/S0034425707004555

Ullman, D. S. & Cornillon, P. C. (2000), 'Evaluation of front detection methods for satellite-derived SST data using in situ observations', *Journal of Atmospheric and Oceanic Technology* **17**, 1667–1675. http://po.gso.uri.edu/poweb/PCC/pcornillon/publications.html

Ullman, D. S., Cornillon, P. C., & Shan, Z. (2007). 'On the characteristics of subtropical fronts in the North Atlantic'. *Journal of Geophysical Research: Oceans* (1978–2012), 112(C1).

Williams, R. G. & Follows, M. J. (2003), Physical transport of nutrients and the maintenance of biological production, *in* 'Ocean Biogeochemistry', Springer, pp. 19–51. http://link.springer.com/chapter/10.1007/978-3-642-55844-3_3

Woods, J. (1988), Mesocale upwelling and primary production, *in* 'Toward a theory on biological-physical interactions in the world ocean', Springer, pp. 7–38. http://link.springer.com/chapter/10.1007/978-94-009-3023-0_2